# Millimetre-Resolution Photonics-Assisted Radar

A thesis submitted to fulfil requirements for the degree of

*Doctor of Philosophy*

by

**Ziqian Zhang**

Supervisors: Dr Yang Liu and Prof Benjamin J. Eggleton
School of Physics, Faculty of Science
The University of Sydney

**Statement of Originality**

I, Ziqian Zhang, certify that to the best of my knowledge, the content of this thesis is my own work. This thesis has not been submitted for any degree or other purposes.

I certify that the intellectual content of this thesis is the product of my own work and that all the assistance received in preparing this thesis and sources have been acknowledged.

**List of Publications**

– Journal Papers

**Zhang, Z.**, Liu, Y., Stephens, T. and Eggleton, B. J., 2022. Photonic Radar for Contactless Vital Sign Detection. ***Nature Photonics***, DOI: 10.1038/s41566-023-01245-6100

**Zhang, Z.**, Liu, Y. and Eggleton, B. J., 2022. Photonic Generation of 30 GHz Bandwidth Stepped-Frequency Signals for Radar Applications. Journal of Lightwave Technology, 40(14), pp.4521-4527.

Liu, Y., **Zhang, Z.**, Burla, M. and Eggleton, B. J., 2022. 11-GHz-Bandwidth Photonic Radar using MHz Electronics. Laser & Photonics Reviews, 16(4), p.2100549. (Equally contributed)

– Conference Papers

**Zhang, Z.**, Liu, Y., Stephens, T. and Eggleton, B. J., 2023, May. Broadband Photonic Radar Enabling Millimeter Resolution for Vital Sign Detection. In the 2023 Conference on Lasers and Electro-Optics (CLEO). (***Invited Talk***)

**Zhang, Z.**, Liu, Y., and Eggleton, B. J., 2022, August. Optical frequency-shifting loop-based wideband-RF signal generation for radar applications. In the 13th International Conference on Information Optics and Photonics (CIOP). (***Invited Talk***)

**Zhang, Z.**, Liu, Y., and Eggleton, B. J., 2021, November. Centimetre spatial-resolution photonic radar using low-speed electronics. In 2021 The Australian and New Zealand Conference on Optics and Photonics (ANZCOP).

**Zhang, Z.**, Liu, Y., and Eggleton, B. J., 2020, August. Centimetre Spatial-Resolution Photonics-Based Stepped-Frequency Radar: Implementation and Comparison. In the 2020 Conference on Lasers and Electro-Optics Pacific Rim (CLEO-PR).

**Zhang, Z.**, Liu, Y., Burla, M., and Eggleton, B. J., 2020, May. 5.6-GHz-bandwidth photonic stepped-frequency radar using MHz-level frequency-shifting modulation. In the 2020 Conference on Lasers and Electro-Optics (CLEO). (***Invited Talk***)

**Authorship Attribution Statement**

– Chapter 4 of this thesis is published as [1, 2, 3].

  Y.L. and B.J.E. conceived the project; Y.L. and Z.Z. designed system architecture; Z.Z. and Y.L. performed experimental demonstrations, data processing, and results analysis; Y.L. and Z.Z wrote the manuscript with inputs and discussions from M.B. and B.J.E.; Y.L. and B.J.E. supervised the project. **Z. Z. and Y. L. contributed equally to this work.**

– Chapter 5 of this thesis is published as [4].

  Y.L. and B.J.E. conceived the project; Z.Z. and Y.L. designed the system structure; Z.Z. conducted the experiments; Z.Z. and Y.L. performed data analysis. Z.Z. wrote the manuscript with contributions from Y.L. and B.J.E.; B.J.E. and Y.L. supervised the project.

– Chapter 6 of this thesis is published as [5, 6].

  Y.L. and B.J.E. conceived the project; Z.Z. and Y.L. designed the system structure; Z.Z. conducted the experiments; Z.Z. and T.S. conducted the animal experiments; Z.Z., Y.L., and T.S. performed the data analysis; Z.Z. and Y.L. wrote the manuscript with contributions from B.J.E. and T.S.; Y.L. and B.J.E. supervised the project.

– Chapter 4 to Chapter 6 contain intellectual properties protected by the patent PCT/AU2021/050396.

  **Zhang, Z.**, Liu, Y., and Eggleton, B. J., A Radar System Having a Photonics-based Signal Generator, PCT/AU2021/050396.

[1] **Zhang, Z.**, Liu, Y., Burla, M. and Eggleton, B. J., 2020, May. 5.6-GHz-bandwidth photonic stepped-frequency radar using MHz-level frequency-shifting modulation. In the 2020 Conference on Lasers and Electro-Optics (CLEO) (pp. 1-2). Optical Society of America. (***Invited Talk***)

[2] **Zhang, Z.**, Liu, Y., Burla, M. and Eggleton, B. J., 2020, August. Centimetre-Spatial-Resolution Photonics-Based Stepped-Frequency Radar: Implementation and Comparison. In the 2020 Conference on Lasers and Electro-Optics Pacific Rim (CLEO-PR) (pp. 1-3). IEEE.

[3] Liu, Y., **Zhang, Z.**, Burla, M. and Eggleton, B.J., 2022. 11-GHz-Bandwidth Photonic Radar using MHz Electronics. Laser & Photonics Reviews, 16(4), p.2100549. (Co-first authorship)

[4] **Zhang, Z.**, Liu, Y. and Eggleton, B.J., 2022. Photonic Generation of 30 GHz Bandwidth Stepped-Frequency Signals for Radar Applications. Journal of Lightwave Technology, 40(14), pp.4521-4527.

[5] **Zhang, Z.**, Liu, Y., Stephens, T. and Eggleton, B. J., 2022. Photonic Radar for Contactless Vital Sign Detection. Accepted by ***Nature Photonics***, DOI: 10.1038/s41566-023-01245-6100

[6] **Zhang, Z.**, Liu, Y., Stephens, T. and Eggleton, B. J., 2023. Broadband Photonic Radar Enabling Millimeter Resolution for Vital Sign Detection. In the 2023 Conference on Lasers and Electro-Optics (CLEO). Optical Society of America. (***Invited Talk***)

In addition to the statements above, in cases where I am not the corresponding author of a published item, permission to include the published material has been granted by the corresponding author.

Name: Ziqian Zhang

Date: Wednesday 28$^{th}$ June, 2023

As the supervisor for the candidature upon which this thesis is based, I can confirm that the authorship attribution statements above are correct.

Name: Benjamin J. Eggleton

Date: Wednesday 28$^{th}$ June, 2023

**Acknowledgements**

Finishing my PhD journey would not have been possible without all the support from my parents, my wife, my supervisors - Professor Benjamin Eggleton and Dr Yang Liu, my friends, and my lovely colleagues. This journey has been fun and rewarding.

First and foremost, I want to express my deepest appreciation to my PhD supervisors, whose dedicated support throughout my research journey was instrumental. Their unparalleled patience, motivation, and profound knowledge served as the foundation for my progression. The journey, far from simple, was made possible through their exceptional mentorship.

I must recall a pivotal moment before my first invited talk presentation at CLEO when Ben shared a piece of wisdom that has since become my guiding philosophy: "What doesn't break you makes you a man". These profound words resonated with me deeply, fortifying my determination and resilience throughout my studies.

I extend additional gratitude to my secondary supervisor, Yang. Your unwavering dedication, commitment, and understanding were a source of constant support throughout this sometimes tumultuous journey. Your guidance saw me through the rough patches and enabled me to stay the course. Your impact cannot be overstated.

Further, I extend my heartfelt thanks to my colleagues, Oliver Bickerton, Matthew Garrett, Luke McKay, Eric Magi, Zihang Zhu, Mingqian Chen, James Coyte, Choon Kong Lai, Nicholas Athanasios, Alvaro Casas Bedoya, Moritz Merklein. They generously contributed their valuable insight and suggestions, providing support and standing by my side when it was most needed.

I must express my profound appreciation to my family, most notably to my wife, Fiona Chen, for their endless support, encouragement, and understanding. To my parents, Chi Zhang and Yun Zhang, my gratitude knows no bounds.

Lastly, but in no way less significant, I dedicate a special mention to my son, Ori Zhang, who graced this world upon the conclusion of my PhD. I penned this thesis listening to your early cries, a sound that motivated and inspired me. You are the most beautiful thing that has happened to me. It is during these moments that I have come to truly appreciate the extent of sacrifices your grandparents made for me. My dearest wish for you is not financial success or a significant contribution to the field of science but rather to

discover and pursue what truly brings you joy, fulfilment, and, most importantly, happiness in life.

**Abstract**

Radar is essential in various applications such as threat warning systems, anti-collision systems for driving assistance, airport security screening, and contactless vital sign detection for medical settings. Radar ranging systems emit microwave signals that are either time or frequency-modulated to gather information about the objects of interest from reflected signals, including their range and velocity. The distance and velocity information is encoded in the form of time delay and instantaneous phase variation on the returned analogue signals, which will then be extracted through digital signal processing.

The demand for high-resolution and real-time recognition in radar applications has been rapidly growing, driving the development of electronic radars with increased bandwidth, higher operating frequency, and improved reconfigurability. However, conventional electronic approaches are challenging to meet these requirements due to the limitations in synthesising and generating radar signals, limiting the radar's ranging performance. Direct digital synthesis (DDS) produces limited bandwidth signals, typically at sub-GHz levels, and voltage-controlled oscillators (VCO) exhibit poor time-frequency linearity, which usually degrades the radar ranging resolution and accuracy. Electronic frequency mixers and multiplexers are standard components for up-converting the baseband radar signal to a higher carrier frequency. However, the electronic mixers lead to elevated noise levels and harmonic spurs, which impair the signal purity and ultimately reduce the accuracy of the radar sensing system.

Microwave photonics-enabled radars have attracted considerable interest over the past decade, primarily because they offer numerous benefits compared to traditional electronic methods. Photonics-assisted techniques facilitate a broad fractional bandwidth at the optical carrier frequency and enable reconfigurable spectrum manipulation, producing wideband and high-resolution radar signals in various signal formats, such as linear-frequency modulated (LFM) and stepped-frequency (SF). These techniques also offer the flexibility to function across multiple frequency bands across the millimetre-wave region for radar performance enhancements, such as improved resolution and accuracy, superior penetration capabilities, and increased resilience against electronic countermeasures.

However, photonic-based methods for RF signal generation face some limitations, such as low time-frequency linearity owing to the

inherent current-frequency nonlinearity of lasers, restricted RF bandwidth, and limited long-term stability of the photonic frequency multipliers (electro-optic modulators), and difficulties in achieving extended time duration for long-range sensing with dispersion-based techniques. Therefore, a photonic approach offering ample bandwidth, system tunability, and high time-frequency linearity is highly desired for radar signal generation. Furthermore, from a practical perspective, eliminating the need for high-speed electronics, often found in photonic frequency multipliers, is preferable to reduce cost and system complexity and enable an optimal balance of size, weight, and power.

In response to these challenges, this thesis presents approaches for generating broadband radar signals with high time-frequency linearity, leveraging recirculated unidirectional optical frequency-shifted modulation. The effectiveness of these methods is demonstrated through high-resolution radar ranging, imaging, and vital sign detection. The photonics-assisted system enables flexible bandwidth tuning, spanning from sub-GHz to over 30 GHz, and necessitates only MHz-level driving electronics. The radar signals produced by this method offer millimetre-level range resolution and a real-time imaging rate of 200 frames per second, making it possible to detect rapidly moving objects with a high resolution based on the inverse synthetic aperture radar (ISAR) technique.

Further improvements to the system led to a high-performance radar with key metrics, such as time-frequency linearity, signal-to-noise ratio, and bandwidth comparable to the state-of-the-art bench-top electronic signal generators. This radar system, exhibiting millimetre-level resolution and micrometre accuracy, enables contactless vital sign detection, as demonstrated by its ability to precisely detect respiratory patterns from breathing simulators and a living body (human proxy) using a cane toad, which poses more challenges than human trials due to the animal's tiny reflection area. In the end, we showcase the potential of combining radar and LiDAR for sensor fusion, foreshadowing the future advancements of the demonstrated photonic radar system for improved sensing accuracy and system resilience.

# Contents

Chapter 1

# Introduction

This chapter provides a brief history of radar from the perspective of radar waveform development, tracing the evolution from the first continuous wave radar in the early 1900s to advanced technologies such as synthetic aperture radar and phased array. These historical developments demonstrate a wide range of applications of modern radar systems, spanning military to civilian industries, including construction and mining, aviation, materials and manufacturing, pharmaceuticals, and medical. Numerous emerging applications require modern high-resolution radar systems with improved performance — higher resolution, lower noise, and electromagnetic interference immunity — and smaller size, weight, and power consumption, which pose significant challenges to conventional microwave-integrated circuits. To overcome these challenges, the use of photonics in radar systems has emerged as a recent trend with the potential to significantly improve performance and maintain low size, weight, and power consumption. Photonics offers a strong candidate for the next-generation radar system, which is capable of meeting the needs of various applications in diverse industries.

## 1.1 A Brief History of Radar to the New Photonic Radar Era

Radio detection and range (Radar) technology was invented during the early twentieth century. The main function of radars is to transmit electromagnetic (EM) signals and detect echoes from objects of interest (targets) within the radiation coverage area [7, 8]. The detection of its echo reveals the presence of a target. Radars provide information about targets, such as range (distance), direction (using directive antenna patterns), velocity (measured by the Doppler effect), and target classification (analysing echoes and their variation with time).

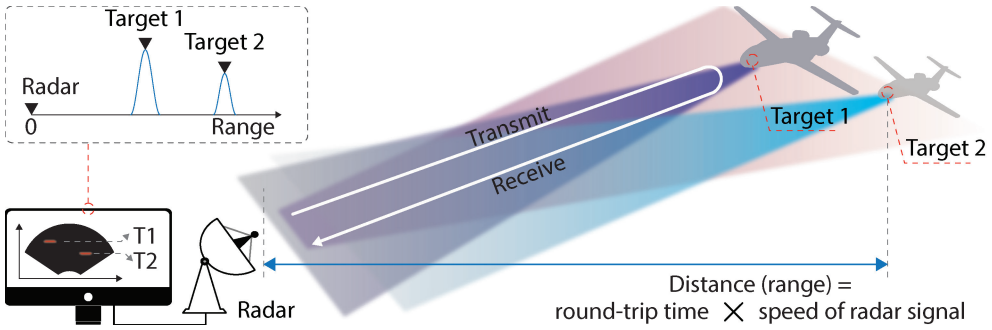


**Figure 1.1:** A primary radar system with a display reveals the presence and range of two aircraft. The underlying principle of radar range detection is calculating the time delay between the sent and received signals.

In the late 1800s, Heinrich Hertz conducted experiments to prove the existence of electromagnetic waves, which had been predicted by James Clerk Maxwell's theory of electromagnetism. Hertz's work was instrumental in developing radio communication technology, which was first used for long-distance communication using Morse code. Although scientists began to realise the potential of radio waves for detecting the presence of objects at a distance, it was not until the early 1900s that radar technology began to be developed in earnest.

During the early stages of radar development, the technology looked different from modern radar systems, such as weather forecasting radars and air traffic control radars that use parabolic or dish-shaped antennas. In contrast, the Klystron tube shown in Figure 1.2 was an early form of radar that utilised a specialised vacuum tube system to generate and amplify high-frequency electromagnetic signals. It was invented by American engineers Russell Varian and Sigurd Varian in 1937. Its

principle is based on velocity modulation, which involves modulating the electron beam's velocity in the tube where the input signal is used to generate high-frequency electromagnetic waves.

Klystron tubes can produce very high power outputs of hundreds of megawatts at microwave frequencies, making them ideal for radar applications. However, due to their relatively large size and high cost, they have primarily been replaced by solid-state devices like the transistor and the microwave integrated circuit (MIC), which are now widely used in various applications.

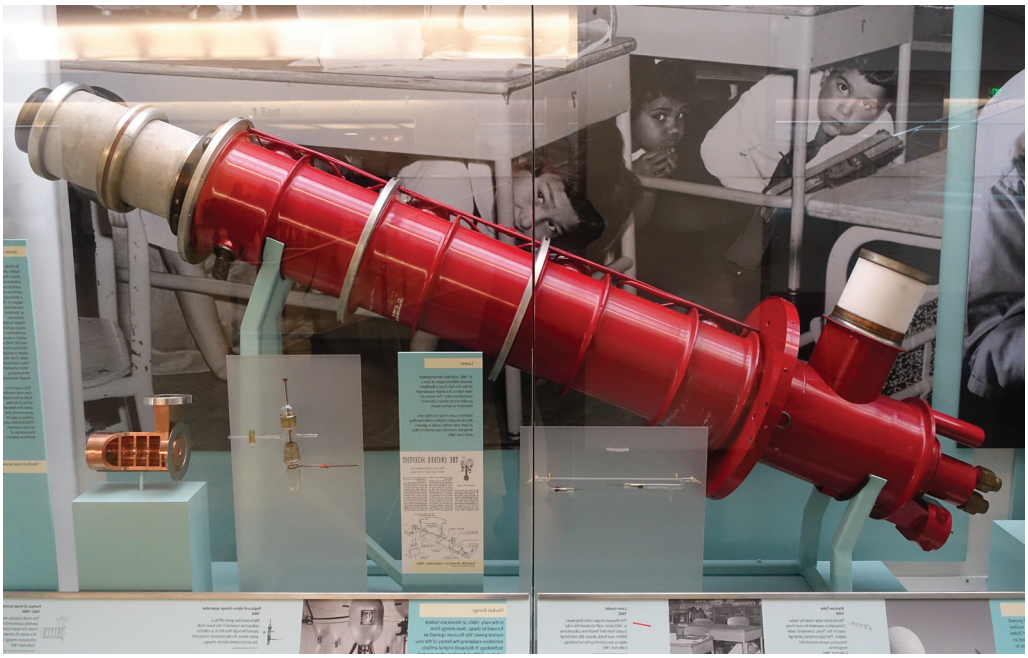

**Figure 1.2:** This Klystron Tube, manufactured by Varian Corporation in 1959, served for three years in the Thule radar station located in Greenland. The item is exhibited in the National Museum of American History, Washington, DC, USA. Attribution: Daderot, CC0, via Wikimedia Commons

One of the early inventors of radar technology was Christian Hülsmeyer, a German inventor who, in 1904, carried out one of the first radar demonstrations using a continuous wave (CW) system [9]. He called his device a "Telemobiloscope" and used it to detect ships in foggy conditions. Continuous waves could detect the existence of targets but not measure the range (distance) due to the lack of *timing marks* to time accurately the transmit and receive cycles and convert the cycle duration

into range with this type of signal.

A British radar pioneer, Robert Watson-Watt, invented pulsed radar in the early 1930s [10]. This technique utilises a waveform consisting of a series of burst, continuous waves. The pulse width can be characterised in seconds, with a pulse repetition frequency in Hertz. The pulse's envelope serves as a system reference clock on the time domain, providing a timing mark that can be used to calculate the range of the targets. On February 26, 1935, Watson-Watt and his team successfully demonstrated pulse radar at Daventry in England, detecting a Handley Page Heyford bomber aircraft at a range of 8 miles (13 km).

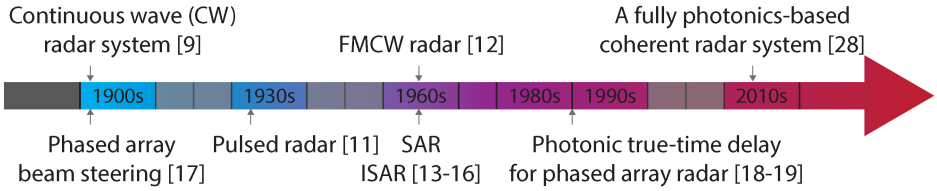


**Figure 1.3:** Brief development history of radar techniques in terms of resolution and performance improvement.

Pulsed radar systems were found to have limitations in detecting distant targets and distinguishing between multiple closely located targets along the same angle [11]. This was due to a fundamental trade-off between the average radiation power required for long-range detection and the shorter pulse width needed for high radar resolution to separate closely spaced targets. Balancing these factors with a fixed pulse repetition rate was challenging. Although shorter pulse widths improved range resolution, they significantly decreased the average transmitting power of the system, determining the maximum range. As a result, the traditional pulsed radar approach may not meet the range and resolution requirements of many real-world applications.

In the 1960s, frequency-modulated continuous waves (FMCWs) were developed and demonstrated to overcome the trade-off in pulsed radar systems [12]. FMCW systems continuously transmit a signal in the time domain, maintaining a high average power for long-range radar sensing. In the time-frequency domain, the frequency linearly changes over time within a specific bandwidth, inversely proportional to the range resolution. This simple waveform allows for high resolution (wideband) and high average power, making it widely used in various applications

such as air traffic control, automotive radar, and weather forecasting.

During the same historical period when the FMCW radar was invented, the need for high-resolution, two-dimensional imaging of the Earth's surface for military purposes also led to the invention of synthetic-aperture radar (SAR) by American mathematician and engineer, Carl A. Wiley [13, 14]. SAR is an imaging radar that is mounted on a moving platform and works by sequentially transmitting electromagnetic waves and collecting the backscattered echoes with the antenna. Due to the movement of the platform, the consecutive time of transmission and reception results in different positions. The received signals are then coherently combined to construct a virtual aperture that is much longer than the physical antenna length. This technology provides high-resolution, day-and-night, and weather-independent images with a wide range of applications, including geoscience and climate change research, environmental and Earth system monitoring, and planetary exploration [15].

Similarly to SAR, Inverse Synthetic Aperture Radar (ISAR) can be used to create a two-dimensional image of one or more targets [16]. The term "inverse" refers to a motion reversal between the radar system and the imaging target. In the context of ISAR, the target's motion provides the second dimension in addition to the range. Unlike SAR, the radar system in ISAR is stationary and not mounted on a moving platform like an aircraft. ISAR is commonly used in ground-based surveillance radar and maritime and air space monitoring to detect moving targets, such as ships and aircraft.

Phased array radar refers to an array of antenna elements fed with properly phase-controlled radio waves to form a beam that can steer in different directions based on constructive spatial interference [17]. The concept of phased array technology in radar has been around for almost as long as the first continuous-wave radar system, which was demonstrated in 1905 by Nobel laureate Karl Ferdinand Braun. Today, the phased array antenna system remains fascinating due to its ability to rapidly scan an area without the use of mechanical parts to rotate the radar antenna. It is faster than mechanical movement and has a fine spatial resolution (range resolution and beam width). Combining it with frequency-modulated radar systems improves range resolution, while increasing the number of antenna elements can enhance spatial resolution by forming a narrower beam lobe. Due to these unique features, phased array systems are widely used in military and civilian applications.

Achieving optimal spatial resolution in a phased array system requires

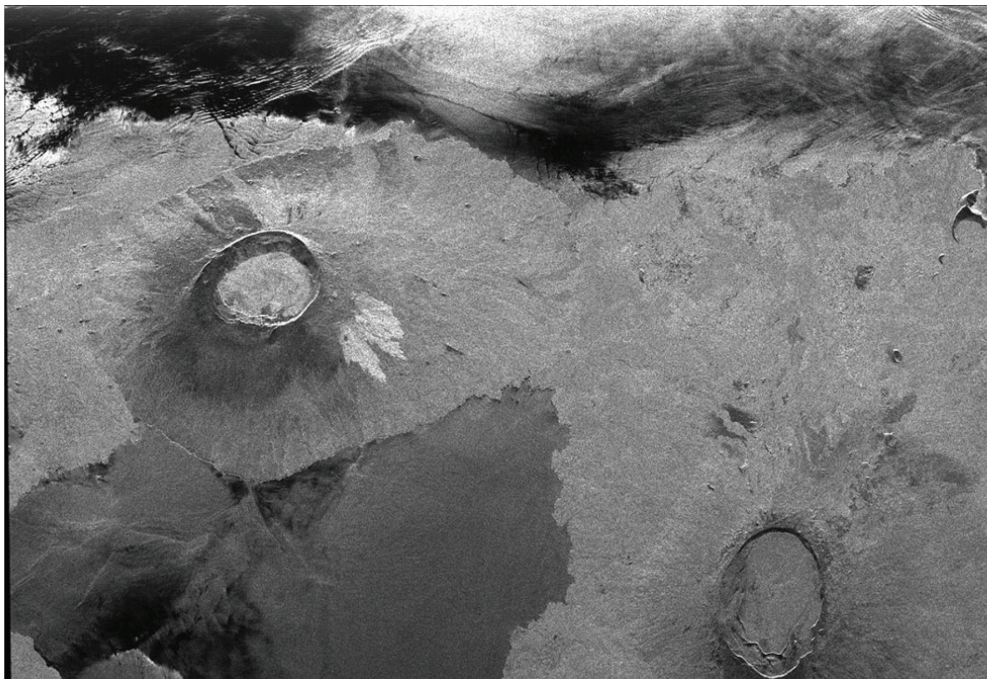

**Figure 1.4:** An example of a synthetic aperture radar image showing a portion of Isla Isabella in the western Galapagos Islands on the 40th orbit of the space shuttle Endeavour in 1996. Image credit: NASA.

fine range resolution and narrow beam width. The fine-range resolution requires a broader bandwidth radar signal. At the same time, a narrow beam width necessitates the use of multiple antenna elements, resulting in larger phased array systems.

To address these challenges, higher radar carrier frequencies have been used to reduce the size of each antenna element. However, this approach poses difficulties for conventional electronics, such as integrated circuits (ICs) and printed circuit boards (PCBs), which must process and distribute large fractional bandwidths of radar signals with low loss (less than 10 dB) and high isolation (greater than 60 dB) against electromagnetic interference (EMI) and crosstalk [18]. Coaxial cables, in particular, are problematic because they are highly susceptible to crosstalk between adjacent lines and are extremely lossy. For example, an 18 GHz signal can attenuate 1000 dB per kilometre in a coax cable with a 1 mm outer diameter, which could result in a heavy and bulky phased array backplate.

Therefore, photonics and optical fibres have been used early on to overcome the limitations faced by conventional electronics in phased array

systems. In the late 1980s, optoelectronic switching and fibre-based photonic true-time delay were introduced as solutions to these challenges [19]. Optical signals oscillating at hundreds of terahertz and ultrawide instantaneous bandwidths enable wideband analogue radiofrequency wave distribution and manipulation. In 1992, a 6-bit integrated photonic true-time delay unit was demonstrated, with a maximum delay of 30 ps and an insertion loss of less than 17 dB for 50 per cent of the fractional bandwidth (3-6 GHz) [18].

Photonics and optical fibres for radiofrequency distribution and manipulation occur earlier than their application in radar systems, which was first used in the radio-over-fibre (RFoF) experimental demonstrations in the 1970s [20, 21], and has since seen extensive growth and diversification across a broad range of applications [22, 23, 24, 25, 26, 27]. Photonics and optical fibres offer several advantages over conventional electronics, including small size (hundreds of $\mu$m in core diameter), low loss (0.25 dB/km @ 1550 nm compared with the coax cable's 1000 dB/km @ 18 GHz), tremendous bandwidth capacity, and immunity to EMI, making photonics and optical fibres ideal for the next-generation radar system [28].

In conclusion, from a historical perspective, the research and applications of radar have evolved from primarily military purposes in response to World War II to encompass more diverse industrial and civilian applications. For instance, industrial radar applications include ground-penetrating radar (GPR), used in the construction industry to detect underground utilities, pipes, and other buried objects. A weather radar is another application used in the aviation industry for detecting and tracking weather patterns and turbulence. Automotive radar is used in the automotive industry for collision avoidance, adaptive cruise control, and other advanced driver assistance systems. Similarly, maritime radar is used in the maritime industry for navigation, collision avoidance, and surveillance of vessel traffic, and air traffic control radar is used in the aviation industry for monitoring and controlling aircraft traffic.

More interestingly, recent trends have seen the development of near-range, high-resolution applications. For instance, radar can accurately measure the thickness of materials, such as metals and plastics, during manufacturing. Meanwhile, radar can detect defects and anomalies in materials that are not visible to the naked eye, such as cracks, voids, and inclusions [12]. Finally, radar technology has also been applied to vital sign detection, providing a non-contact method for monitoring the

respiration and heartbeat of people.

From a technical standpoint, photonic techniques for radar applications have become important due to high-speed and high-frequency signal processing [29, 30]; however, the electrical components can limit traditional electronic-based systems, which can cause performance degradation at high frequencies. In contrast, photonic-based systems offer advantages, including low-loss transmission, wide bandwidth, and electromagnetic interference immunity. Furthermore, photonic-based systems can be combined with other optical technologies, such as fibre-optic sensors, to enhance performance and sensing capabilities. As a result, photonic techniques are becoming an important area of research in developing future radar systems, particularly in applications that require high-resolution imaging and detection.

## 1.2 Thesis Background

Radar sensing has progressed into the millimetre-wave (MMW, 30-300 GHz) and terahertz-wave (THz-wave, 0.1-10 THz) regions to meet the growing demands of high spatial resolution imaging in real-world applications. To image small and kinetic targets such as drones with fast rotating propellers, centimetres, or millimetre-level range resolution is necessary. The requirements become even more challenging, for instance, for radar contactless vital sign detection of animals or humans, where the respiration displacement can be around one centimetre, and cardiac contraction is around sub-millimetre-level.

High-resolution radar imaging requires sufficient bandwidth and high spectral purity, reflected in a higher signal-to-noise ratio (SNR) and spurious-free dynamic range (SFDR). These characteristics are critical for preventing unwanted interference from coexisting with radar signals after processing, which could lead to ghost targets or false detections. In addition, high-resolution, wideband radars are preferable for cost-effectively transmitting, distributing, and duplicating radar signals with minimal loss and maximum efficiency in practical, real-world applications.

Radar systems that operate at multiple frequency bands are highly desirable as they offer the flexibility to adapt to different sensing environments and enable multi-functionality. For instance, lower-frequency radar is more effective at penetrating materials due to its longer wavelength, making it well-suited for penetrating detection or hybrid sensing-communication systems.

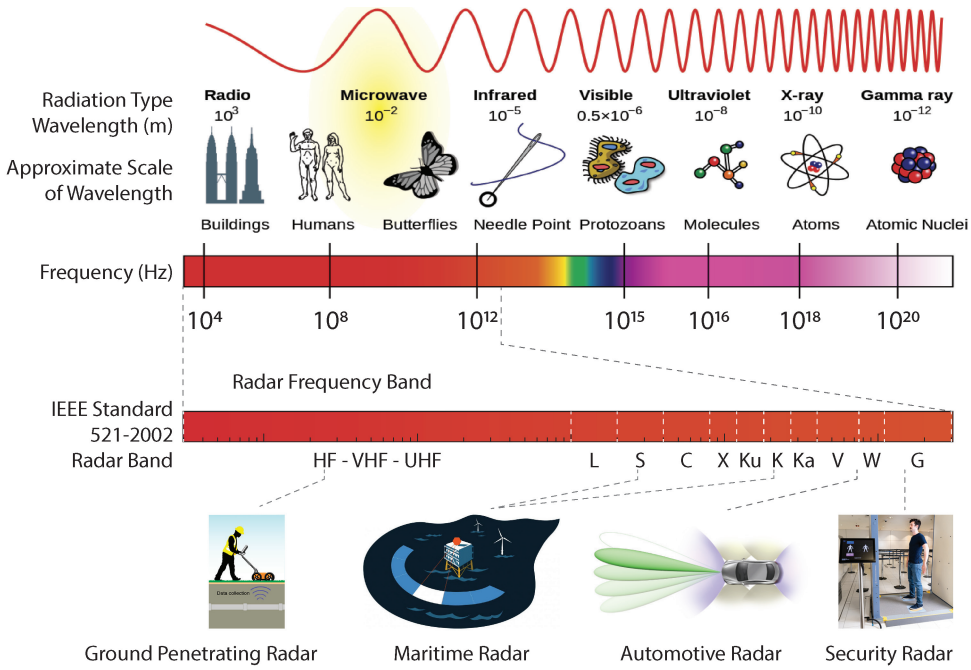


**Figure 1.5:** An illustrative figure demonstrating the signal's wavelength, objects in the same physical scale, and corresponding frequency. It also shows the radar frequency bands in the IEEE Standard 521-2002 with several application scenarios from the lower frequency HF-band to the higher frequency above the W-band.

However, conventional electronic techniques face significant challenges in meeting such requirements. The bandwidth of signal generation using digital microwave components, e.g., direct digital synthesizer (DDS), is limited below the gigahertz level, resulting in insufficient resolution above tens of centimetres. Alternative approaches that use voltage-controlled oscillators (VCO) have slightly improved bandwidth scalability in the baseband or intermediate band but suffer from poor time-frequency linearity, worsening the system's range performance and long-term stability. Multi-stage frequency mixing required in radar signal processing raises the system noise level by a few dB, which deteriorates accuracy and stability. Frequency multiplexing and spectrum stitching for bandwidth broadening introduce noise and spectrum spurs that compromise overall sensing accuracy and performance. Moreover, conventional electronic radars cannot achieve significant bandwidth tunability (fractional bandwidth >20%) and multi-band operation flexibility without requiring parallel or multiplexed electronic architectures that generally come with a high price tag and noticeable device footprint, which is unsuitable for mobile or distributed sensing scenarios.

Microwave photonics-enabled radar technology is becoming increasingly popular due to its numerous advantages over conventional electronic approaches. Photonic-assisted techniques provide wideband and high-resolution radar capabilities that generate various signal formats, such as linear-frequency modulated (LFM) and stepped-frequency (SF), and have the flexibility to operate at multiple frequency bands across the millimetre-wave region, allowing for performance optimisation based on the sensing environment.

Photonic-based radar signal generation approaches have shown significant advantages in generating ultra-wideband radar signals, achieving range resolution at millimetre levels. Dispersion-based approaches have an adequate bandwidth of up to 40 GHz, enabling super fine radar range resolution below 4 mm, but achieving extended time duration (>10 ns) for long-range (>1.5 meters) sensing applications is challenging and constrained by the dispersive element properties.

Frequency-sweeping light sources can achieve an even broader bandwidth with a sub-millimetre-level resolution by leveraging the flexibility of tunable lasers commonly used in light detection and ranging (LiDAR) systems. However, radar signals generated by such an approach require adaptive pre-distorted RF control signals for time-frequency linearity compensation to avoid degradation of sensing resolution and accuracy.

Another approach to photonic frequency multiplication uses the higher-order sidebands of electro-optic modulators to double or quadruple the radio-frequency input. Two sidebands of interest are selected to beat in a photodetector to broaden the radio-frequency input bandwidth, which has a relatively low system complexity, decent signal bandwidth (>12 GHz), and high time-frequency linearity. However, this technique typically relies on high-speed benchtop electronics and elaborately biased electro-optic modulators with limited RF bandwidth, long-term operational stability issues caused by bias-drifting, and high insertion loss in the optical link (>20 dB), and low optical-RF output efficiency in the photodetector.

A photonic digital-to-analogue converter (DAC) is an intriguing way to synthesise radar waveforms by imitating the principle of electronic digital-to-analogue converters. Existing approaches rely on high-speed digital pulse pattern generators and multiple electro-optic modulators to generate a series of weighted optical harmonics, in parallel or serial, to achieve arbitrary waveform synthesising. However, such an approach suffers from the trade-off between system stability and performance

regarding waveform quality (signal-to-noise ratio), the effective number of bits (ENOBs), and dynamic range.

Therefore, the next-generation high-performance radar system is highly desired for a photonic approach that provides adequate bandwidth, system tunability, high time-frequency linearity and avoids high-speed electronics.

## 1.3 Chapter Summaries

Chapter 1 presents an overview of radar waveform development, tracing its origins from the early 1900s to contemporary advancements. It highlights the emergence of photonics as a promising approach for substantially improving next-generation radar systems across various industries. The chapter explores this trend from both historical and technical perspectives, emphasising the potential of photonics-based technology in radar systems.

Chapter 2 lays the groundwork for understanding radar sensing, delving into the fundamentals, such as EM wave scattering and radar cross section (RCS), and their integration into radar equations to evaluate performance. The chapter compares widely-used waveform formats, analysing their capabilities and limitations, and introduces the inverse synthetic aperture radar (ISAR) imaging technique to facilitate a better understanding of imaging demonstrations in subsequent chapters.

Chapter 3 examines the potential of photonic technologies to improve radar systems, providing enhanced performance compared to conventional electronics. Understanding traditional electronic radar systems' fundamental components and limitations is crucial before exploring photonic alternatives. The chapter offers an overview of electronic and photonic radar operations, subsequently analysing the functionality and potential drawbacks of elementary components and building blocks, emphasising areas where photonics may present superior solutions.

Chapter 4 presents a novel photonics-based radar system with a bandwidth exceeding 11 GHz, driven and processed by MHz-level-electronics-based acoustic-optic modulation. This approach eliminates the need for ultra-fast GHz-speed electronics in wideband radar signal generation and processing, achieving centimetre-level spatial resolution and a real-time imaging rate of 200 frames per second. The innovative radar system enables high-resolution detection of rapidly moving objects, such

as unmanned aerial vehicle blades, and reduces system complexity. This development paves the way for next-generation broadband radars essential for various sensing applications, including autonomous driving, environmental monitoring, and vital sign detection, revolutionising radar capabilities.

Chapter 5 showcases a photonic SF waveform generation with a tunable bandwidth exceeding 30 GHz and MHz-level frequency steps for high-resolution radar detections. By stabilising polarisation and minimising inter-pulse interference in the optical frequency-shifting loop, the SNR of SF signals is significantly improved from 17 dB to 34 dB, achieving imaging performance comparable to high-speed equipment. The system offers a solution to overcome analogue bandwidth limitations of digital waveform generators for broadband radar signals, enabling high-resolution radar sensing while reducing hardware requirements.

Chapter 6 introduces a photonic vital sign detection system with high resolution and accuracy, enabling multi-target detection without compromising comfort or privacy. The system outperforms state-of-the-art electronic vital sign radars regarding bandwidth and flexibility. It supports radar and LiDAR sensing and demonstrates versatility and potential for hybrid detection and sensor fusion, ensuring consistent and accurate results. While radar offers better penetration through clothes and thin walls, it faces challenges in spatial information and susceptibility to interference. Conversely, LiDAR provides a superior range and spatial resolution but limited penetration abilities, making it a complementary approach to radar in vital sign detection.

Chapter 7 concludes the thesis and discusses the capabilities and challenges of synthesising wideband chirp waveforms using the frequency-shifting loop. It presents preliminary results using LiDAR in industrial quality control by successfully imaging a printed circuit board (PCB) and a 50-cent coin with micrometre-scale surface variations. The chapter explores integrating key components onto a photonic chip for compact and efficient implementations and examines the commercial potential of sensor fusion systems in sectors such as aged care, agriculture, and sleep apnoea diagnostics. This conclusion highlights the possibilities and challenges of implementing the frequency-shifting loop in diverse applications, aiming to unlock its full potential and contribute to innovative solutions across industries.

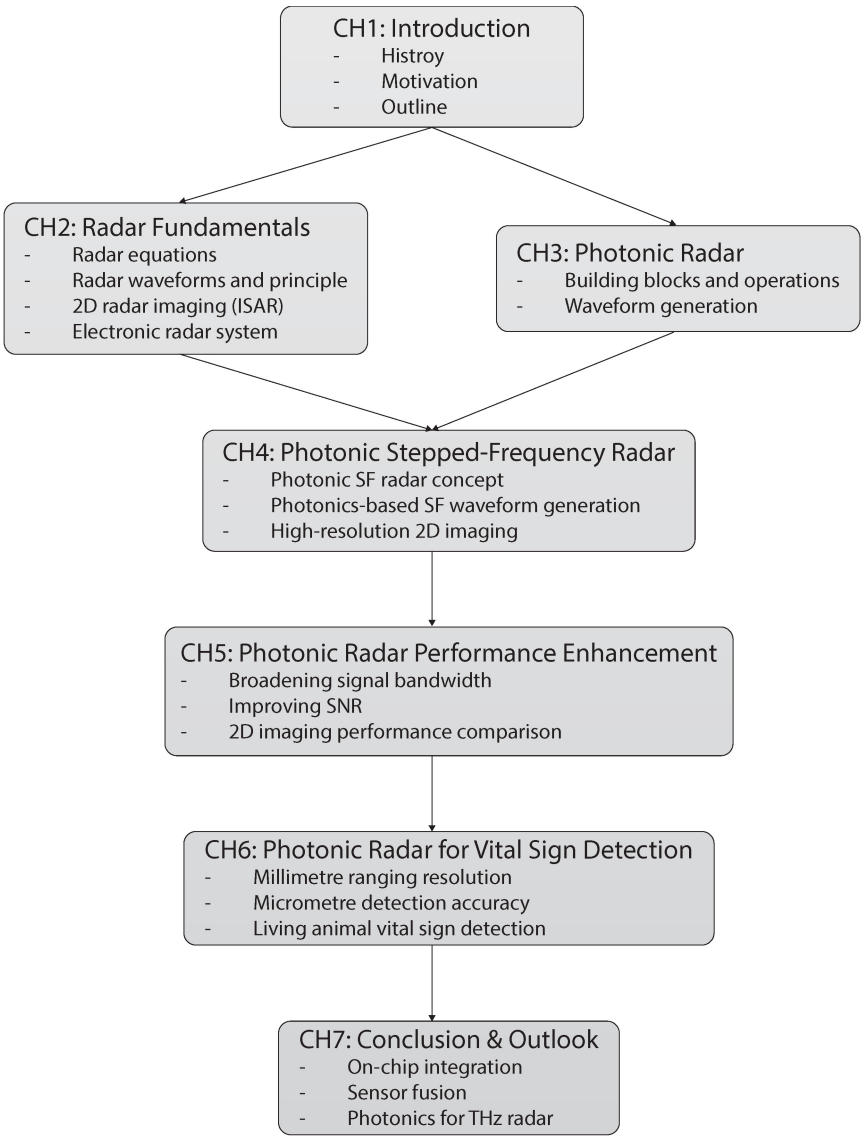


**Figure 1.6:** Thesis structural diagram

Chapter 2

# Radar Fundamentals

Radar operates on the principle of utilising electromagnetic (EM) waves, specifically radiofrequency (RF) waves ranging from 3 Hz to 300 GHz, which scatter off of a target or targets. The process of radar detection generally proceeds via the following steps:

- The radar emits a signal toward a target or object.
- Upon striking the target, the signal is scattered due to discontinuity of the electric and/or magnetic properties between the target and the surrounding medium.
- The radar captures and processes the scattered signals (or reflected signals) propagating in the direction of the receiving antenna.

The radar signal scatters differently depending on multiple factors, including the wavelength of the electromagnetic wave and the target's shape, size, and electromagnetic properties. Therefore, understanding and analysing the behaviour of scattered signals are essential for comprehending radar sensors' operation and performance and characterising the targets' properties.

This chapter aims to build a foundation for understanding radar sensing, starting with the basics of EM wave scattering and an essential radar parameter called radar cross section (RCS) used to characterise the detectability of an object quantitatively. We then integrate the RCS into the radar equations to analyse radar sensing performance regarding the maximum detection range and the system's signal-to-noise ratio.

Next, this chapter discusses several widely-used radar waveform formats, comparing them in terms of ranging principle, range resolution, range-

Doppler sensing capability, and ambiguity range. This chapter provides a comprehensive analysis of their strengths and limitations.

Then, this chapter introduces a two-dimensional imaging technique called inverse synthetic aperture radar (ISAR), which helps understand the imaging demonstrations in the later chapters.

In the final section, the chapter delves into the intricacies of the electronic frequency-modulated radar system, investigating the fundamental building blocks and operating principles. The following discussion examines these basic components' functionality and potential drawbacks, highlighting areas where photonics might offer superior solutions.

## 2.1 Electromagnetic (EM) Scattering

Scattering is a physical phenomenon in which an electromagnetic wave is deflected or redirected from its original path after encountering an obstacle or material with different electrical properties. It is the fundamental principle of radar detection and imaging, as radar relies solely on the scattered energy of the target of interest.

The interaction between electromagnetic radiation (such as radiofrequency waves and light) and matter can be explained by the classical mechanism of polarisation [31]. When charged particles (such as electrons and protons) associated with atoms and molecules are exposed to an electromagnetic field, they are stretched to form dipoles. Since atomic charges interact with each other, countless dipole combinations are created. This process also involves energy absorption, which forms a secondary field that may not propagate in the same direction or with the same phase as the initiating field. These interactions are dependent because the induced dipole fields affect neighbouring dipoles.

In radar, scattering is often characterised by the wavelength of the radar signals and the shape of the object being sensed. Three common types of scattering are optical region scattering [31], Mie scattering [32], and Rayleigh scattering [33], which occur when the wave's wavelength is smaller, comparable (within a few wavelengths), or much longer than the scatterer, respectively. In this thesis, the radar signals operate at a centre frequency of around 30 GHz, with a wavelength of about one centimetre. Since the size of the imaging objects in Chapters 4-6 is larger than the wavelength, the optical region scattering model would be a better fit. Due to the situation's complexity, it is common to characterise

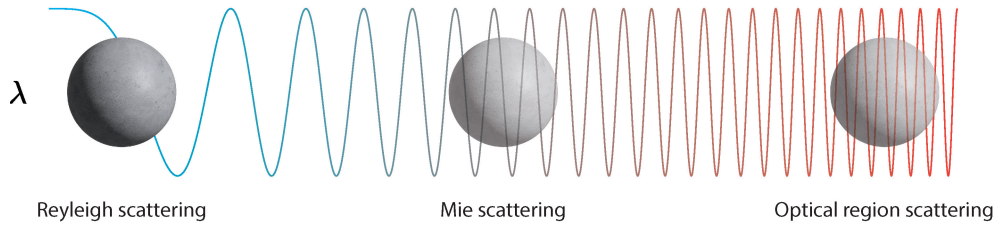


**Figure 2.1:** An illustrative figure showing the three common types of scattering concerning the signal's wavelength and the size of the object, i.e., Rayleigh scattering, Mie scattering, and optical region scattering, that exist in radar detection and imaging. $\lambda$ is the wavelength of the signal.

larger scattering bodies using various macroscopic quantities such as reflectivity, transmissivity, and index of refraction, which results from averaging millions of loosely coupled scatter events and typically defies a complete analytical description.

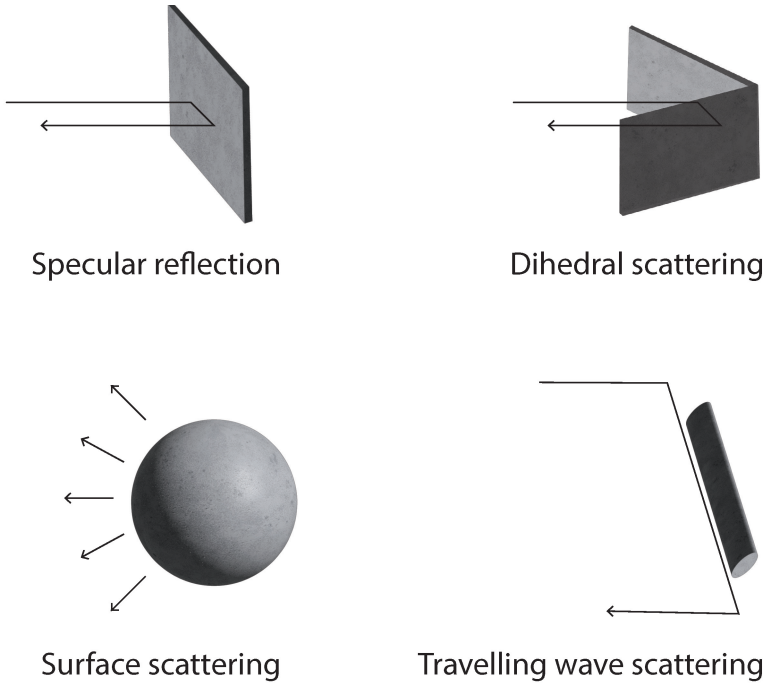


**Figure 2.2:** Several scattering objects' structures and the electromagnetic wave's propagation trajectory, including specular reflection from a planar surface, multiple scattering as demonstrated by the reflection from a dihedral reflector, surface scattering, and travelling wave scattering, e.g., from wires.

Scattering can also be classified based on the object's structure and the

electromagnetic wave's propagation trajectory, such as specular scattering, surface scattering (as shown in the inverse synthetic-aperture radar imaging demonstration in Chapters 4 and 5), edge diffraction, and travelling wave scattering. It is worth noting that most artificial objects provide mainly specular reflections, which consist of multiple localised scattering centres with strong energy reflection [16]. For example, the human chest area in the vital sign detection experiment in Chapter 6 could be considered specular scattering, i.e., the reflection from a planar surface.

## 2.2 Radar Cross Section (RCS)

Radar cross section (RCS) measures a target's detectability by a radar system based on its effective area for energy reflection. A larger RCS indicates that an object is easier to be detected, with higher levels of reflected energy, than a smaller RCS. For example, a cargo aircraft has an RCS of up to 100 $m^2$, while a bird's RCS is as low as 0.01 $m^2$, making the aircraft easier to be detected. [34, 35].

RCS is critical in various applications and has been widely studied. In target detection and identification, the RCS of different targets is measured to identify and classify them based on their radar signature. RCS is also used to test and improve the performance of radar systems. For example, a respiration simulator was designed with an RCS close to the actual human area of interest (chest) for preliminary testing of photonic radar for vital sign detection. This served as a pilot study before animal experiments were conducted, as described in Chapter 6 of this thesis.

### 2.2.1 Basic RCS Definitions

According to the IEEE Standard Definitions of Terms, RCS is defined as the portion of the scattering cross section corresponding to a specified polarisation component of the scattered wave for a given scatterer upon which a plane wave is incident.

Consider a target of interest located at a distance (range) of $d$, as illustrated, and covered by the radar beam, where the wavefront can be approximated as a plane wave, shown in Figure 2.3. By definition, the radar cross section (RCS), denoted as $\sigma$, is the ratio of the power ($P_r$) reflected by the target to the power density $W_i$ of a plane wave incident

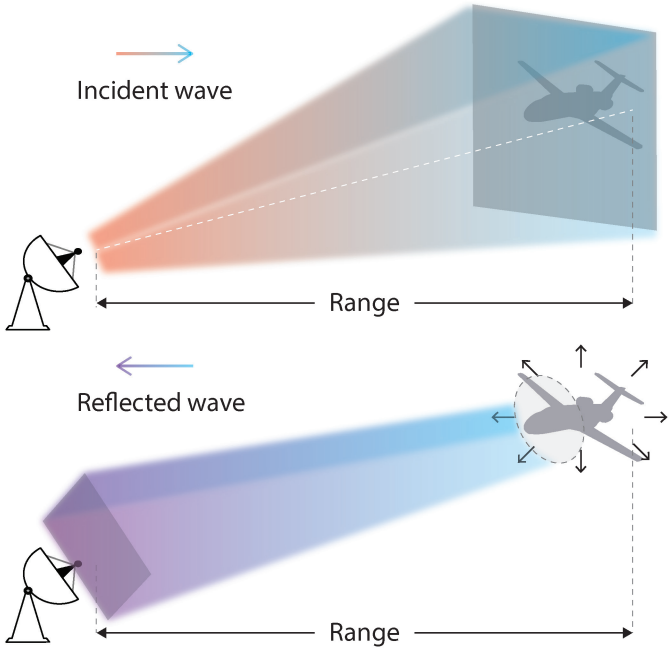


**Figure 2.3:** Illustration of the incident of radar signal onto an object and the following reflection.

on the target, which is expressed as follows [34, 16]:

$$\sigma = \frac{P_r}{W_i} \tag{2.1}$$

Assume the reflected radar signal scatters isotropically (in all directions). The reflected signal's power density, $W_s$, at the radar receiver is

$$W_s = \frac{P_r}{4\pi d^2} \tag{2.2}$$

By substituting Eq. (2.1), Eq. (2.2) can be rewritten as

$$W_s = \sigma \frac{W_i}{4\pi d^2} \tag{2.3}$$

Considering the power density of both the incident and reflected waves, which can be written as

$$W_i = \frac{E_i H_i}{2} = \frac{Y_0 |E_i|^2}{2} \tag{2.4}$$

and

$$W_s = \frac{E_s H_s}{2} = \frac{Y_0 |E_s|^2}{2} \tag{2.5}$$

where $E_i$ and $H_i$ are the strengths of the incident electric and magnetic fields. $Y_0$ is the admittance of free space and the unit of the power density is watts per square metre. By substituting Eq. (2.4) and Eq. (2.5), the RCS area can be written as

$$\sigma = 4\pi r^2 \frac{|E_s|^2}{|E_i|^2} \tag{2.6}$$

or

$$\sigma = 4\pi r^2 \frac{|H_s|^2}{|H_i|^2} \tag{2.7}$$

where both expressions do not consider polarisation. It is worth mentioning that an object's RCS is angle- and frequency-dependent. Therefore, the RCS of an object is characterised together with the look angle and the particular frequency of operation.

### 2.2.2 RCS of Simple Objects

The calculation of radar cross section (RCS) for objects of specific shapes is a critical step in the early stages of photonic radar development. Analytical expressions for simple-shaped objects are particularly important in investigating and evaluating the performance of a photonic radar prototype. For example, in a laboratory setting where the maximum radiation power is around 10 dBm for a signal operating at 30 GHz, it is crucial to select a simple-shaped object with a higher RCS to successfully detect the range of a target under such low-power conditions. This selection of a simple-shaped object with higher RCS can aid in the first photonic radar ranging demonstration and subsequent optimisation of the system's performance, such as improving the radar receiver's signal-to-noise ratio (SNR).

Calculating the RCS of a target involves solving Maxwell's equations with boundary conditions. As mentioned previously, the RCS of a target depends on its aspect angle, radar signal frequency (wavelength), and polarisation but is not necessarily related to its physical area. However, objects with simple geometries can be analysed using the physical area. When the object's size is larger than the wavelength, such as in the optical region scattering, the RCS of a perfect electric conductor (PEC) observed from certain directions (e.g., parallel viewing) can be estimated based on its physical area. The relationship between the estimated RCS of simple shaped objects and their physical areas is given by [36, 37]:

$$\sigma = G_e \cdot A = \frac{4\pi A^2}{\lambda^2} \tag{2.8}$$

| Object | Viewing Angle | RCS ($\sigma$) | Symbol |
|---|---|---|---|
| Sphere | Any | $\pi a^2$ | $a$: Radius |
| Cone | Axial | $\frac{\lambda^2}{16\pi} tan^4\theta$ | $\theta$: Cone half angle |
| Cylinder | Axial | $\frac{2\pi a L^2}{\lambda}$ | $a$: Radius; L:Height |
| Flat square plate | Axial | $\frac{4\pi a^4}{\lambda^2}$ | $a^2$: Plate area |
| Dihedral | Maximum | $\frac{8\pi a^2 b^2}{\lambda^2}$ | $a/b$: Length/width |
| Trihedral | Maximum | $\frac{4\pi a^4}{3\lambda^2}$ | $a$: Length |
| Square trihedral | Maximum | $\frac{12\pi a^4}{\lambda^2}$ | $a$: Length |

**Table 2.1:** Approximate RCS Formulas of several simple objects for particular aspects.

As shown in Table 2.1, the RCS of objects is mostly dependent on the viewing angle and wavelength. Therefore, a small change in the aspect angle could cause significant fluctuations in the RCS.

The analytic expression of the RCS of simple objects is a fascinating topic with numerous practical applications. The RCS measures the amount of electromagnetic radiation scattered by an object in a specific direction relative to a reference signal. The ability to calculate the RCS of simple objects is crucial because it provides insights into the scattering properties of more complex targets and can help characterise targets for real-world applications. For instance, in meteorology, the RCS of precipitation targets such as rain and snow can be used to determine their size, shape, and density. By measuring the RCS of precipitation targets, meteorologists can obtain information about the amount and type of precipitation in a specific area, which is essential for weather forecasting.

## 2.3 Radar Equations

Radar equations are a set of fundamental equations used to analyse and predict the performance of radar systems. These equations describe the relationship between the transmitted power, the target range, and the received signal strength of a radar system. Radar equations can be used to estimate the maximum range of a system, determine the minimum detectable signal, and understand the system's limitations [38, 39]. This knowledge is essential for designing, operating, and optimising radar

systems for specific applications. Therefore, *understanding radar equations is a crucial aspect of radar engineering for designing, developing, or operating (photonic) radar systems*.

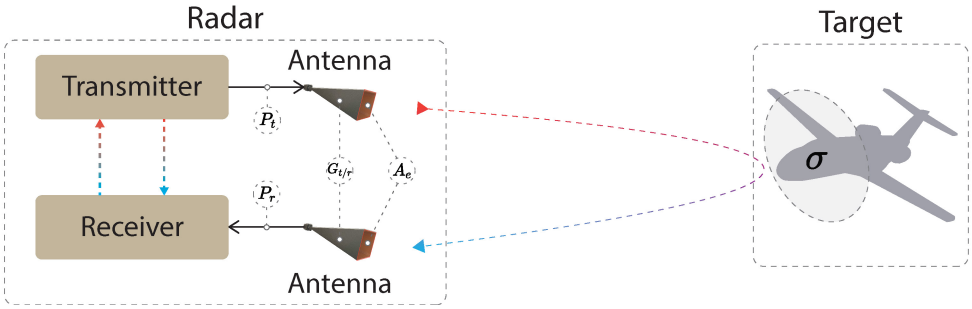


**Figure 2.4:** Block diagram of a fundamental radar with all the necessary basic building blocks, including a transmitter, a receiver, and antennas.

A fundamental radar system (Figure 2.4) consists of a transmitting antenna radiating the signal generated by a signal source and a receiving antenna passing through the returned energy to a radar receiver to extract information such as the target's range and velocity (Doppler).

If the power of the signal generated by the transmitter is denoted by $P_t$, which is radiated by an omnidirectional antenna, the power density $W_d$ at a distance $d$ from the radar system can be calculated using the formula:

$$W_d = \frac{P_t}{4\pi d^2} \tag{2.9}$$

where $4\pi d^2$ represents the surface area of a sphere with radius $d$, which is the total area over which the transmitted power is distributed. Dividing the transmitted power $P_t$ by the surface area of the sphere gives us the power density $W_d$ at a distance $d$ from the radar system.

Understanding that an omnidirectional antenna serves as an idealised mathematical model, radiating energy uniformly across all directions is necessary. This concept of an omnidirectional antenna proves beneficial for theoretical calculations and modelling purposes. However, it is essential to recognise that, in reality, such an antenna does not exist. Instead, actual antennas possess directional characteristics that can concentrate the transmitted energy, denoted as $P_t$, within specific directions or areas, for instance, the horn antenna shown in Figure 2.4.

As a result, when given the same amount of transmitted energy ($P_t$), antennas with improved EM wave confinement or directionality exhibit

a higher energy density compared to an omnidirectional antenna. This attribute is defined as antenna gain, represented by $G_t$ for transmitting or $G_r$ for receiving, respectively.

Consequently, the power density ($W_t^G$) at the target location when using an antenna with a gain of $G_t$ can be articulated as follows:

$$W_t^G = \frac{P_t G_t}{4\pi d^2} \tag{2.10}$$

Upon the signal hitting the target, a portion of the transmitted energy reflects and propagates back towards the radar system, which can be mathematically expressed as:

$$P_t^R = \frac{P_t G_t}{4\pi d^2} \cdot \sigma \tag{2.11}$$

where $\sigma$ represents the RCS, which measures the target size as seen by the radar. Assuming that the reflected energy re-radiates isotropically in all directions, the power density at the radar receiver can be calculated as follows:

$$W_r = \frac{P_t G_t \sigma}{(4\pi d^2)^2} \tag{2.12}$$

The radar-receiving antenna captures a fraction of the scattered energy associated with the antenna's effective capture area, denoted by $A_r$ (or $A_e$, shown in Figure 2.4). Consequently, the energy at the radar receiver is determined as follows:

$$P_r = \frac{P_t G_t \sigma A_r}{(4\pi d^2)^2} \tag{2.13}$$

Antenna theory establishes the relationship between antenna gain and effective area as follows:

$$G_t = \frac{4\pi A_t}{\lambda^2} \tag{2.14}$$

and

$$G_r = \frac{4\pi A_r}{\lambda^2} \tag{2.15}$$

where $G_t$ and $G_r$ denote the transmitting and receiving antenna gains, respectively, and $A_t$ denotes the antenna's effective illuminating area.

In practical scenarios, radar systems often employ monostatic or bistatic configurations, signifying that the transmitting and receiving antennas can be either co-located or positioned at separate locations, respectively.

*A monostatic radar configuration is utilised for the photonic radar demonstrations presented in this thesis*. Therefore, the following simplifications can be found:

$$G_t = G_r = G \tag{2.16}$$

and

$$A_t = A_r = A_e \tag{2.17}$$

Therefore, Eq. (2.13) can be rewritten as

$$P_r = \frac{P_t \sigma A_e^2}{4\pi d^4 \lambda^2} \tag{2.18}$$

or

$$P_r = \frac{P_t G^2 \sigma \lambda^2}{(4\pi)^3 d^4} \tag{2.19}$$

If $d_{max}$ denotes the maximum detectable range of a radar system, it occurs when the received power equals the minimum detectable signal $P^r_{min}$. Thus, the maximum radar range $d_{max}$ can be written as:

$$d_{max} = (\frac{P_t A_e^2 \sigma}{4\pi \lambda^2 P^r_{min}})^{\frac{1}{4}} \tag{2.20}$$

or

$$d_{max} = [\frac{P_t G^2 \sigma \lambda^2}{(4\pi)^3 P^r_{min}}]^{\frac{1}{4}} \tag{2.21}$$

or in terms of radar and target properties

$$d_{max} = [\frac{P_t G \sigma A_e}{(4\pi)^2 P^r_{min}}]^{\frac{1}{4}} \tag{2.22}$$

The minimal detectable signal level $P^r_{min}$ of a radar receiver refers to the lowest power level of a signal that the receiver can reliably detect and process. This minimum detectable signal is primarily determined by the noise present in the receiver, most commonly the thermal noise floor.

Thermal noise, also known as Johnson-Nyquist noise, is generated by the random motion of electrons and other charge carriers within electronic components, such as resistors and amplifiers.

$$P_{n,th} = kTB_n \tag{2.23}$$

where $P_{n,th}$ denotes for the available thermal-noise power, $k = 1.38 \times 10^{-23}$ joule/deg is the Boltzmann's constant, $B_n$ is the noise bandwidth of the receiver at temperature $T$. It should be noted that $B_n$ is an equivalent rectangular filter that has the same noise power as the radar receiver's filter. $B_n$ is not characterised by the engineering -3 dB bandwidth [38].

This noise is present in all electronic systems, including radar receivers, and sets a baseline for the receiver's sensitivity [40, 41].

The thermal noise floor represents the background noise level, which typically limits the receiver's ability to detect weak signals. For a radar receiver to reliably detect a target, the reflected signal's power level must be above the noise floor. This requirement is usually expressed as a signal-to-noise ratio, quantifying the relationship between the received signal power and the background noise power. However, other factors, such as system losses, component non-linearities, and external noise sources, can also affect the receiver's sensitivity and performance.

The total noise at the output of the receiver could be simplified as the product of the thermal-noise power from an ideal receiver and a factor called noise figure ($F_n$). The $F_n$ of a receiver is defined as

$$F_n = \frac{N_o}{kT_0B_nG_a} \tag{2.24}$$

where $F_n$ can be considered as the ratio between the noise out of the practical receiver and the noise out of the ideal receiver at a standard deviation temperature $T_0$, and $G_a$ is the available gain from the receiver (e.g., RF amplifiers) which is the ratio of the signal out and in. The noise $N_o$ is usually measured at the output of the intermediate frequency amplifier. Therefore, Eq. (2.24) could be rewritten as

$$F_n = \frac{S_i/N_i}{S_o/N_o} \tag{2.25}$$

where $S_i/N_i$ is the signal-to-noise ratio at the input of an ideal receiver and $S_o/N_o$ is the signal-to-noise ratio at the output for radar detection (signal processing). Then, the minimal detectable signal level of a radar receiver ($P^r_{min}$) can be characterised as corresponding to the minimum output signal-to-noise ratio of a practical receiver:

$$P^r_{min} = kT_0B_nF_n(\frac{S_o}{N_o})_{min} \tag{2.26}$$

then, Eq. (2.22) can be rewritten as

$$d_{max} = [\frac{P_t G \sigma A_e}{(4\pi)^2 k T_0 B_n F_n (S_o/N_o)_{min}}]^{\frac{1}{4}} \tag{2.27}$$

In practice, it is typical for radar system performance to be worse than predicted by the equations due to multiple factors, such as:

- Approximation of the incident plane wave: The theoretical calculations assume an ideal plane wave incident on the target. However, in real-world scenarios, the incident wave can deviate from this ideal representation, leading to discrepancies between the actual and predicted performance.
- Isotropic re-radiation of the target: The equations assume that the target re-radiates the incident energy uniformly in all directions (isotropically). In reality, targets can have complex shapes and materials, which may cause non-uniform re-radiation patterns. This non-uniformity can result in a reduced radar cross-section and a lower probability of detection.
- Device non-linearity: The electronic components used in radar systems, such as amplifiers and mixers, often exhibit non-linear behaviour, especially when operating near their limits. These non-linearities can introduce distortion and additional noise, which can degrade the overall performance of the radar system.
- Device temperature variations: Temperature fluctuations can cause changes in the performance characteristics of electronic components. For example, temperature variations can affect the noise figure, gain, and bandwidth of amplifiers, as well as the phase noise of oscillators. These changes can result in reduced sensitivity and an increased probability of false detections.

It is also worth noting that the radar's maximum range is related to the energy level that the radar receiver cannot detect. This concept is distinct from the ambiguity range associated with radar signal formats and parameters, which will be introduced in the following sections of this chapter. The ambiguity range refers to the maximum distance beyond which the radar system cannot uniquely determine a target's position due to ambiguities introduced by the radar's pulse repetition frequency and waveform characteristics. In contrast, the maximum range is determined by the radar's ability to detect weak signals above the noise floor and is influenced by factors such as transmitter power, antenna gain, and receiver sensitivity.

## 2.4 Radar Waveform, Ranging Principle, and Range Ambiguity

This section provides an in-depth analysis of radar waveforms and their role in determining the performance and capabilities of radar systems. Various waveforms are examined—including pulsed, frequency-modulated, stepped-frequency, stepped-frequency chirp, and pseudorandom signals—unveiling their distinct attributes and impact on ranging principles and ambiguity range. Investigating these waveforms and their fundamental principles enables a more profound understanding of radar design complexities. This section is particularly significant as it lays the foundation for photonics-based RF radar signal generation, shedding light on enhancing range resolution by exploiting the broad spectrum offered by photonics and optics. Additionally, this section sets the stage for the following chapters discussing existing photonic approaches for signal generation.

### 2.4.1 Continuous Wave (CW)

A continuous wave radar system transmits an unmodulated radio frequency signal ($f_0$), which reflects off objects and returns to the receiver. This enables the system to detect the presence of objects and track their movement (velocity or Doppler).

#### The Doppler Effect

The Doppler effect, a well-known phenomenon in the fields of optics and acoustics, is particularly relevant to continuous wave radar. This effect occurs when the oscillation source or the receiver (observer) is in motion, resulting in a frequency shift. Here, a general description of the Doppler frequency shift is provided. The total number of wavelengths is given by $2d/\lambda$, where $d$ represents the distance between the radar and target, and $\lambda$ denotes the wavelength of the continuous wave. Because one wavelength corresponds to a $2\pi$ angular excursion, the total phase excursion, $\varphi$, experienced by the electromagnetic wave as it travels along the two-way path, is $4\pi d/\lambda$.

When the target is in motion, the total phase excursion, $\varphi$, changes along with the distance, $d$. Consequently, the angular frequency, $\omega_d$,

characterising the Doppler effect, can be expressed as:

$$\omega_d = 2\pi f_d = \frac{\Delta\varphi}{\Delta t} = \frac{4\pi v_r}{\lambda} \tag{2.28}$$

where $f_d$ is the Doppler frequency shift in Hertz, $v_r$ is the target's relative velocity with respect to the radar, and $\Delta\varphi$ is the total phase change over time $\Delta t$. Then, Eq. (2.28) can be reorganised as

$$f_d = \frac{2v_r f_0}{c} \tag{2.29}$$

where $f_0$ is the signal's frequency of the continuous wave radar and $c$ is the propagation speed of radar signals (electromagnetic wave) in the propagation medium (299,792,458 metres per second in the vacuum). Here, it is worth mentioning that the Doppler shift is zero when the target moves perpendicularly to the radar line of sight.

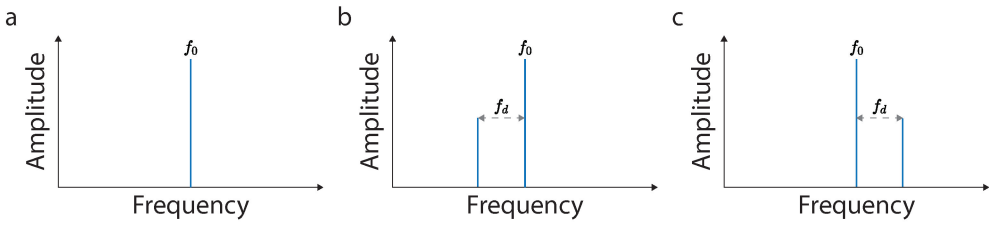


**Figure 2.5:** Illustration of the radar received spectra. **(a)** No target or target has no motion; **(b)** Target is receding; **(c)** Target is approaching.

### Advantages and Limitations of CW Radar

One advantage of continuous wave radar is its low system complexity compared to other radar systems, such as frequency-modulated or pulsed radar. This results in a more favourable size-weight-power ratio. Continuous wave radar can operate effectively with virtually no minimum range required for targets. Additionally, it can distinguish moving targets from stationary clutter due to its underlying operating principle.

A primary limitation of continuous wave radar is its inability to determine the range of a target. Nonetheless, range information is not essential for specific applications, making the low-cost continuous wave radar a more suitable choice. For example, speed camera systems utilise Doppler radar to measure a vehicle's speed, where range information is unnecessary.

Meanwhile, this limitation can be addressed by employing alternative signal formats that retain the Doppler sensing capability, such as pulsed and frequency-modulated radars. These options will be explored in the following sections.

### 2.4.2 Narrow Pulse

Pulsed radar is a widely used radar system that transmits short, powerful bursts of electromagnetic energy and listens for the echoes returned by targets. The waveform of a pulsed radar refers to the shape and structure of the transmitted electromagnetic energy during each pulse.

In a typical pulsed radar system, the waveform generally comprises a sequence of short, high-power pulses interspersed with comparatively long periods of silence. The radar system listens for target echoes during these quiet intervals. This article will outline the essential characteristics of pulsed radar waveforms, encompassing pulse width, pulse repetition frequency, pulse peak and average power, duty cycle, and the integration of pulse and frequency-modulated waveforms for enhanced performance, known as pulse compression.

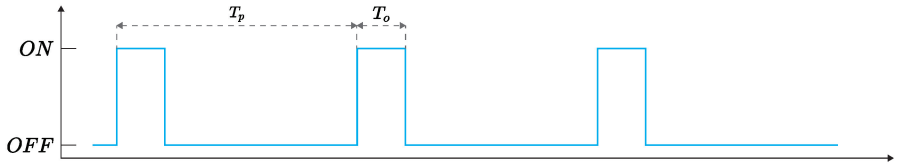


**Figure 2.6:** Pulse waveform envelope with a pulse width of $T_o$ and a repetition period of $T_p$.

Pulse radar waveform and pulsed radar are often used with time-gating techniques, i.e., turning on and off the radar receiver. Thus, the radar can focus on the reflection from specific ranges.

#### Basic Waveform Parameters

The pulse waveform is distinguished by its intermittent envelope, which alternates between active ($ON$) and silent ($OFF$) periods. This waveform is characterised by the pulse repetition frequency ($f_r = 1/T_p$) and the pulse duration ($T_o$), as illustrated in Figure 2.6. Another vital parameter is the pulse duty cycle ($\eta$), which represents the ratio between the pulse

width ($T_o$) and the pulse period ($T_p$):

$$\eta = \frac{T_o}{T_p} \tag{2.30}$$

The average power of a pulse waveform in a radar system significantly affects the system's performance, detection capabilities, and power consumption. It is calculated as the mean power of the transmitted pulses over time, accounting for both active and silent transmission intervals when the radar receives echoes. The peak power, denoted as $P_{pk}$, is the maximum power of a single transmitted pulse. The pulse average power, $P_{avg}$, can then be expressed as:

$$P_{avg} = P_{pk} \times \frac{T_o}{T_p} = P_{pk} \times \eta \tag{2.31}$$

Consequently, the average power can be regarded as the equivalent power level of a continuous wave signal, reflecting the system's overall energy consumption and signal-to-noise ratio. This parameter plays a crucial role in determining the radar's performance, as it impacts detection range, power efficiency, and potential thermal issues. Balancing the average power with other radar system parameters is essential to achieve the desired performance within the given constraints.

#### Ranging Principle Based on Time-of-Flight (ToF)

Pulse radar systems primarily function by determining the range of a target based on the time-of-flight (ToF) principle. This process begins with the radar emitting a brief, high-energy pulse of radio waves, which travel through the atmosphere at the speed of light. Upon encountering a target, such as an aircraft or a ship, a portion of the emitted signal is reflected toward the radar system. By measuring the time it takes for the initial pulse to travel to the target and return as an echo, the radar can accurately calculate the distance to the object. This is achieved by multiplying the round-trip time by the speed of light and dividing the result by two, considering that the signal has to travel to the target and back. In this way, pulse radar systems provide critical range information, enabling the tracking and detection of objects in real time.

Figure 2.7 presents a detailed visual overview of the core principles of radar range detection using pulsed waveforms and the time-of-flight method. The time-domain pulse waveform envelope depicted in Figure

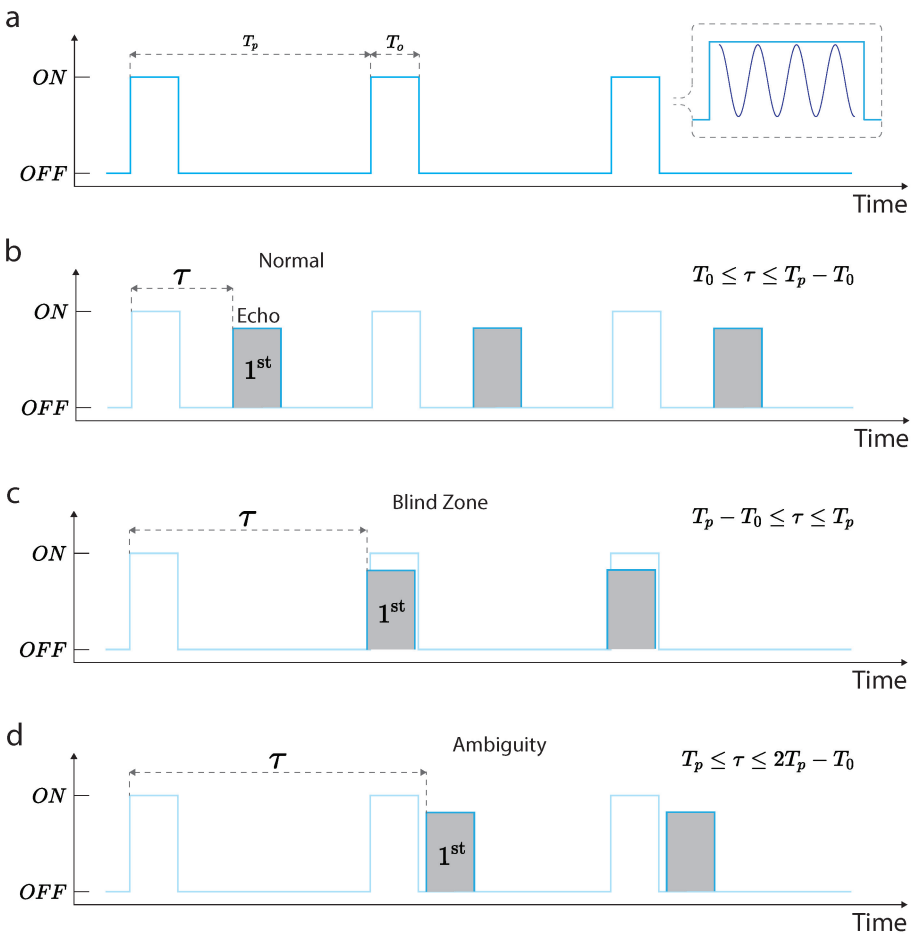


**Figure 2.7:** This figure presents an overview of the ranging principle in radar systems using pulsed waveforms and time-of-flight (ToF) concepts. **(a)** Time-domain pulse waveform envelope illustrating a single oscillating sine frequency, distinct from pulsed radar with intra-pulse frequency modulations; **(b)** Fundamental approach for determining the round-trip time, $\tau$, for accurate range detection; **(c)** A scenario resulting in a blind zone, where the target(s) may be missed due to overlapping received pulses with adjacent transmitted pulses; **(d)** A situation leading to range ambiguity, in which the actual round-trip time or range differs from the radar detection results.

2.7**a** emphasises a single oscillating sine frequency, setting it apart from radar systems utilising intra-pulse frequency modulations, i.e., pulse compression techniques, which will be explored in later sections of this chapter.

Under these time-of-flight ranging conditions, the target's range, denoted as $d$, can be computed using the product of the round-trip delay of the reflected signal (echo), represented by $\tau$, and the propagation speed of

the radar signal, denoted as $c$. This relationship is expressed as:

$$d = \frac{c\tau}{2} \tag{2.32}$$

where the denominator accounts for the two-way travel path of the radar signal.

Pulse radar systems exhibit a minimum detection range under certain conditions. The minimum detection range occurs when the receiver is not activated in a radar setting, 1) when a single antenna is used for both transmitting and receiving through an electronic switch and time-gating methods or 2) when the reference pulse (i.e., a copy of the transmitted pulse) is too close to the received pulse, making them indistinguishable.

In the first scenario, the minimal detection range is related to the switching time and pulse width $T_0$. In the second scenario, the range is typically half the pulse width, assuming a more realistic pulse shape with a noticeable roll-off time rather than the ideal rectangular envelope illustrated in Figure 2.7. The minimum detection range, $d_{min}$, is given by:

$$d_{min} = \frac{cT_0}{2} \tag{2.33}$$

It is essential to note that Equation 2.33 is not strictly accurate, as it does not account for variations in pulse shape. For example, if the pulse width is considerably longer than the pulse leading edge time, $T_{lead}$, and the pulse shape is asymmetrical, the minimum detection range is related to the threshold of the leading edge detection (assuming 50 per cent of the leading edge time):

$$d_{min} = \frac{c(T_0 - T_{lead}/2)}{2} \tag{2.34}$$

This equation better represents the minimum detection range in relation to pulse shape variations.

### Range Resolution, Blind Zone, and Ambiguity

The **range resolution** of pulse radar measures the radar's ability to distinguish between two closely spaced targets along the same line of sight. In other words, it is the minimum separation between two targets at which the radar can still identify them as separate entities. The transmitted pulse's duration and the pulse waveform characteristics primarily determine the range resolution.

For a simple pulse radar system, the range resolution, denoted as $\Delta d$, can be calculated using the following formula:

$$\Delta d = \frac{c \times T_0}{2} \tag{2.35}$$

According to this equation, shorter pulse widths, for instance, at nanosecond levels, result in better range resolution, allowing the radar to discern between targets closely located together. However, shorter pulses also contain less energy, which can limit the radar's maximum detection range. Therefore, a trade-off exists between range resolution and detection range when determining the optimal pulse width for a specific application.

Advanced radar systems, such as those employing pulse compression techniques, can achieve improved range resolution without sacrificing detection range. These systems use intra-pulse frequency modulation or phase coding to compress the received pulse, resulting in a more precise range estimation while maintaining a high transmitted pulse energy.

The pulsed radar experiences a *blind zone* when the time delay of the received pulse is close to an integer multiple of the pulse period $T_p$, as illustrated in Figure 2.7**(c)**. In such situations, the radar system may fail to detect targets within these range windows, leading to gaps in the radar's coverage.

As the target moves further away, range ambiguity becomes a concern. As shown in Figure 2.7**(d)**, the detected range is determined by the time delay associated with the nearest reference pulse, which may not accurately reflect the actual range of the target, thereby introducing ambiguity. Figure 2.7**(d)** demonstrates that a more extended pulse period (or lower pulse repetition rate) results in a more extensive maximum unambiguous range. As a result, the unambiguous range of the pulse radar system can be expressed as follows:

$$d_{\text{amb,max}} = \frac{cT_p}{2} \tag{2.36}$$

This equation shows the relationship between the pulse period and the radar system's maximum unambiguous range, highlighting the importance of balancing the pulse repetition rate to mitigate range ambiguity while maintaining effective target detection and tracking capabilities.

### 2.4.3 Stepped-Frequency (SF) Signal

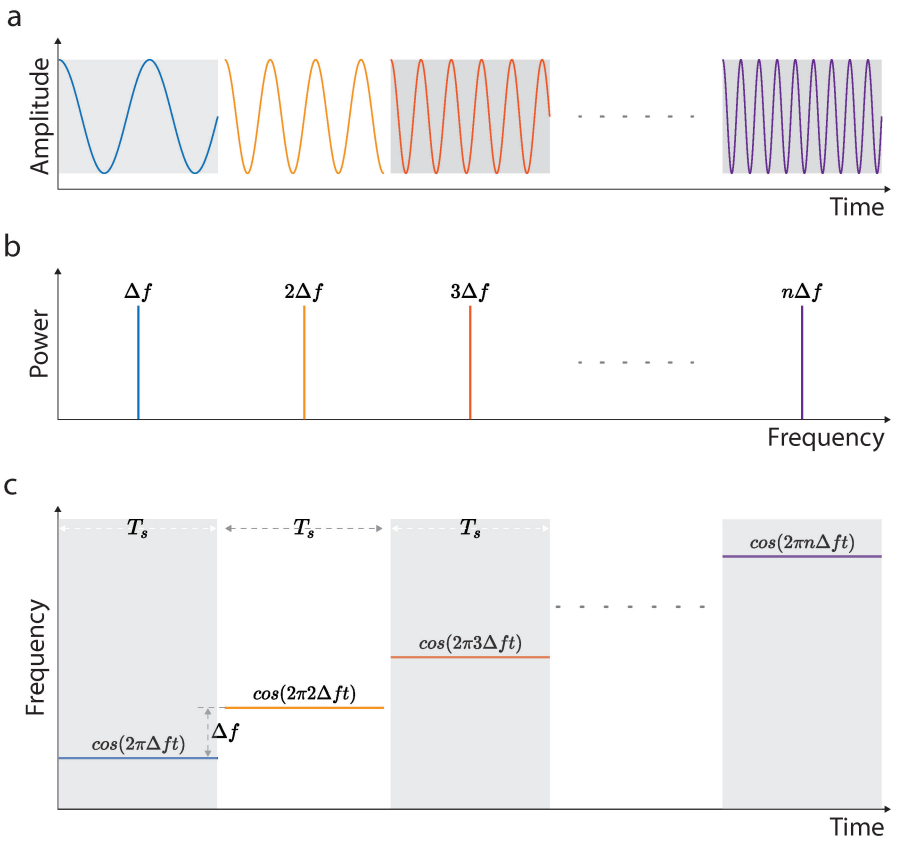


**Figure 2.8:** The stepped-frequency (SF) waveform in the **(a)** time domain, **(b)** frequency domain, and **(c)** time-frequency domain.

The stepped-frequency waveform is a highly effective technique employed in radar sensing to enhance target detection and resolution capabilities. This innovative approach entails transmitting a sequence of discrete frequency pulses, wherein each consecutive pulse experiences an incremental frequency shift determined by a predefined step size. The stepped-frequency waveform offers considerable advantages in various aspects, such as high-resolution imaging, enhanced clutter rejection, and heightened sensitivity. As a result, these benefits lead to a more precise depiction of the target's attributes, thus enabling high-performance radar imaging.

In order to better understand the stepped-frequency waveform, this section delves into an analysis of its core waveform parameters, elucidating

the principles of ranging, range resolution, range accuracy, and range ambiguity. These elements form the foundational basis for the photonic stepped-frequency radar systems discussed in subsequent chapters.

### Stepped-Frequency Waveform and Ranging Principle

The waveform shape of a stepped-frequency signal is characterised by a series of continuous wave pulses, where each pulse exhibits a constant frequency for its duration but varies in frequency between successive pulses (Figure 2.8). The frequency variation between these pulses follows a predetermined step size $\Delta f$, resulting in a staircase-like pattern across the entire sequence (Figure 2.8**c**). This stepped pattern comprises multiple frequency components, forming a wideband signal together.

The stepped-frequency signal can be expressed as:

$$s(t,n) = E(t,n)\Pi(t)e^{i2\pi(f_c+n\Delta f)t}e^{\theta_n} \tag{2.37}$$

where

$$\Pi(t) = \begin{cases} 1, & \text{if } t \in \left[(n-1)T_s, nT_s\right] \qquad (n = 1, 2...N) \\ 0, & \text{otherwise.} \end{cases} \tag{2.38}$$

represents an ideal rectangular windowing function, $f_c$ is the radar system's carrier frequency, $n$ is the step number (with a total of $N$ steps), $T_s$ is the time duration of each continuous wave pulse, and $E(t,n)$ denotes the energy of each pulse's envelope. Therefore, the stepped-frequency waveform has a synthesised bandwidth of $B = N \cdot \Delta f$. The analytical expression in Eq. (2.37) is preferable for theoretical analysis and numerical simulations. It can also be re-expressed from an engineering perspective as:

$$s_{\text{Eng}}(t,n) = A(t,n)\Pi(t)\cos[\,2\pi(f_c + n\Delta f)t + \theta_n] \tag{2.39}$$

where $A(t,n)$ denotes the envelope shape of each continuous wave pulse, and $\theta_n$ represents the initial phase of each stepped-frequency pulse. In subsequent discussions, $A(t,n)$ is simplified to a constant, $\alpha$.

Assuming a target is situated at a distance, $d$, the received stepped-frequency waveform can be expressed as:

$$r_{\text{Eng}}(t,n) = \beta \cdot \Pi(t)\cos[\,2\pi(f_c + n\Delta f)(t-\tau) + \theta_n] \tag{2.40}$$

where $\tau = 2d/c$ is the round-trip delay of the reflected stepped-frequency signal and $\beta$ represents the envelope of the received signal. The simplified transmitted signal is given by:

$$s_{\text{Eng}}(t,n) = \alpha \cdot \Pi(t) \cos[\, 2\pi(f_c + n\Delta f)t + \theta_n] \tag{2.41}$$

Once the radar receiver captures the reflected stepped-frequency signal, as described in Eq. (2.40), it combines the transmitted signal, given by Eq. (2.41), with the received signal to produce a demodulated signal. This process is executed in traditional electronic radar systems using a frequency mixer and an appropriate low-pass filter. However, in the photonic radar extensively explored in this thesis, the demodulation process is carried out by directing both signals into a device known as a photo-detector. This device generates a beat note between the two signals, effectively demodulating the reflected signal for further processing and analysis.

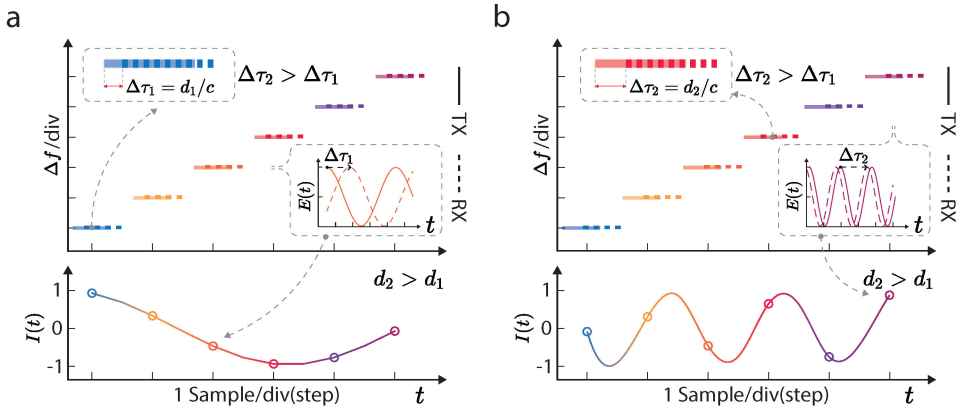


**Figure 2.9:** Stepped-frequency radar ranging principle, demonstrating the ranging at two distance instances, $d_1$ and $d_2$, respectively.

Regardless of the method employed, the demodulated signal, after passing through an appropriate low-pass filter, can be expressed as:

$$s_{\text{demo}}(t,n) = \gamma \cdot \Pi(t) \cos(2\pi n \Delta f \tau) \tag{2.42}$$

where $\gamma$ represents the output amplitude of the demodulated signal. As indicated by Eq. (2.42), a new phase term, $\omega_{\text{demo}} = 2\pi\Delta f\tau n$, emerges, where $\Delta f\tau$ remains constant, assuming no relative motion between the target and the radar system. The analogue-to-digital converter takes

one sample per frequency step (for each $n$), which corresponds to a sampling rate of $1/T_p$. Thus, the received signal can be regarded as a time-dependent phase change with respect to $n$ and the target's range $d$, which is shown in Figure 2.9.

The phase change rate, $\Delta f \tau$, corresponds to the target range, which can be extracted by examining the analytical form of Eq. (2.42). This extraction can be achieved either by utilising a coherent receiver [42] or by applying the Hilbert transform [43] followed by an inverse discrete Fourier transform (IDFT) [44, 16, 45].

### Range Resolution, Accuracy, and Ambiguity

**Range resolution** in radar refers to the system's ability to separate closely spaced targets in terms of their range. The resolution is inversely proportional to the signal's bandwidth for wideband radar systems employing linear frequency modulation and stepped frequency. This relationship is defined as follows [16]:

$$\Delta d = c/2\mathrm{B} \tag{2.43}$$

where $c$ represents the signal's propagation speed, and B is the total synthesised bandwidth. Therefore, enhancing the signal's bandwidth can improve the radar's range resolution, enabling more accurate target detection and characterisation in various applications.

**Range accuracy**, distinct from range resolution, denotes the uncertainty in the measured range in comparison to the actual value, characterised by a probability distribution. In the context of a stepped-frequency radar system, the range accuracy (or error) can be quantified using a root-mean-square (RMS) value [44]:

$$\delta d = \frac{c}{2\mathrm{B}\sqrt{2\mathrm{SNR}}} \tag{2.44}$$

where SNR represents the signal-to-noise ratio of the detected radio frequency signals. The above equation demonstrates that radar-ranging accuracy can be improved by augmenting the signal's bandwidth and SNR. Enhanced range accuracy is crucial for various applications, as it allows for a more precise estimation of the target's position, contributing to better situational awareness and decision-making in both civilian and military contexts. Optimising the radar system's parameters, such as bandwidth and SNR, can achieve higher performance levels and more excellent reliability in challenging operational environments.

The **unambiguous range** represents a radar system's maximum range to accurately determine target positions without encountering range ambiguities. In the context of a stepped-frequency radar, the maximum unambiguous range can be analysed as follows. Based on Eq. (2.42), the demodulation process allows for the extraction of phase differences between transmitted and received signals, which can be expressed as:

$$\omega_n = 2\pi \cdot n\Delta f \cdot \frac{2d}{c} \tag{2.45}$$

where $n = 1, 2, ...N$, $N\Delta f$ denotes the total bandwidth, $\Delta f$ is the frequency step, $d$ is the target distance, and $c$ is the propagation speed of the radio frequency signal.

Eq. (2.45) can provide insights into the unambiguous range associated with using stepped-frequency signals for detection. Assuming a relative distance change to the original location $d$ as $\Delta d$, the corresponding phase changes can be described as [46]:

$$\Delta\omega = 2\pi \cdot n\Delta f \cdot \frac{2\Delta d}{c}, \tag{2.46}$$

If the relative phase changes exceed the period ($2\pi$), ambiguities are introduced ($\Delta\omega > 2\pi$). By substituting the maximum phase changes, $2\pi$, into Eq. (2.46) and isolating $\Delta d$, the unambiguous range can be expressed as:

$$\Delta d_{max} = \frac{c}{2\Delta f}. \tag{2.47}$$

This equation highlights the relationship between the unambiguous range, the propagation speed of the RF signal, and the frequency step, offering insights into the factors that can influence range ambiguity in stepped-frequency radar systems.

Compared to conventional pulse radar systems, stepped-frequency radar achieves enhanced range resolution, which is not limited by pulse width. This allows the radar to distinguish targets more accurately based on their range. Utilising multiple frequency steps, the radar spreads the overall transmitted energy across a broader frequency range at different times, making it more difficult to intercept and counteract hostile electronic systems or countermeasures.

### 2.4.4 Linear Frequency-Modulated (LFM) Signal

More accurate range measurements can be achieved using sharper and more distinct timing marks. This is because the timing marks allow the

system to identify the time of transmission and return. However, a more distinct timing mark often results in a broader transmitted spectrum. By leveraging the properties of the Fourier transform, a more accurate time or range can be measured.

The spectrum of a narrowband continuous-wave radar waveform can be broadened by applying frequency modulations. For example, stepped-frequency and other frequency-modulated signals are widely used in radar sensing to overcome the limitations of the simple continuous-wave radar in range measurement. These frequency-modulated signals employ changing frequency as a distinct timing mark, encoding the target's range information as the difference in frequency based on the reflected and transmitted signals. A larger transmitting frequency deviation within a given time yields a more accurate measurement of the range.

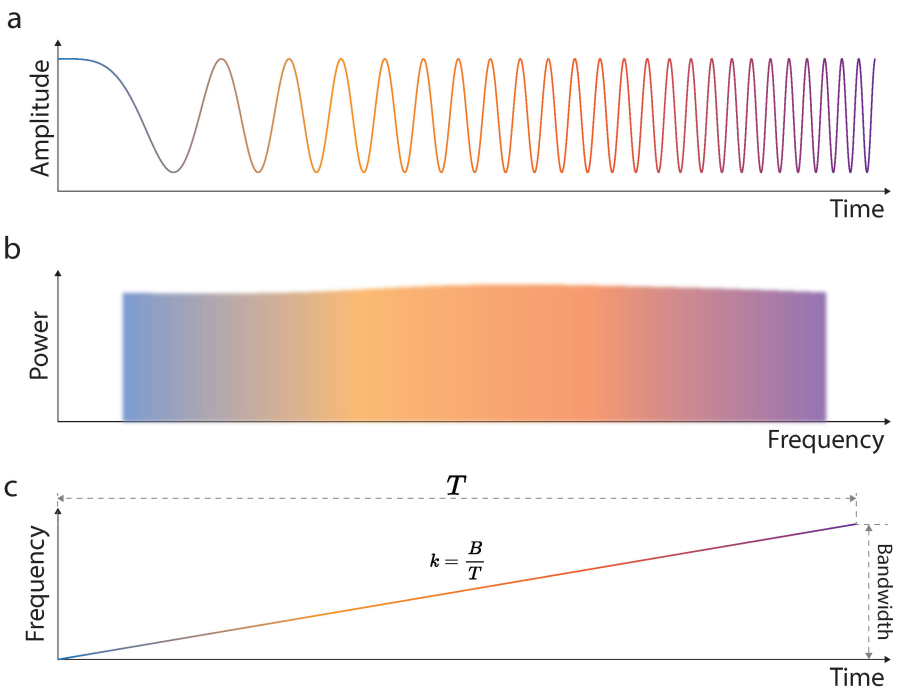


**Figure 2.10:** Linearly frequency-modulated signal illustrated on the **(a)** time domain, **(b)**, the frequency domain, and **(c)** the time-frequency domain. $k$ is the chirp rate, the ratio between the bandwidth $B$ and the chirp period $T$.

### Ranging Principle, Resolution, and Ambiguity

A popular frequency modulation waveform uses linear frequency changes as a function of time, known as a linearly frequency-modulated signal or LFM (Figure 2.10). Assume an object is located at a distance $d$, and the radar will receive the echo after a time $\tau = 2d/c$. A beat note will be generated by physically mixing the transmitted and received signals (i.e., heterodyne).

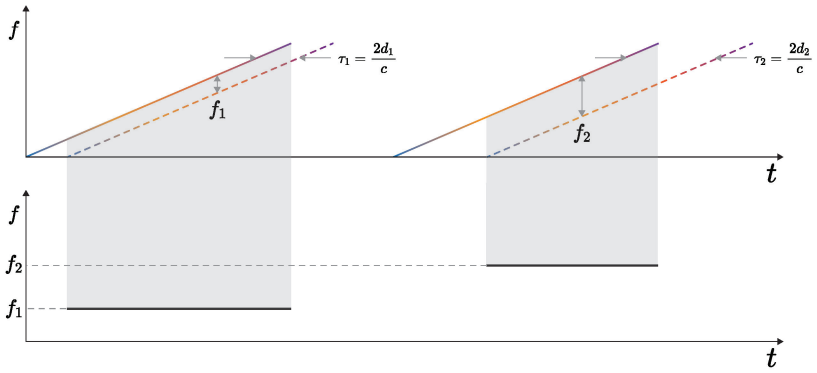


**Figure 2.11:** A descriptive illustration of the chirp signal demodulation process, which produces distinct beating frequencies, $f_1$ and $f_2$, corresponding to targets situated at varying ranges, $d_1$ and $d_2$, respectively.

This section presents the *basic ranging principle* for radar systems that utilise frequency-modulated signals. Consider an up-chirp signal, as shown in Eq. (2.48):

$$s_t(t) = \alpha \cdot \cos(2\pi \cdot kt \cdot t) \tag{2.48}$$

where $k$ represents the chirp rate, defined as the ratio between the bandwidth $B$ and the chirp period $T$. The radar signal received with a time delay of $\tau = 2d/c$ can be expressed as:

$$s_e(t) = \beta \cdot \cos[2\pi \cdot k \cdot (t - \tau)^2] \tag{2.49}$$

To demodulate the signal, the transmitted signal, $s_t(t)$, and the received signal, $s_e(t)$, are mixed, resulting in a simplified form shown in Eq. (2.50):

$$s_r(t) = |s_t(t) + s_e(t)|^2 \tag{2.50}$$

Next, we expand Eq. (2.50) using trigonometric identity and apply a low-pass filter. This yields the filtered signal, as given by Eq. (2.51):

$$s^F r(t) = \gamma \cdot \cos(2\pi f_r t) \tag{2.51}$$

where $f_r$, as described in Eq. (2.52), represents the beat note:

$$f_r = 2k\tau \tag{2.52}$$

As a result, the target range, $d$, can be expressed as:

$$d = \frac{f_r c}{4k} \tag{2.53}$$

Eq. (2.52) highlights the importance of the beat note's frequency, $f_r$, which increases with a fixed chirp rate, $k$, as illustrated in Figure 2.11. This relationship is crucial when designing frequency-modulated radar systems. For example, the chirp rate must be carefully selected in relation to the analogue-to-digital converter's speed. This ensures that the time-domain data at a frequency of $f_r$ is sampled with a sufficient sampling speed (based on the Nyquist theorem), corresponding to the desired detection range (or round-trip time delay $\tau$).

As previously stated, the **range resolution** for a frequency-modulated waveform is inversely proportional to the signal's bandwidth, as depicted in Eq. (2.43).

**Range ambiguity** arises when the received signal can only beat with adjacent or subsequent transmitted chirp signals, specifically when $\tau > T$. This phenomenon occurs regardless of whether the signal is a pulsed chirp or a frequency-modulated continuous wave.

### Chirp Signal Variations

In terms of frequency-modulated signal, two variants are particularly interesting, i.e., the triangular chirp and the stepped-frequency chirp signal (Figure 2.12).

A triangular chirp radar signal, also known as a symmetric linear frequency modulated waveform, displays a linear increase in frequency followed by an equally linear decrease, as illustrated in Figure 2.12. The transmitted signal's frequency varies linearly over time, with an initial ramp-up phase succeeded by an equally ramp-down phase.

The triangular chirp radar signal shares the same principles of ranging, range resolution, and range ambiguity as the simple chirp signals discussed earlier. For example, when the target is stationary, and the chirp rate is the same as that of the simple up-chirp signal, an identical beating frequency is generated, as demonstrated in Figure 2.13.

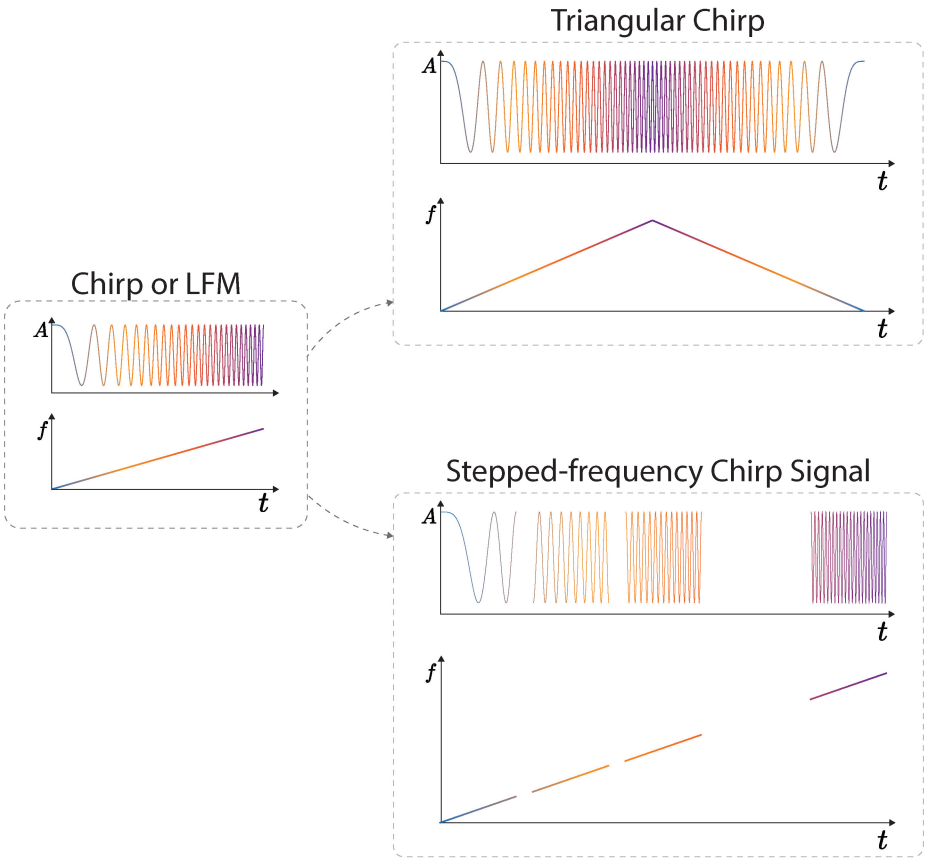


**Figure 2.12:** Comparison of two chirp signal variants: the triangular chirp waveform and the stepped-frequency chirp waveform.

A notable advantage of the triangular chirp waveform is its ability to resolve both range and Doppler information simultaneously without relying on a two-dimensional Fourier analysis, unlike other frequency-modulated signals such as stepped-frequency and simple chirp signals. This can be achieved by analysing the two beating frequencies within a single up-down chirp period, which are influenced by the relative movement of the target.

As depicted in Figure 2.14, a beating frequency of $f_r - f_D$ is produced during the first half of the chirp period (up-chirp), while a frequency of $f_r + f_D$ is generated during the latter half (down-chirp). Here, $f_r$ represents the beating frequency when the target is stationary, and $f_D$ denotes the frequency shift introduced by the Doppler effect and the target's movement.

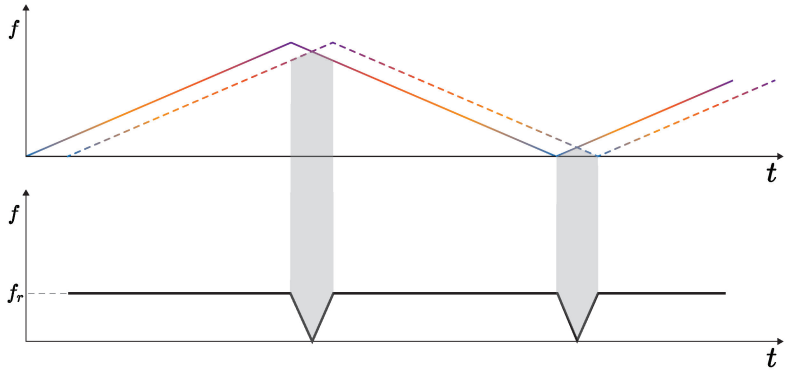


**Figure 2.13:** Illustration of the demodulation process in a radar system employing a triangular chirp signal with a stationary target.

As a result, employing a single Fourier transform can decode both the target's range and velocity information, making the triangular chirp radar signal more efficient than other frequency-modulated signals in terms of signal processing and resource utilisation.

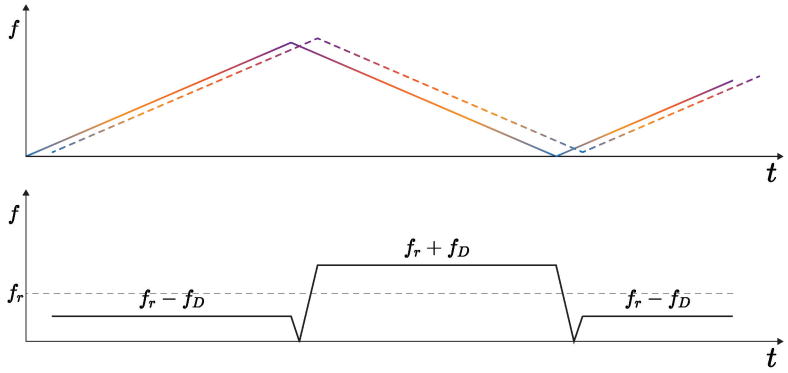


**Figure 2.14:** Illustration of the demodulation process in a radar system employing a triangular chirp signal with a moving target.

Stepped-frequency chirp signals represent a unique class of radar waveforms characterised by their distinct blend of time and frequency domain properties. These signals comprise a series of linear frequency sweeps, or chirps, in which the carrier frequency is systematically varied over a specific bandwidth in a step-wise fashion (see Figure 2.12). This feature allows the stepped-frequency chirp signal to attain high-range resolution.

A key advantage of this signal type is its relatively small instantaneous

bandwidth compared to the total processing bandwidth. This aspect enables the transmission of waveforms with an exceptionally wide overall bandwidth without the need for costly hardware to accommodate the wide instantaneous bandwidth [47, 48, 49].

### 2.4.5 Pseudorandom Signal

In many modern digital and analogue systems, noise and chaotic signals are generally considered undesirable, as they are unpredictable, lack order, and are often generated as byproducts from electronic or photonic circuits. This can lead to system performance degradation in applications such as radar, communications, and signal processing. However, despite these drawbacks, chaotic signals have been found to offer unique benefits in specific radar application scenarios.

Introducing a chaotic signal in radar systems can potentially enhance both performance and security by making the signal more challenging for unauthorised parties to detect or jam. Chaotic signals are inherently unpredictable and possess a wide bandwidth, offering several advantages for radar systems [50, 51].

The deterministic and noise-like properties of chaotic signals have been found to be particularly useful in the following three applications :

- Feature extraction in radar-sensing scenarios: In some cases, the return signals from radar systems exhibit chaotic properties, which can be utilised to extract specific features of the detected objects [52, 53]. This can complement conventional radar signal processing methods and improve overall system performance.
- Encoded or modulated chaos for increased information capacity: By encoding the transmitted waveform with coded or modulated chaos, flexible codes can be developed that possess the desired randomness for increased information capacity, as Shannon's information theory describes. This approach can enhance the performance and robustness of radar or communication systems [54, 55, 56].
- Continuous random signal implementation for noise radar sensing: The third category of applications involves using or generating chaotic signals for noise radar sensing [51, 57]. This approach exploits the noise-like properties of chaotic signals to improve the radar system's ability to detect targets in challenging environments or to make it more resistant to interference and jamming.

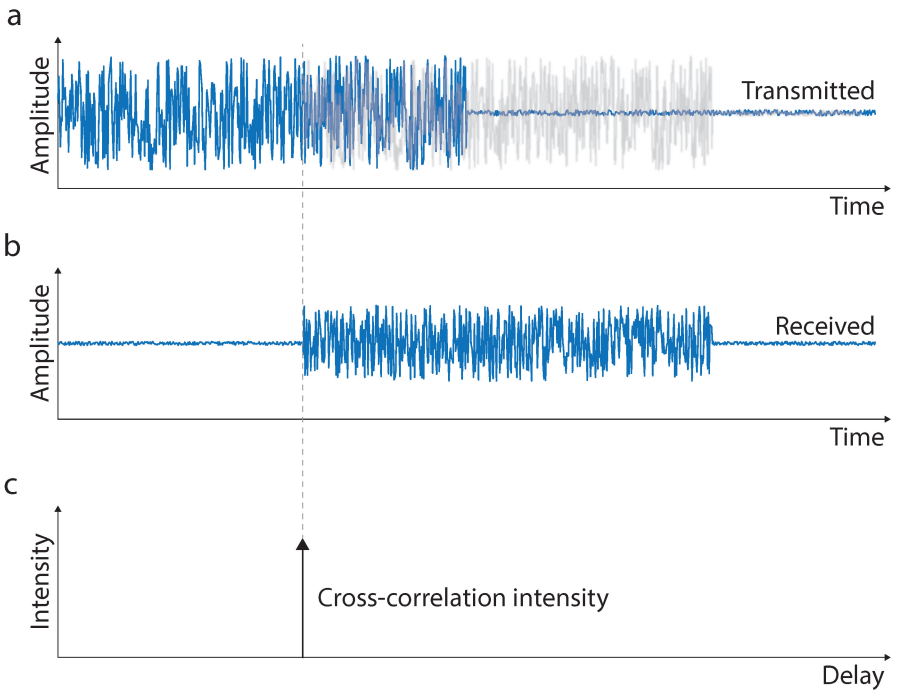


**Figure 2.15:** Depiction of radar ranging employing chaotic signals. **(a)** Transmitted signal sampled by a high-speed analogue-to-digital converter with an adequate bandwidth. **(b)** Received signal, also sampled by a high-speed analogue-to-digital converter with sufficient bandwidth, triggered upon signal transmission. **(c)** Cross-correlation analysis utilised to determine the target range.

While noise and chaotic signals are typically unwelcome in many modern systems, their unique properties can be harnessed to improve radar performance and security. By carefully implementing and managing chaotic signals in these applications, radar systems can benefit from their unpredictable nature and wide bandwidth, ultimately leading to better overall performance.

A chaotic or pseudorandom signal can be generated in many ways using electronic or photonic approaches, such as operating and amplifying the nonlinearity in the electronic circuits [51], Lorenz electronic chaotic system [58], driving nonlinear optical microresonators under the highly coherent low noise states (dissipative Kerr solitons) [59, 60, 61], and even the wideband noise from an erbium-doped fibre amplifier [62, 63]. The core principle behind chaotic radar-ranging shares similarities with the synchronisation process commonly found in contemporary wireless communication systems. Specifically, both techniques employ

the mathematical cross-correlation operation to determine the similarity between two signals or functions by comparing them as one signal shifts in time relative to the other, as illustrated in Figure 2.15.

Chaotic radar systems provide potential benefits in terms of performance and security, but they also come with several drawbacks associated with complexity and implementation challenges. For example, there is a trade-off between range resolution and computational time. As the bandwidth of the chaotic signal increases, the computational time required for direct sampling of the received signal grows significantly. This contrasts with the demodulation process in frequency-modulated radar, where the time delay is projected onto a lower-frequency oscillation. Furthermore, obtaining Doppler or velocity information of a target using chaotic radar can be challenging due to the incoherent nature of the signal. This inherent characteristic makes it more difficult to extract accurate information about the target's motion, which is essential for many radar applications.

| Waveform Format | Doppler | Range | Bandwidth | Range Resolution | Repetition Period | Ambiguity Range |
|---|---|---|---|---|---|---|
| CW | Y | N | - | - | - | - |
| Short Pulse | Y | Y | $\frac{1}{T_0}$ | $\frac{c \times T_0}{2}$ | $T_p$ | $\frac{cT_p}{2}$ |
| SFCW | Y | Y | $N \cdot \Delta f$ | $\frac{c}{2B}$ | $T_p$ | $\frac{c}{2\Delta f}$ |
| LFMCW | Y | Y | $k \cdot T_p$ | $\frac{c}{2B}$ | $T_p$ | $\frac{cT_p}{2}$ |
| TCCW | Y | Y | $k \cdot T_p$ | $\frac{c}{4B}$ | $T_p$ | $\frac{cT_p}{2}$ |
| Chaotic Signal | N | Y | $B_{\text{min}}$ | $\frac{c}{2B}$ | $T_p$ | $\frac{cT_p}{2}$ |

**Table 2.2:** Comparative Analysis of Common Radar Waveforms: Continuous Wave (CW), Short Pulse, Stepped-Frequency Continuous Wave (SFCW), Linear Frequency-Modulated Continuous Wave (LFMCW), Triangular Chirp Continuous Wave (TCCW), and Chaotic Signal. $B_{\text{min}}$ is the minimum bandwidth of the basic system building blocks.

## 2.5 Inverse Synthetic Aperture Radar (ISAR)

Inverse synthetic aperture radar (ISAR) is a two-dimensional radar imaging technique that serves as an alternative to synthetic aperture radar (SAR). Primarily employed for target recognition, tracking, and surveillance applications, ISAR differs from SAR in its reliance on the target's motion to create a synthetic aperture, as opposed to SAR, which utilises the relative motion between the radar and a stationary target to generate high-resolution images [16, 64].

The ISAR image comprises two distinct components: the range and the cross-range. The range is obtained through radar ranging, which employs either frequency-modulated signals or pulsed signals to measure the distance between the radar and the target. Meanwhile, the cross-range is reconstructed based on the ranging results over time and the angular diversity provided by the target's motion.

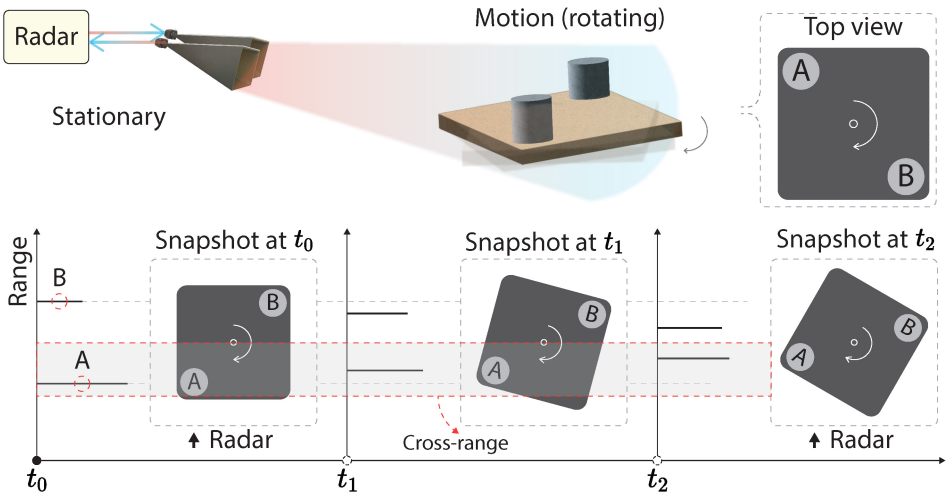


**Figure 2.16:** Schematic representation of the inverse synthetic aperture radar (ISAR) imaging process using two cylindrical objects mounted on a rotating platform. The procedure begins with multiple ranging (fast time imaging axis) within a short time window, during which the objects can be considered stationary. Subsequently, Fourier analysis is applied to the fast-time ranging results to generate the second dimension, namely the cross-range or slow time axis.

One interesting aspect of ISAR radar imaging is the two-dimensional representation, containing both the range and cross-range dimensions, also known as the fast and slow time axes [65, 66, 67]. These terms refer to the distinct time scales associated with the range and cross-range axes, which are affected by the radar signal's travel time and the target's

motion. The range axis, or fast time, corresponds to the time required for a radar signal to travel to the target and back, happening rapidly as radar signals propagate at the speed of light. The fast time scale measures the distance between the radar and the target. The signal bandwidth determines the range resolution. Conversely, the cross-range axis, also known as the slow time, pertains to the time scale over which the target's motion is observed. Typically, this motion is slower in comparison to the fast time scale, where the object can be assumed to be stationary. The slow time scale arises from the target's movement, which calculates the target's velocity along the cross-range axis. For example, another Fourier transform applied to the range results sampled at the slow time axis ($t_0, t_1, ...t_n$, as shown in Figure 2.16) allows the changes in the object's range to be interpreted as velocity information.

The following equation can define the cross-range resolution [16]:

$$\Delta y = \frac{c}{2 f_c \Omega} \tag{2.54}$$

where $c$ represents the propagation speed of the radar signal, $f_c$ denotes the centre frequency of the wideband radar signal, and $\Omega$ indicates the azimuth angles through which the object rotates during the time it takes to form a single two-dimensional ISAR image.

The combination of range and cross-range information in ISAR imaging techniques enables the generation of intricate, high-resolution images of moving targets. This capability makes ISAR a vital and versatile tool in numerous defence and surveillance applications, providing enhanced target recognition, tracking, and situational awareness.

In the following chapters, a deeper investigation of the practical implementation of a photonic radar system, which leverages ISAR imaging techniques, will be presented. The generation of two-dimensional ISAR images in real-world scenarios, such as imaging the rapidly rotating propeller of a drone, will be showcased. These demonstrations will further illustrate the efficacy and potential of ISAR imaging in combination with advanced photonic radar technology, paving the way for future advancements and applications in radar imaging.

## 2.6 Electronic Frequency-Modulated Radar System

Grasping the fundamental components and processes of traditional electronic radar systems, along with their constraints, is essential prior to explore the photonic alternative. The following discussion presents an overview of electronic radar system operations. Subsequently, the conversation examines the functionality and potential drawbacks of the elementary components and building blocks, highlighting areas where photonics may offer superior solutions.

### 2.6.1 Electronic Radar Basic Building Blocks and Operation

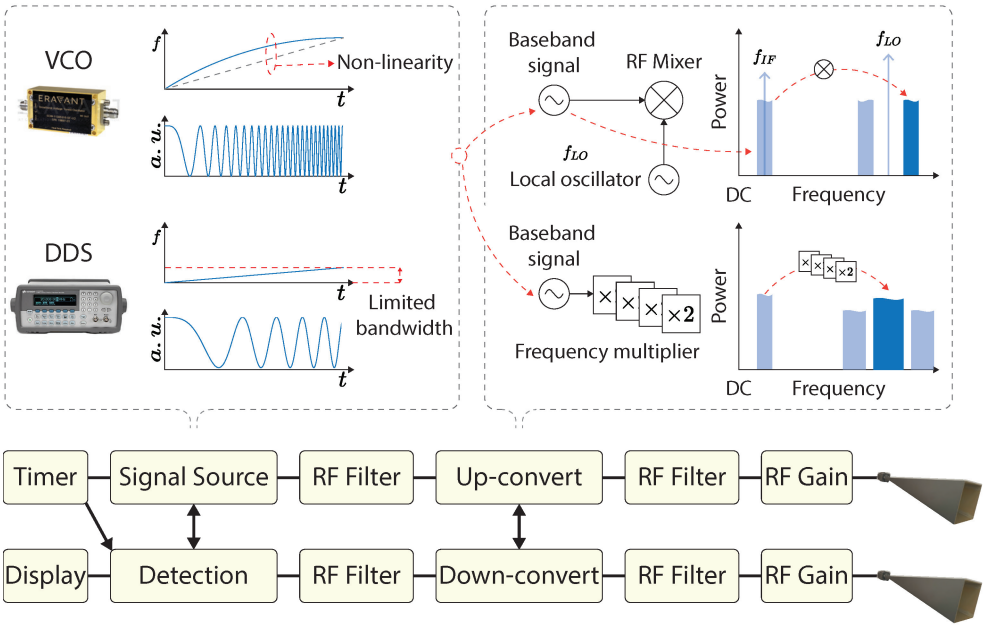


**Figure 2.17:** A block diagram of a fundamental radar system, showcasing its essential components. The diagram highlights two standard direct radar signal generation methods: a voltage-controlled oscillator (VCO) and a direct digital synthesiser (DDS). The VCO-based technique demonstrates time-frequency non-linearity when generating an up-chirp signal. At the same time, the DDS-based method exhibits a restricted synthesising bandwidth. Additionally, the diagram illustrates two typical up-conversion strategies for transforming the baseband signal into a carrier band, including an RF mixer and a frequency multiplier. Both up-conversion methods result in a higher noise floor and increased harmonic spurs.

Figure 2.17 presents a block diagram illustrating the fundamental components of a frequency-modulated radar system. The diagram commences with the essential building block, the "Timer," located in the top left corner. A series of narrow timing (trigger) pulses at a specific repetition frequency is required for a radar system or most electronic systems to function effectively. These pulses activate events within each building block, such as the generation of baseband radar signals, and synchronise these events logically and functionally, enabling the system's components to work collaboratively.

Triggered by the timer, the signal source produces a radar signal in either the baseband or intermediate frequency (IF) band. An appropriate RF filter is necessary if the signal source lacks a built-in filter. The block diagram in Figure 2.17 demonstrates two direct radar signal generation methods: a voltage-controlled oscillator (VCO) and a direct digital synthesiser (DDS).

Following the signal generation and appropriate filtering to eliminate unwanted sidebands and harmonic spurs, two common up-conversion methods are employed to shift the baseband signal into a carrier band. These methods, illustrated in Figure 2.17, utilise either an RF mixer or an RF multiplier. A key distinction between the two approaches is that the multiplier expands the baseband signal's bandwidth by a factor of its multiplication, while the RF mixer preserves the original bandwidth. RF gain control units are implemented to ensure sufficient power for transmission and reception, accounting for the energy needed for the radar's maximum range, radiation power adhering to local regulations, and limiting the maximum input power to protect the receiver from damage.

Upon receiving the reflected radar signal, a down-conversion process is carried out, similar to the up-conversion. When employing an RF mixer, the same local oscillator is often shared between the up- and down-conversion circuits. After another filtering process to remove unwanted harmonics and spurs introduced by the down-conversion, demodulation, digitisation, and signal processing are utilised to extract and analyse the target's information.

### 2.6.2 Voltage-Controlled Oscillator (VCO) for Radar Signal Generation

A voltage-controlled oscillator is an electronic circuit that generates a periodic output signal with a frequency determined by an input voltage [68, 69, 70]. The primary purpose of a voltage-controlled oscillator is to transform input voltage (control voltage) into oscillation frequency. Typically, a voltage-controlled oscillator includes an active device, such as a transistor, and a resonant circuit that sets the oscillation frequency. It is worth noting that the output signal's oscillation frequency fluctuates as the control voltage.

A voltage-controlled oscillator's operating frequency or bandwidth hinges on its design and application requirements, which exhibit a broad range of operating frequencies, extending from a few hertz to multiple gigahertz. However, the resonant circuit and the active device incorporated within the voltage-controlled oscillator circuitry dictate the specific operating frequency range.

Voltage-controlled oscillators show certain drawbacks. For instance, frequency stability constitutes a significant limitation, as it is susceptible to temperature changes, power supply variations, and component ageing. Furthermore, voltage-controlled oscillators can display phase noise, a phenomenon that compromises the output signal's spectral purity and results in diminished performance in radar systems.

Time-frequency non-linearity represents an important limitation in voltage-controlled oscillators, substantially limiting radar-ranging performance. In a frequency-modulated radar, time-frequency non-linearity refers to the complex relationship between the radar signal's time and frequency domain, which occurs due to the inherently variable nature of frequency modulation (see Figure 2.17).

Here, a numerical simulation is provided to illustrate radar ranging using an ideally linear chirp signal and a non-linear chirp signal, which is commonly observed when generating radar signals with a voltage-controlled oscillator. The simulation parameters are detailed in the accompanying table (Table 2.3), while the results are depicted in Figure 2.18.

Consider a frequency-modulated radar system that utilises an up-chirp signal. This numerical simulation generates signals with perfect linear and manually induced quadratic time-frequency relationships in the baseband, as illustrated in Figure 2.18**a**. The frequency deviation is also computed, yielding a root-mean-square (RMS) value of 58.6306

MHz, constituting 14.66 per cent of the total bandwidth, as shown in Figure 2.18**a**.

The demodulation process is grounded in the discussions presented in Chapter 2.4. After appropriate low-pass filtering, the demodulated signal exhibits a single oscillating frequency for a perfectly linear chirp signal, as depicted in Figure 2.18**b**. However, the demodulated signal derived from a chirp signal with a quadratic time-frequency relationship experiences significant degradation.

The frequency domain analysis of the demodulated signal presented in Figure 2.18**b** and Figure 2.18**c** can be converted into range measurements (distances) using Eq. (2.53). In the case of a signal exhibiting perfect time-frequency linearity, the simulation result demonstrates a range of 5.019 meters, compared to an ideal value of 5 meters. Conversely, the radar system fails to resolve the target range for a signal with such high nonlinearity (58.6306 MHz RMS).

This numerical simulation, to some extent, illustrates an extreme case intended to highlight a scenario of radar ranging with high nonlinearity,

| Parameters | Values |
|---|---|
| **Radar Signal** | |
| Bandwidth (MHz) | 400 |
| Starting Frequency (MHz) | 100 |
| Stopping Frequency (MHz) | 500 |
| Sweeping Time ($\mu$s) | 1 |
| Sampling Speed (MSa/sec) | 5000 |
| Target Distance (metres) | 5 |
| **Filtering and FFT** | |
| Number of FFT | $2^{23}$ |
| Low Pass Filter Type | IIR |
| Low Pass Filter Cut-off Frequency (MHz) | 50 |

**Table 2.3:** Numerical simulation settings to illustrate and contrast radar ranging using an ideally linear chirp signal and a non-linear chirp signal. FFT, fast Fourier transform; IIR, infinite impulse response filter.

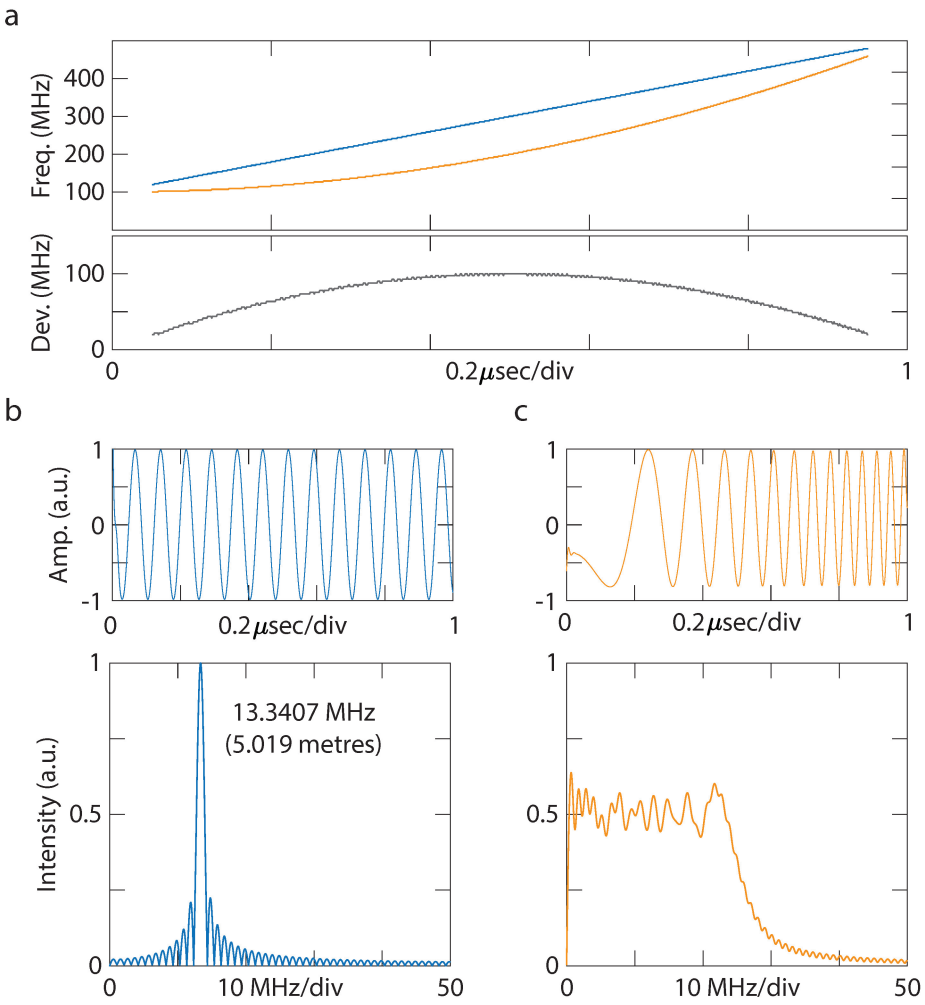


**Figure 2.18:** Numerical simulation illustrating the effects of nonlinearity on radar ranging. **(a)** Time-frequency analysis comparing linear and quadratic time-frequency relationship signals in the baseband. **(b)** Demodulated signal exhibiting a single oscillating frequency for a perfectly linear chirp signal, accompanied by its Fourier analysis results for range determination. **(c)** Deteriorated demodulated signal stemming from a chirp signal with a quadratic time-frequency relationship, alongside its Fourier analysis, results for range estimation.

in which almost no range resolution is maintained. It is more typical to observe range resolution degradation and diminished ranging accuracy as consequences of nonlinearity in radar sensing applications. However, in real-world applications, various strategies, such as employing pre-distortion techniques [71] or implementing advanced digital signal processing [72], can be utilised to mitigate the detrimental effects caused by nonlinearity.

### 2.6.3 Direct Digital Synthesiser (DDS) for Radar Signal Generation

A direct digital synthesiser (DDS) is a device capable of addressing the time-frequency nonlinearity limitations often exhibited by voltage-controlled oscillators in radar systems. A direct digital synthesiser generates precise, software-definable signals by employing a digital-to-analogue converter (DAC) to create a periodic waveform with high accuracy and frequency stability.

Direct digital synthesisers offer numerous advantages for radar systems, such as high-frequency accuracy and rapid frequency hopping. Its digital nature allows for highly stable and repeatable performance and seamless integration with other digital components. Additionally, direct digital synthesisers provide precise control over phase and amplitude, which is important for radar applications like beamforming.

Despite its benefits, some drawbacks are associated with implementing direct digital synthesisers in radar systems. One primary disadvantage is the presence of spurious signals arising from the quantisation noise inherent in the digital-to-analogue conversion process. These spurious signals can adversely impact the radar's performance and may necessitate additional filtering to mitigate their effects. Moreover, direct digital synthesisers typically have limited system bandwidth, often below gigahertz levels. Therefore, the range resolution of such radar systems is limited.

The numerical simulation presented in Figure 2.19 compares low-resolution and high-resolution radar range detection capabilities. This radar-ranging simulation employs two distinct bandwidths of chirp signals with ideal time-frequency linearities.

In Figure 2.19**a**, the time-frequency analyses of both signals can be observed, with the yellow line representing a bandwidth of 100 MHz and the blue line depicting a bandwidth of 400 MHz. Meanwhile, Figure 2.19**b** displays the demodulated frequencies corresponding to each signal. The ranging results, indicating a target situated at a distance of 5 meters, are illustrated in Figure 2.19**c**. The ranging results show that the radar system with a lower bandwidth possesses a reduced range resolution, as demonstrated by the more wide main lobe width shown in Figure 2.19**c**.

As a result, radar systems relying solely on direct digital synthesisers, without incorporating additional bandwidth-broadening techniques, face difficulties in satisfying the high-resolution ranging and imaging de-

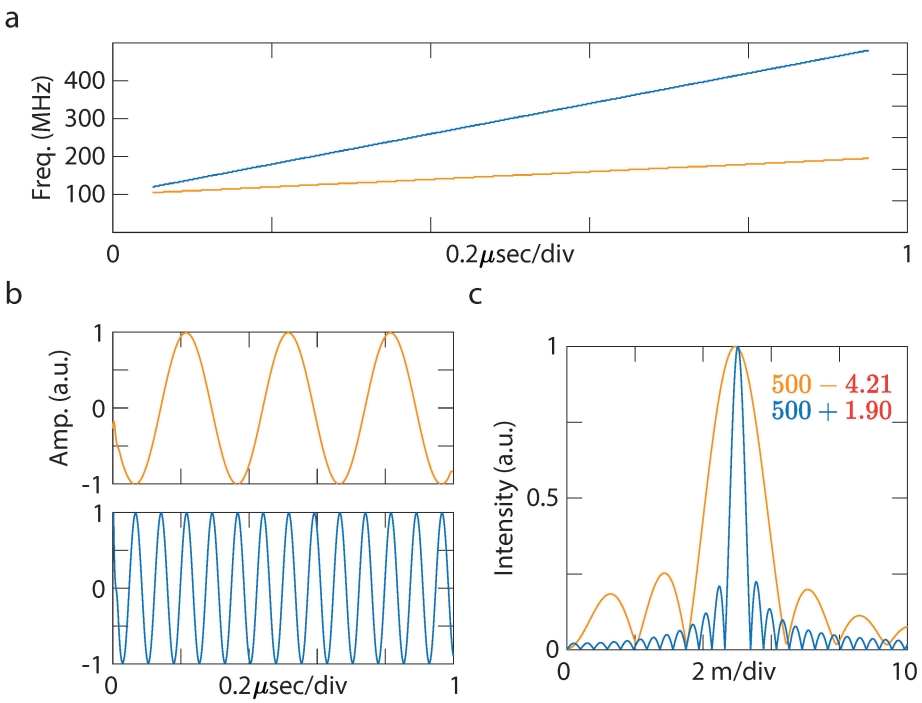


**Figure 2.19:** Numerical simulation illustrating the impact of constrained signal generation bandwidth on radar ranging performance. **(a)** Time-frequency analyses of chirp signals with 100 MHz (yellow) and 400 MHz (blue) bandwidths. **(b)** Corresponding demodulated signals for each bandwidth. **(c)** Ranging results highlighting a measurement error of 1.90 cm for the 400-MHz chirp signal and an error of 4.21 cm for the 100-MHz chirp signal, emphasising the influence of bandwidth on ranging accuracy.

mands of various applications, such as drone imaging, security screening, building displacement monitoring, and human vital sign detection.

### 2.6.4 Electronic Signal Mixing and Multiplexing for Radar

RF mixers and multipliers are commonly used components in traditional radar systems, playing a critical role in bandwidth expansion, up-conversion, and down-conversion of signals between baseband (or intermediate frequency) and carrier band frequencies. Theoretically, frequency mixing and multiplexing is a non-linear process to create new frequencies from the input.

The following discussion will examine the fundamental principles of frequency mixing (multiplexing shares similar drawbacks), along with an analysis of their respective advantages and drawbacks. The discussion will facilitate a more comprehensive understanding of the role of RF

mixers and multipliers in radar systems.

| Parameters | Values |
|---|---|
| $f_{\text{IF}}$ (Figure 2.20**c**) | 100 MHz (30 dB SNR) |
| $f_{\text{IF}}$ (Figure 2.20**e**) | 100-200 MHz chirp (30 dB SNR) |
| $f_{\text{LO}}$ | 1 GHz (30 dB SNR) |
| Ideal Mixing | $\alpha \sin\big[\omega_{\text{LO}}(t)\big] \times \beta \sin\big[\omega_{\text{IF}}(t)\big]$ |
| Real Mixing [73] | $i_{current} \approx a_0 + a_1 v + a_2 v^2 + a_2 v^3$ |

**Table 2.4:** Numerical simulation settings to illustrate and contrast RF mixing between an ideal and real-world scenario. $\alpha$ and $\beta$ represent the voltage of the local oscillator and baseband RF signals, $a_n$ are the Taylor coefficients, and $v = \alpha \sin\big[\omega_{\text{LO}}(t)\big] + \beta \sin\big[\omega_{\text{IF}}(t)\big]$.

In an ideal scenario, RF frequency mixing seamlessly sums and subtracts two distinct frequency components to generate a signal at the desired frequency (Figure 2.20**c** and **e**). However, achieving this level of precision in the real world is not feasible. For example, the output of a commonly employed diode mixer can be described by the following equation, as presented by [73]:

$$i_{current} = a_0 + a_1 v + a_2 v^2 + a_2 v^3 + \cdots \tag{2.55}$$

where $a_n$ represents the Taylor coefficients and $v = \alpha \sin\big[\omega_{\text{LO}}(t)\big] + \beta \sin\big[\omega_{\text{IF}}(t)\big]$.

As Eq. (2.55) demonstrates, the desired frequency signals are accompanied by various undesired frequency components, including higher-order harmonics and inter-modulation products. These unwanted elements are commonly referred to as mixing spurs [74]. To gain a deeper understanding of these phenomena, numerical simulations (settings are shown in Table 2.4) have been conducted to examine the typical output of a noisy RF mixer, revealing the challenges encountered in real-world applications.

The numerical simulations examined two distinct types of RF input signals: a single frequency at 100 MHz and band-limited signals, specifically a chirp with an upward 100 MHz time-frequency sweep. The simulation sought to mimic the process in which the baseband RF signal is up-converted to the carrier frequency band utilising a 1 GHz local oscillator and RF mixer.

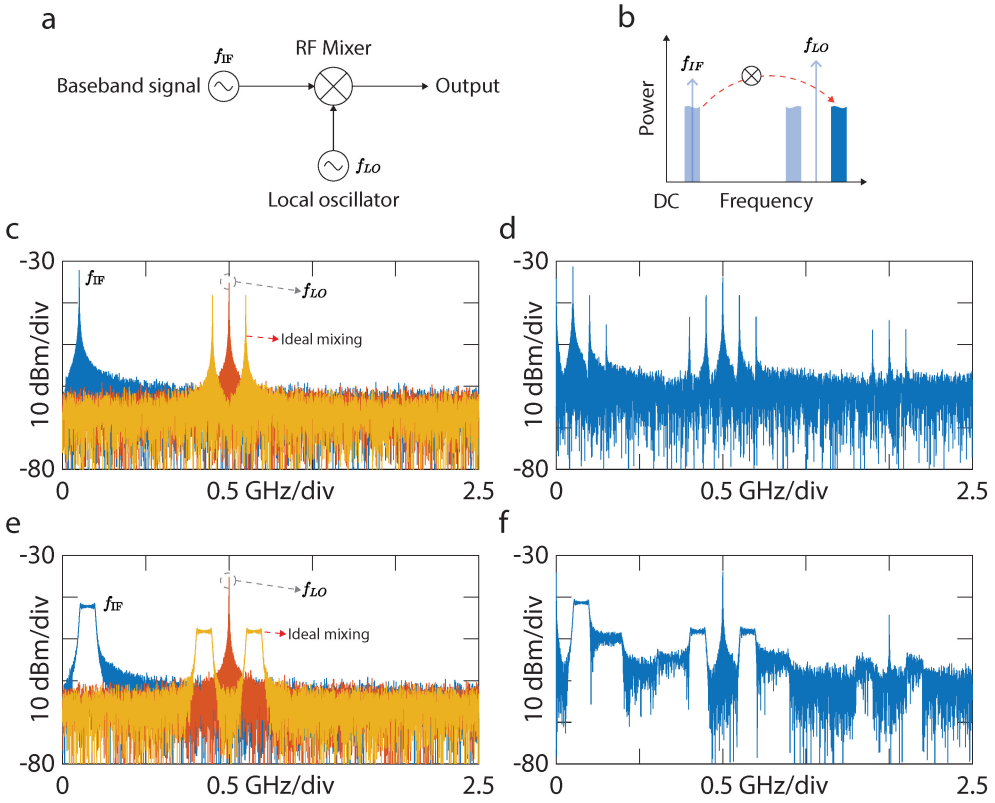


**Figure 2.20:** Comparing ideal and real-world RF mixing scenarios through numerical simulation results. **(a)** Block diagram representing an electronic mixing process. **(b)** Visual depiction of RF mixing in the frequency domain. **(c)** RF spectrum displaying a single-frequency baseband signal ($f_{\text{IF}}$), local oscillator ($f_{\text{LO}}$), and the ideal mixing output. **(d)** Diode mixer output spectrum juxtaposed with the ideal scenario in **(c)**. **(e)** RF spectrum presenting a wideband baseband signal ($f_{\text{IF}}$), local oscillator ($f_{\text{LO}}$), and the ideal mixing output. **(f)** Diode mixer output spectrum compared to the ideal case in **(e)**.

As depicted in Figure 2.20**c**, the ideal mixer output, visually represented in yellow, displays two distinct peaks on the left ($f_{LO} - f_{\text{IF}}$) and right ($f_{LO} + f_{\text{IF}}$) sides of the local oscillator's frequency. In contrast, Figure 2.20**d** demonstrates the mixer output in a real-world scenario compared to the ideal case. This process generates numerous unwanted frequency components that impact the signal quality.

Upon analysing and comparing the mixer output for both a single-frequency signal (Figure 2.20**d**) and a band-limited chirp signal (Figure 2.20**f**), it becomes clear that the desired, up-converted chirp signal overlaps with neighbouring undesired frequency components. This overlap substantially compromises signal purity and diminishes the spurious-

free dynamic range. As a result, the undesired mixing spurs constrain the mixer's operational bandwidth and dynamic range. In the context of a radar system, this limitation translates to reduced range resolution and range accuracy, ultimately affecting the overall radar performance.

Chapter 3

# Microwave Photonics for Radars

Microwave photonics (MWP) is a technology that connects optical, microwave, and electrical engineering to explore the interaction of signals, spanning from below 1 kHz in the radio-frequency (RF) domain to hundreds of terahertz in the optical domain [75]. The initial progress in this field was driven by the use of optical fibres to distribute RF signals — radio-over-fibre (RFoF) — as a means to replace the high loss associated with electrical distribution lines [20, 21, 25] for applications such as wireless communication and cable television signals (CATV).

With time, photonics' wide bandwidth and low-loss characteristics led to a growing interest in generating, manipulating, distributing, and measuring microwave or RF signals with exceptional speed and extensive bandwidth. These developments found application in a broad range of areas, including wireless communications, sensor networks, and radar [21, 23, 76, 77]. The advancement of microwave photonics could not have been achieved without the advancement of photonic building blocks, including semiconductor lasers [78, 79], photodetectors [80, 81, 82], optical fibres [83], and electro-optic modulators [84]. These innovations helped alleviate the burden on conventional electronics in meeting the developing needs in communications [42] and RF sensing [29]. As a result, this research field has witnessed significant advancements in recent years.

Notable achievements in this field include demonstrations of photonics-enhanced radio-frequency functionalities [85, 86], such as ultra-wideband signal generation [30], low-loss RF signal distribution over fibre [87], tunable microwave photonic filters [88, 89], and ultra-high precision reference clocks [90, 91, 92]. These proven advantages have solidified microwave photonic technologies as strong candidates for the next-generation, high-

performance radar systems. Key benefits include wide bandwidth for high-resolution sensing, system compactness with shared versatile optical components for multiband radar operation and multifunctionality, distributed sensing capabilities using low-loss and distortion fibres, and precise intra-system synchronisation using optical clocks. This chapter delves into the ways in which photonic technologies can enhance and uplift radar systems, offering superior performance compared to conventional electronics.

## 3.1 Photonic Frequency-Modulated Radar System

Photonic radars, also known as microwave photonic radars or photonics-assisted radars, are frequently found in the diverse research literature. These terms refer to a radar system that utilises photonic technologies to enhance the performance of traditional electronic radar systems. It is important to recognise that despite incorporating photonics-based techniques, these systems still rely on radiowaves or microwaves for sensing. Oscillating frequencies range from a few Hertz up to the millimetre-wave and terahertz wave regions. The specific wavelength or frequency distinguishes the radar system from another prominent sensing technology, LiDAR (Laser Ranging and Detection). By employing photonic technologies, these radar systems retain the benefits of conventional electronic radars, including the ability to penetrate obstacles and maintain robustness in extreme weather conditions.

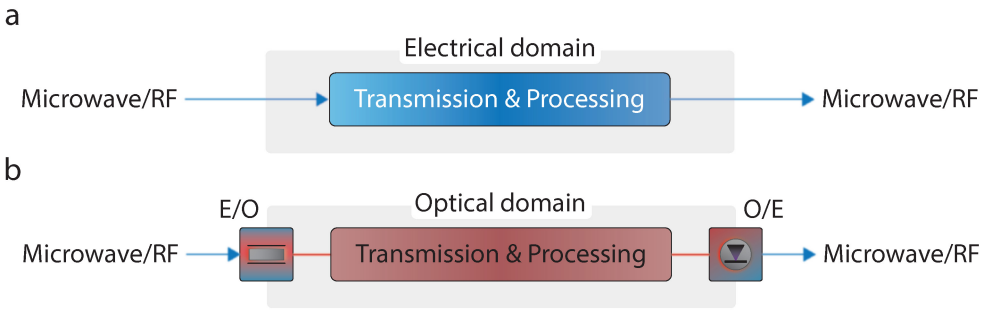


**Figure 3.1:** Schematic comparison between two distinct radar systems that use a traditional electronic microwave system (**a**) and a microwave photonic system (**b**) for microwave signal transmission and processing.

Traditional electronic radar systems process and transmit radar signals

within the electrical domain (Figure 3.1**a**), utilising electronic components (Figure 2.17). In contrast, photonic radar systems employ technologies (Figure 3.1**b**) that enable the conversion between electronic and optical signals (electrical-to-optical, E/O, and optical-to-electronic, O/E). This approach allows them to harness the power of modern photonics for processing RF signals within the optical domain using optical components. Additionally, photonic radar systems can distribute these signals over long distances with minimal loss and distortion, thanks to the properties of optical fibres.

Before exploring the specific, widely-recognised advantages that photonics can offer in enhancing a radar system's performance, it is important to provide an overview of the performance and key metrics improvements achieved in various commonly-used components (Figure 3.2) that enable photonic radar systems.

The performance of devices involved in E/O and O/E conversion is fundamental to determining the overall performance of microwave systems, as it affects key factors such as link gain, bandwidth, dynamic range, signal-to-noise ratio (SNR), and conversion efficiency. Owing to rapid advancements in optoelectronic devices, the performance of lasers, which are essential to microwave photonic systems, has significantly improved [30].

For example, the relative intensity noise of **laser diodes**, which impacts the noise floor of the microwave photonic system, has improved from -135 dB/Hz in the 1980s [93] to the current -168 dB/Hz (e.g., Thorlabs, YLN15PC and APIC LN-1550-16X-XXX). Moreover, the linewidth, which can be converted into microwave amplitude, phase, or frequency noises in different microwave photonic systems, has decreased from 7.5 GHz to 0.01 Hz [94, 95, 96].

Significant improvements have been made in **electro-optic modulators (EOMs)** as well, with the half-wave voltage being reduced from 84 V to 0.8 V and the 3-dB bandwidth increasing from 1 GHz to 500 GHz [97, 98, 99, 100]. Furthermore, photodetectors (PDs) with high responsivity and large bandwidths are now available, such as UTC-PDs with a 3-dB bandwidth of over 300 GHz (NTTElectronics, IOD-PMAN-13001, from 300 GHz to 3000 GHz with 6-dB bandwidth of 700 GHz), a responsivity of 1.02 A/W, or an output power as high as 22 dBm [101, 102, 103].

Over the past few decades, advanced optical-RF functionalities have been achieved using microwave photonics devices and approaches, demonstrating promising features surpassing conventional, state-of-the-art elec-

tronic methods. What is even more intriguing is the progress made in nanofabrication and the development of on-chip photonic components through hybrid and heterogeneous integration [77, 104, 105]. This progress paves the way for implementing photonic technologies in radar sensing while maintaining a comparable size, weight, and power, opening up a brighter future for this field.

### 3.1.1 Photonic Radar Basic Building Blocks and Operation

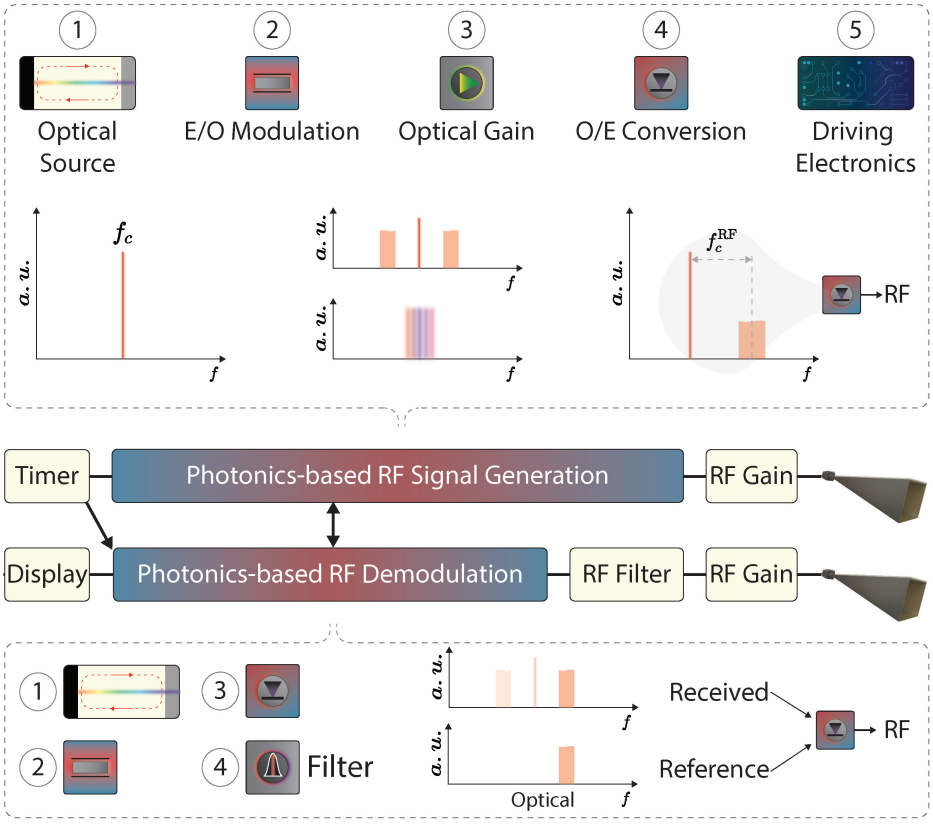


**Figure 3.2:** A block diagram of a typical photonic radar system, highlighting its fundamental components. For photonics-based RF signal generation, the system typically includes an optical source, an electro-optic (EO) modulator, an optical gain medium, an optical-electro converter (OE), and associated driving electronic devices or components. Meanwhile, photonics-based RF signal demodulation generally comprises an optical source, an electro-optic (EO) modulator, an optical-electro converter (OE), and an optical filtering component.

In this section, we introduce the fundamental components and opera-

tion of a photonic radar system, specifically focusing on systems that utilise frequency-modulated signals. As depicted in Figure 3.2, a typical photonic radar system can be differentiated from conventional electronic radar systems (previously discussed in Figure 2.17) by its two distinct features: *photonics-based RF signal generation* and *photonics-based RF demodulation or reception process*.

Although the basic operating principle is similar to electronic radar systems, as illustrated in Figure 2.17, photonic radar systems generate and process signals in the optical domain before converting them back to the RF domain using conversion components such as electro-optic modulators and photodetectors. It is important to note that the schematic presented in Figure 3.2 does not encompass all photonic radar configurations and approaches. For example, some methods incorporate photonics-based signal generation and distribution while retaining electronic receivers [106], primarily due to the bandwidth limitations of commercial electro-optic modulators. However, ultra-wideband electro-optic modulators (EOMs) show significant promise and have been frequently reported with RF bandwidths exceeding 500 GHz [107, 108].

A photonic radar system leverages the inherent advantages of photonics technology, which includes low loss, high bandwidth, and immunity to electromagnetic interference. These characteristics make photonic radars particularly suitable for applications that require high-performance radar systems.

### Photonics-based RF Signal Generation

The primary component of a photonic radar system is the photonics-based RF signal generation, which relies on optical components to create the necessary radio frequency (RF) signals. This process incorporates a variety of optical devices, including lasers, modulators, and optical filters, to generate frequency-modulated signals crucial for radar operation. Utilising photonics for RF signal generation produces highly precise, stable signals across a wide frequency range, resulting in enhanced radar performance regarding range and resolution.

Ultra-broadband RF signals can be efficiently generated by the expansive optical spectrum and advanced light-wave manipulation techniques. For example, a linearly-frequency modulated signal with a bandwidth exceeding 600 GHz can be easily produced using a wavelength-tunable laser to beat with a reference laser (carrier or local oscillator laser), a technique demonstrated for ultra-fine resolution THz imaging [109,

110]. This approach presents both advantages and disadvantages. The advantages include the following:

- Direct signal generation with a bandwidth that greatly surpasses conventional RF voltage-controlled oscillators (e.g., 2.5 GHz tuning bandwidth, Eravant SOW-11305316-SF-U2) and direct digital synthesisers.
- The ability to directly generate wideband RF signals at the carrier frequency, eliminating the need for noisy multi-stage RF mixing or multiplexing.

As a result, such a system offers superior radar range resolution due to its ultra-broad bandwidth, a streamlined structure with fewer basic building blocks (utilising just two lasers), and exceptional flexibility in terms of bandwidth and operating frequency bands. This flexibility is achieved by simply adjusting the frequency difference between the carrier laser and the wavelength-sweeping laser.

Nevertheless, this approach presents two primary limitations: 1) the signal quality, including aspects such as the signal-to-noise ratio (SNR) and time-frequency linearity, is compromised by the relatively high noise levels of free-running lasers; 2) the laser's sweeping tunability, encompassing factors such as sweeping speed and radar signal repetition rate, may also be limited.

#### Photonics-based RF Signal Demodulation

Contrasting with the modulation process on the radar transmitter side, which facilitates wideband and high-resolution radar sensing, the demodulation process extracts target information, leading to the second distinctive feature of a photonic radar system: the photonics-based RF demodulation process. This process involves detecting and processing the reflected radar signals using optical components such as photodetectors, electro-optic modulators, and optical filters. Photonics-based RF processing offers several advantages over electronic alternatives by converting the received RF signals into optical signals.

One significant advantage is the utilisation of the extended electro-optical bandwidth of optical modulators, which enables the translation of ultra-broad radar receiving signals into simplified, low-speed analogue signals for subsequent sampling and digital signal processing. This approach reduces the sampling speed requirements for analogue-to-digital converters (ADCs), lowering the cost of electronic units and eliminating the

need for noisy, multi-stage RF mixers for down-conversion. As a result, less phase and amplitude noise is introduced [29]. Another advantage is that the broad bandwidth of the photonics-based RF demodulator can be shared in a multi-band radar setup, replacing the need for a complex, parallel electronic architecture. This simplifies the overall system design while maintaining high performance in the radar system.

### 3.1.2 Photonic Radar Waveform Generation

Radar performance is heavily dependent on the waveform generated by the system. High-quality radar waveforms, characterised by a high signal-to-noise ratio (SNR) and time-frequency linearity, will likely exhibit better range resolution and accuracy (Eq. (2.44)) for a given bandwidth. High-resolution radar imaging necessitates sufficient bandwidth and high spectral purity, demonstrating a higher SNR and a spurious-free dynamic range (SFDR).

Compared to advanced photonics-based techniques, traditional electronic approaches to RF signal generation face several disadvantages. For instance, the bandwidth of signal generation using digital microwave components, such as direct digital synthesisers (DDSs), is restricted below a few gigahertz levels. This results in inadequate resolution above tens of centimetres. Alternative methods employing voltage-controlled oscillators (VCOs) offer slightly better bandwidth scalability in baseband or intermediate band but suffer from poor time-frequency linearity, limiting the system's range performance and long-term stability. Furthermore, multi-stage frequency mixing, required in radar signal processing, increases system noise levels by a few dB, reducing accuracy and stability. Frequency multiplexing and spectrum stitching for bandwidth expansion introduce noise and spectrum spurs that undermine overall sensing accuracy and performance. Additionally, conventional electronic radars struggle to achieve significant bandwidth tunability (fractional bandwidth $> 20\%$) and multi-band operational flexibility without relying on parallel or multiplexed electronic architectures, which are typically expensive and bulky, unsuitable for mobile or distributed sensing applications.

In contrast, photonic-based radar signal generation techniques have demonstrated considerable advantages in generating ultra-wideband radar signals, achieving range resolution at millimetre levels. Here, we will discuss five prevalent photonics-based RF signal generation methods, which are listed as follows:

- Dispersion-based approaches [106, 111, 112, 113, 114, 115] for spectral shaping and time-frequency mapping to expand the injected narrow-band optical pulse to a broader bandwidth
- Techniques that employ frequency-sweeping light sources [109, 110, 116, 117, 118, 119, 120, 121], such as optical injection locking and optoelectronic oscillator (OEO) for chirp signal generations
- Photonic frequency multiplication [122, 123, 124], which leverages the higher-order sidebands of electro-optic modulators to double or quadruple the radio-frequency input
- Photonic digital-to-analogue converters [125, 126, 127], which offer an innovative way to synthesise radar waveforms by emulating the principle of electronic digital-to-analogue converters
- Optical frequency-shifting loops [1, 3, 4, 5, 128, 129, 130, 131, 132] that facilitate time-to-frequency mapping

### Approaches using Optical Dispersion

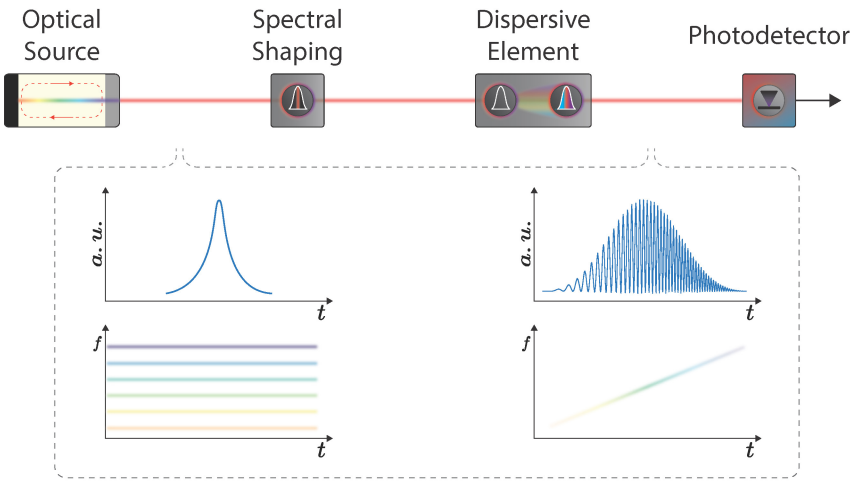


**Figure 3.3:** Schematic representation of dispersion-based methods for spectral shaping and time-frequency mapping, utilised to modulate the time-frequency relationship and generate broad bandwidth chirp signals.

The optical dispersion-based approach for radar signal generation generally involves utilising optical dispersive elements to manipulate light properties such as phase, amplitude, or polarisation by introducing wavelength-dependent delays or phase shifts. When employed in chirp

signal generation, these elements can create linear or nonlinear frequency sweeps across a specified bandwidth.

A typical schematic diagram for generating photonic radar waveforms using optical dispersion is depicted in Figure 3.3. The system comprises four fundamental building blocks [115]:

- Optical source: A broadband light source like a supercontinuum laser or a mode-locked laser is typically used. It emits light across a broad range of wavelengths, exploiting dispersive element properties to create frequency sweeps through frequency-to-time mapping.
- Spectral shaping element: This component, essentially an optical filtering element or approach (e.g., employing fibre Bragg gratings [111]), is used to align the broadband light source with the dispersive element, generating the output signal with desired properties after dispersion.
- Dispersive element: Components such as kilometres-long single-mode fibres [114] are employed to ensure different wavelengths experience varying phase delays, resulting in a frequency sweep or chirp signal. The chirp properties, including chirp rate and bandwidth, can be controlled by adjusting the element's dispersion characteristics and the input light's spectral properties (spectral shaping).
- Optoelectronic conversion: A high-speed (here, it means wide RF bandwidth) photodiode is typically used for this step.

By refining the system's components and their interactions, the optical dispersion-based approach for radar signal generation offers a robust method for creating frequency sweeps across specified bandwidths.

To date, dispersion-based techniques for radar sensing shows a maximum demonstrated RF bandwidth of 37.4 GHz [106], excluding those employing laser sweepings. These methods exhibit moderate system complexities, requiring only a limited number of photonic processing steps. However, they also possess certain drawbacks in comparison to alternative approaches, which are outlined below:

- Limited chirp duration: As previously mentioned, the fundamental principle of the dispersion-based approach involves using dispersive elements to map the superimposed frequency components onto a new time-frequency dependency manner. Consequently, the mapping time duration typically depends on the dispersive

element, such as the fibre length, when using a single-mode fibre. For radar sensing, this is not suitable for long-range detection, as discussed in Chapter 2. For example, a ten ns chirp duration can detect 1.5 metres without introducing ambiguity.

- Dispersion management: Maintaining precise control over the dispersion characteristics of the dispersive element can be challenging, particularly in cases where high levels of dispersion are required. Additionally, managing chromatic dispersion and higher-order dispersion may be necessary for some applications, which can further complicate the system.
- Sensitivity to environmental factors: The system's performance may be affected by environmental factors such as temperature fluctuations, vibrations, and mechanical stress, which can introduce variations in the dispersion properties of the dispersive element. These uncertainties will translate into deteriorated range and imaging performance for radar sensing.

#### Techniques employing Frequency-Sweeping Light Sources

Approaches using frequency-sweeping light sources fall into a category containing various methods, such as optical injections under master-slave laser schemes, simple laser sweeping [109, 110], and the use of optoelectronic oscillators (OEO) for phase noise improvement [119]. However, they can ultimately be summarised as one category because they share a common feature: the use of a tunable laser source.

The simplest way of generating wideband radar signals could be by using a tunable laser, which has an enormous bandwidth that can easily exceed hundreds of gigahertz. In addition to this approach, other methods, such as optical injection locking [116, 120], utilise two lasers where a master laser is injected into a slave laser to pull the intracavity field oscillation. Therefore, the relative frequency difference between these two lasers changes, thereby generating a chirp-like signal in the RF domain. The sweeping laser can also be combined with an optoelectronic oscillator, which has low-phase noise properties due to the mode-locking from its electro-optic cavity. However, the generation of a chirped radar signal relies on laser sweeping, sharing some common inherent drawbacks.

Time-frequency nonlinearity occurs when the frequency of a laser is swept or tuned over time, and the relationship between the sweeping time and the frequency change is not linear. In other words, the rate at which

the laser's frequency changes is not constant across the entire sweeping range. This nonlinearity can introduce distortions in the generated signals, affecting the radar performance.

Laser frequency sweeping can be achieved through various techniques, including current injection, temperature tuning, or mechanical adjustment of the laser cavity [133]. However, attaining a perfectly linear frequency sweep is difficult due to intrinsic laser dynamics, thermal effects, and mechanical constraints. When time-frequency nonlinearity appears in laser frequency sweeping, it can lead to consequences, such as inaccuracies in radar ranging, diminished resolution, increased system complexity owing to the employment of nonlinearity compensation methods [134, 135, 72], and ultimately, a reduction in the overall radar system performance.

It is important to note that some approaches suggest that signal generation based on laser sweeping is free of RF sources. However, this notion can be debated, as even the tuning of the laser driving current signal with a sawtooth format could potentially be considered an RF signal source. Furthermore, this discussion becomes even more relevant when considering that the driving current is pre-distorted to compensate for the laser sweeping nonlinearity.

#### Photonic Frequency Multiplication

Photonics-based RF signal multiplexing shares intriguing similarities with RF multiplexing, mainly because 1) both require a narrowband RF signal as input and 2) both depend on the byproduct arising from the non-linear process of a component.

In the context of photonic frequency multiplexing, the Mach-Zehnder modulator (MZM) is the most commonly employed non-linear component. Here, we provide a concise mathematical description of a lithium niobate MZM, for which the output can be expressed as [136]:

$$E_{\text{out}}(t) = E_c \cos\left[\frac{\varphi\big[V(t)\big]}{2}\right] \cdot \cos(\omega_c) \tag{3.1}$$

where $E_c$ and $\omega_c$ represent the electric field amplitude and angular frequency of the input optical carrier (shown in Figure 3.4 as frequency $f_c$), respectively. $V(t)$ denotes the applied electrical drive voltage, while $\varphi[V(t)]$ signifies the optical phase difference induced by $V(t)$ between the two arms (hence being an intensity modulator) of the MZM.

When the driving voltage $V(t)$ is a sinusoidal electrical signal and the modulator is biased at a constant voltage, $\varphi[V(t)]$ can be written as:

$$\varphi\big[V(t)\big] = \varphi_0 + \frac{\pi}{V_\pi} \cdot V_e \cos(\omega_e t) \tag{3.2}$$

where $\varphi_0 = \pi V_{\text{Bias}}/V_{\pi\text{-DC}}$ is a phase constant related to the bias voltage $V_{\text{Bias}}$ (DC bias shown in Figure 3.4) and DC half-wave voltage $V_{\pi\text{-DC}}$, $V_\pi$ is the half-wave voltage at a certain frequency and $V_e$ and $\omega_e$ are the amplitude and angular frequency of the RF input signal, respectively. Then, Eq. (3.1) can be rewritten using the Bessel function as:

$$\begin{aligned} E_{\text{out}}(t) = {} & E_c \cos\left(\frac{\varphi_0}{2}\right) \cdot J_0(\beta) \cos(\omega_c t) \\ & + E_c \cos\left(\frac{\varphi_0}{2}\right) \times \left\{ \sum_{n=1}^{\infty} J_{2n}(\beta) \Big[ cos(\omega_c t - 2n\omega_e t + n\pi) \right. \\ & \qquad \left. + cos(\omega_c t + 2n\omega_e t - n\pi) \Big] \right\} \\ & - E_c \sin\left(\frac{\varphi_0}{2}\right) \times \left\{ \sum_{n=1}^{\infty} J_{2n-1}(\beta) \Big[ \sin\left(\omega_c t - (2n-1)\omega_e t + n\pi - \frac{\pi}{2}\right) \right. \\ & \qquad \left. - \sin\left(\omega_c t + (2n-1)\omega_e t - n\pi + \frac{\pi}{2}\right) \Big] \right\} \end{aligned} \tag{3.3}$$

where $J_n$ is the first kind Bessel function of the $n^{th}$ order and $\beta = (V_e/V_\pi) \cdot (\pi/2)$ is the modulation index.

Eq. (3.3) holds notable importance when compared to the mathematical expression for the output of an RF frequency mixer, as depicted in equation Eq. (2.55) because both embody the superposition of an infinite number of harmonics. Eq. (3.3) delivers improved clarity and ease of interpretation due to its characterisation by three fundamental elements: zero-order, odd-order, and even-order terms.

The amplitude terms of the odd and even orders are associated with the phase constant $\varphi_0 = \pi V_{\text{Bias}}/V_{\pi\text{-DC}}$ and exhibit orthogonality. The odd-order term features a sine function, $E_c \sin(\varphi_0/2)$, while the even-order term presents a cosine function, $E_c \cos(\varphi_0/2)$. Consequently, it becomes apparent that by fine-tuning the DC bias of the modulator, the amplitude (or energy) of the odd and even harmonics will display an inverse correlation, i.e., as one increases, the other decreases. This

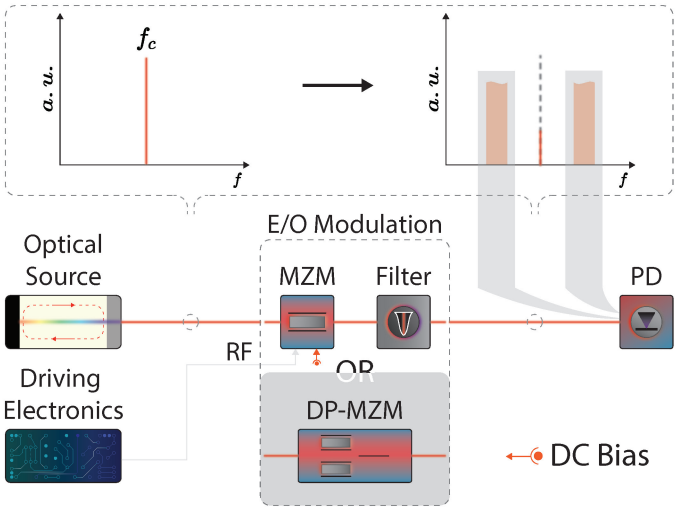


**Figure 3.4:** Depiction of optical frequency multiplexing utilising a Mach-Zehnder modulator (MZM) combined with optical filtering for higher-order sideband selection (typically first-order for frequency doubling, second-order for frequency quadrupling), or using a dual-parallel MZM (DP-MZM).

property allows for maximising the energy of one harmonic set over the other, providing enhanced control over the system's performance.

Adjusting the bias of an MZM is a common technique employed in microwave photonics applications to regulate the amplitude and phase of harmonics. This method is also utilised in photonics-based frequency multiplexing, where a typical schematic for photonic frequency multiplexing using an MZM is depicted in Figure 3.4.

A continuous wave optical source generates an optical carrier at frequency $f_c$, enabling electro-optic modulations that produce higher-order harmonics for frequency multiplexing. In this context, two prevalent approaches are employed. The first approach involves using a single MZM with a bias to maximise the energy of the first-order sidebands. Subsequently, frequency doubling is achieved by sending the selected sidebands (isolated using optical filters) into a photodetector (see Figure 3.4). The second approach entails using a dual-parallel MZM (DP-MZM) with specific bias voltages applied to the DP-MZM to attain particular phase conditions. This configuration ensures unwanted harmonics undergo destructive interference, eliminating the need for additional optical filters.

Optical-RF frequency multiplexing presents two primary advantages, which are elaborated on below:

- Simplified system architecture: An example of this is a system based on a Mach-Zehnder modulator MZM. This approach requires fewer optical components, making it a promising candidate for photonic on-chip integration while maintaining a favourable size-weight-and-power profile [137]. Moreover, these methods do not necessitate extra photonics-based up-conversion using an additional optical carrier, as the frequency multiplexing process simultaneously multiplexes the RF input's carrier frequency. This results in a more efficient and streamlined system design.
- Inherent time-frequency linearity from RF input devices: This advantage becomes particularly relevant when the RF input exhibits high signal quality, characterised by excellent time-frequency linearity, signal-to-noise ratio (SNR), and spurious-free dynamic range (SFDR). This is because the quality of the frequency-multiplexed signal is intrinsically dependent on the RF input signal's characteristics. Consequently, a high-quality RF input ensures that the frequency-multiplexed signal will also exhibit desirable performance attributes, thus maintaining signal integrity throughout the system.

Nevertheless, this approach also exhibits several drawbacks like any other system.

Firstly, the system's suitability for long-term operation is compromised due to the use of MZMs. MZMs are sensitive to fluctuations in bias voltage over time ($V_\pi$), which can lead to performance degradation [138]. Additionally, MZMs are typically sensitive to the polarisation state of the input optical signal, necessitating the use of polarisation-maintaining fibres or other polarisation control measures to ensure stable and reliable performance. Moreover, MZMs are susceptible to ambient temperature changes.

Secondly, the system presents a trade-off between signal quality and the speed of the driving RF electronics. High-speed electronics with acceptable SNR, SFDR, and time-frequency linearity would outperform the relatively low-cost VCO, albeit at a higher cost. It is also worth noting that the driving electronics may introduce a certain degree of complexity since the RF input signal must operate at a specific carrier frequency: 1) to avoid further up-conversion and 2) to prevent overlaps between adjacent harmonic orders for a decent SFDR.

Lastly, the system exhibits limited flexibility regarding MZM modulation bandwidth (which may be further constrained by RF components, such

as the bandwidth of an RF hybrid coupler, as some approaches require two RF driving signals with a 90-degree phase difference). Therefore, this limitation could restrict the range of RF frequencies that can be effectively multiplexed, considering the RF bandwidth of both the driving electronics and the MZM and the frequency range of overlap-free harmonics.

### Photonic Digital-to-Analogue Converters

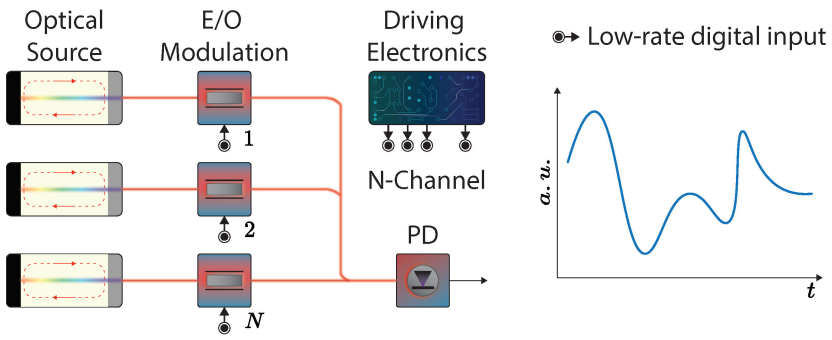


**Figure 3.5:** Illustration of a photonic digital-to-analogue converter (DAC) employing an electro-optical modulator network alongside a multi-channel low-rate bit pattern generator to generate high-speed, arbitrary waveforms.

A photonic digital-to-analogue converter (DAC) is an interesting way to synthesise radar waveforms by imitating the principle of electronic digital-to-analogue converters. Existing approaches rely on high-speed digital pulse pattern generators and multiple electro-optic modulators to generate a series of weighted optical harmonics, in parallel or serial, to achieve arbitrary waveform synthesising.

Using a parallel weighted photonic digital-to-analogue converter (DAC) as an example (illustrated inFigure 3.5), an optical carrier is divided into $N$ channels. Each channel is allocated a power level equivalent to $2^n$ times the power of the first channel. These channels are then individually modulated by their corresponding $n^{\text{th}}$ sequence. Once modulated, the channels are combined in a photodetector (PD), where their signals are summed together. Following the photodetection process, the combined signal passes through an electrical filter, ultimately generating the desired radar waveform.

The principal advantage of waveform generation using a photonic DAC lies in its exceptional flexibility. This allows for customising the temporal

duration and waveform profile to suit various application requirements. For example, an array of waveforms, including triangular, parabolic, rectangular, and saw-tooth shapes, can be generated using a photonic DAC [126]. This adaptability enables the system to cater to various radar signal demands, making it an attractive option for versatile and high-performance applications. However, such an approach suffers from the trade-off between system stability and performance regarding waveform quality (signal-to-noise ratio), the effective number of bits (ENOBs), and dynamic range.

### Radar Signal Generation through Frequency-Shifting Loop Techniques

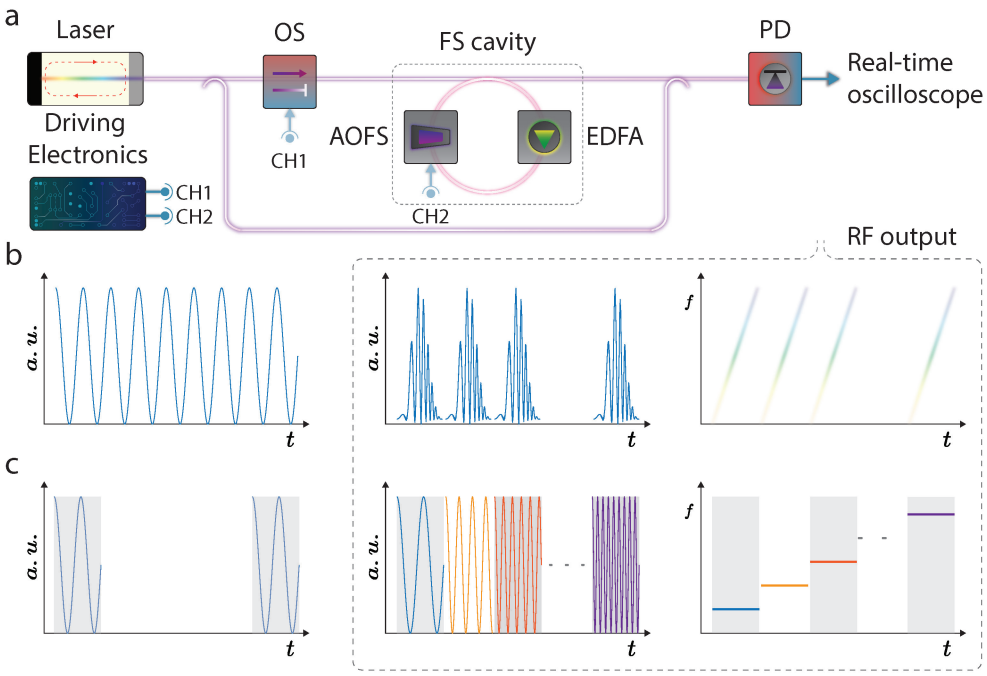


**Figure 3.6:** Illustration of radar signal generation using a frequency-shifting loop for creating chirp and stepped-frequency signals. **(a)** Schematic of a standard frequency-shifting loop experimental setup. **(b)** Introduction of a single-frequency continuous wave into the loop generates chirp signals. **(c)** Input of a single-frequency pulsed signal into the loop results in the production of stepped-frequency signals.

An optical frequency-shifting loop serves as a versatile tool for generating various radar signal types, including stepped-frequency (SF), linearly frequency-modulated (LFM), and stepped-frequency chirp signals (SFCS). The system operates in two distinct modes: continuous wave injection

(Figure 3.6**b**) and pulsed signal injection (Figure 3.6**c**).

In the continuous wave injection mode, a single-frequency continuous wave is introduced into the loop, generating LFM signals with bandwidths up to 28 GHz while preserving phase continuity [139]. However, the repetition rate of these signals is constrained by the loop cavity's round-trip time, limiting the ambiguity range for such a radar system. For example, in an optical frequency-shifting loop with a 100 ns round-trip time, the range ambiguity is 15 metres.

In the pulsed signal injection mode, a substantially broader bandwidth is attained, producing SF signals with a 300-fold increase in bandwidth [4]. This method will be thoroughly examined from Chapter 4 to Chapter 6, showcasing a wide array of demonstrations.

To generate SFCS signals, frequency modulation is applied to the injected pulsed signals. This mode can also produce a stitched LFM signal with phase discontinuity between adjacent pulses and exhibits envelope modulation [140], necessitating additional signal processing for correction and potentially impacting radar-ranging performance. The feasibility and challenges of this approach for both radar and LiDAR sensing will be discussed in the final chapter of this thesis.

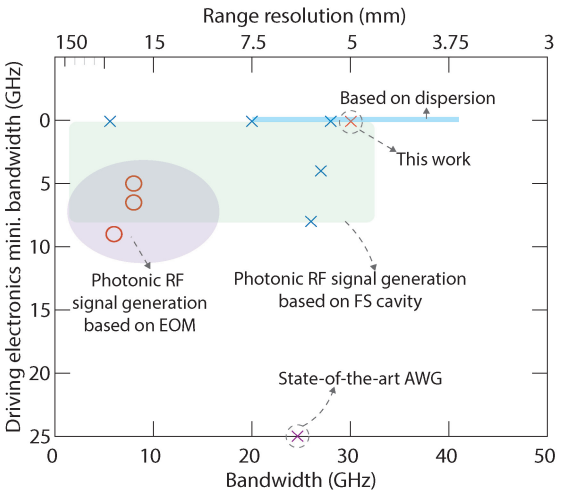


**Figure 3.7:** Comparison of the photonics-based wideband RF signal generation in terms of the speed of the system's driving electronics and the radar signal bandwidth across various photonic approaches. This plot is based on Table 3.1.

We provide a table that compares the system used in this thesis with several other photonic approaches previously mentioned for generating

radar signals (Table 3.1). Figure 3.7 illustrates a figure of merit based on Table 3.1. This figure contrasts the photonics-based wideband RF signal generation by evaluating the speed of the system's driving electronics and the showcased radar signal bandwidth across various photonic strategies. These include using frequency-shifting cavities, laser sweeping, EOMs, and engineered fibre dispersion.

Thus far, radar signal generation techniques employing frequency-shifting loops have demonstrated a bandwidth of over 30 GHz (5 mm range resolution) [4] while utilising a relatively simple to moderately complex optical system setup and relying solely on MHz-level driving electronics. This achieves an optimal balance between sufficient bandwidth, system tunability, high time-frequency linearity, and avoidance of high-speed electronics.

| Demonstrated bandwidth (GHz) | Formality | linearity (%) | Mini. RF bandwidth (GHz) | Reference |
|---|---|---|---|---|
| **30** | **SF** | **0.0036** | **0.1** | **This Work** |
| Photonic RF signal generation based on FS cavity | | | | |
| 5.6 | SF | NA | 0.08 | [2] |
| 26 | LFM,SFCS | NA | 8 | [130] |
| 20 | SF | NA | 0.08 | [131] |
| 27 | SF | NA | 4 | [132] |
| ¿28 | LFM | NA | 0.08 | [139] |
| Photonic RF signal generation based on laser sweeping | | | | |
| 4 | LFM | NA | NA | [141] |
| 2 | LFM | 7.8** | NA | [1] |
| 7.5 | LFM | NA | NA | [119] |
| 18.5 | LFM | NA | 0.12 | [142] |
| Photonic RF signal generation based on dispersion | | | | |
| ¿30 | LFM | NA | NA | [106] |
| Photonic RF signal generation-based EOM | | | | |
| 8 | LFM | NA | 12 Gbit/s | [127] |
| 6 | LFM | NA | 9 | [137] |
| 8 | LFM | NA | 6.5 | [123] |
| State-of-the-art AWG | | | | |
| 25 | SF | 0.0013 | 25 | Keysight |

**Table 3.1: Comparison with reported photonic approaches.** SF, stepped-frequency; LFM, linear-frequency modulated waveform; CW, continuous wave; NA, data not available or not mentioned in the literature; **, the linearity in the reference is the ratio between the maximum frequency deviation to the total bandwidth; -, not applicable.

Chapter 4

# Photonic Stepped-Frequency Radar and ISAR Imaging

The ever-increasing demand for high resolution and real-time recognition in radar applications has fuelled the development of electronic radars with increased bandwidth, high operation frequency and fast processing capability. However, the generation and processing of wideband radar signals increase the hardware burden on complex and high-speed electronics, limiting its capability for applications that demand high spatial resolutions. Progress is being made; photonics-assisted radars offer higher frequencies but still heavily rely on costly and sophisticated high-frequency electronic devices such as benchtop digital microwave waveform generators that fundamentally constrain the bandwidth and the practical utility. Here, we demonstrate a photonics-based radar with $>$11 GHz bandwidth (exceeding 20 GHz without RF antenna bandwidth limitation) driven and processed by simple MHz-level-electronics-based acoustic-optic modulation, which radically eliminates the requirement for ultra-fast GHz-speed electronics for wideband radar signal generation and processing. This wideband radar achieves centimetre-level spatial resolution and a real-time imaging rate of 200 frames per second, allowing high-resolution detection of rapidly moving blades of an unmanned aerial vehicle. This radar provides an important technological basis for next-generation broadband radars with greatly reduced system complexity essential to ubiquitous sensing applications such as autonomous driving, environmental surveillance, and vital sign detection.

## 4.1 Photonic Stepped-Frequency Radar

Radio detection and ranging (radar) is an essential technology for various applications in both civilian and security sectors, including autopilot assistance, anti-collision warning systems, target identification, hand gesture recognition, and remote heartbeat detection [143, 144, 145, 146, 147]. Radar systems emit time or frequency-modulated microwave signals to illuminate objects of interest. The resulting snapshots of objects' spatial and velocity information are encoded in the returned analogue signals as time delay and instantaneous phase variation, which can then be extracted through digital signal processing.

Modern applications increasingly demand radar systems that can accurately locate and recognise objects, necessitating finer spatial resolution that is inversely related to the radar signal bandwidth. However, the development of ultra-broadband electronic radars with high carrier frequencies faces fundamental limitations due to achievable electronic circuit clock rates, which typically only reach a few gigahertz (GHz), and the increased complexity in frequency up- and down-conversion.

Moreover, using wideband radar signals for sampling echo signals at receivers places a more significant burden on hardware, particularly for analogue-to-digital converters (ADCs), and reduces the sampling precision [148]. Consequently, there is a pressing need to explore alternative technologies that can overcome these challenges and deliver radar systems with improved performance in terms of spatial resolution, bandwidth, and signal processing capabilities.

In recent years, photonics-assisted radar technology has emerged as a promising solution to overcome the electronic limitations of bandwidth and operation frequency. This approach leverages the ultra-wide fractional bandwidth at optical frequencies (typically in the range of hundreds of terahertz) for the generation and processing of microwave radar signals [28, 29, 87, 30]. Significant improvements in radar ranging performance have been demonstrated by employing microwave photonic technology [23, 76]. For instance, ultra-broadband radars with bandwidths exceeding GHz levels enable unprecedented centimetre-level spatial resolution [106, 123], which allows for identifying fine object features and accurate recognition.

Photonics-assisted multiple-input and multiple-output radars [149] and multi-band radars [85, 150, 151] have also been demonstrated, exhibiting enhanced flexibility and low loss coherent RF photonic signal distribu-

tion. However, despite these advancements, reported photonics-assisted radars often rely on sophisticated and expensive electronic devices such as arbitrary waveform generators (AWGs) and tunable high-frequency oscillators [152, 153, 132, 154]. Using these benchtop high-frequency electronic devices, like ultra-fast AWGs, ultimately sets the upper limit for achievable radar signal bandwidth and hinders the transition of demonstrated radar systems from laboratories to practical applications.

Optical frequency doubling or quadrupling [122] and photonic digital-to-analogue converters [127] have been employed to reduce the bandwidth requirement by half or a quarter. However, these methods come at the cost of modulator bias instability, additional complexity, unavoidable frequency spurs, and limited agility. Alternative approaches, such as frequency sweep light sources [116, 155, 94], laser pulse shaping [106], time stretching [156], and chirped optoelectronic oscillators [119], have also garnered significant interest.

Nonetheless, it remains challenging for these techniques to simultaneously achieve high frequency-time linearity for accurate ranging, wide bandwidth for high detection resolution, and long pulse duration for precise kinetic target capturing [157]. Therefore, a photonic analogue radar system driven by MHz-level electronic components that can achieve high spatial resolution enabled by broad bandwidth, real-time detection, and high time-frequency linearity is highly desirable for practical radar applications.

This chapter delves into a photonic stepped-frequency radar system based on a frequency-shifting loop. We start from its conceptual implementation to experimental radar ranging and 2D imaging demonstrations, highlighting the potential of an approach that offers a broad bandwidth using a relatively low-complexity system setup, ideal for high refresh rate 2D radar imaging applications. Notably, the system explored in this chapter was developed using single-mode fibre without using polarisation-maintaining components, thus highlighting the effects of polarisation scrambling and polarisation-dependent noise originating from such a non-polarisation-maintaining system, setting the stage for substantial performance enhancements discussed in Chapter 5.

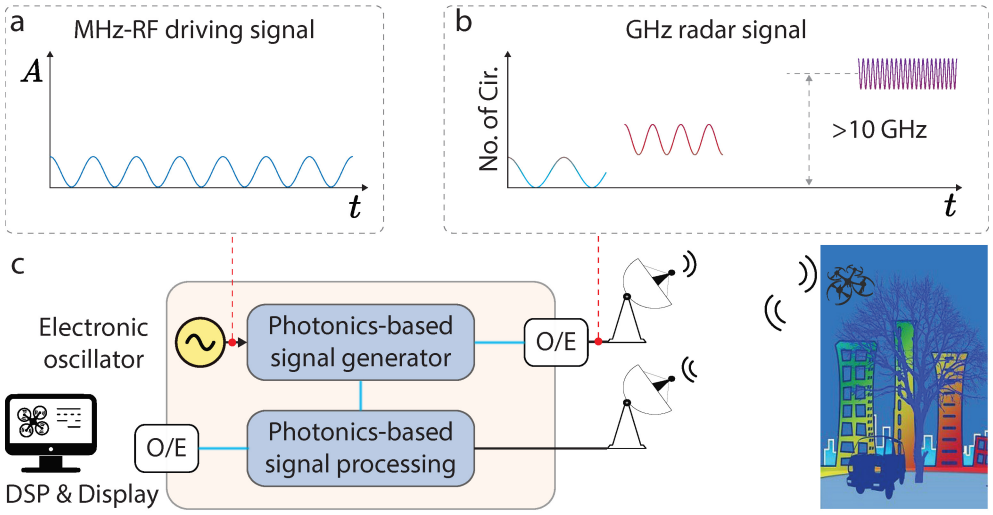


**Figure 4.1:** A schematic of the photonic wideband stepped-frequency radar system for target ranging and sensing driven by MHz-speed electronics. This radar system features key components such as a photonics-based radar signal generator, a photonic signal demodulation unit, O/E and E/O converters, and microwave antennas. An electronic oscillator operating at MHz frequency (Figure 4.1**a**) drives the signal generator to produce optical stepped-frequency (SF) signals with a fixed-step progressive centre frequency shift. Microwave SF signals (Figure 4.1**b**) are generated through O/E conversion and transmitted by a microwave antenna. Returned radar signals are mixed with a photonic reference signal to create a baseband demodulated electric signal. Object distance and velocity data, such as for unmanned aerial vehicles, can be extracted using low-speed digital signal processing (DSP). O/E, optical-to-electrical conversion; E/O, electrical-to-optical conversion; No. of Cir., number of circulation.

### 4.1.1 Concept and Implementation of the Photonic SF Radar System

The conceptual diagram of the proposed photonic wideband stepped-frequency radar (Figure 4.1) is constructed with several components, including a photonic signal generator, an optical-to-electrical (O/E) converter, RF antennas, a photonics-based signal mixing unit, and an electrical-to-optical (E/O) converter.

The photonic signal generator is responsible for creating ultra-wideband photonic radar signals, generated using an electronic oscillator, which oscillates at an MHz-level RF frequency (Figure 4.1**a**). This oscillator drives the production of stepped-frequency signals in the optical domain. The instantaneous frequency of the photonic stepped-frequency signal is meticulously shifted by a constant frequency step within an ultra-low-loss optical circulating loop, determined by the electronic os-

cillator's frequency. This precise shifting process achieves a substantial accumulative bandwidth three orders of magnitude broader than the drive signal.

Following the signal generation, the optical-to-electrical (O/E) converter translates the photonic signals into microwave signals (Figure 4.1**b**). This conversion process is crucial for the system's compatibility with existing RF technologies. After conversion, the microwave-domain SF signals are transmitted using RF antennas, which send the signals into the environment for radar applications.

One of the key features of this radar system is the photonics-based signal mixing unit, which enables signal demodulation directly in the optical domain, offering a significant advantage in terms of processing speed and efficiency. Furthermore, the electrical-to-optical (E/O) converter facilitates electric signal processing, ensuring seamless integration with existing electronic systems. Due to the intrinsic properties of the stepped-frequency signal, the demodulated radar signals possess a bandwidth of MHz-level. This comparatively narrow bandwidth allows for MHz-level speed data acquisition, resulting in rapid signal processing.

A receiver antenna captures the radar signals reflected by objects and subsequently combines them with an optical reference signal, which is derived from a portion of the transmitted photonic stepped-frequency signal. This optical-optical signal mixing process generates a demodulated signal that contains the phase difference between the received echo signal and the reference signal. This crucial information can be utilised to determine the object's range and velocity. Via a photodetector that provides a self-heterodyne measurement, the optical demodulated signal is translated into an electrical signal in the baseband with a narrow bandwidth. The baseband electrical signal can be rapidly sampled and precisely processed by a small-bandwidth digital signal processor, greatly reducing the hardware burden on the radar receiver.

The experimental implementation of the photonic wideband stepped-frequency radar is depicted in Figure 4.2**a**, consisting of a transmitter unit, a receiver unit, and a pair of RF horn antennas for radar signal emission and reception. Schematic illustrations of signals at different positions (marked by **i-vi**) within the radar transmitter and receiver are presented in Figure 4.2**b** and Figure 4.2**c**, respectively.

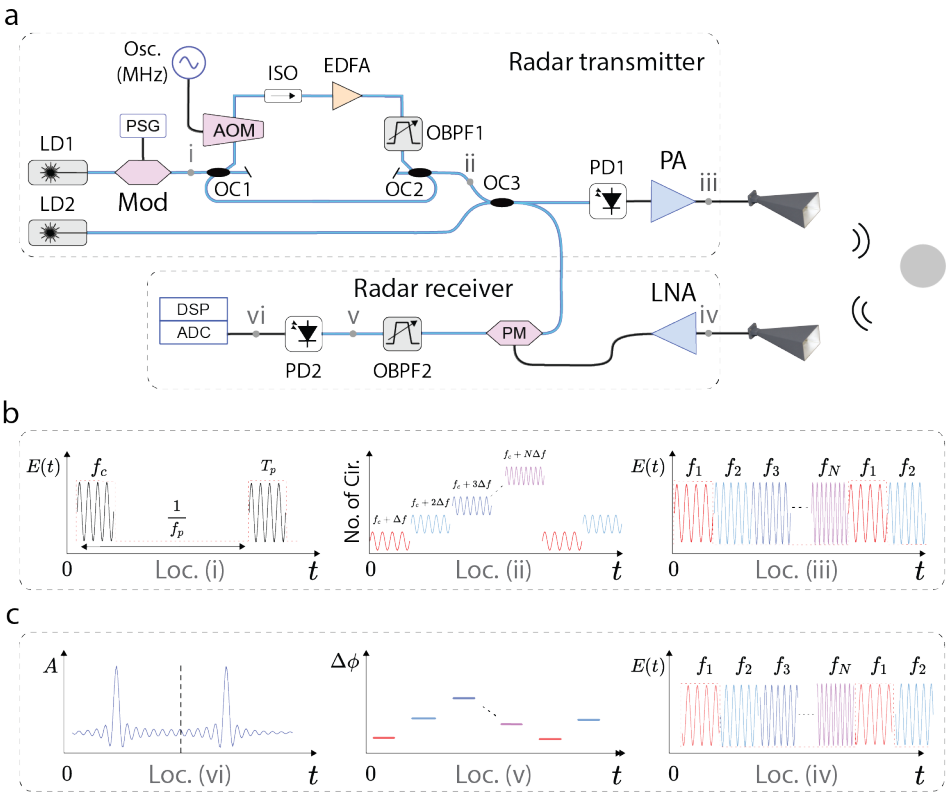


**Figure 4.2:** Experimental setup of the photonic wideband stepped-frequency radar system for ranging and imaging applications. **a** The proposed photonics-based SF radar platform consists of a radar transmitter that optically generates broadband RF signals, driven by an MHz-frequency electrical oscillator and a radar receiver that provides optical signal mixing to form baseband demodulated electrical signals through photodetection. **b** Schematic illustrations of temporal waveforms at different locations (i-iii) of the radar transmitter. **c** Schematic illustrations of returned radar signals at the radar receiver's different locations (iv-vi). LD, laser diode; Mod, optical switch; Osc, electronic oscillator; OC, optical coupler; AOM, acousto-optic modulator; ISO, optical isolator; EDFA, erbium-doped fibre amplifier; OBPF, optical bandpass filter; PD, photodiode; PA, power amplifier; LNA, low-noise amplifier; PM, phase modulator; No. of Cir., number of circulation.

### 4.1.2 Principle of Photonic Wideband Radar Transmitter

In the radar transmitter, a continuous-wave laser (LD1) with a central frequency of $f_c$ is converted into a series of rectangular pulses with a pulse duration of $\tau_p$ and a repetition rate of $f_p$ using an optical switch driven by an electronic pulse signal generator. A 10% portion of the seed pulse is injected into a fibre-based optical frequency-shifted cavity [158, 159] via an optical coupler (OC1), employing an acousto-optic modulator

(AOM) to adjust the pulse centre frequency by a fixed step incrementally. The frequency step $\Delta f$ can be positive or negative, contingent upon the AOM's frequency shift direction. The absolute frequency shift $|\Delta f|$ is determined by a low-frequency electronic oscillator set to 40/80 MHz in subsequent experimental demonstrations. For clarity, we illustrate the photonic wideband stepped-frequency radar principle based on positive frequency-shifting modulation.

After $n$ circulations within the optical loop, the light frequency is shifted to $f_c + n \times \Delta f$, where $n = 1, 2, 3 \ldots N$, generating an optical SF signal as shown in Location (**ii**) of Figure 4.2**b**. The seed pulse duration $\tau_p$ is regulated to equal or slightly fall short of the transient time $\tau_c$ for one recirculation in the cavity, preventing interference due to overlapping adjacent pulses. Within the cavity, an optical isolator defines the light circulation direction (clockwise), while an erbium-doped fibre amplifier (EDFA) compensates for optical losses. An optical bandpass filter (OBPF1) determines the spectral range of the frequency-shifted optical signal and minimises amplifier noise.

A 10% portion of the optical SF signal is combined with a local optical oscillator at $f_{LO}$ ($f_{LO} \leq f_c$, which is provided by LD2) in a photodetector through heterodyne detection, yielding an SF signal in the microwave domain with an instantaneous frequency of $f_n = |f_c - f_{LO} + n \times \Delta f|$ and a total bandwidth of $N \times \Delta f$ (Location (**iii**)). An ultra-wideband signal is produced when the circulation number $N$ is set to a large value defined by OBPF1's bandwidth, forming the foundation for wideband radar signal generation. The microwave SF signal is amplified before being emitted by a horn antenna. It is worth noting that the RF carrier frequency can be flexibly adjusted by modifying the frequency difference between the two lasers, enabling the potential for frequency-agile capability in multi-band operation.

### 4.1.3 Principle of Photonic Wideband Radar Receiver

In the radar receiver, radar signals reflected by targets are captured by a microwave horn antenna before being amplified and optically processed, as depicted in Figure 4.2**a**. The reflected radar signal exhibits a time delay $\tau$ compared to the emitted signal, as demonstrated in Location (**iv**) of Figure 4.2**c**. This time delay originates from the round-trip travel time $\tau = 2d/c$ over distance $d$ between the antennas and the target, with $c$ representing the speed of light in the air. Owing to the time delay, each frequency-shifted pulse acquires a distinct phase shift $\Delta\varphi =$

$(n\Delta f) \times \tau$. This frequency-dependent phase shift serves as the foundation for extracting target distance information, as distance $d$ can be determined once the phase shift is obtained.

To convert the time-varying phase shift into a measurable parameter, an optical phase modulator is employed to mix the returned radar signal with the reference signal, subsequently enabling the translation of phase shift to directly measurable intensity variation. By phase modulating the optical local oscillation frequency $f_{LO}$, a first-order sideband is generated within the frequency range from $f_c + \Delta f$ to $f_c + N\Delta f$, coinciding with the optical SF signal's spectral range. Nevertheless, the two spectrally overlapping components exhibit a phase difference governed by $\Delta\varphi$. An optical bandpass filter (OBPF2) isolates the spectrally overlapping signals and eliminates spurs at other frequencies.

The interference between these two spectrally overlapping signals translates the frequency-dependent phase difference into a time-varying amplitude envelope proportional to $cos[\Pi(t) \times 2\pi n\Delta f\tau]$, where $\Pi(t)$ represents a train of frequency-shifted rectangular pulses, as shown in Location (**v**) of Figure 4.2**c**. Through photodetection in PD2, the demodulated optical signal is converted to electrical signals in the baseband, possessing an instantaneous bandwidth significantly smaller than $\Delta f$, which allows for rapid and precise processing by electronic components. By applying an inverse Fourier transformation (IFFT) to the detected electrical signal, the time delay $\tau$ and, consequently, the target distance $d$ can be retrieved from the IFFT spectrum. It is worth noting that the phase relationship between two adjacent frequencies is fixed due to the physical length of the fibre used in the loop.

### 4.1.4 Electric Field Generated at the Photonic Demodulator

The output electric field of $n$-th frequency-shifted pulse at the output of the optical loop (Figure 4.2**a**, Location (**ii**)) can be written as [160, 159, 161]

$$s(t,n) = E_0\Pi(t)g(f)e^{i2\pi(f_c+n\Delta f)t}[e^{-i2\pi nf_c\tau_c}e^{-i\pi n(n+1)\Delta f\tau_c}], \tag{4.1}$$

where

$$\Pi(t) = \begin{cases} 1, & \text{if } t \in \left[(n-1)\tau_c, n\tau_c\right] \qquad (n = 1,2...N) \\ 0, & \text{otherwise.} \end{cases} \tag{4.2}$$

is a time window function with a unity gain, and $g(f)$ is the spectral envelop function determined by intra-loop components such as the OBPF1 and the EDFA, which is mapped to the temporal envelop window of the frequency-shifted pulses [161]. Eq. (4.1) indicates that the $n$-th frequency-shifted pulse picks up an accumulated phase term $\varphi_n = -i2\pi n f_c \tau_c - i\pi n(n+1)\Delta f \tau_c$. After combined with the optical local oscillation, the mixed signal is given by $S_{mix}(t,n) = s(t,n) + E_{LO}e^{i2\pi f_{LO}t}$ where $E_{LO}$ is the LO amplitude. The transmitted RF SF signal is generated by the heterodyne mixing via photodetection, given by

$$S_T(t,n) \propto E_0 E_{LO} \Pi(t) g e^{i2\pi(f_n)t+\varphi_n}, \tag{4.3}$$

where the shifted frequency is $f_n = |f_c - f_{LO} + n\Delta f|$. The transmitted RF radar signal is reflected by an object of interest given by

$$S_R(t,n) = \alpha E_0 E_{LO} \Pi(t) g e^{i2\pi(f_n)(t-\tau)+\varphi_n}, \tag{4.4}$$

where $\alpha$ is the gain coefficient. $\tau$ is the round-trip delay between the radar and the object, which can be time-variant for moving objects.

One tap of the mixed optical signal $S_{mix}(t,n)$ is modulated by the returned RF radar signal $S_R(t,n)$ through a phase modulator. The modulated optical signal is expressed as

$$S_{Demod}(t,n) = S_{mix}(t,n) e^{\frac{S_R(t,n)}{V_\pi}}, \tag{4.5}$$

where $V_\pi$ is the half-wave voltage of the phase modulator. Under a small signal model, using Jacobi-Anger expansion, Eq. (4.5) can be re-written in series as

$$\begin{aligned} S_{Demod}(t,n) \propto & \left\{ E_0 \Pi(t) g e^{i2\pi(f_c+n\Delta f)t+\varphi_n} \left[ J_0(\beta) + \sum_{k=1}^{\infty} J_k(\beta) e^{ik2\pi f_n(t-\tau)+\varphi_n} \right.\right. \\ & \left.\left. + \sum_{k=1}^{\infty} (-1)^k J_k(\beta) e^{-ik2\pi f_n(t-\tau)+\varphi_n} \right] \right\} \\ & + \left\{ E_{LO} \Pi(t) e^{i2\pi f_{LO}t} \left[ J_0(\beta) + \sum_{k=1}^{\infty} J_k(\beta) e^{ik2\pi f_n(t-\tau)+\varphi_n} \right.\right. \\ & \left.\left. + \sum_{k=1}^{\infty} (-1)^k J_k(\beta) e^{-ik2\pi f_n(t-\tau)+\varphi_n} \right] \right\} \end{aligned} \tag{4.6}$$

where $J_k$ denotes the $k^{th}$ order Bessel function of the first kind, and the modulation index is $\beta = (\alpha E_0 E_{LO} g(f))/V_\pi$. If we expand Eq. (4.6), we

could find out that two spectral components of interest are spectrally overlapped in the frequency span from $f_c$ to $f_c + n\Delta f$, which will be used to generate the demodulated signal. Then, the output field after the OBPF2 can be expressed as

$$S_F(t,n) \propto \left\{ E_0 \Pi(t) g J_0(\beta) e^{i2\pi(f_c+n\Delta f)t+\varphi_n} \right\} \tag{4.7}$$

$$+ \left\{ E_{LO} \Pi(t) J_1(\beta) e^{i2\pi f_{LO} t} e^{i2\pi f_n(t-\tau)+\varphi_n} \right\}$$

$$= \left\{ A_0 \Pi(t) e^{i2\pi(f_c+n\Delta f)t+\varphi_n} \right\} \tag{4.8}$$

$$+ \left\{ A_1 \Pi(t) e^{i2\pi(f_c+n\Delta f)(t-\tau)+\varphi_n+i2\pi f_{LO}\tau} \right\}, \tag{4.9}$$

where $A_0 = E_0 g J_0(\beta)$ and $A_1 = E_{LO} J_1(\beta)$. Then, the signal after the photodetection (PD2) can be expressed as:

$$S_{out}(t,n) \propto A_0 A_1 \Pi(t) e^{i2\pi|f_c-f_{LO}|\tau+i2\pi n\Delta f\tau}. \tag{4.10}$$

Since the linear phase term $e^{i2\pi|f_c-f_{LO}|\tau}$ corresponds to an overall time delay of the radar signal, the detected current of the demodulated radar signal when neglecting the phase offset (i.e., $e^{i2\pi|f_c-f_{LO}|\tau}$) can be expressed as

$$S_{out}(t,n) \propto \Pi(t) \cos(2\pi n\Delta f\tau). \tag{4.11}$$

The demodulated signal presented in Eq. (4.11) shares the same structure as the demodulated signal from an electronic stepped frequency radar that employs a signal of identical bandwidth. Therefore, range data can be obtained using Fourier-based signal processing techniques [162]. The range ambiguity arises when the phase shifts corresponding to two objects at different distances are equal, with the more distant object exhibiting a phase shift exceeding $2\pi$. In such cases, both targets seem to be at the same location. The range ambiguity is defined by the expression $c/2\Delta f$.

It is crucial to emphasise that the phase differences between transmitted and received signals within each step are the determining factors for extracting range information. The proposed radar system does not depend on the interpulse phase relationship between two consecutive frequencies, which falls outside the unambiguous range.

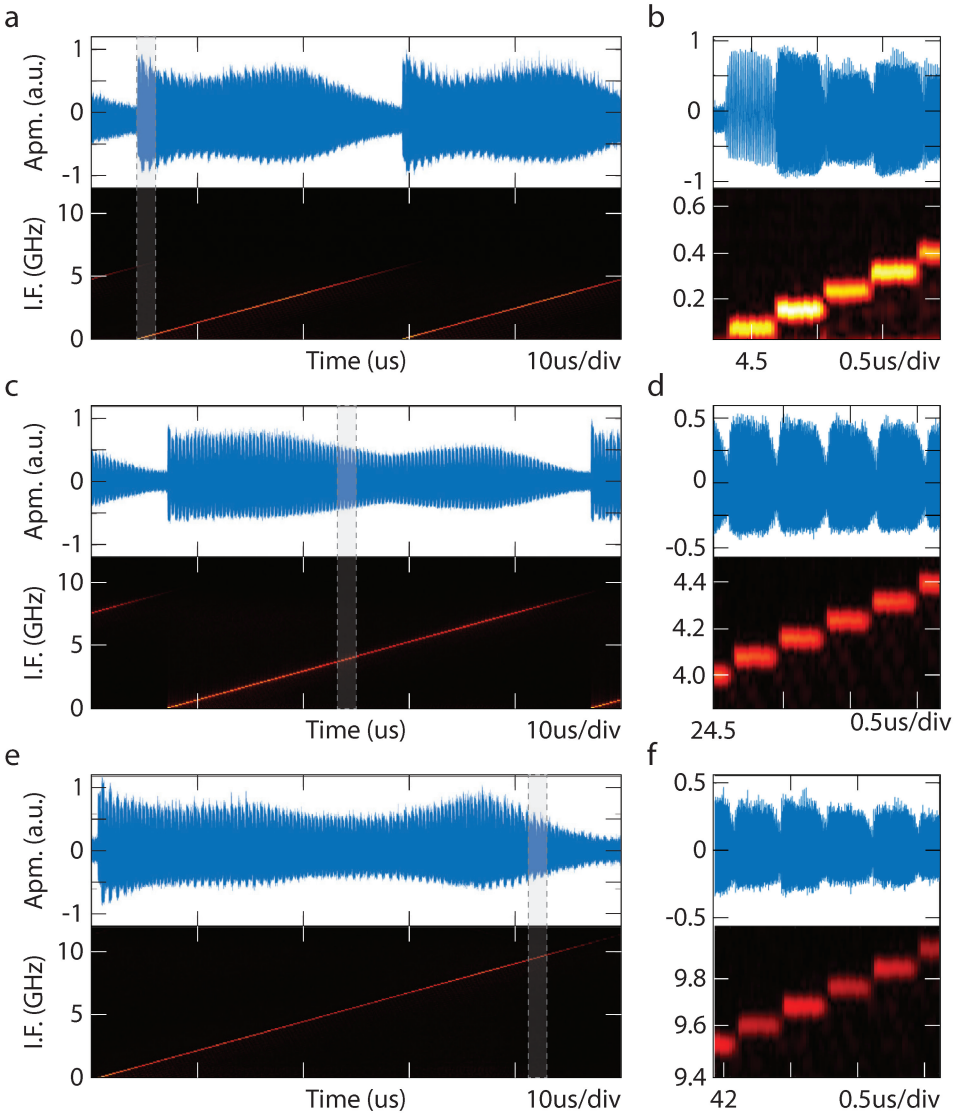


**Figure 4.3:** Flexible tuning of radar signal bandwidth from 5.76 GHz to 11.52 GHz. **a, c, e** display the temporal waveforms and corresponding time-frequency mappings for a radar pulse duration of 25 $\mu$s, 40 $\mu$s, and 50 $\mu$s, respectively, resulting in radar signal bandwidths of 5.76 GHz, 9.20 GHz, and 11.52 GHz. **b, d, f** provide a magnified view of the temporal waveforms and associated time-frequency relationships derived from short-term Fourier transform (STFT) results. I.F. denotes instantaneous frequency.

### 4.1.5 Broadband SF Signal

Broadband radar signals featuring adaptable bandwidth tunability are essential for applications that demand high spatial resolution and multi-band operation, a challenge often encountered in conventional electronic

radars. In this section, the flexible tuning of radar signal bandwidth within the proposed photonic stepped-frequency radar system is experimentally showcased. By employing the configuration depicted in Figure 4.2**a**, we achieve an RF bandwidth exceeding 11.52 GHz, ultimately attaining centimetre-level spatial resolution.

Figure 4.3 presents the time-domain waveforms of microwave stepped-frequency radar signals with varying bandwidths, measured at Location (**iii**) in Figure 4.2**a**. These detected microwave waveforms are transformed into baseband frequencies for observation through self-heterodyne mixing of the photonic stepped-frequency signal and a continuous-wave signal derived from LD1.

Figure 4.3**a** displays a periodic stepped-frequency signal's temporal and instantaneous frequency, featuring a bandwidth of 5.76 GHz and a temporal duration of 25 $\mu s$. The passband bandwidth of OBPF1 governs the attainable bandwidth, while the decaying envelope observed at the pulse train's tail results from the roll-off response of the filter edge. Each period of the recurring stepped-frequency signals comprises 72 frequency-shifted sub-pulses, with an 80 MHz frequency step, amounting to a total bandwidth of 5.76 GHz.

Figure 4.3**b** depicts the magnified waveform and corresponding instantaneous frequency for the first four sub-pulses. The dashed red trace represents the envelope of the seed pulse produced by a function generator (PSG), characterized by a pulse duration ($\tau_p$) of 340 $ns$ (full width at half maximum) and a repetition rate ($f_p$) of 40 kHz (25 $\mu s$ period interval).

Figure 4.3 clearly demonstrates that the stepped-frequency wave's carrier frequency continuously and steadily increases over time. This observation is confirmed by the frequency-time image acquired through short-term Fourier transform (STFT). In this experiment, the optical loop length within the radar transmitter was configured to have a round-trip time of approximately 340 $ns$, aligning with the pulse length of each frequency-shifted sub-pulse. By detuning $f_{LO}$ by 28 GHz from $f_c$, a 5.76-GHz-wide stepped-frequency signal originating at 28 GHz is synthesized in the microwave domain, which is shown in Figure 4.4.

The flexible broadening of synthesised microwave SF signal bandwidth can be achieved by increasing the passband bandwidth of OBPF1 within the optical loop depicted in Figure 4.2**a**. Throughout the demonstrations, the temporal duration ($\tau_p$) of the seed pulse, approximately 340 ns, and

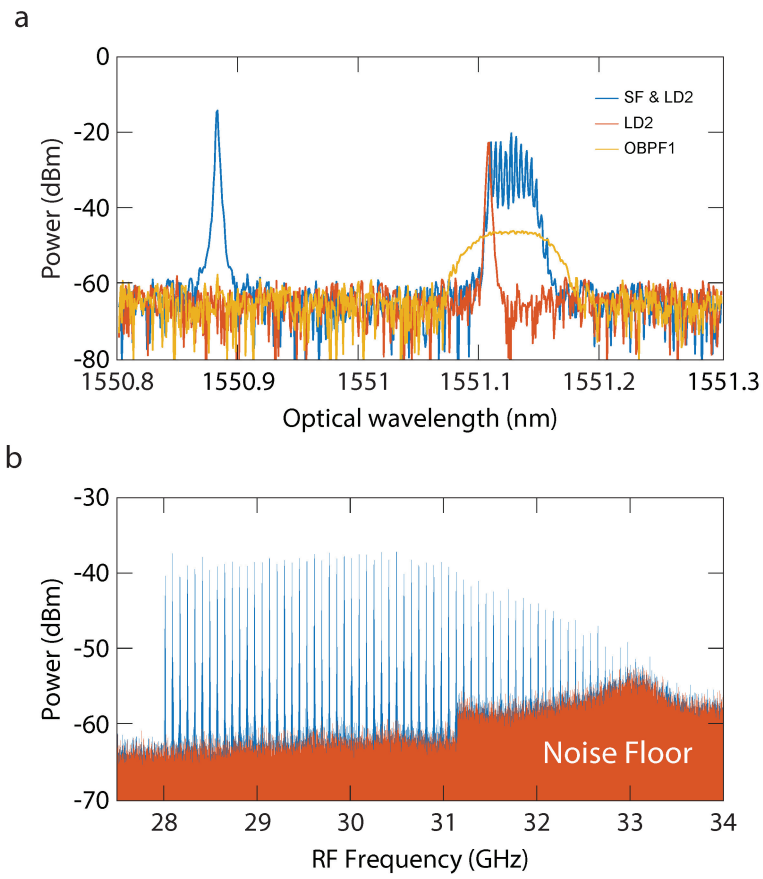


**Figure 4.4:** Spectra of the generated optical and microwave stepped-frequency (SF) signals. **a** The optical spectra illustrate the spectral relationship between LD1, LD2, the optical SF signal, and the OBPF1 response. **b** A comparison of the electrical spectra for the generated microwave SF signals and the noise floor of the ESA equipment. The electrical spectra measurements employed 5001 points, a 3 MHz bandwidth resolution, and a 100 ms sweep time without time averaging. The noise floor was determined by disconnecting the input to the ESA (Agilent E4448A).

the optical loop length, approximately 70 m of single-mode optical fibre, were kept constant.

To accommodate a greater number of frequency-shifted pulses in the time domain, the seed pulse period was increased to 40 $\mu$s and 50 $\mu$s, corresponding to repetition rates ($1/f_p$) of 25 kHz and 20 kHz, respectively. These extended pulse intervals enable the achievement of enhanced bandwidths of 9.2 GHz (115 sub-pulses) and 11.52 GHz (144 pulses), as depicted in Figure 4.3**c** and Figure 4.3**e**, respectively. The magnified temporal waveforms and instantaneous frequencies reveal that the centre frequency of the sub-pulses sequentially hops by a fixed frequency step

of 80 MHz while maintaining a relatively stable amplitude between adjacent sub-pulses. The SF signal with an 11.52-GHz bandwidth and a long pulse duration of 50 $\mu$s results in an ultra-large time-bandwidth product of $5.76 \cdot 10^5$.

Subsequent experiments will concentrate on the demonstration utilising an 11.52 GHz bandwidth, given the available operation bandwidth of the microwave antennas during the experiments.

### 4.1.6 High-Resolution SF Radar Ranging

Proof-of-concept demonstrations for high-resolution radar ranging are conducted using generated broadband microwave SF signals. Figure 4.5**a** presents the experimental configuration diagram for these radar-ranging demonstrations, featuring one or two reflectors emulating targets of interest. In Figure 4.5**b**, a single period of demodulated electrical signals detected by the receiver photodetector is displayed, with none, one, and two reflectors present, respectively. Rectangular pulse amplitudes in each trace represent the relative phase shifts acquired by the frequency-shifted sub-pulses, which are attributable to the signal flight time $\tau$ between objects and radar antennas. This is based on the operational principle depicted in Figure 4.5.

Digitally sampled time-dependent phase information is processed to determine the corresponding time delay and distance. When no objects are present, the blue trace exhibits an almost uniform amplitude envelope, signifying that no returned radar signal is detected. Consequently, a non-detectable ranging signal is obtained from the inverse fast Fourier transform (IFFT) of the temporal signal, as demonstrated in Figure 4.5**c**.

When a single reflector is present, the demodulated signal exhibits periodic amplitude modulation, which is converted into a dominant peak in the distance space via IFFT, as depicted in Figure 4.5**c**. With two reflectors placed 3 cm apart, the electrical signal displays more intricate amplitude modulation in the pulses, resulting in two closely spaced peaks in Figure 4.5**c**. However, due to the demonstration's limited radar signal bandwidth of approximately 4.8 GHz, the two reflectors cannot be clearly distinguished. The Fourier can explain this transform theorem, which states that more sampling points (number of pulses and bandwidth) are needed for finer spectral resolution in the Fourier space (and, consequently, spatial resolution in range).

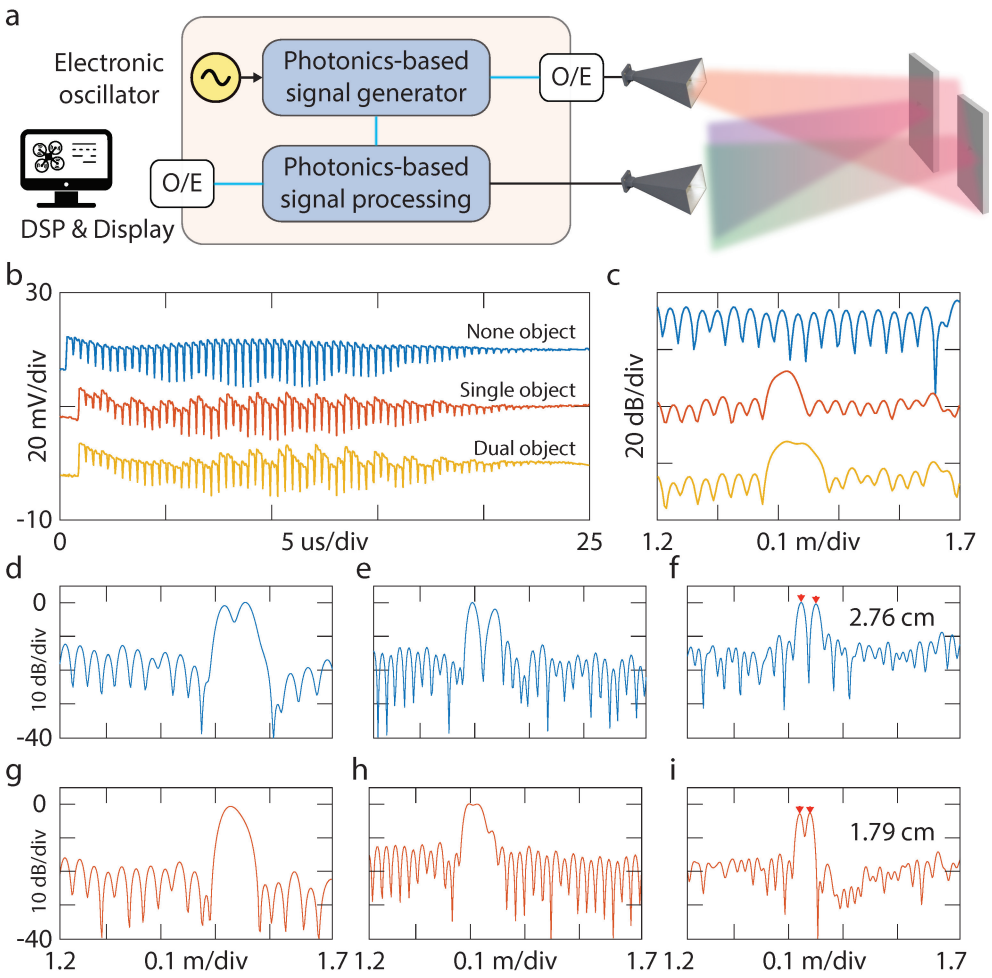


**Figure 4.5:** High-resolution radar ranging demonstration. **a** Experimental setup schematic. **b** Temporal waveforms of detected demodulated electrical signals with no, one, and two reflectors present. **c** Ranging results derived using inverse fast Fourier transform. **d-f** Ranging outcomes for two reflectors separated by 3 cm, employing radar bandwidths of 5.76 GHz, 9.20 GHz, and 11.52 GHz, respectively. **g-i** Ranging findings for two reflectors with a 1.5 cm separation, utilising bandwidths of 5.76 GHz, 9.20 GHz, and 11.52 GHz, respectively.

It is worth noting that the signal processing demands only a low sampling rate of greater than 2.9 MSa/s, as the demodulated sub-pulses have a repetition rate of around 2.9 MHz (the inverse of the optical loop's round-trip time). Increasing the seed pulse duration can further reduce the required sampling rate to below the MSa/s level, substantially easing the burden on digital signal processing. In these proof-of-concept demonstrations, a real-time electrical oscilloscope operating at a sampling rate of 31.25 MSa/s was utilised for data acquisition. As a result, the photonic

wideband stepped-frequency radar holds considerable promise for enabling rapid and even real-time radar ranging capabilities, as low-speed electronics can effectively manage data acquisition and processing.

As demonstrated in Figure 4.5**d-f**, finer spatial resolutions are attainable through increased radar bandwidth. These figures display the ranging results of the photonic radar with various signal bandwidths of 5.76 GHz, 9.20 GHz, and 11.52 GHz, respectively, for two plane reflectors separated by 3 cm. The 3-cm separation can be accurately identified by the P-WSF radar operating with these three bandwidths; however, the demonstration employing an 11.52 GHz-wide bandwidth (from 28 GHz to 39.52 GHz) reveals a much finer ranging resolution in comparison to the other two instances.

When the separation is reduced to 1.5 cm, only the radar operating with an 11.52 GHz bandwidth can discern this smaller spatial gap, as illustrated in Figure 405g-i. This discrepancy can be comprehended by examining the corresponding theoretical ranging resolutions; an 11.52 GHz bandwidth enables a theoretical spatial resolution of 1.3 cm, calculated as $c/(2N \times \Delta f)$, while 5.72 GHz and 9.20 GHz bandwidths yield ranging resolutions of 2.6 cm and 1.6 cm, respectively.

It is important to note that no windowing function was applied in digital signal processing at the receiver. Experimental investigations reveal that polarisation-maintaining components can mitigate gain fluctuations induced by polarization scrambling in the optical loop, thereby reducing inter-pulse amplitude fluctuations and enhancing signal SNR.

## 4.2 High-Resolution 2-D Radar Imaging

The advanced photonic stepped-frequency radar system enables two-dimensional (2D) imaging of dynamic objects, a highly desirable feature for target identification in radar applications. This 2D imaging is achieved by incorporating a Doppler dimension to assess the velocity of moving objects, referred to as the cross-range dimension. The system captures object movements through a series of consecutive microwave stepped-frequency (SF) pulses, which record both instantaneous distances and the Doppler frequency shifts caused by the objects' motion. By employing 2D Fourier transform signal processing, the range and cross-range dimensions of moving targets can be reconstructed into 2D images using the principle of inverse synthetic aperture radars (ISARs), as detailed in Chapter 2.

### 4.2.1 ISAR Imaging of Kinetic Objects

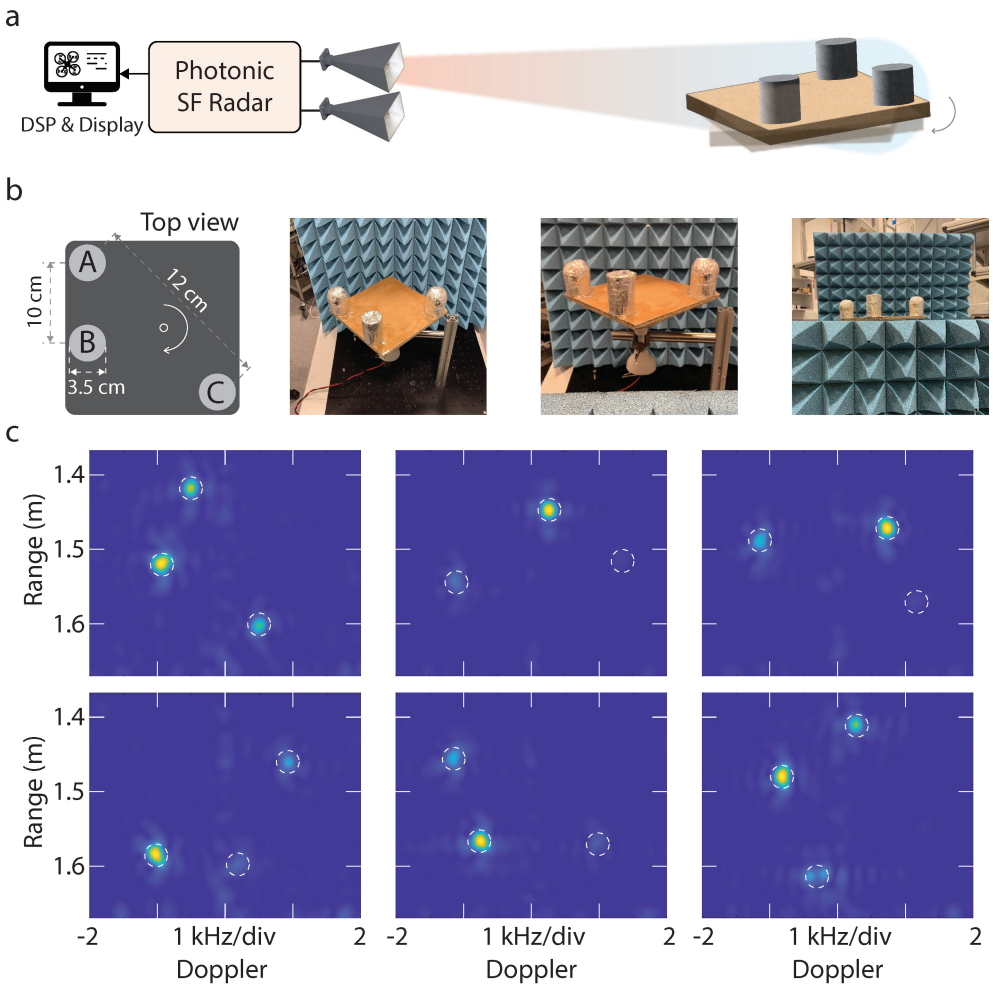


**Figure 4.6:** High-resolution radar imaging demonstration. **a** Experimental setup illustration for radar imaging, featuring three 3 cm radius and 4 cm height cylinders on a rotating plate to simulate moving objects. **b** Side and inclined views of the moving objects, with microwave absorbers employing artificial structures to minimize reflections from the surroundings. **c** Reconstructed 2D images of the moving objects at different angles, with dashed circles highlighting the anticipated locations of the objects of interest.

Figure 4.6**a** depicts the experimental setup for demonstrating 2D radar imaging. Three cylindrical objects (top view) with a radius of 3 cm and a height of 4 cm were mounted on a rotating platform to simulate dynamically moving objects. The objects are placed in a non-symmetric arrangement for unambiguous rotation angle identification. The rotating platform is situated approximately 1.52 m away from the radar antennas

that transmit and receive 11.52 GHz-wide radar pulses. The platform rotates at an angular speed of roughly 50 rad/s clockwise, corresponding to around 477 revolutions per minute (RPM).

Figure 4.6**b** displays the side view and the inclined view of the objects under test, with microwave absorbers employed to prevent reflections and interference from the surrounding environment. Figure 4.6**c** presents the constructed images of the moving objects at various rotational angles, covering the entire 360 degrees. In Figure 4.6**c**, the three moving objects can be discerned with high resolutions, which correspond well to their expected locations denoted by dashed circles. It is worth noting that the lower detected amplitude of the object located at the edge of the radar view range is due to the 8-degree view angle of the antennas with high beam directionality in an indoor measurement condition. This phenomenon can be mitigated by using antennas with larger beam angles or conducting outdoor measurements with increased object distance.

Each 2D radar imaging frame displayed in Figure 4.6**c** is constructed from 100 consecutive returned radar stepped-frequency pulses, which corresponds to a viewing time of 5 ms ($100 \times 50 \mu s$). The 11.52-GHz-wideband photonic radar offers a Doppler resolution of 200 Hz, as the resolution for the Doppler frequency shift is the inverse of the viewing time (see Chapter 2). This translates to a radial velocity resolution of 1 m/s when the radar centre frequency is 34 GHz.

Considering the short viewing time of 5 ms, the photonic radar imaging can achieve an impressive refresh rate of 200 frames per second (FPS). Such a high FPS is highly desirable for imaging rapidly moving objects in real-time, as data acquisition and processing only necessitate low-speed electronic processors. However, the current implementation's refresh rate is constrained by the unoptimized data transfer process and data computation for the fast Fourier transform.

It is worth noting that a higher frame rate can be attained by employing a continuously moving time window with a one-period duration, as opposed to discretely truncating 100 periods of SF pulses. This approach would enhance the radar's imaging capability for fast-moving objects, further improving its performance in real-time applications.

### 4.2.2 ISAR Imaging of an Unmanned Aerial Vehicle (UAV)

In this application example of wideband photonic stepped-frequency radar, we demonstrate the 2-D imaging of an unmanned aerial vehicle

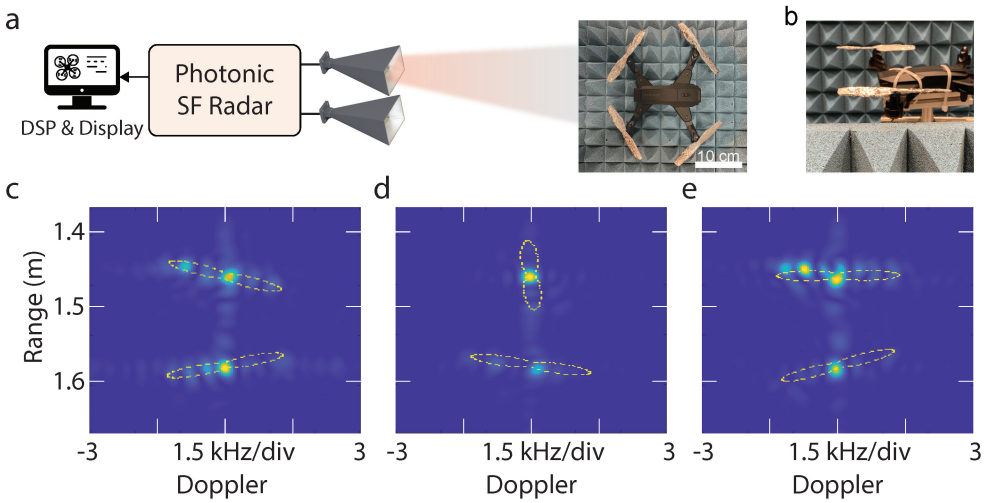


**Figure 4.7:** Imaging rotating blades of an unmanned aerial vehicle (UAV). **a** Top view of the drone. **b** Inclined perspective of the propellers. **c-e** Reconstructed 2D images of the blades at different orientations. Dashed outlines represent the instantaneous positions of the rotating blades.

(UAV) by successfully resolving its fast-spinning propellers. The demonstration took place in a laboratory setting to ensure safety and adhere to regulations. We mounted a commercial UAV (Zero-X Banshee) on a holder to simulate a hovering UAV under detection, with rapidly rotating blades ranging from 1.2 cm to 1.9 cm in width. Figure 4.7**a** illustrates the experimental setup for radar imaging of the UAV, using a radar signal bandwidth of 11.52 GHz.

Throughout the experiment, we concentrated on imaging the two propellers of the drone within the viewing angle of the wideband photonic stepped-frequency radar, as depicted in Figure 4.7**b**. We slightly tilted the drone vertically to prevent obstructing the returned radar signal from the farther blades.

Figure 4.7**c-e** present the reconstructed images of rapidly moving blades rotating at 7500 degrees/s (equivalent to 1250 RPM). Dashed envelopes outline the anticipated blade orientation. Each radar imaging result was obtained using 60 consecutive microwave SF pulses. The UAV's blades can be resolved by discerning the envelope from the retrieved image, although the low reflection cross-section of the narrow blades constrains the imaging quality. Additionally, twisted blade planes diminish the strength of returned radar signals to the receiver. In this demonstration, we applied an aluminium coating to enhance reflectivity.

Figure 4.7**d** displays the radar imaging result of a propeller with its blade tip directed toward the radar antennas, which exhibits a lower imaging SNR due to the minimal reflection cross-section. The intensity variation in Figure 4.7**e** results from the blade's rotational motion compared to the outcome in Figure 4.7**e**. The background spurs in Figure 4.7**c-e** originate from stationary reflections off the drone body.

The antennas used in this study (from L3 Harris Corp.) exhibit high RF beam directionality with a narrow horizontal beam width of approximately 18 cm at 1.4 metres (beam angle of 8-10 degrees), which is inadequate to cover the area of four propellers with a horizontal separation of around 40 cm. Broader imaging view angles can be achieved through well-established methods such as smaller horn antennas, RF beam scanning, and additive receiving antennas.

This application example of the wideband photonic stepped-frequency radar in UAV detection demonstrates the potential for detecting and identifying rapidly moving targets with centimetre-level resolution in real-world applications.

## 4.3 Summary and Discussion

The photonic wideband stepped-frequency radar system, driven by MHz-level electronics, has demonstrated a tunable bandwidth of up to 11.52 GHz, enabling centimetre-level spatial resolution for ranging and imaging. The SF radar signal bandwidth can be further expanded to achieve tens of GHz, significantly surpassing the capabilities of high-speed electronics by broadening the bandpass filter bandwidth and increasing the number of frequency-shifted sub-pulses.

However, the accumulation of optical amplifier noise during light recirculation restricts the maximum achievable number of frequency-shifted pulses. Consequently, the signal-to-noise ratio of these pulses degrades progressively after numerous round trips. A promising alternative to achieving a much broader bandwidth without impacting ranging performance is a parallel frequency-shifted scheme. In this method, multiple seed pulses ($M$) with distinct carrier frequencies (e.g., frequency combs) are frequency-shifted simultaneously, and the resulting multiple SF signals are combined in the microwave domain through spectrum stitching. This approach holds the potential to increase the photonic wideband stepped-frequency radar bandwidth by a factor of $M$.

In future developments, radar systems can be feasibly simplified and miniaturised by using a miniature EDFA and replacing the bulky optical tunable filter. Specifically, compact optical filters based on fibre Bragg gratings or electrically gating the on-off state of the AOM in the optical loop can effectively substitute the bulky and expensive tunable optical filters. This would achieve desirable bandwidth tuning flexibility and sharper roll-offs.

We observed an SNR of 17 dB for the SF radar transmitter, which is sufficient for near-range applications requiring safe RF power transmitting. However, a further increase in SNR would be beneficial for improving ranging accuracy (as discussed in the following chapters). One way to enhance the signal's SNR is by using polarisation-maintaining components to suppress environment-dependent polarisation scrambling. This would achieve a stable sub-pulse amplitude and a broader synthesised bandwidth.

Radar waveforms based on linear frequency modulation (LFM) and stepped-frequency (SF) modulation are both widely used, yet they possess fundamental differences in mapping the round-trip time of flight for range detection. LFM radar encodes range information (time delay of the detected signal's round-trip, $\Delta\tau$) onto a new oscillating frequency $f_{dechirp} = k\Delta\tau$, proportional to the chirp rate $k = bw/T$, where $bw$ is the bandwidth and $T$ is the chirp repetition rate.

In contrast, SF radar maps the time delay onto phase changes (see Eq. (2.42)). Compared to LFM radars that utilise continuously chirped signals, SF radar, which is based on discrete frequency steps, has a smaller unambiguous range (approximately 100 metres commercially [163]), constrained by the step frequency $\Delta f$. As a result, SF radars can serve as a complementary approach for near-range practical applications, offering high resolutions and lower sampling speeds.

The unambiguous range of an SF radar can be increased by using smaller frequency steps. In practical implementation, the frequency step is determined by the operating frequency of the AOM, typically ranging from a few MHz to 100s MHz. This corresponds to an unambiguous range spanning from a few metres to over 100 metres. For instance, a commercially available AOM operating at 5.5 MHz (Brimrose, AMF-55-1.3) allows for an unambiguous range of approximately 30 metres.

A feasible alternative approach to extending the unambiguous range involves utilising the differential frequency of two AOMs with opposite

frequency shifts (positive and negative). This method generates a sub-MHz frequency shift corresponding to an unambiguous range exceeding 150 metres.

In summary, we demonstrate a photonic ultra-wideband stepped-frequency radar with a bandwidth of up to 11.52 GHz, driven by MHz-level electronics. For the first time, this photonic stepped-frequency radar simultaneously combines the high spatial and velocity resolution enabled by the ultra-wide radar bandwidth and the rapid radar detection due to the low demodulation processing bandwidth. Leveraging these superior features, we present high-resolution radar ranging and 2D radar imaging of reflectors and a commercial unmanned aerial vehicle. This innovative photonic radar offers a new direction towards high-resolution, rapid-response, and cost-effective radar modules with reduced system complexity for demanding practical applications such as autopilot assistance, gesture recognition, environmental sensing, and medical imaging.

In the upcoming chapter, we will demonstrate that the photonic stepped-frequency radar system exhibits performance on par with photonic radars based on high-speed digital microwave frequency synthesisers, such as those employing arbitrary waveform generators (AWGs). This performance equivalence applies to ranging resolution, signal-to-noise ratio (SNR), and imaging quality. The photonic stepped-frequency radar's comparable range and imaging capabilities can be attributed to its broad radar bandwidth and efficient frequency-shifted modulation. This, in turn, significantly reduces the need for high-speed digital electronics in signal generation and processing. Consequently, the photonic radar system offers numerous benefits, including high resolution, swift signal generation and processing, low complexity and cost, as well as flexible tunability.

It is important to note that in the proof-of-concept demonstrations, the two lasers (LD1 and LD2) are not phase-locked, resulting in increased phase noise. To enhance the SNR further, the implementation of two injection-locked lasers or coherent light sources, such as stabilised optical frequency combs, can help minimise the noise in the heterodyne signal mixing via photodetection.

Looking towards future developments and miniaturisation of the photonic stepped-frequency radar system, recent advancements in photonic integration of key functional units hold promise. Examples include on-chip acousto-optic frequency shifters [164], ultra-compact integrated optical passband filters [165] with sharp spectral roll-off, and on-chip op-

tical amplifiers [166] with over 30 dB small signal gain. These innovations provide a crucial and promising technical foundation for the realisation of compact photonic radars.

Chapter 5

# Enhancing the Bandwidth of the Photonic Radar System

Wideband microwave signals with high time-frequency linearity for high-resolution radar applications can be optically generated using high-speed electronic waveform generators. Frequency-shifting modulation in an optical cavity provides an attractive approach to generating broadband microwave signals with reduced complexity requiring only MHz-level electronics. However, the in-loop signal instability and inter-pulse interference usually cause amplitude fluctuations, leading to a limited signal-to-noise ratio and signal bandwidth. Here, we overcome these challenges and demonstrate, for the first time, the photonic generation of 30-GHz-wide stepped-frequency (SF) signals with 100 MHz frequency steps defined by an MHz-level electrical oscillator. We achieved this performance by mitigating the in-loop polarisation scrambling and inter-pulse interference using a polarisation-maintaining cavity and a high-extinction optical switch. This allows stable consecutive acousto-optic frequency-shifting modulation that significantly improves the signal-to-noise ratio. While achieving a bandwidth surpassing the state-of-the-art demonstrations based on wideband electronics, our approach alleviates the necessity for high-speed signal generators or wideband tunable lasers. To exemplify the utility, we systematically evaluate the signal quality and show its applications in radar imaging compared to those using electrical waveform generators.

## 5.1 Overcoming Radar Signal Bandwidth Limitations

Radar sensing has been expanding into the millimetre-wave (MMW, 30-300 GHz) and terahertz-wave (THz-wave, 0.1-10 THz) regions to accommodate ultra-wide bandwidths and meet the increasing demand for high spatial resolution imaging in real-world applications. These applications include non-destructive testing, automotive driving assistance, industrial quality inspection, and non-invasive medical imaging [167, 168, 169, 170, 171]. However, developing wideband radars operating at high frequencies presents challenges for conventional electronic technologies, particularly in synthesising ultra-broadband signals. Multi-stage frequency up-conversion can reduce efficiency and increase noise levels as frequencies become higher [172]. Moreover, techniques such as frequency multiplexing and spectrum stitching, employed to broaden bandwidth, can introduce noise and spectrum spurs due to device nonlinearity and interference [173], ultimately compromising sensing accuracy and overall performance.

Microwave photonics has demonstrated significant advantages in radio-frequency (RF) signal generation, up-conversion [28, 174, 94, 175, 176], and demodulation [152, 87, 173, 177], offering flexible tunability of signal bandwidth and operational frequency [86, 178, 77, 179, 180, 181, 182]. Optically synthesised ultra-wideband linear-frequency modulated (LFM) signals are widely used in radar and sensing applications [183, 184, 127, 119, 185, 30, 1, 186]. However, existing photonic methods for LFM generation typically depend on high-speed benchtop electronics or intricately biased electro-optic modulators (EOMs), leading to bandwidth limitations due to electronic speed constraints and long-term operational stability issues arising from EOM bias-drifting [138, 30]. Alternative approaches employing dispersion-based time-stretch [156] and frequency-sweeping light sources [116, 119, 141] have demonstrated promising bandwidth capabilities. However, they necessitate intricate pre-distorted RF control signals for linearity compensation.

Another widely-used signal format in radar systems is the stepped-frequency (SF) waveform. This format offers high time-frequency linearity and minimal spontaneous processing bandwidth while maintaining the same range resolution as linear frequency modulation (LFM) signals for the same bandwidth [44]. Recent advancements in the photonic generation of SF signals have used frequency shifting modulation to exhibit

benefits such as flexible bandwidth and high time-frequency linearity in radar ranging and imaging system demonstrations [159, 2, 130, 3]. In general, the SF signal bandwidth can be adjusted through various methods. These include tuning the passband of an optical filter [2, 3], modifying the radiofrequency (RF) applied to the electro-optic modulator (EOM) [130], and using electronically controlled in-loop switches [131]. However, achieving an ultra-wide bandwidth of more than 20 GHz with an MHz-level frequency step for an extended unambiguous range remains challenging. This is due to loop instability, particularly after numerous re-circulations, which often result in increased signal amplitude fluctuations and low signal-to-noise ratio (SNR), limiting the system's achievable bandwidth. Moreover, a comprehensive comparison of SF radar signal quality and performance with conventional photonic radar schemes has yet to be explored.

In this chapter, we build upon our previous demonstration by addressing the frequency-shifting loop instability and presenting, for the first time, a stepped-frequency signal with a tunable bandwidth of up to 30 GHz using MHz-level electronics-enabled photonic signal synthesis. Our methodology benefits from a polarisation-maintaining optical cavity that is robust against ambient environmental perturbations and immune to modulation bias drift. As a result, our approach achieves a signal-to-noise ratio exceeding 34 dB in signal generation, comparable to that produced by high-end benchtop electronics.

We apply this signal generation scheme to an inverse synthetic aperture radar system and experimentally compare the imaging performance to photonic radars using a high-speed waveform generator, illustrating its practical utility in various applications. Given the achieved bandwidth and the potential for further expansion, this approach offers a complementary solution for ultra-wideband microwave waveform synthesis in millimetre-wave and terahertz-wave radar systems.

The synthesis of swept-frequency waveforms is achieved by circulating a rectangular optical pulse signal within a frequency-shifting loop (FSL) [139, 159, 2], as depicted in Figure 5.1**a**. An optical switch (OS) transforms a continuous wave (CW) laser signal into an initial rectangular optical pulse signal, then subjected to frequency shifting within the loop. An acousto-optic modulator (AOM) accurately adjusts the pulse frequency for each round-trip, generating a bandwidth of B after N recirculations (N steps) and employing a consistent frequency shift $\Delta f$ in the megahertz range, as shown in Figure 5.1**b**.

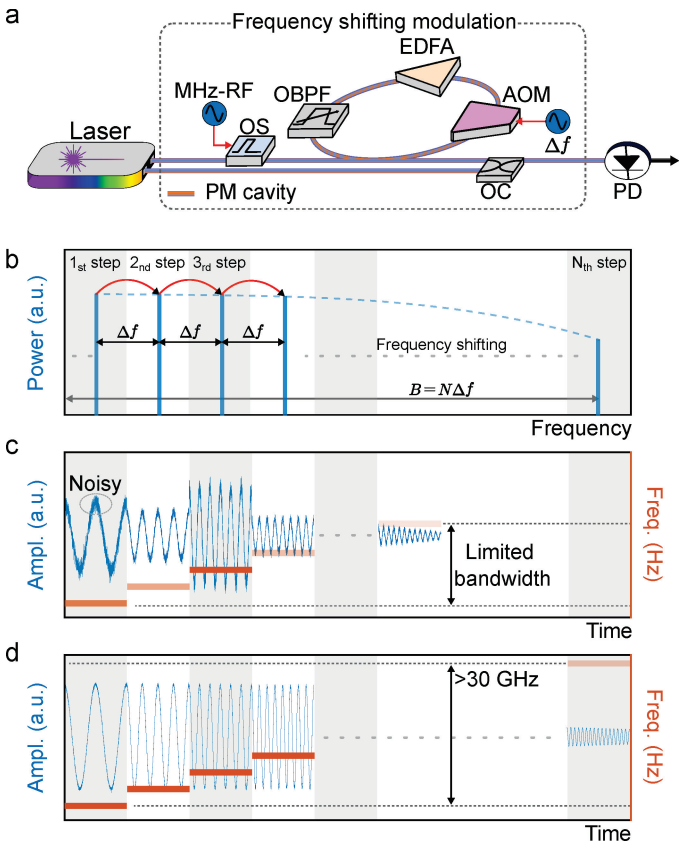


**Figure 5.1:** Principle of stepped frequency (SF) signal generation with improved bandwidth and signal-to-noise ratio (SNR). (a) Schematic of the demonstrated SF signal generation using optical frequency-shifting modulation based on the polarisation-maintaining (PM) cavity for radar applications. (b) Principle of the SF signal generation using optical frequency-shifting modulation on the frequency domain. The signal's frequency will be shifted by $\Delta f$ for each recirculation time in the cavity, thus synthesising a total bandwidth $BW = N\Delta f$. Schematic illustrations of generated stepped-frequency waveforms based on (c) an unoptimized frequency-shifting loop using a low-extinction ratio optical switch ($\sim$ 20 dB) and single-mode fibre components, and (d) an optimised loop using a high-extinction ratio optical switch ($>$ 40 dB) and polarisation-maintaining components to suppress the amplitude fluctuations caused by polarisation scrambling, respectively. RF, radio-frequency; OS, optical switch; OBPF, optical bandpass filter; EDFA, erbium-doped fibre amplifier; AOM, acousto-optic modulator; OC, optical coupler; PD, photodetector.

The high-extinction, bias-free AOM-based frequency shifting method presents a significant advantage over electro-optic modulators (EOMs) used for single-sideband modulation (SSB), as the latter is plagued by bias drifting and parasitic harmonics [138, 130]. In order to counteract optical modulation and coupler losses, an erbium-doped fibre amplifier (EDFA) is employed. The steady ratio between the frequency shift ($\Delta f$)

and the loop round trip time guarantees the time-frequency linearity of the synthesised SF waveform, ensuring accurate detections.

In proof-of-concept demonstrations, a tunable optical bandpass filter (OBPF) is utilised to ascertain the bandwidth of the generated microwave SF signal and eliminate the amplifier's out-of-band noise. As a result, the time-domain waveform comprises a series of sub-pulses, with the sub-pulse frequency discretely hopping at a spacing equivalent to the AOM's RF driving frequency $\Delta f$, as demonstrated in Figure 5.1**c** and Figure 5.1**d**. The SF signal is mixed with a frequency-shifted CW laser in photodetection, facilitating microwave up-conversion to elevated frequencies.

As illustrated in Figure 5.1**c**, a common challenge in generating broadband and stable microwave photonic SF signals is the instability of the circulating optical signals within the loop, which consequently leads to amplitude fluctuations and, in turn, affects the single-pass optical gain in the loop. These amplitude variations can cause transient gain suppression and heightened noise due to the gain dynamics in the erbium-doped fibre amplifier (EDFA), resulting in a limited number of circulations and, ultimately, a restricted achievable bandwidth.

In the subsequent discussion, we construct two photonic stepped-frequency signal generators based on the schematic depicted in Figure 5.1**a**, both with and without polarisation-maintaining components. We evaluate system stability improvements by examining the achievable number of recirculations (the bandwidth) and the improved SNR of the generated signal, aiming to understand the impact of polarisation scrambling and the polarisation-dependent amplified spontaneous emission noise.

## 5.2 SF Waveform SNR and Bandwidth Improvements

A polarisation-maintaining optical cavity is implemented to minimise the signal polarisation scrambling to address this issue. As depicted in Figure 5.1**d**, by stabilising the polarisation and enhancing robustness against ambient perturbations, broader bandwidth SF signals with reduced amplitude fluctuations and noise can be synthesised. These approaches significantly improve the signal-to-noise ratio (SNR) and effectively increase the achievable bandwidth for more excellent spatial resolution [187, 44].

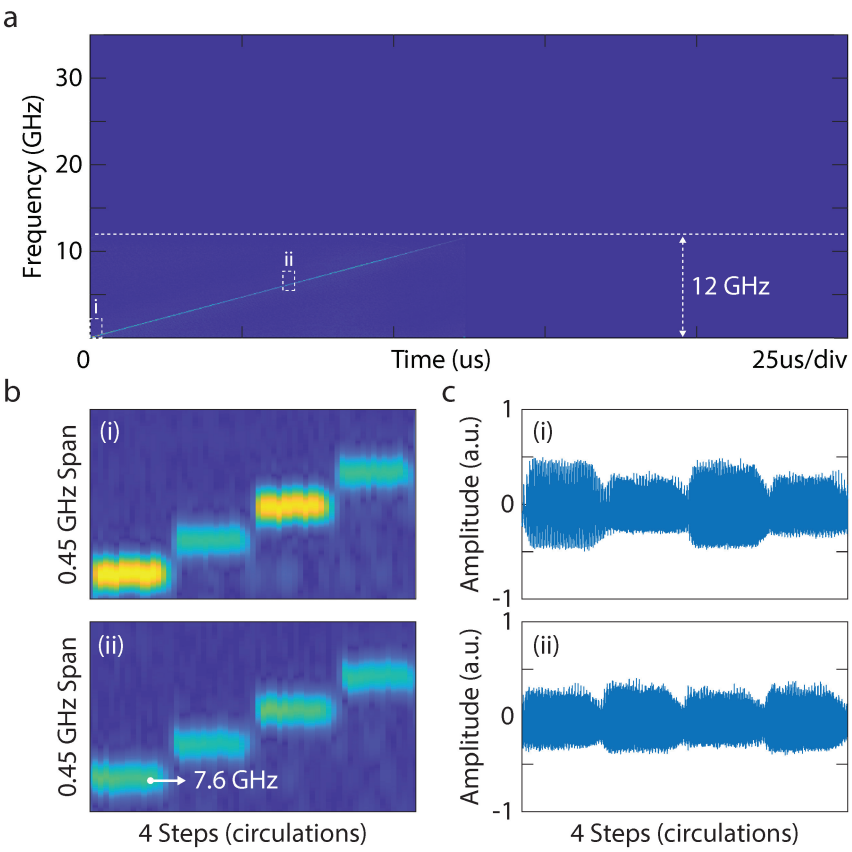


**Figure 5.2:** Comparisons of the maximum achievable bandwidth and signal quality between SF generators with and without polarisation stabilisation. (a) Time-frequency analysis of the signal generated through an un-optimised FSL using single-mode fibres with a bandwidth of 12 GHz. (b) Two insights of the 12-GHz SF signal showing: (i) the first four frequency steps and (ii) four frequency steps with a starting frequency of 7.6 GHz, in the time-frequency domain. (c) The corresponding time-domain waveforms of the 12-GHz insights.

To ensure high resolution and accuracy, a high-quality signal with a broad bandwidth and less noise is highly desirable when deploying SF signals for various applications. In principle, the demonstrated system can achieve arbitrary bandwidth tuning by changing the passband and central frequency of the OBPF, thereby enabling range resolutions down to the millimetre level. However, in practice, such broadband synthesising is challenging for single-mode fibres (SMFs) since the signal's polarisation state is scrambled in the optical cavity, which deteriorates the phase stability, signal coherence, and, ultimately, the sensing performance. As shown in Figure 5.2**a**, the time-frequency plot of the SF signal generated through an FSL using SMFs struggles to achieve experimentally a 12 GHz

bandwidth. Figure 5.2**b** provides insights into the time-frequency domain with the corresponding time-domain waveforms plotted in Figure 5.2**c**, revealing the amplitude fluctuations across different frequency steps, caused by the polarisation and gain instabilities. These instabilities degrade the quality of the signal, specifically the SNR, thus deteriorating the radar's performance, such as the maximum detection range and ranging accuracy [16, 44]. Notably, the OBPF is tuned to have a passband close to 15 GHz, with its central frequency being adjustable to control the SF signal's bandwidth.

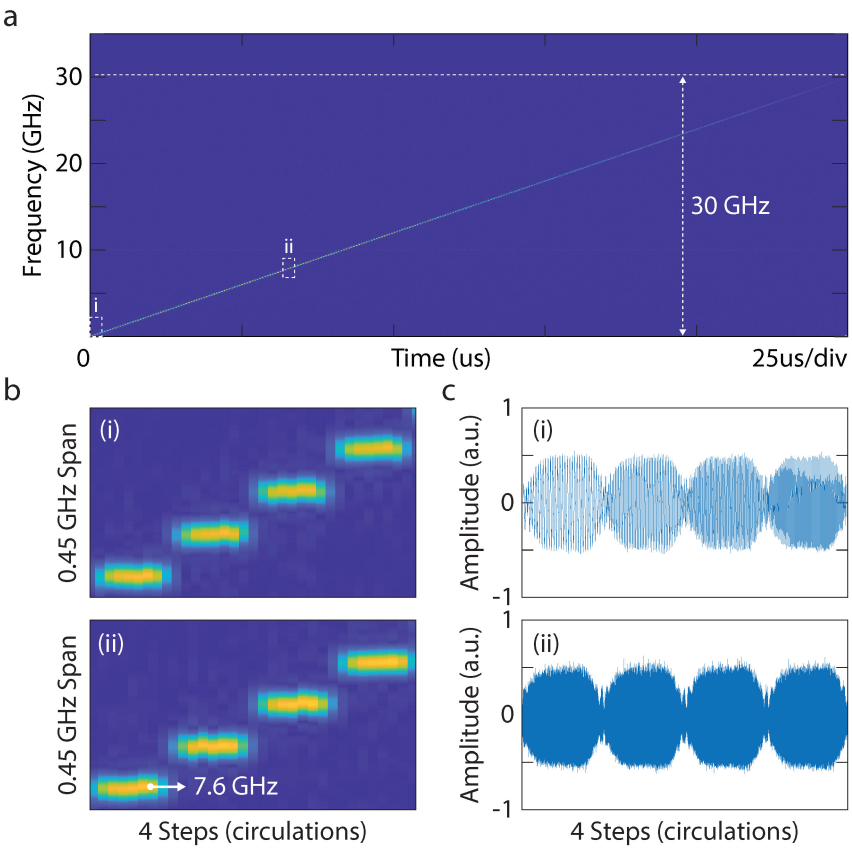


**Figure 5.3:** Comparisons of the maximum achievable bandwidth and signal quality between SF generators with and without polarisation stabilisation. (a) Time-frequency analysis of the signal generated through an optimised FSL using PMFs with a bandwidth exceeding 30 GHz. (b) Two insights of the 30-GHz SF signal showing: (i) the first four frequency steps and (ii) four frequency steps with a starting frequency of 7.6 GHz, in the time-frequency domain. (c) The corresponding time-domain waveforms of the 30-GHz insights.

In contrast, the signal bandwidth and stability can be significantly in-

creased using polarisation-maintaining fibres (PMFs) and components that can minimise the polarisation scrambling and suppress the polarisation-dependent amplified spontaneous emission (ASE) noise from the EDFA [159]. This improvement allows ultra-broad bandwidth synthesising over 30 GHz to be achieved (Figure 5.3**a**). Additionally, using a high on-off extinction ratio OS (from $\sim$ 20 dB to $>$ 40 dB extinction ratio) can suppress the seed pulse tails that recirculating in the FSL. Therefore, the background noise and amplitude fluctuation in Figure 5.3**b** is significantly reduced compared with Figure 5.2**b**. As a result, Figure 5.3**c** shows that the system generates a more stable pulse circulation with significantly reduced amplitude noises.

To better understand signal quality, we examine the signal-to-noise ratio (SNR) of signals generated using various schemes. Figure 5.4**a** displays the SNRs of the single-mode fibre (SMF)-based system with a synthesised bandwidth of 12 GHz at two specific step numbers, namely, 10-time (blue) and 60-time (red) recirculation, yielding an SNR of 17.75 dB. In contrast, Figure 5.4**b** demonstrates a minimum SNR of 34.10 dB at 60-time (red) recirculation for a 25 GHz bandwidth SF signal using a polarisation-maintaining fibre (PMF)-based loop, resulting in a 14 dB SNR improvement. Notably, even after 200-time recirculation (yellow), the optimised system exhibits only a 2.2 dB degradation, as shown in Figure 5.4**b**.

An SNR analysis for the scheme based on an arbitrary waveform generator (AWG, Keysight M8195A 65GSa/s, 25 GHz analogue bandwidth) is depicted in Figure 5.4**c** to benchmark the performance. In the analysis mentioned above, waveform clips with a time window of 25 ns are extracted at specific step numbers (recirculation times) for Fourier analysis. The comparison reveals that the demonstrated system maintains an SNR above 34 dB after 60-time recirculation in the PMF-based FSL, as opposed to the 39 dB SNR provided by high-end electronics in Figure 5.4**c**. These results suggest that the demonstrated polarisation-maintaining (PM)-based system can achieve a similar SNR performance to that of high-speed electronic synthesisers while eliminating the need for wideband AWGs for SF signal generation.

## 5.3 ISAR Imaging Performance Comparison

To showcase the competitive performance and practicality, we compare the radar imaging performance based on the demonstrated SF signal

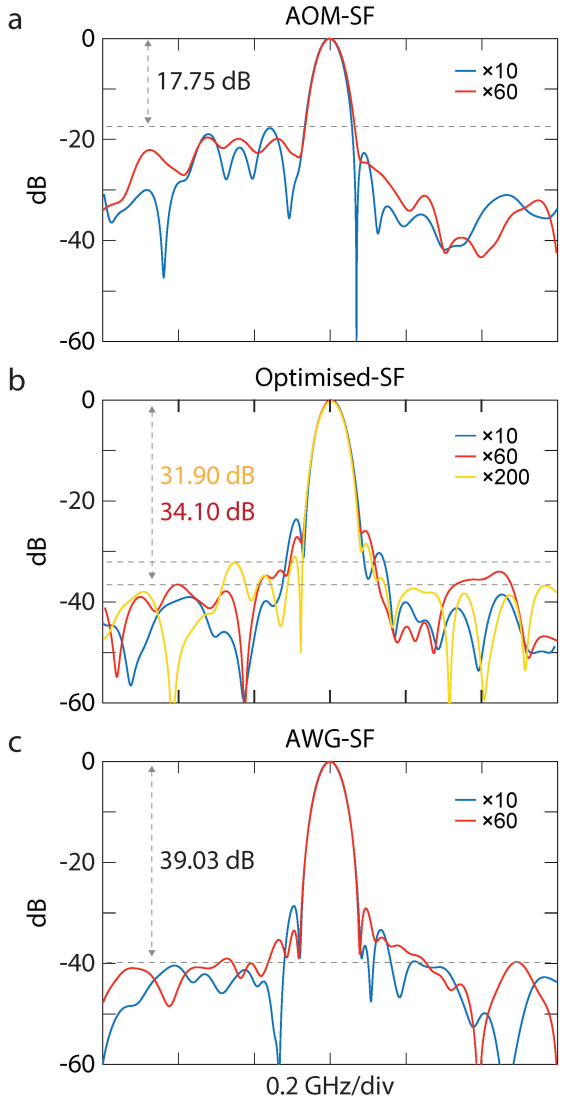


**Figure 5.4:** SNR comparisons among systems based on SMFs, PMFs, and a 65 GSa/s AWG (∼25 GHz analogue bandwidth). (a) SMF-based system's SNR plots at 10-time (blue) and 60-time (red) recirculations, with SNRs ∼17.75 dB and bandwidth ∼12 GHz. (b) PMF-based system's SNR plots at the same frequency instances, showing 34.10 dB at 60-time recirculation and 31.90 dB at 200-time recirculation (yellow); bandwidth ∼25 GHz. (c) SF signal SNRs using AWG at the same frequency instances, calculated from 25 ns time-domain clips.

generator with those employing high-speed electronic AWGs, as depicted in Figure 5.5**a**. We conduct 2D imaging experiments using the inverse synthetic aperture radar (ISAR) technique, which involves stacking multiple ranging results to extract 2D images of a moving target, as illustrated in Figure 5.5**b**. The experiment also benchmarks the performance of the

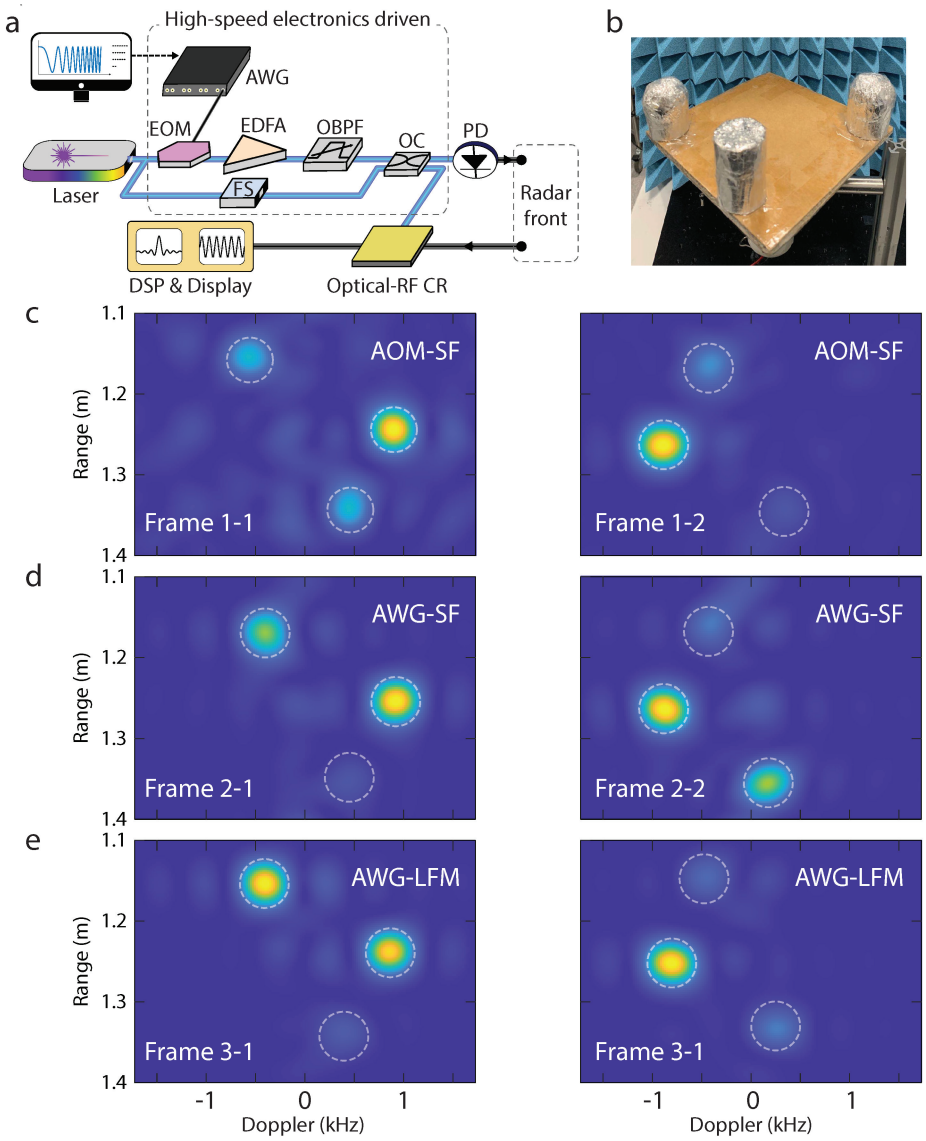


**Figure 5.5:** Experimental 2D imaging comparison of the proposed system and an AWG-enabled photonic radar using SF and LFM signals. **(a)** Schematic of a high-speed signal generator-driven photonic radar system. **(b)** Radar imaging target with three cylindrical objects on a rotating platform. **(c-e)** 2D imaging results. FS, optical frequency shifter; CR, coherent receiver.

SF waveform against the LFM waveform.

For comparison, we implement AWG-based radar systems with the same bandwidth (approximately 5.76 GHz), carrier frequency (30.5 GHz), repetition rate (25 $\mu$s), and RF radiation power (approximately 10 dBm). The signal bandwidth in the demonstration was chosen based on the

bandwidth availability of the RF antennas and RF amplifiers without compromising the performance comparison's generality. Wideband-RF signals generated by the AWG modulate a continuous wave (CW) laser carrier through electro-optic single-sideband modulation before beating with a separate optical carrier for optical-RF up-conversion.

As depicted in Figure 5.5**b**, three cylindrical objects mounted on a rotating platform (at a speed of approximately 30 rad/s) serve as the target. Each ISAR image shown in Figure 5.5**c-e** utilises 100 continuous ranging results (2.5 ms in total) to extract Doppler information. Imaging results in Figure 5.5**c-e** are selected at two specific instances to provide an adequate performance illustration and comparison, proving the demonstrated system's reliability for imaging moving objects.

It is worth noting that the rotational motion of the objects primarily causes the speckle-like noise in the images' background, which can be mitigated using motion compensation algorithms [16, 44]. More importantly, the demonstrated system successfully reconstructed ISAR images of the objects without discernible differences from the SF- and LFM-based radars driven by the wideband AWG.

## 5.4 Summary and Discussion

The SF waveforms have shown several advantages over the LFM signals. For instance, it possesses an increased dynamic range due to each frequency step's narrow instantaneous noise bandwidth for signal processing while preserving the range resolution, and the overall bandwidth [170]. However, the SF waveform has a smaller unambiguous range defined by $c/2\Delta f$, where $c$ is the propagation speed of the RF signal in the air. The 100 MHz frequency shift in the demonstrated system has a theoretically unambiguous range of 1.5 meters. This limitation can be feasibly overcome by using a minor frequency step ($\Delta f$). One way of achieving the minor frequency step is to cascade two AOMs with the opposite frequency shift (e.g., a frequency shift from -10 to +10 MHz has been demonstrated in [188]) to achieve an unambiguous range over 100 meters, comparable to the 120 meters unambiguous range window (1.25 MHz frequency shift) from the CARABAS system – a very early airborne synthetic aperture radar that employed SF signals – mounted on an aircraft [163]. It should be noted that the radar's maximum detection range is not limited by its unambiguous range [44, 46]. In the demonstrated system, long-range detection can be realised similarly to the CARABAS,

i.e., introducing a variable time delay to the reference SF signal, setting the radar to detect targets on top of a distance corresponding to the time delay. As a result, both factors, i.e., the unambiguous and maximum detection range, can be further extended, thus not limiting the system for practical applications.

The demonstrated system is also promising to be developed with a small form factor. The reflection of fibre Bragg grating combined with an optical circulator can form a bandpass filter with a compact size to replace the benchtop optical filters for ASE noise suppression. The synthesised bandwidth can be controlled by simply turning on-off of the RF driving signal of the AOM to determine the round-trip times. The benchtop EDFA can be replaced with a compact EDFA (such as ACL-PM-mini-EDFA-24) that can offer sufficient gain to offset the in-loop losses. On-chip components, such as AOM [189, 164], bandpass filter [165], and waveguide amplifier [166], are also promising to reduce the optical system's size further. A commercial data acquisition (DAQ) unit could be sufficient to simultaneously generate the RF driving signal and acquire the demodulated signal, therefore minimising the system's electronic footprint. Such a device could be used in many resolution-demanding scenarios, such as hand gesture control [190, 191] and fall detection [192].

In conclusion, we have demonstrated a photonic SF waveform generation with a tunable bandwidth exceeding 30 GHz and MHz-level frequency steps for high-resolution radar detections. By stabilising the polarisation and minimising inter-pulse interference in the optical FSL, we have significantly improved the SNR of the SF signals from 17 dB to 34 dB, enabling imaging performance comparable to that achieved using high-speed equipment. The demonstrated system offers a viable approach to overcoming the analogue bandwidth limitations of digital waveform generators for synthesising broadband radar signals, facilitating high-resolution radar sensing and presenting an appealing combination of wideband signal synthesis, high SNR, and reduced hardware requirements. This work serves as a foundational study and experimental basis for future ultra-high-resolution, compact, and mobile millimetre-wave devices with superior performance and flexibility.

Chapter 6

# Photonic Radar for Contactless Vital Sign Detection

Vital sign detection is used across ubiquitous scenarios in medical and health settings. Contact and wearable sensors have been widely deployed. However, they are unsuitable for patients with burn wounds or infants with insufficient attaching areas. Contactless detection can be achieved using camera imaging, but it is susceptible to ambient light conditions and creates privacy concerns. Here, we report the first demonstration of a photonic radar for non-contact vital signal detection to overcome these challenges. This photonic radar can achieve millimetre range resolution based on synthesised radar signals with a bandwidth of up to 30 GHz. The high resolution of the radar system enables accurate respiratory detection from breathing simulators and a cane toad as a human proxy. Moreover, we demonstrated that the optical signals generated from the proposed system can enable vital sign detection based on light detection and ranging (LiDAR). This demonstration reveals the potential of a sensor-fusion architecture that can combine the complementary features of radar and LiDAR for improved sensing accuracy and system resilience. The work provides a novel technical basis for contactless, high-resolution, and high-privacy vital sign detection to meet the increasing demands in future medical and healthcare applications.

## 6.1 Vital Signs and Detection Approaches

Vital signs – a group of clinical measurements reflecting the essential body functions – are used as diagnostic parameters for monitoring medical and health conditions. Vital sign detection is widely employed across ubiquitous scenarios, such as intensive care units (ICUs) for patients with critical health conditions, day-and-night health monitoring in aged care facilities to prevent unattended medical emergencies, and vehicles to determine the occurrence of drivers' drowsiness [193, 194]. Conventional vital sign detection relies on contact-based devices, such as pulse oximeters that use electrodes to detect weak electrical changes as a consequence of cardiac contractions (electrocardiography, ECG) and smartwatches based on the intensity variation of infrared probe light caused by changes in blood flow and volume (photoplethysmography, PPG) [195]. Although widely deployed, contact-based methods can cause discomfort for round-the-clock monitoring [196, 197, 198]. Despite improved user experience for wearable sensors in bands or clothes, they are unsuitable for patients with burn wounds, skin irritations, or infants with insufficient attaching areas [199]. Non-contact methods based on optical sensors have been explored, for instance, using cameras to track certain body regions of interest [200, 201, 202, 203, 204]. However, camera-based systems (including infrared and conventional cameras) exhibit sensitivity to skin colour and lighting conditions. These systems typically rely on complex computing algorithms and thermal videos generated by the infrared camera, often with limited resolution. Additionally, the high resolution of camera-based systems can lead to privacy concerns, particularly when invasive monitoring practices are involved, and insufficient security measures exist within cloud computing and data storage infrastructure.

Radar using radio-frequency (RF) waves can remotely access targets' vital signs to overcome the drawbacks of contact-based sensors. Vital sign information is produced based on RF sensing rather than camera filming, naturally providing the desired privacy protection. Electronic radar vital sign detection has recently been explored using single-tone and frequency-modulated waves. Single-tone radars that rely on the Doppler principle can acquire vital signs by obtaining the phase information of the reflected signal from a moving object. However, this technique lacks the basis to detect the round-trip time to access targets' range information. As a result, they cannot utilise range information to separate closely located targets and isolate the target from surrounding clutter

[205, 206], which limits the performance and practicality in real-world deployments. On the contrary, frequency-modulated radars can extract the range information to overcome this issue [207, 208, 209, 210]. More importantly, the range resolution and accuracy of frequency-modulated radars can be increased by broadening the sensing signals' bandwidth. However, conventional electronic radar systems usually have limited sub-GHz bandwidths that lead to a resolution of tens of centimetres [211, 145, 212], which is insufficient to accurately detect delicate human vital sign signals (e.g., human respiration with chest displacement of around 1 cm). This limited resolution would greatly limit the capability of adequately cancelling body motions and tracking multiple targets. Moreover, distributed sensing at multiple frequency bands and deployment locations is needed in emerging applications. However, it is challenging for conventional electronics without a complicated parallel hardware architecture [213].

## 6.2 Photonic Radar enabled Vital Sign Detection

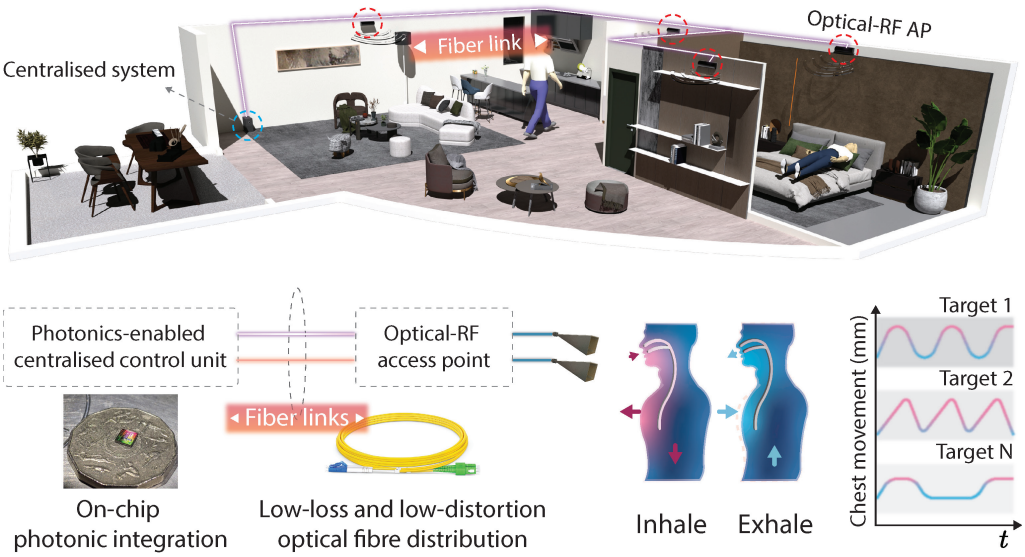


**Figure 6.1: A photonics-enabled radar system for contactless vital sign detection.** Conceptual drawings of vital sign radar with distributed sensing access points (APs) enabled by low-loss fibre and a centralised, photonics-assisted radar platform.

Photonics-assisted approaches have shown significant advantages in achieving wideband and high-resolution radars [30, 179] with the capability to generate different formats of radar signals, such as the linear-frequency modulated (LFM) [127, 106, 185, 155] and stepped-frequency (SF) signals [2, 130, 3, 4, 131]. They are flexible to operate at multiple frequency bands [87, 214, 215, 216, 217] across the millimetre-wave region, adapting the radar carrier frequencies for performance optimisation based on operating conditions (e.g., weather and target material [85]). These attractive features overcome the limitations of their electronic counterparts, making them well-suited for vital sign detection. Moreover, photonic radar allows for the potential to achieve a simplified, centralised system using low-loss fibre-based radar signal distribution without scaling the number of electronic components. However, photonic radar systems for vital sign detection have remained unexplored in real-world scenarios.

Here, we demonstrate a photonic radar for vital sign detection using human respiration simulators and a living animal – a cane toad – serving as a human proxy. This radar generates 10-GHz-wide stepped-frequency (SF) RF signals in the Ka-band (26.5-40 GHz) to detect respiratory activities of the simulators, achieving 13.7 mm range resolution with a $\mu$m-level accuracy. Such high resolution and accuracy are essential to resolve the delicate vital signs of the cane toad, even with an undersized animal radar cross-section. We demonstrated the bandwidth scalability up to 30 GHz without the limitation of the RF antennas and amplifiers. We further demonstrated a LiDAR vital sign detection system based on the same microwave photonic source, showing the system's potential to enable complementary features of radar and LiDAR.

We envisage applying such a high-performance, distributed radar system in various healthcare scenarios, such as round-the-clock vital sign monitoring in aged care facilities, hospitals, and custodial settings. For instance, a distributed photonic radar sensing network with multiple radar optical-RF access points (APs) uses RF waves to detect human vital signs (Figure 6.1). This approach can continuously track uncooperative, back- or side-facing targets compared with only a single radar AP deployment. As illustrated, one optical radar signal source enabling multiple optical-RF APs could cover diverse perspectives to monitor one or multiple targets using low-loss optical fibres.

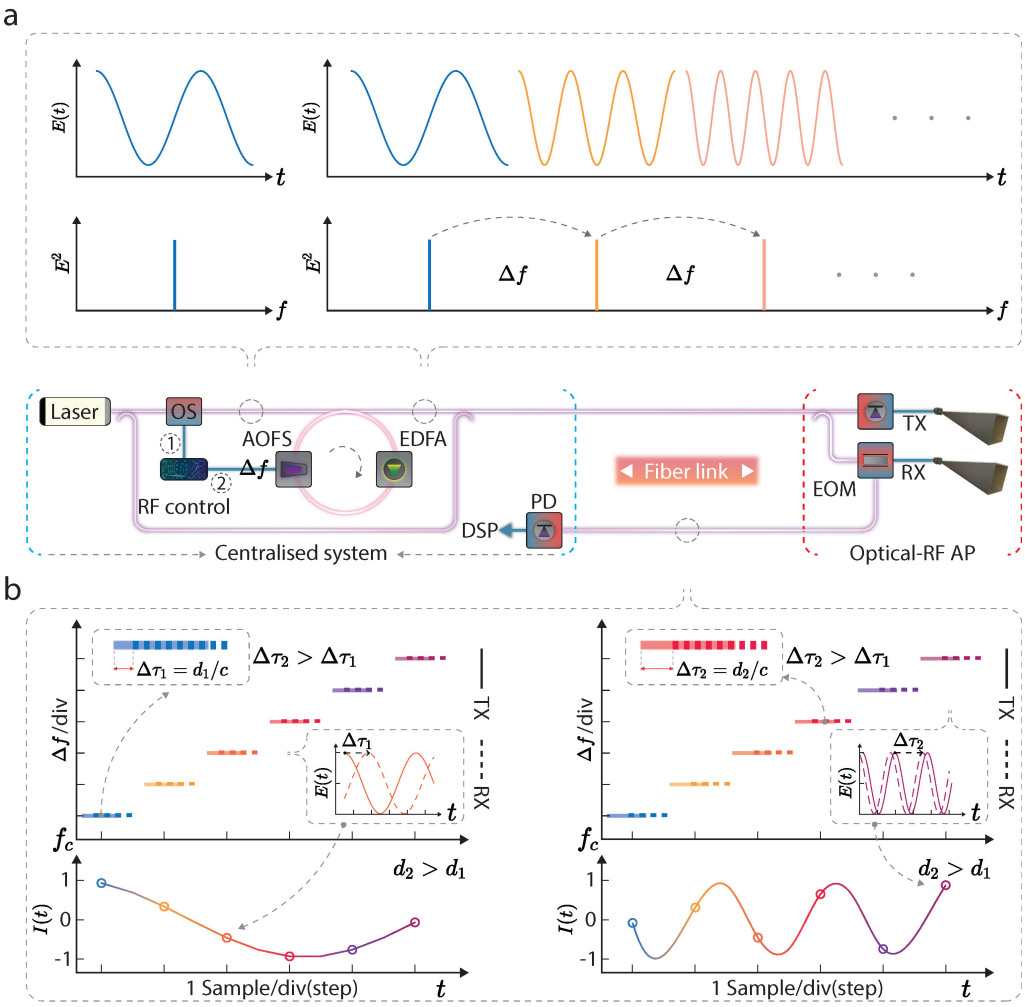


**Figure 6.2: A photonics-enabled radar system for contactless vital sign detection.** (**a**) Schematic of the demonstrated photonic radar for vital sign detection based on a frequency-shifting (FS) fibre cavity. (**b**) The optical coherent ranging principle is realised by mixing the transmitted and received optical SF signals in a photodetector (PD). After the PD, the demodulated RF signals are illustrated at the bottom panel, demonstrating the ranging at two distance instances, $d_1$ and $d_2$, respectively. OS, optical switch; FS, frequency-shifting; AOFS, acousto-optic frequency shifter; EDFA, erbium-doped fibre amplifier; EOM, electro-optic modulator; PD, photodetector; DSP, digital signal processing. $\Delta f$, the FS introduced by AOFS.

### 6.2.1 Photonic Vital Sign Radar System Schematic

An advanced SF photonic radar is employed to detect the respiratory activities of humans and animals (Figure 6.2**a**). The system is mainly

structured with an optical frequency-shifting (FS) fibre cavity to generate radar signals in the optical domain, an optical fibre distribution network, and optical-RF APs for electro-optic conversion and RF transceiving. In the FS fibre cavity, an acousto-optic frequency shifter (AOFS) shifts the frequency of an optically injected pulse (with a single frequency of $f_c$) by 100 MHz in the succession of each round-trip ($\Delta f = 100$ MHz). An erbium-doped fibre amplifier (EDFA) inserted in the optical loop compensates for the power loss from optical propagation and coupling.

This approach generates an optical SF signal consisting of a series of sine waves with linearly increased frequency at a precisely determined step (Figure 6.2**a** and Figure 6.2**b**). In the optical-RF APs, SF radar signals in the RF domain are generated through heterodyne mixing with a reference laser. The optical signal source only requires cost-effective and low-speed electronic devices (a dual-channel electrical function generator with an analogue bandwidth of 100 MHz) to precisely control the total synthesised bandwidth of the SF signal, tunable from sub-GHz level to 30 GHz. The function generator could be replaced using 100 MHz reference oscillators and RF switches with reduced complexity.

The radar vital sign detection starts with using the SF signal in the RF domain to illuminate the targets' area of interest (e.g., the chest area for humans) using a transmitting antenna element (TX). Another antenna element (RX) receives the reflected radar signals that carry the vital sign information, which is converted back to the optical domain using an electro-optic modulator (EOM). Demodulated SF signals are generated through a coherent detection process (Figure 6.2**b**), i.e., optically mixing the transmitted reference signal (solid lines) with the received signal (dashed lines). Thus, targets at different ranges, e.g., $d_1$ and $d_2$ have demodulated signals with different oscillating frequencies (Figure 6.2**b**). These oscillating frequencies can be extracted through Fourier analysis, showing different peak locations on the frequency domain [3]. One advantage of using the SF signal format over other FM approaches is that the radar receiver has a much lower sampling rate favoured for fast signal processing, owing to the fact that only one sample is required per round-trip time. For the same bandwidth, the SF signals sustain the exact resolution as other wideband radar waveforms, e.g., the LFM [16]. As a result, such a system requires less computational power for digital signal processing, enabling real-time, multi-target respiration detection.

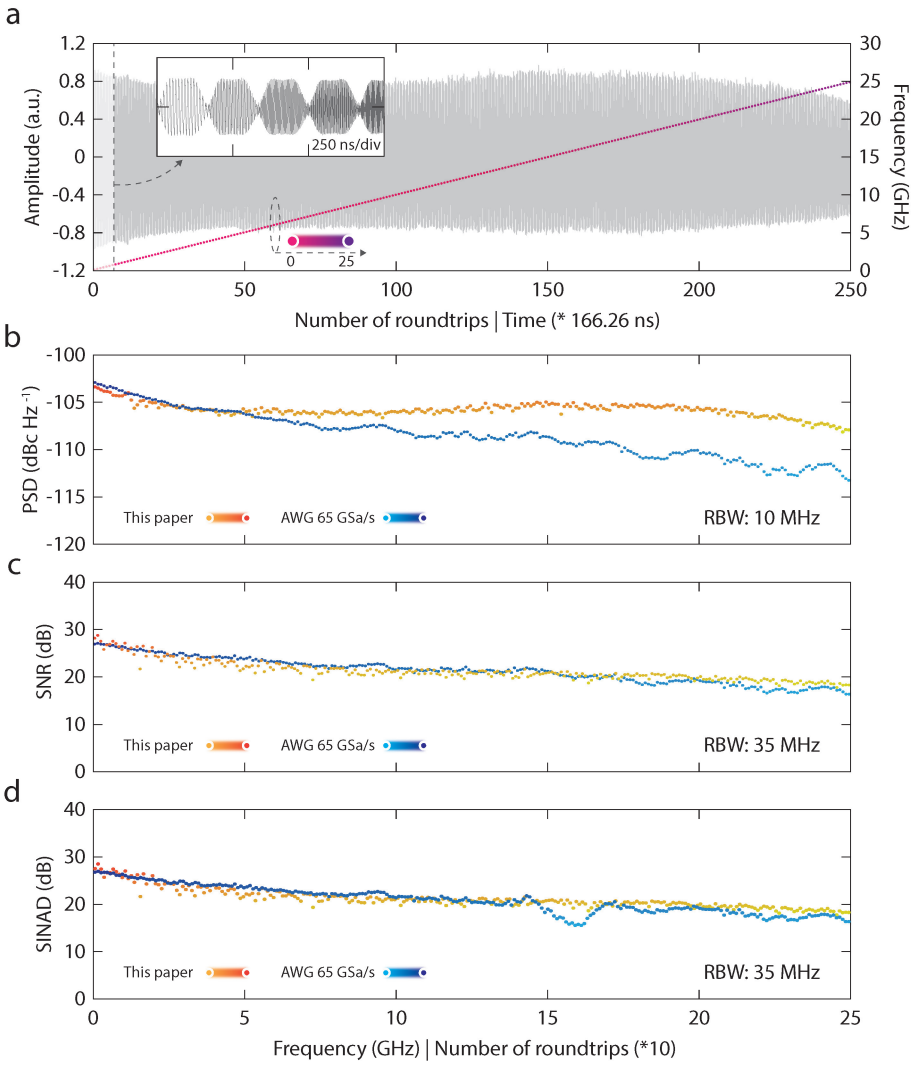


**Figure 6.3: Radar signal quality analyses.** (**a**) The demonstrated SF waveform with the corresponding frequency shows an overall bandwidth of 25 GHz. (**b**) The demonstrated signal's power spectrum density (PSD) is compared with an SF signal generated from an arbitrary waveform generator (AWG) with a sampling rate of 65 GSaps. (**c**) Signal-to-noise ratio (SNR) of the signals generated by the demonstrated system and the AWG. (**d**)Signal-to-noise and distortion ratio (SINAD) calculation based on PSD.

### 6.2.2 Photonic Vital Sign Radar Signal Quality

In a vital sign detection radar system, radio frequency (RF) sensing signals necessitate a broad bandwidth and exceptional time-frequency linearity [218] to maintain range resolution and minimise measurement errors, thereby enhancing accuracy. As depicted in Figure 6.3**a**, the

frequency-shifting cavity generates a signal with a 25 GHz bandwidth (30 GHz as shown in Figure 6.12), which can be compared to the 25-GHz analogue bandwidth of an arbitrary waveform generator (AWG). The frequency-shifting cavity features a round-trip time of 162.26 ns and a consistent 100-MHz frequency-shifting facilitated by the AOFS. As a result, a fully synthesised 25 GHz SF signal can be produced after the initial injected pulse completes 250 round trips within the FS cavity. The outstanding time-frequency linearity stems from the constant and stable frequency-time shifting enabled by the AOFS [4], which is challenging to accomplish using alternative photonics-based methods [119, 141].

The power spectral density (PSD) of the generated SF waveform maintains a consistent level of approximately -103.7 dBc/Hz throughout the entire recirculation process, as illustrated in Figure 6.3**b**. It slightly decreases to -108.3 dBc/Hz upon reaching the 250th circulation. Conversely, the PSD of the electronic counterpart displays a noticeable decline, from -103.0 dBc/Hz to -113.6 dBc/Hz, due to the AWG's constrained adequate analogue bandwidth.

As shown in Figure 6.3**b**, the power spectral density is determined based on a one-sided periodogram [219] using the time-domain data presented in Figure 6.3**a**. Each power spectral density estimation employs a 100 ns time-domain segment with an 8000-point rectangular window and a resolution bandwidth of 10 MHz. The signal-to-noise ratio (SNR), depicted in Figure 6.3**c**, is estimated using a one-sided power spectrum based on a 100 ns time-domain segment with an 8000-point Kaiser window (shape factor $\beta = 38$) to maximise energy concentration in the main lobe [220]. This results in an equivalent rectangular noise bandwidth of 35.08 MHz. Furthermore, we calculated the signal-to-noise and distortion ratio (SINAD) to evaluate the signal quality more comprehensively, using the power spectral density displayed in Figure 6.3**b**.

The signal-to-noise ratio is derived from the power spectral density results and compared with the signal generated by the AWG (Figure 6.3**c**). The signal-to-noise findings reveal no significant disparities between these two signals across the 25 GHz bandwidth, demonstrating that the proposed system can generate radar signals with quality comparable to that of an AWG. Utilising the same time-domain signals, the signal-to-noise and distortion ratio is calculated, further substantiating the signal quality of the showcased system. It is important to note that signal quality is not anticipated to degrade through photonics-based up-conversion, unlike conventional electronic up-conversion methods [221, 222].

### 6.2.3 Photonic Vital Sign Radar Ranging Accuracy

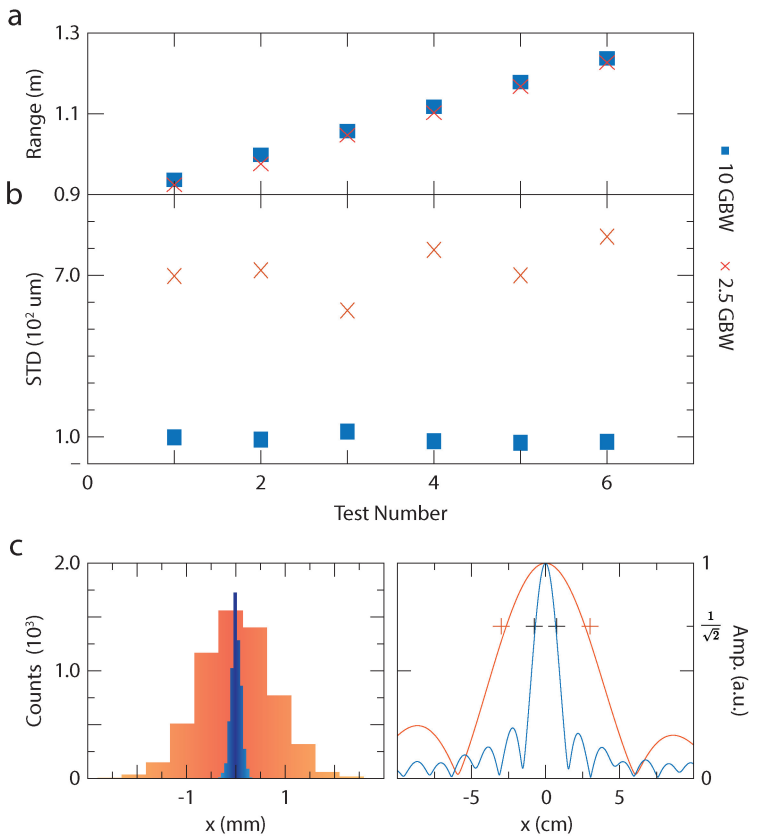


**Figure 6.4: Radar signal ranging accuracy analyses.** (**a**) Ranging and (**b**) accuracy, in terms of standard deviation (STD), results using 2.5 GHz (cross) and 10 GHz (square) bandwidth signals. (**c**) STDs (left) of the 2.5 GHz and 10 GHz SF signals. Over 6,000 measurements, the 2.5 GHz and 10 GHz SF signals show an STD of 725.90 $\mu$m and 93.28 $\mu$m, respectively. Experimental and theoretical (-3 dB, plus) ranging resolutions of the two signals are plotted accordingly.

Furthermore, we investigate the range resolution (Figure 6.4**a**) and accuracy characterised in standard deviation (STD) (Figure 6.4**b**) of the presented vital sign detection photonic radar system. The results were measured using 2.5 GHz (cross) and 10 GHz (square) bandwidth SF signals based on a metal plane reflector with a dimension of $4 \times 5 \times 0.3$ cm. The SF signal with a wider bandwidth (10 GHz) shows a significant accuracy improvement compared with the narrower band (2.5 GHz) SF signal (Figure 6.4**c**), revealing a reduction in STD to 93.28 $\mu$m from 725.90 $\mu$m based on the signals with experimental range resolutions of 13.7 and 53.2 mm, respectively. These results proved that increasing the sensing

signal bandwidth will simultaneously improve the range resolution and accuracy, which is greatly preferable for a radar system to detect delicate respiratory activities from multiple targets.

### 6.2.4 Vital Sign Detection using Respiration Simulator

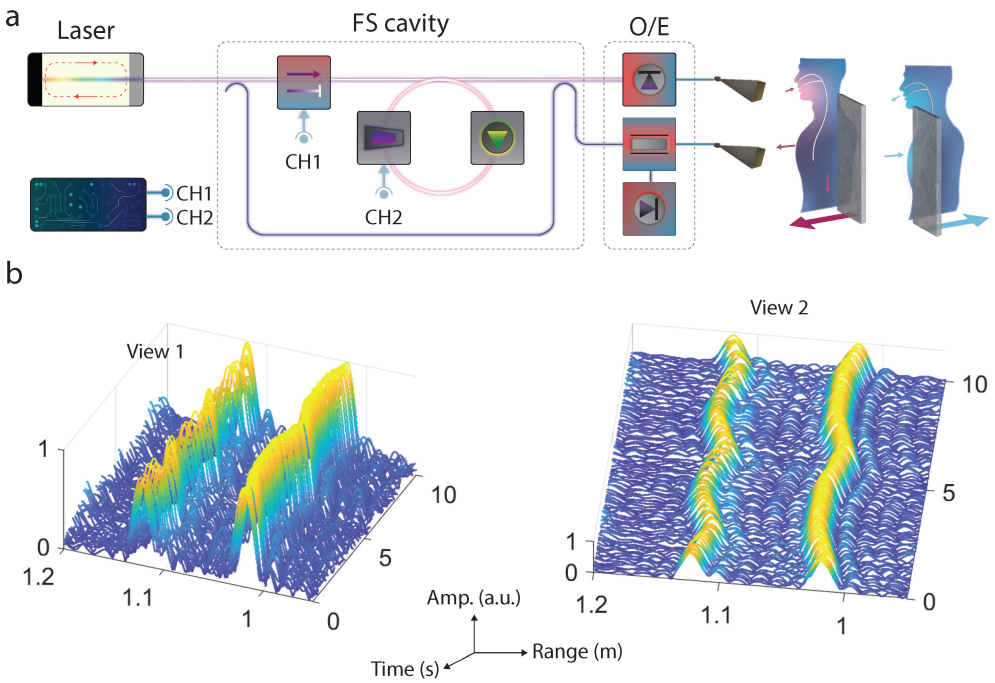


**Figure 6.5: Multi-target vital sign detection results based on respiration simulators.** (**a**) Experimental setup using the demonstrated photonic SF radar with an RF bandwidth of 10 GHz. Two metal plates ($4 \times 5 \times 0.3$ cm) separately mounted onto two stepper motors are used here to emulate the chest movement of human breathing. (**b**) Contactless vital sign detections of two closely located targets. Two perspectives of the identical two-target detection results are presented in **b**

Next, we applied the photonic radar to multi-target respiration detection based on two human breathing simulators (Figure 6.5**a**). Our radar can successfully detect respiratory activities from the two closely located targets (∼10 cm apart) in real-time (Figure 6.5**b**). Over a 60-second time window, the relative 'chest' movements of the two targets are extracted (Figure 6.6**a**). The corresponding respiratory frequencies, in terms of breath per minute (bpm), are acquired by taking the Fourier transform of the trajectories (Figure 6.6**d**) with a respiratory rate (RR) of 12 bpm and 16.5 bpm for the upper and lower targets, respectively. These two frequencies are deliberately chosen to fit the typical RR of an adult at rest

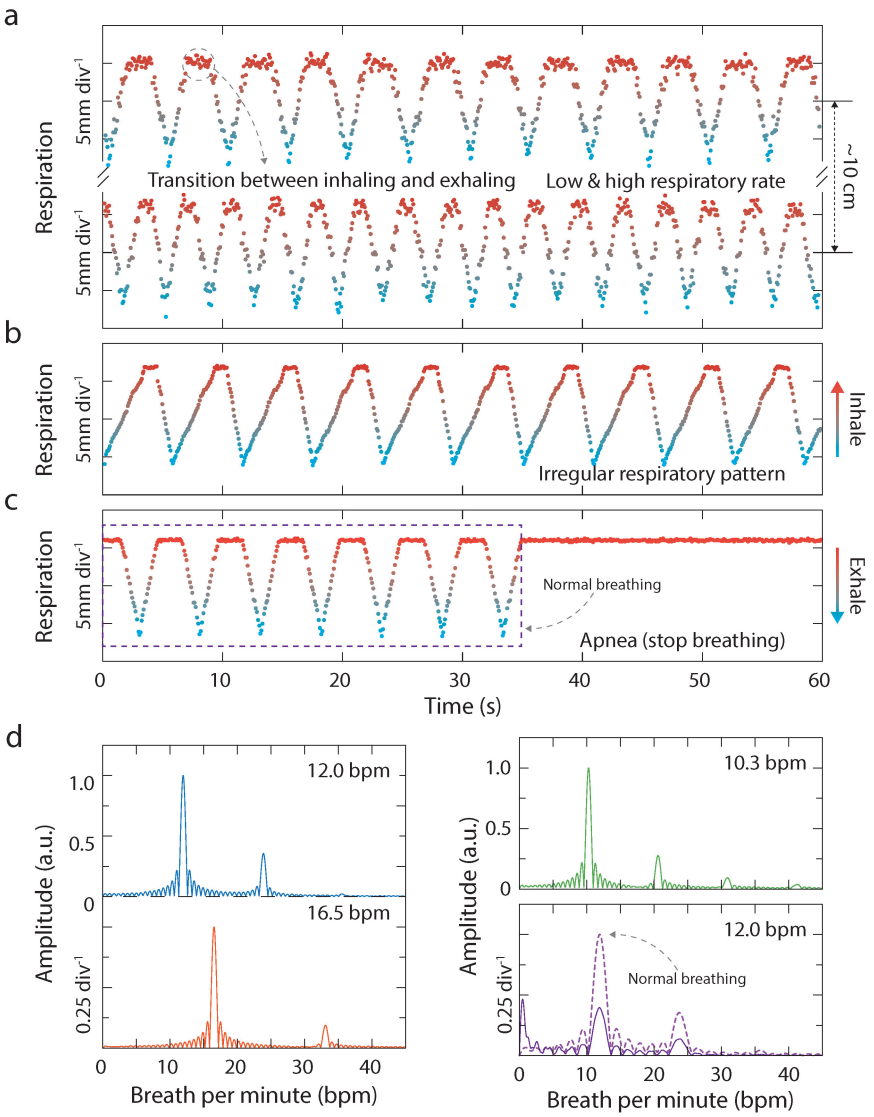


**Figure 6.6: Multi-target vital sign detection results based on respiration simulators.** (**a**) Chest movements of the two targets. (**b**) Chest movement showing irregular (longer inhale and shorter exhale) breathing patterns. (**c**) Chest movement shows stopped breathing, which could be a sign of apnea. (**d**) Fourier transform results based on the chest movement in Fig. 3**a-c**.

[223, 224]. Meanwhile, the superior accuracy allows the radar system to detect irregular respiration patterns with subtle movements (around mm-level), such as irregular breathing with longer inhalations and shorter exhalations and stop breathing (Figure 6.6**b** and Figure 6.6**c**). Therefore, it could help accurately identify or even predict respiratory abnormalities

linked to many medical conditions, such as asthma, anxiety, congestive heart failure, and lung disease. The demonstrated results proved that the accuracy enabled by the demonstrated system offers sufficient precision to pick up respiratory abnormalities.

## 6.3 Vital Sign Detection using Cane Toads

### 6.3.1 Cane Toad Respiration


**Figure 6.7:** An illustration of a cane toad's buccal cavity, a key component in its sophisticated multi-organ respiratory system.

Cane toads have more complex respiration patterns than humans due to the complexity of multi-organ gas exchange, including skin, gills, and lungs [225]. Lungs are the organ responsible for air-breathing, which contains a series of events that cause buccal movement (Figure 6.7). In general, one air-breathing cycle comprises the following events. First, fresh air is drawn into the lower half of the buccal cavity through buccal depression. Second, the air from the previous air-breathing cycle exits from the mouth (nares) through the upper half of the buccal cavity. Finally, the fresh air is forced into the lungs with two possibilities occurring after this final cycle: 1) the entire cycle is repeated (single breaths), and 2) only the cycle is repeated without lung ventilation (doublets). Either single breaths or doublets have a regular, non-discontinuous interval. Two female cane toads are approved for the experiment. These two cane toads are slightly different in body size. The radar and LiDAR experiments use different cane toads.

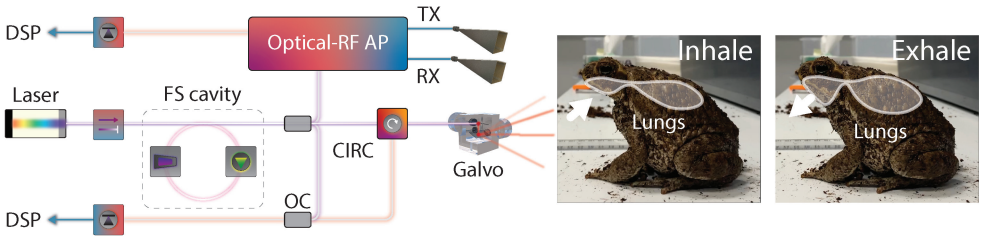


**Figure 6.8: Vital sign detection results using a cane toad as a human proxy.** Experimental setup using the demonstrated system for radar sensing, which also shows its flexibility and capability to enable LiDAR detection. OC: optical coupler; CIRC: optical circulator; Galvo: 2-D scanning mirrors.

### 6.3.2 Photonic Radar Enabled Respiration Detection of a Cane Toad

To prove its suitability in practical applications, we demonstrate animal respiratory detection using a female cane toad as a human proxy (a pilot study before human trials) to evaluate the radar performance (Figure 6.8). The cane toad has a radar cross-section (the buccal area, $\sim 2 \times 2.5$ cm) smaller than the human chest, making the experiment more challenging than human trials. The buccal cavity was connected to the lungs as a part of its air-breathing activity [226, 227, 225]. The toad was located about 1 meter from the radar antenna, with the beam pointing to the toad's buccal area. The data extracted from the photonic radar reveals the real-time trace of the toad's buccal movement with a displacement of around 5 mm (Figure 6.9**a**). Meanwhile, the radar data is cross-referenced with the data extracted from a video clip (see Section 6.5.4) recorded simultaneously, showing a cross-correlation coefficient of 0.746 (Figure 6.9**b**). It is worth mentioning that the camera has a different perspective from the radar beam direction, which might slightly decrease the correlation coefficient. The Fourier domain analyses based on radar and camera data further prove the accuracy and performance of the photonics-enabled radar system (Figure 6.9**c**). The respiration data shows that the cane toad has an irregular respiration pattern, owing to the fact that intermittent or discontinuous breathing patterns (see Cane Toad Respiration, Section 6.3.1) are common in amphibians [226, 227, 225], which agrees with both the radar and camera-based results.

The proposed radar system can also be employed for LiDAR sensing, as shown in Figure 6.8. In this context, RF components like the RF amplifier and antennas no longer dictate the system's bandwidth.

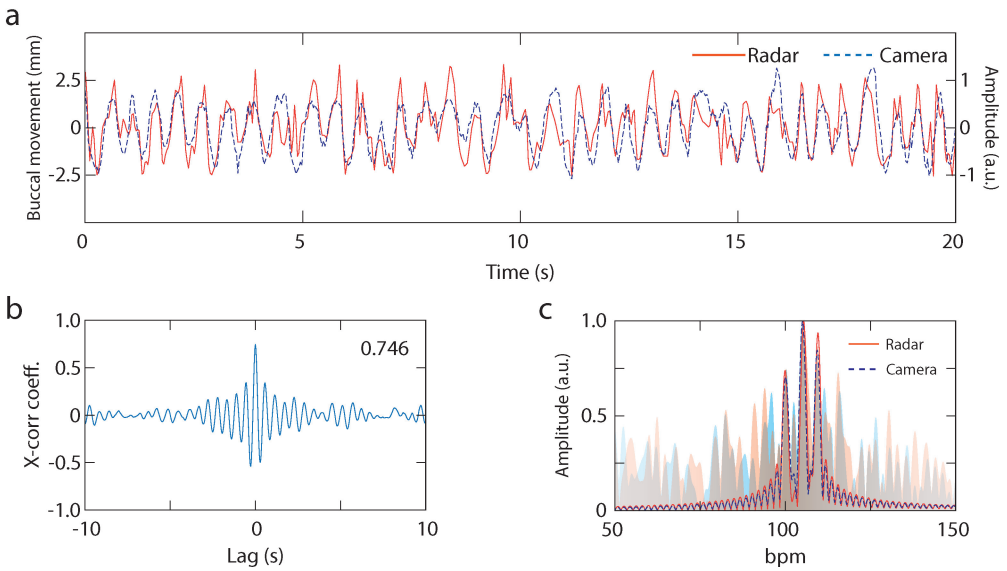


**Figure 6.9: Vital sign detection results using a cane toad as a human proxy.** (**a**) Experimental results of detecting the buccal cavity movement of the cane toad using the demonstrated radar system. The camera-extracted data is used as a reference. (**b**) Cross-correlation between radar and camera data, showing a coefficient of 0.746. (**c**) Frequency domain analyses of radar (red shadow) and camera data (blue shadow) with three top-weighted Fourier coefficients in solid and dashed lines, respectively.

Both the radar and LiDAR systems utilise the same optical source. The optically generated SF signal, boasting a bandwidth of 25 GHz, is directed to an optical circulator, which is then guided by a 2D scanning mirror (Galvo scanner) to focus the beam on the buccal area of the cane toad, thereby detecting its movements. Scattered light returns to the circulator and mixes with a tap of the transmitted optical signal for coherent LiDAR demodulation. The ambiguity range of the LiDAR is consistent with that of the radar, as they share the same frequency shift (100 MHz) that ultimately determines the ambiguity range. Consequently, the integrated sensor system retains this ambiguity range.

Notably, the energy of the received LiDAR signal is influenced by several factors related to the objects, including surface roughness, reflectivity, and the aperture of the fibre collimator, all of which play pivotal roles. In our experiment, we employ an optical amplifier to elevate the energy level to approximately 20 mW, well below the safety threshold for this wavelength, even though the peak power can surge to kilowatt levels. Consequently, the ambiguity range can be expanded by minimising the step size, for instance, by using AOMs with opposing frequency shifts.

Simultaneously, by augmenting the optical power on the transmitter end, we can increase both the received signal's energy level and the detection range.

The demonstrated system enables the LiDAR system with a total synthesised bandwidth of 25 GHz (6 mm range resolution), sufficient to catch the toad's buccal movement (Figure 6.10**a**). The performance is also validated by cross-referencing the LiDAR data with the camera data using cross-correlation (Figure 6.10**b**) and Fourier analyses (Figure 6.10**c**). This provides an approach to achieve a hybrid radar-LiDAR system that can combine complementary detection techniques for improved sensing accuracy and system resilience.

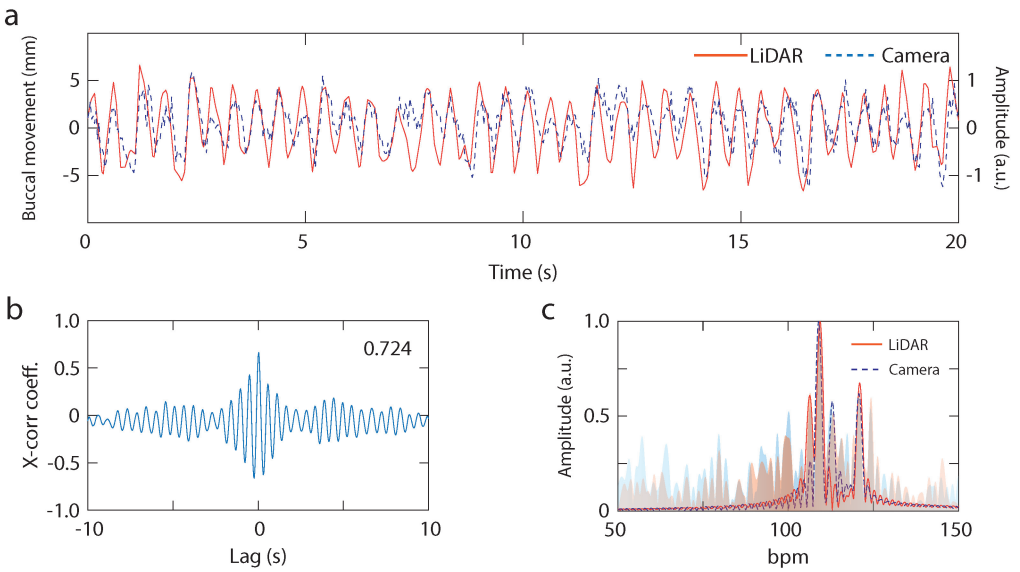


**Figure 6.10: Vital sign detection results using a cane toad as a human proxy.** (**a**) Experimental results of detecting the buccal cavity movement of the cane toad using a LiDAR system. (**b**) Cross-correlation between the LiDAR and camera data, showing a coefficient of 0.724. (**c**) Frequency domain analyses of the LiDAR (red shadow) and camera data (blue shadow) with three top-weighted Fourier coefficients in solid and dash lines, respectively

## 6.4 Summary and Discussion

In summary, we have demonstrated a photonic vital sign detection system offering fine resolution down to 6 mm and micrometre-level accuracy, which enables multi-target detection without compromising comfort and privacy. Experimental validations confirmed its capability and ef-

fectiveness in detecting subtle respiratory abnormalities and accurately extracting the buccal movement of cane toads. Moreover, it features a streamlined system structure with enhanced bandwidth and flexibility that current state-of-the-art electronic vital sign radars cannot achieve without resorting to parallel or multiplexed electronic architectures.

The system supports both radar and LiDAR sensing, showcasing its unprecedented versatility and potential for hybrid detection and sensor fusion, which yield more consistent and accurate sensing results [214]. The radar system operates similarly to LiDAR, as both rely on the same ranging and detection principles. However, radar uses radio waves instead of light waves, resulting in superior penetration through clothes and thin walls. The longer wavelength (typically at the centimetre level) of radio waves makes confining the signal more challenging, leading to limited spatial information and necessitating larger antennas to enhance gain and directionality. The increased beam size of radar systems, compared to LiDAR, heightens their susceptibility to reflections from surrounding clutter, crosstalk with other vital sign radar systems, and interference from unknown RF signals within the same frequency band. In contrast, LiDAR, which employs light with much shorter wavelengths, boasts a superior range and spatial resolution due to its broader sensing bandwidth and 2D scanning capabilities. However, LiDAR's micrometre optical wavelength limits its ability to penetrate objects such as clothing, making it a complementary approach to assist radar in vital sign detection.

The proposed radar system can maximise its bandwidth potential by integrating available photonic and RF technologies. This includes using commercially available components such as uni-travelling-carrier photodiodes (UTC-PD) with a frequency range of up to 900 GHz and a bandwidth exceeding 340 GHz [228], as well as RF amplifiers [229] and antennas designed for compatible frequencies. Furthermore, the system is compatible with the photonic distributed, multi-band operation radar technique [213], allowing multiple sensors powered by one centralised photonic system to work together seamlessly without interference for broader detection coverage at lower overall complexity and cost. To advance the miniaturisation of the photonic system, recent developments in photonic integration of essential building blocks, such as on-chip acousto-optic frequency shifters [189, 164] and optical waveguide amplifiers [230, 166], provide a promising foundation for achieving a compact size suitable for portable sensing [214, 137]. This innovative photonic approach paves the way for high-resolution, rapid-response,

and cost-effective hybrid radar-LiDAR modules designed for distributed, contactless vital sign detection.

## 6.5 Experimental Setup and Performance Comparison

### 6.5.1 Software-defined Flexible Radar Bandwidth Tuning

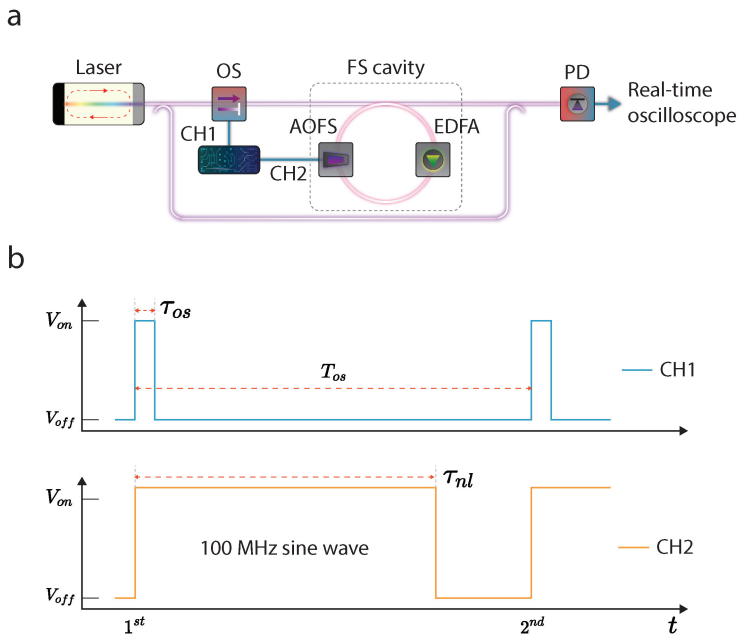


**Figure 6.11: Flexible bandwidth tuning based on a software-definable MHz-level RF source.** (**a**) System schematic for generating based SF signals in the RF domain. (**b**) MHz-level system control signals generated by a two-channel RF source.

A laser is connected to an optical coupler as the optical source in the system (Figure 6.11**a**). A dual-channel function generator generates the RF control signals that drive the FS cavity with an analogue bandwidth of 100 MHz. As illustrated in Figure 6.11**b**, one channel (CH1) generates a periodic on-off signal to control an optical switch (OS) so that the optical pulse has a dwell time of $\tau_{os}$ and a repetition rate of $T_{os}$. The other channel (CH2) generates a $\Delta f$-Hz sine wave to drive the AOFS. In order to control the total number of roundtrips $N$ (the synthesised bandwidth), a rectangular envelope is applied on top of the $\Delta f$-Hz sine wave in CH2 (Figure 6.11**b**), with a duty cycle of $\tau_{nl}$ ($N \times \tau_{os}$) and repetition rate of

$T_{nl}$ to switch on-off the AOFS [131]. Thus, bandwidth tuning from the sub-GHz level to 30 GHz can be realised by adjusting the duty cycle $\tau_{nl}$ (Figure 6.12).

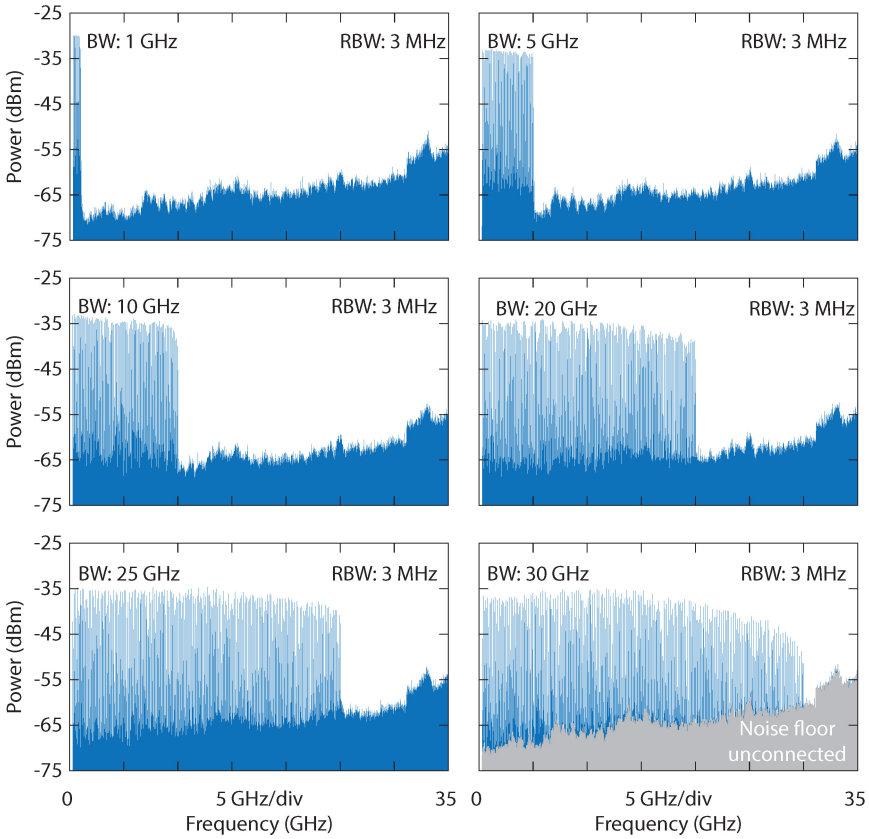


**Figure 6.12: Flexible bandwidth tuning based on a software-definable MHz-level RF source.** Baseband RF bandwidth tuning from 1 to 30 GHz by adjusting the RF control signals.

### 6.5.2 Time-domain Waveform Measurement

Baseband RF signals are acquired by mixing the optical SF signal with a tap of the CW laser in a 50 GHz photodetector (PD). A real-time oscilloscope, with a sampling speed of 80 GSa/s, measures the time-domain data in Figure 6.3. Each point of the time and frequency data is extracted based on a 100 ns time window located at the middle of each frequency step.

### 6.5.3 Comparison with Electronic Vital Sign Radars and Photonic Radars

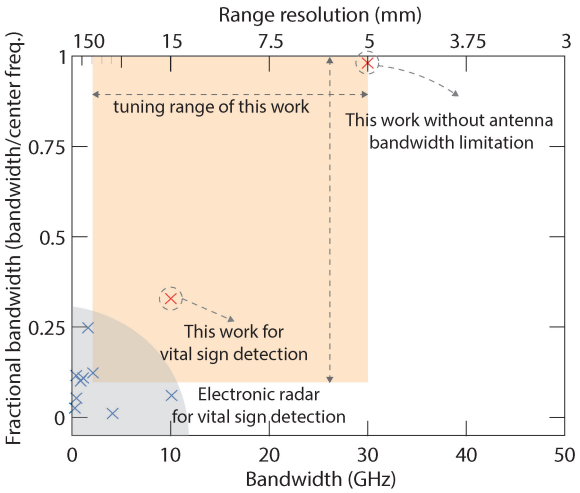


**Figure 6.13:** Evaluation of the demonstrated photonic radar system against conventional electronic vital sign radars in terms of fractional bandwidth (the ratio between frequency tuning range and centre frequency) and the system's range resolution.

We provide a table to compare the demonstrated system with existing electronic vital sign radars (Table 6.1). Figure 6.13 visualises several figures of merit based on Table 6.1. Figure 6.13 evaluates the demonstrated photonic radar system against conventional electronic vital sign radars regarding fractional bandwidth (the ratio between frequency tuning range and centre frequency) and the system's range resolution. Figure 6.13 clearly shows that the demonstrated system has superior sensing bandwidth and range resolution compared with several existing vital sign radars; thus, it offers better performance and accuracy for vital sign detection. This further proves photonic radars have greater frequency flexibility and tunability (fractional bandwidth) than conventional electronics.

We provide a table to compare the demonstrated system with existing electronic vital sign radars (Table 6.1) and several photonic approaches for generating radar signals (Table 3.1). Figure 6.13 and Figure 3.7 visualised several figures of merit based on Table 6.1 and Table 3.1. Figure 6.13 evaluates the demonstrated photonic radar system against conventional electronic vital sign radars in terms of fractional bandwidth (the ratio between frequency tuning range and centre frequency) and the system's range resolution. Figure 6.13 clearly shows that the demonstrated system

has superior sensing bandwidth and range resolution compared with several existing vital sign radars; thus, better performance and accuracy for vital sign detection. It further proves that photonic radars have better frequency flexibility and tunability (fractional bandwidth) than conventional electronics. Figure 3.7 compares the photonics-based wideband RF signal generation in terms of the speed of the system's driving electronics and the demonstrated radar signal bandwidth across various photonic approaches, including using frequency-shifting cavity, laser sweeping, EOMs, and engineered fibre dispersion. It further proves that the demonstrated photonic radar based on the FS cavity requires simple electronics but sustains undiminished signal generation bandwidth, which reaches an optimal balance between the bandwidth limitation (the RF bandwidth of both the EOM and the driving electronics) from those based on EOMs and the bandwidth tuning flexibility of those based on dispersion.

### 6.5.4 Camera vital sign detection

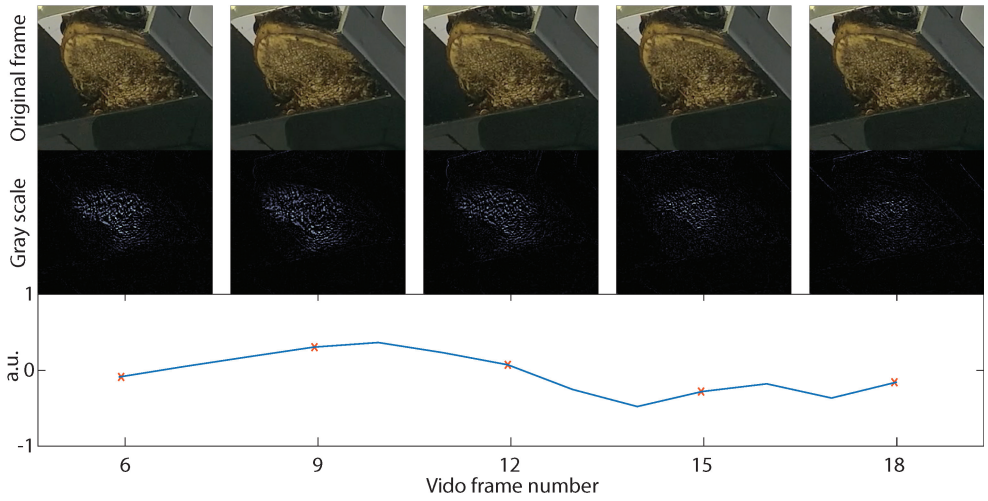


**Figure 6.14:** Camera-based respiration extraction of a cane toad.

While using the demonstrated photonic radar to detect the buccal movement of the cane toad, we also used a camera to record the activity simultaneously as a reference. The video clip is recorded with a speed of 30 frames per second (FPS). Each video frame is converted into a numerical, grey-scale ($[0, 1]$), 2D matrix and then subtracted with a reference frame. Therefore, body motions (buccal movement) will be translated into intensity changes, which can be used to extract the cane toad's

respiration (Figure 6.14).

| Bandwidth (GHz) | Range resolution (mm) | Carrier Frequency (GHz) | Formality | Frequency tuning range (GHz) | Reference |
|---|---|---|---|---|---|
| Photonic vital sign detection radar | | | | | |
| **10 (30)** | **13.74 (4.99)** | **30** | **SF** | **[MHz,>300]** | **This Work** |
| Electronic vital sign detection radar | | | | | |
| 1 | 150 | 9 | SF | [8.5,9.5] | [145] |
| 4 | 43 | 78-79 | LFM | [77,81] | [209] |
| 0.16 | 937.5 | 5.8 | LFM | [5.72,5.88] | [207] |
| 10 | 14.99** | 80 | LFM | [75,80] | [231] |
| 2 | 74.95** | 8 | SF | [7,9] | [208] |
| 1.5 | 100 | 3 | FM | [2.25,3.75] | [211] |
| 0.3 | 499.65** | 2.55 | SF | [2.4,2.7] | [224] |
| 0.75 | 200 | 7.3 | LFM | [7.3,8.05] | [210] |
| 0.32 | 468.43** | 5.8 | CW+LFM | [5.64,5.96] | [232] |
| - | - | 3 | CW | NA | [211] |
| - | - | 5.8 | CW | NA | [206] |
| - | - | 2.4 | CW | NA | [233] |
| - | - | 60 | CW | [56,62] | [234] |
| - | - | 103 | CW | [93,105] | [154] |

**Table 6.1: Comparison with reported electronic vital sign detection radars**. SF, stepped-frequency; LFM, linear-frequency modulated waveform; CW, continuous wave; NA, data not available or not mentioned in the literature; **, range resolution not mentioned but calculated theoretically based on the reported bandwidth; -, not applicable.

Chapter 7

# Conclusion and Outlook

## 7.1 Conclusion

This thesis began with a historical review, tracing the evolution of radar technology from its beginning to its current use across a wide range of applications and then shifted to technical analysis, highlighting the emergence of high-resolution, near-range applications. These historical and technical perspectives revealed the growing importance of radar sensing technology, which is evolving towards the millimetre-wave and terahertz-wave regions in response to the need for high-resolution imaging in practical applications such as drone tracking and vital sign detection. However, conventional electronic techniques are hindered by constraints in bandwidth, noise level, and cost-effectiveness. Emerging microwave photonics-enabled radar technology provides a promising alternative with wideband, high-resolution capabilities and multi-frequency adaptability but faces system complexity and stability challenges.

In light of these considerations, a photonic approach that delivers sufficient bandwidth, system tunability, high time-frequency linearity, and minimises the dependence on high-speed electronics is crucial for developing next-generation, high-performance radar systems. Adopting photonics-based techniques for radar applications has proven historically inevitable due to the immense needs and pressures posed by demanding applications requiring high-performance radar systems. Conventional electronic technologies face significant challenges in meeting these requirements, which substantiates photonics' suitability as a robust candidate to address these needs. Photonics offers considerable technological advantages unparalleled by conventional electronics.

Given that both conventional electronic and advanced photonic radar systems utilise electromagnetic (EM) waves for sensing and share the same fundamental principles, Chapter 2 established a foundation for radar sensing, achieved by delving into the basics of EM wave scattering and introducing the essential radar parameter, the radar cross section (RCS), which quantitatively characterises an object's detectability. RCS was then incorporated into the radar equations to analyse radar sensing performance regarding maximum detection range and the system's SNR. Chapter 2 further explored various widely-used radar waveform formats, comparing their range principles, range resolution, range-Doppler sensing capabilities, and ambiguity ranges, thus extensively analysing their strengths and limitations. Concluding the chapter, the two-dimensional inverse synthetic aperture radar (ISAR) imaging technique and the electronic frequency-modulated radar system were introduced, examining their fundamental building blocks and operating principles in preparation for the following chapters.

Chapter 3 served as a bridge between conventional electronic and photonic radar systems, examining their fundamental building blocks and operations to underscore the potential of photonic technologies in enhancing radar performance. This chapter addressed wideband radar signal generation and low-phase noise local oscillators. Chapter 3 showcased the advantages of bandwidth, flexibility, and distributed sensing capabilities offered by photonic technologies.

Chapter 4 presented a photonic ultra-wideband stepped-frequency radar, possessing a bandwidth of up to 11.52 GHz and driven by MHz-level electronics. This innovative system simultaneously combined high spatial and velocity resolution with rapid radar detection, enabled by its ultra-wide bandwidth and low demodulation processing bandwidth of a few MHz. Demonstrations of high-resolution radar ranging and 2D imaging showcased the potential of this photonic radar for practical applications such as autopilot assistance, gesture recognition, environmental sensing, and medical imaging. By reducing system complexity and eliminating the need for ultra-fast GHz-speed electronics, Chapter 4 built an important foundation for developing next-generation broadband radars, offering centimetre-level spatial resolution and a real-time imaging rate of 200 frames per second, ultimately transforming the capabilities of radar for widespread sensing applications.

Building upon the initial findings and demonstrations in Chapter 4, Chapter 5 tackled the challenges of in-loop signal instability and inter-pulse

interference, which typically caused amplitude fluctuations and led to a limited SNR and signal bandwidth when employing a frequency-shifting loop for generating wideband radar signals. This was accomplished by mitigating the in-loop polarisation scrambling and inter-pulse interference using a polarisation-maintaining cavity and a high-extinction optical switch, enabling stable consecutive acousto-optic frequency-shifting modulation and significantly improving the SNR. As a result, we demonstrated the photonic generation of 30-GHz-wide stepped-frequency (SF) signals with 100 MHz frequency steps defined by an MHz-level electrical oscillator for the first time. Furthermore, the system surpassed state-of-the-art demonstrations based on wideband electronics regarding bandwidth while alleviating the necessity for high-speed signal generators or wideband tunable lasers. To exemplify its utility, we systematically evaluated the signal quality and demonstrated its applications in radar imaging compared to those employing electrical waveform generators. As a result, the demonstrated system offered a viable approach to overcoming the analogue bandwidth limitations of digital waveform generators for synthesising broadband radar signals, facilitating high-resolution radar sensing and presenting an appealing combination of wideband signal synthesis, high SNR, and reduced hardware requirements.

Chapter 6 demonstrated the high-performance radar system for contactless multi-target vital sign detection. The demonstrated photonic vital sign detection system offered fine resolution down to 6 mm and micrometre-level accuracy, enabling multi-target detection without compromising comfort and privacy. Experimental validations confirmed its capability and effectiveness in detecting subtle respiratory abnormalities and accurately extracting the buccal movement of cane toads. Moreover, it featured a system structure with enhanced bandwidth and flexibility that current state-of-the-art electronic vital sign radars could not achieve without complicated parallel electronic architectures. The system supported radar and LiDAR sensing, proving its unprecedented flexibility and potential for hybrid detection and sensor fusion, offering more consistent and accurate sensing results.

## 7.2 Outlook

An optical frequency-shifting loop serves as a promising approach for synthesising broadband signals for both radar and LiDAR applications. In this outlook, the prospect of future explorations can be outlined as follows:

- Synthesising Linear Frequency Modulated (LFM) signals with an optical frequency-shifting loop for higher bandwidth and superior time-frequency linearity.
- Employing a chip-based frequency-shifting loop for compact photonic radar systems.
- Utilising a single frequency-shifting loop as an optical source for concurrent radar and LiDAR sensing in a sensor fusion system.
- Exploring terahertz radar sensing for enhanced performance and functionality.

From the radar perspective, this approach generates ultra-broadband radar signals with an inherent high time-frequency linearity while maintaining signal quality comparable to high-speed electronics. Consequently, it enables high-range resolution and accurate radar sensing for a diverse array of applications, such as drone imaging and contactless vital sign detection. This relatively straightforward system capitalises on the broad optical spectrum, offering flexibility and software-defined control through MHz-level electronics, which is important for future optical-RF hybrid systems with optimal size-weight-power ratios.

From the LiDAR standpoint, the high time-frequency linearity is equally significant for ensuring accurate detection. LiDAR systems can benefit from the inherent linearity by employing the optical frequency-shifting loop, leading to enhanced precision in measuring distances and generating detailed, high-resolution point clouds. This advantage bolsters LiDAR's performance in applications such as industrial quality control, 3D surface mapping, and environmental monitoring, ultimately contributing to developing more sophisticated and reliable sensing technologies.

Expanding on this concept, the ability of such a system to facilitate both radar and LiDAR sensing as part of a sensor fusion arrangement is particularly intriguing. This sensor fusion combines the features of radar, such as the penetration capacity using RF signals, with the detailed spatial information provided by LiDAR, resulting in a complementary array of capabilities. This fusion is essential, as single sensors alone cannot satisfy the diverse requirements of today's application scenarios.

For instance, consider vital sign detection. A radar system can achieve contactless vital sign detection while disregarding the target's clothing. However, the performance of a standalone radar system for vital sign detection is significantly influenced by the target's random body movements and strong reflectors from the environment. LiDAR's 2D spatial

information could prove invaluable to counteract these unwanted motions and interference. By integrating the information from radar and LiDAR, the radar system can utilise body motion data extracted from the LiDAR to optimise and isolate the target's vital sign information, thereby enhancing system performance in real-world situations.

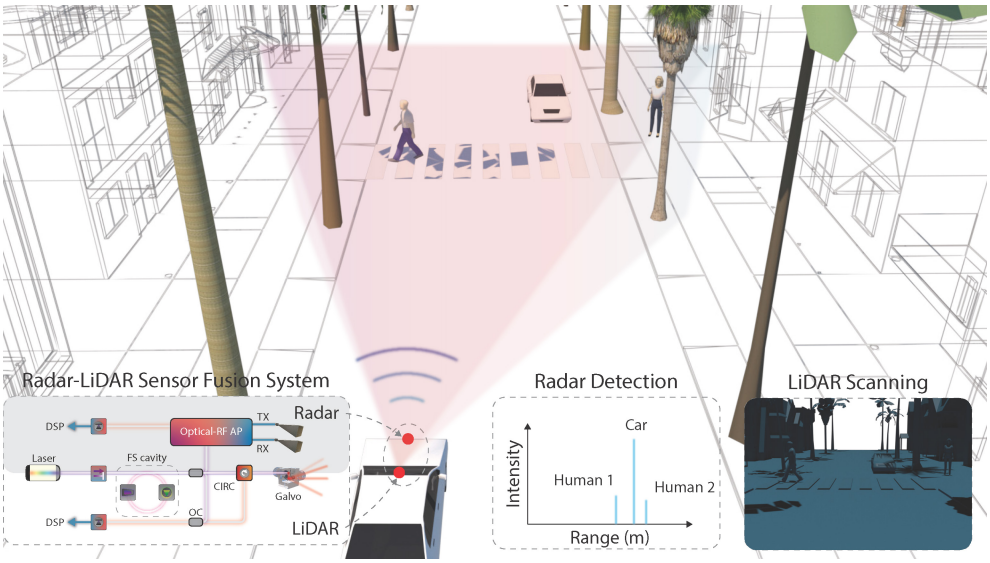


**Figure 7.1:** A schematic diagram representing the deployment of the proposed photonic radar-LiDAR sensor fusion system for autonomous vehicle navigation.

Sensor fusion systems, integrating radar and LiDAR capabilities, possess a promising potential for applications, such as autonomous vehicle navigation (Figure 7.1), security, surveillance, and industrial automation. The fusion leverages the complementary strengths of these sensing technologies, offering enhanced accuracy, reliability, and robustness in sensing solutions, thus catalysing innovation across numerous sectors. This thesis includes a viable advance towards realising this concept, with further exploration of sensor fusion envisaged for the future.

In the following sections of this outlook chapter, we will examine the capabilities of the demonstrated frequency-shifting loop for synthesising wideband chirp waveforms and the potential challenges that should be addressed. We will then present some preliminary results of employing the generated signal for industrial quality control purposes, as evidenced by successful imaging of a printed circuit board (PCB) and a 50-cent coin featuring micrometre-scale surface variations.

Furthermore, we will extend the discussion to envision integrating key

components onto a photonic chip, paving the way for compact and efficient implementations of such systems. Lastly, we will explore the commercial potential of a sensor fusion system in alignment with real industry needs in various sectors. We will discuss its application for vital sign monitoring and alert systems in aged care facilities, livestock monitoring in agriculture, and sleep apnoea diagnostics and monitoring.

This outlook aims to provide a clear understanding of the possibilities and challenges associated with the implementation of the frequency-shifting loop and its potential applications in diverse fields. By addressing these challenges and capitalising on the demonstrated capabilities, we can unlock the full potential of this technology and contribute to the development of innovative and practical solutions across various industries.

### 7.2.1 Synthesising Linear Frequency Modulated Waveform using an Optical FSL

Before delving into the forthcoming discussion, it is important to revisit a key concept: the ambiguity range of stepped-frequency signals.

$$\Delta d_{max} = \frac{c}{2\Delta f}. \tag{7.1}$$

where $c$ is the propagation speed of the radar signal in air and $\Delta f$ is the frequency shift.

It is apparent that by reducing the frequency shift, denoted as $\Delta f$, the ambiguity range of a given signal can be significantly extended. For example, our research has demonstrated frequency shifts of 40, 80, and 100 MHz utilising a single acousto-optic frequency shifter (AOFS), corresponding to an ambiguity range of 3.75, 1.875, and 1.5 metres, respectively. By employing commercially available components, such as the Brimrose AMF-25-XX-2FP, the frequency shift can be further reduced to 25 MHz, accompanied by an ultra-low insertion loss of approximately 2 dB. This reduction results in an expanded ambiguity range of 6 metres.

Nonetheless, it is also evident that a trade-off exists between the maximum synthesised bandwidth and the frequency shifted per roundtrip, particularly when considering the accumulation of noise after a certain number of roundtrips within the optical frequency-shifting cavity. As Figure 6.3 shows, the SNR experienced a decline of approximately 10 dB following 250 recirculations.

Therefore, the demonstrated photonic stepped-frequency radar system proves to be unsuitable for long-range detection without introducing ambiguity. In light of this, further advancements and optimisations are required to enhance the performance of the radar system for extended-range applications.

Following the aforementioned discussion, it is logical to consider an approach that utilises a reduced number of roundtrips to maintain a high SNR while simultaneously overcoming the ambiguity range limitations associated with employing a high-frequency shift. Therefore, such a system would preserve the advantages of utilising frequency-shifting loops for signal generation, including high signal quality, characterised by both SNR and time-frequency linearity, as well as the cost-effective and software-definable features of employing elementary MHz-level electronics.

The solution to this challenge is relatively straightforward and involves substituting the initial injected optical pulse with a chirped pulse, as depicted in Figure 7.2. This modification enables the system to maintain its advantageous attributes while addressing the constraints imposed by the ambiguity range and the inherent trade-offs between the maximum synthesised bandwidth and frequency shifted per roundtrip.

The proposed approach for arbitrary waveform generation, specifically that of a chirp, commences with injecting a chirp pulse into the frequency-shifting loop (Figure 7.2). This pulse's duration closely approximates the loop's roundtrip time, thus synthesising a broadband chirp signal. In this instance, we employ the signal for LiDAR demonstrations.

After mixing the reflected signal with a duplicate of the transmitted signal, the resultant signal undergoes demodulation to produce an oscillating frequency directly proportional to the target's range. In the case of a stationary target, the demodulated signal comprises a series of non-continuous sine waves in time, attributable to the time-frequency stitching process.

To overcome this discontinuity, coherent stitching, underpinned by time-domain interpolation, may be employed to connect these disparate signals seamlessly (Figure 7.2). This method ensures the accurate representation and analysis of the target's range and promotes the overall efficacy of the LiDAR system.

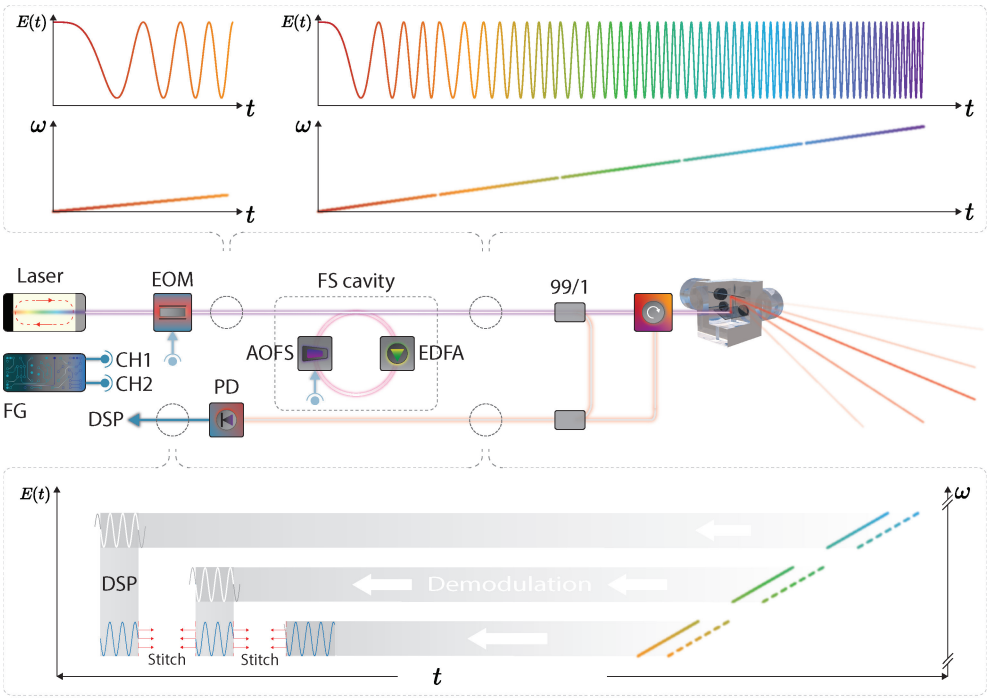


**Figure 7.2:** A schematic diagram illustrating the production of a stitched broadband chirp signal through the utilisation of a frequency-shifting loop for LiDAR applications.

### 7.2.2 FSL-Enabled LiDAR with Enhanced Detection Accuracy

Owing to the inherent time-frequency linearity of the chirp signal generated utilising a frequency-shifting loop, the LiDAR range detection demonstrates superior detection accuracy. This accuracy is characterised by the standard deviation observed when repeating the same range measurement thousands of times. As illustrated in Figure 7.3, the LiDAR system's ranging accuracy improves with the signal's bandwidth increase. The standard deviation decreases from 412.10 $\mu$m when employing a 5 GHz stitched chirp signal to 48.59 $\mu$m with a 30 GHz stitched chirp signal. This observation is consistent with the theoretical framework (Eq. (2.44)) discussed in Chapter 2.

Simultaneously, we have showcased the system's performance in real-world application scenarios, which serve as practical examples of industrial quality control. These demonstrations include imaging a Printed Circuit Board (PCB) using a 10 GHz chirp signal (Figure 7.4) and a 50-cent coin with a 90 GHz chirp signal (Figure 7.5). By doing so, we

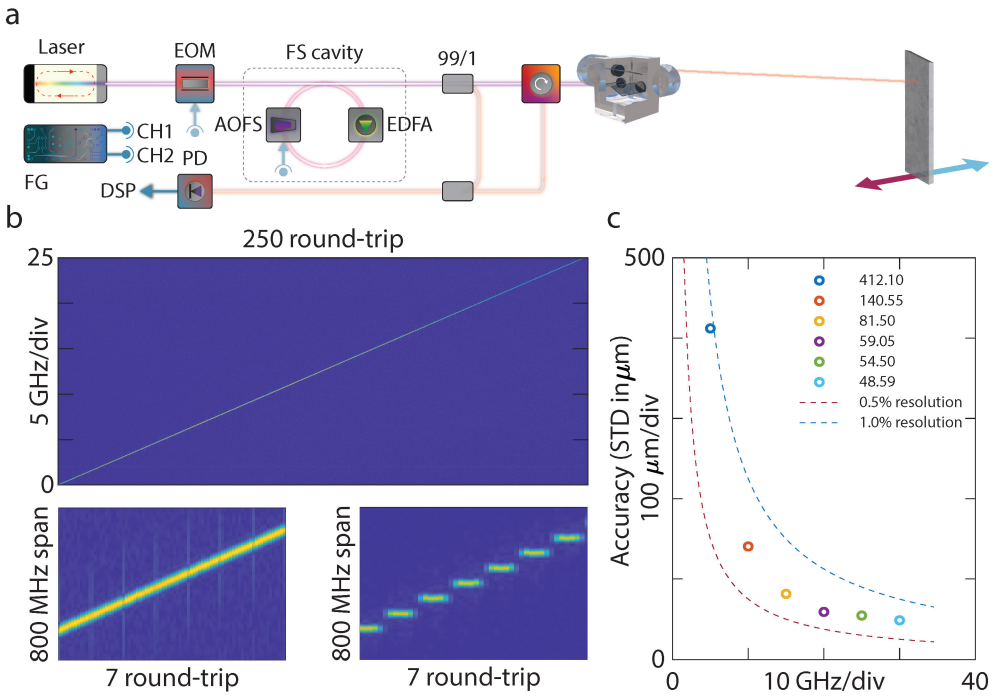


**Figure 7.3:** Utilising the stitched chirp signal for laser ranging and detection. **(a)** Experimental arrangement for range detection. **(b)** Time-frequency domain examination of the stitched chirp signal, featuring an enlarged version in the bottom left corner and a stepped-frequency signal on the right for comparison. **(c)** Ranging precision outcomes for signals with bandwidths of 5, 10, 15, 20, 25, and 30 GHz, assessed through 1000 repeated ranging measurements and quantified via standard deviation.

have provided valuable insights into the system's capabilities and potential applications within the context of industrial inspection and quality assurance.

Nonetheless, based on this approach, the current system presents several issues that require further attention. One such issue is the phase discontinuity of the synthesised chirp waveform, which refers to the phase discontinuity between two adjacent synthesised time-domain waveforms. This issue results in the demodulated signal not being a continuous sine wave (see Appendix B), necessitating the use of additional digital signal processing methods for coherent stitching [235, 236].

For successful and accurate coherent stitching, two conditions must be met. Firstly, the subpulse's dwell time should be long enough to accommodate multiple oscillating periods of the demodulated sine wave signals. This ensures sufficient data length for time-domain interpolation and successful time-domain stitching. While increasing the sampling

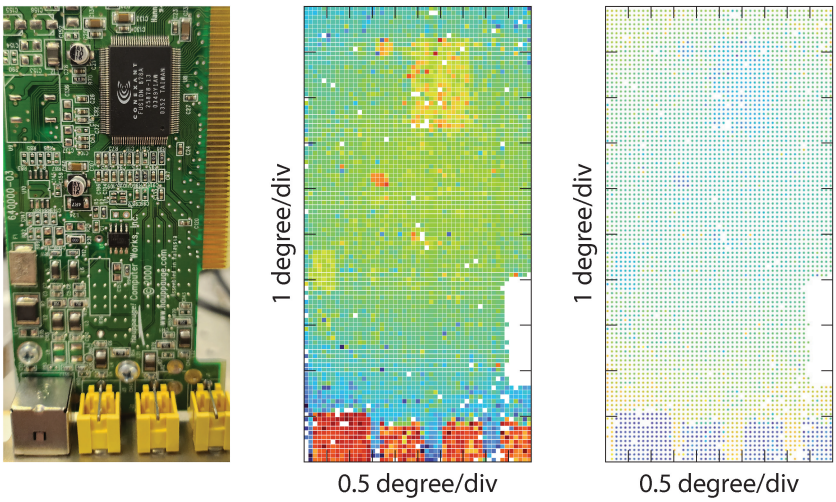


**Figure 7.4:** Demonstration of 2D imaging of a PCB board utilising the generated chirp signal with a 10 GHz bandwidth.

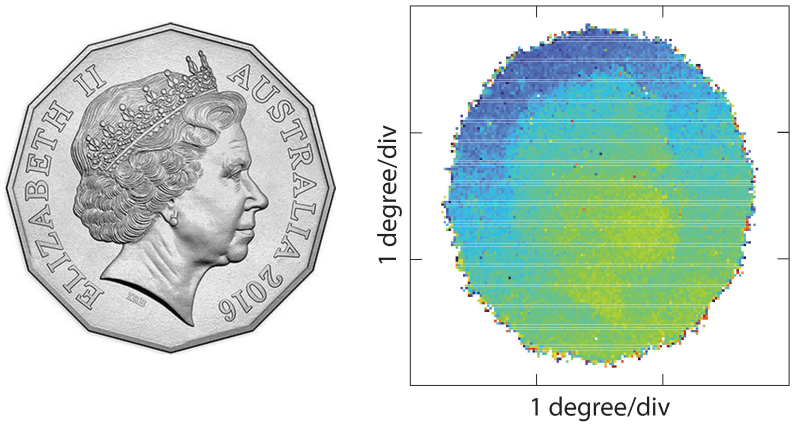


**Figure 7.5:** Demonstration of 2D imaging of a 50-cent coin utilising the generated chirp signal with a 90 GHz bandwidth.

rate could be helpful in this scenario, it may lead to longer processing times due to the generation of more data.

Secondly, the demodulated signal must possess an adequate SNR to maintain sensing accuracy. As discussed earlier, ranging accuracy represents a statistical distribution of multiple range detections around the true range. In the context of chirp-ranging settings, this implies that the demodulated signal's oscillating frequency is unstable or the SNR is poor. When utilising these demodulated signals to stitch a longer time-domain signal to improve range resolution, it is essential for these

sub-demodulated signals to have a sufficient SNR. Failing to meet this requirement may result in a stitched signal generating ranging results with extremely poor accuracy.

On the other hand, it is possible to extract the range information without resorting to digital stitching methods. However, the demodulated signal obtained after Fourier analysis exhibits several interferences. These interferences are primarily due to the phase discontinuity of the synthesised pulse, amplitude fluctuations caused by pulse recirculation within the fibre cavity, and noise accumulation through recirculation. As a result, the ambiguity range is further reduced, rendering the system impractical for real-world applications.

One potential solution involves employing digital stitching methods while utilising a reduced number of roundtrips and extended fibre cavity time to ensure successful stitching. It is crucial to highlight that, up to this point, the author has only succeeded in developing a stitching method that operates under restricted conditions. The LiDAR demonstration provided is based on the result of direct Fourier transforms with unidentified interference occurring in the frequency domain. Further research and development efforts are indispensable to surmount these limitations and improve the system's practicality and overall performance.

Therefore, utilising such a system to generate the stepped-frequency signal remains a favourable balance for maintaining the system's inherent advantages.

### 7.2.3 Photonic Radar On-chip Integration

The exhibited frequency-shifting loop possesses the capacity for integration onto a photonic chip. Considering the intricacy and practicality of the nanofabrication procedure, employing a reduced number of on-chip components is a more rational approach for subsequent proof-of-concept on-chip integration. Therefore, a schematic representation of the aforementioned frequency-shifting loop is depicted in Figure 7.6, encompassing a single laser, one optical gain element, an acousto-optic frequency shifter, and the requisite optical couplers.

Figure 7.6 illustrates the chip-scale frequency-shifting loop. Founded on a lithium niobate ($LiNbO_3$) platform [237, 238, 239], the on-chip signal generation procedure commences with an on-chip laser operating at 1550 nm, which can be modulated to alternate between producing a pulsed signal or functioning in continuous mode. Under the pulsed operational

mode, the on-chip system can generate the exhibited stepped-frequency signal. Simultaneously, the system could also produce chirp signals by regulating the phase correlation between the driving frequency of the acousto-optic frequency shifter and the round-trip duration of the on-chip cavity.

After the signal's frequency shift by the on-chip acousto-optic frequency shifter, it will be co-injected with a pump laser operating at 980 nm within an optical coupler. A low-loss taper shall be employed at this juncture to efficaciously couple the light from the chip's left side to its right side, entering a metre-scale erbium-doped aluminium oxide ($Al_2O_3$) waveguide to introduce on-chip gain [230, 166]. Following this, a portion of the amplified signal will be coupled out as the output via a grating coupler (g1), while the remainder will be redirected to the acousto-optic frequency shifter for subsequent recirculation.

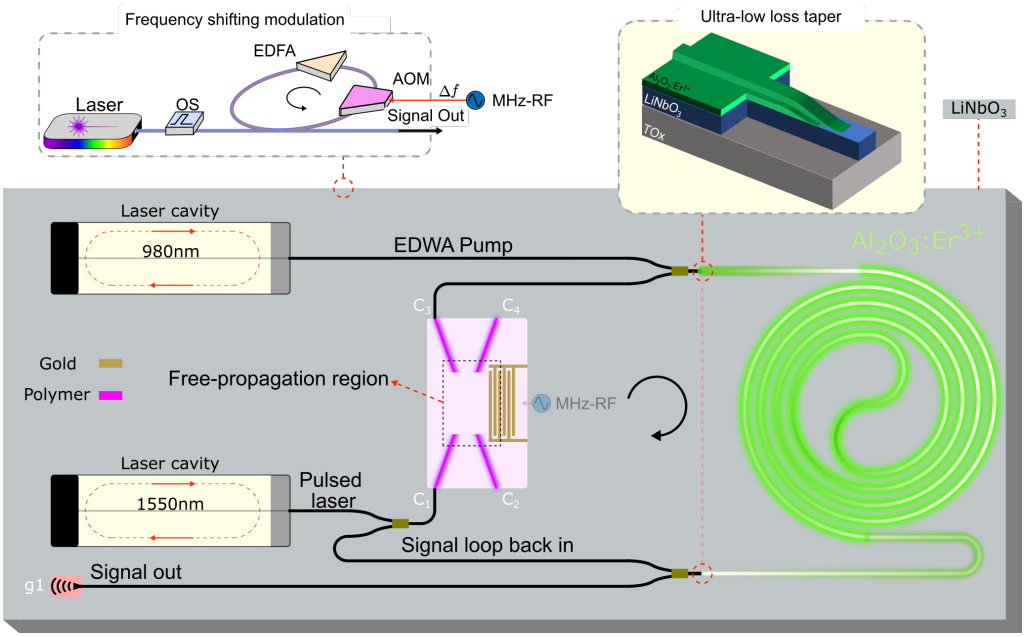


**Figure 7.6:** A schematic representation of an on-chip frequency-shifting loop, featuring an acousto-optic frequency shifter, an erbium-doped waveguide amplifier, and a laser cavity for efficient and compact design.

Nonetheless, such a design is challenging owing to numerous factors, excluding the fabrication process considerations, such as whether the on-chip waveguide amplifier would yield adequate gain to counter-

balance the optical loss and if the acousto-optic frequency shifter can introduce a frequency shift sufficiently small to ensure the generated stepped-frequency possesses an extended ambiguity range. Due to these factors, operating the on-chip frequency-shifting cavity might be a more favourable option in the mode for generating chirp signals. The metre-scale cavity holds the potential to introduce a round-trip time of approximately ten nanoseconds, thereby enabling the generated pulse with a sufficient pulse dwell time (ambiguity range, refer to Chapter 2) for near-range radar applications.

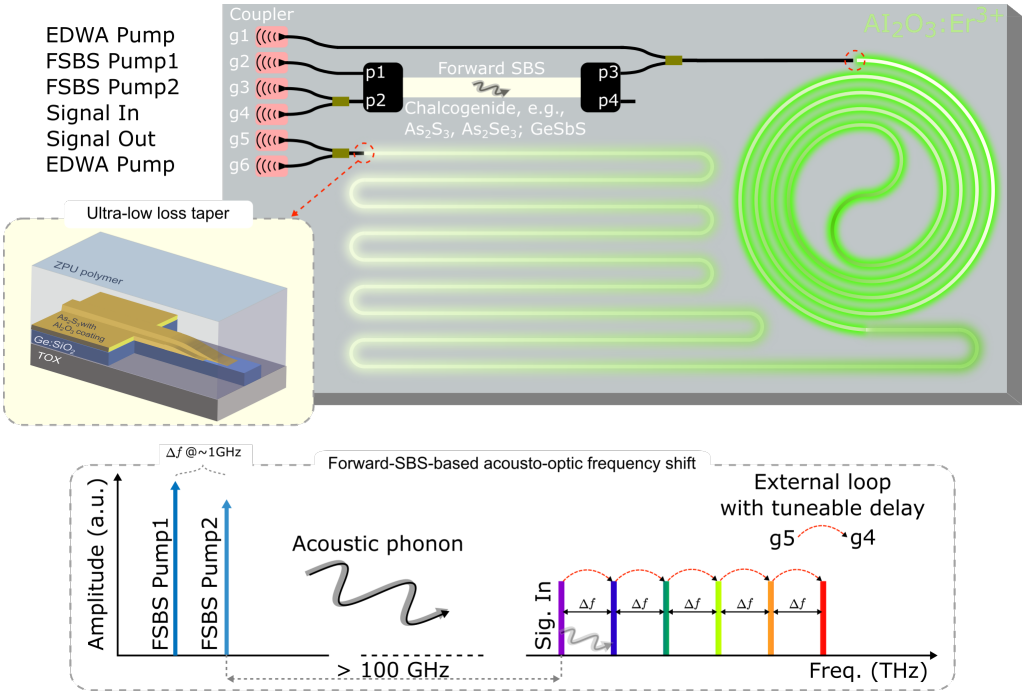


**Figure 7.7:** An on-chip frequency-shifting device leveraging forward-inter-mode stimulated Brillouin scattering, combined with integrated mode couplers and a waveguide amplifier for enhanced performance.

An interesting idea regarding the introduction of the frequency shift occurred during a discussion (with Dr Choon Kong Lai). Due to the fact that the phonon is the underlying cause of the frequency shift in an acousto-optic apparatus, we could generate the "sound wave" utilising an alternative non-linear optic phenomenon, specifically, Brillouin scattering.

The frequency-shifting procedure is predicated on forward-inter-mode stimulated Brillouin scattering (FIBS) and two-mode couplers [240, 241,

242]. This process commences with the injection of two optical pump signals from the grating couplers, g2 and g3. Simultaneously, the signal designated for frequency shifting is introduced via the grating coupler g4. The two optical pump signals, possessing distinct spatial modes and co-propagating through the chalcogenide waveguide, will induce a coherent acoustic oscillation. Therefore, the incoming signal at a different frequency (approximately 100 GHz higher than the pump signals) will experience an approximate one-gigahertz frequency shift due to the coherent acoustic oscillation resulting from electrostriction and radiation pressure. As the input signal is transmitted in the fundamental mode via the mode coupler at p2, the frequency-shifted signal will undergo a mode conversion attributable to the FIBS process, ultimately coupled through the mode coupler at p3.

This approach presents an array of advantages and challenges. On the positive side, the FISB-based methodology constitutes an all-optical platform, eliminating the need to employ RF signals or EOMs and reducing the device's complexity. However, the design necessitates narrow waveguides prone to side-wall scattering loss, resulting in higher insertion loss. Additionally, on-chip FISB has not been previously demonstrated utilising chalcogenide materials, rendering the performance uncertain. Moreover, mode couplers serve as key components within this approach, augmenting design complexity and increasing insertion loss.

From the perspective of radar sensing, the generated signal displays a frequency shift of approximately 1 GHz, equal to an ambiguity range of 15 centimetres. This range is unsuitable for the majority of radar applications. Therefore, as previously discussed, the time-domain stitching method or other ambiguity-range broadening techniques become necessary.

### 7.2.4 Photonic Radar as Part of Sensor Fusion and its Potentials

Contemporary sensing applications, such as autonomous vehicles, vital sign detection, and situational awareness in healthcare and aged care environments, pose considerable challenges for single-sensor-based systems. For example, while cameras are essential in autonomous driving and function as the primary sensors within such systems, their utility is often supplemented by additional sensors, such as radar [243, 244]. This intended sensor redundancy enhances the reliability of driving-related decision-making, particularly in scenarios where cameras exhibit vulner-

ability under specific conditions, including inclement weather or reduced visibility due to rain and fog.

Sensor fusion combines data from various sensors, enhancing accuracy and reliability and yielding a comprehensive environmental understanding beyond individual sensors' capability. This integration bolsters system robustness, advancing precision and efficacy across applications. For instance, radar-camera sensor fusion enables comprehensive patient monitoring in healthcare, facilitating prompt emergency response and intervention coordination. Moreover, this multi-sensor approach mitigates inherent limitations of single sensors, such as false alarms, ensuring a resilient and dependable system across varied applications.

Photonic radar, as a technology demonstrating superiority over conventional radar systems, offering numerous advantages, such as spectrum flexibility, the capacity for multi-band operation without the need for parallel electronic architectures, and distributed sensing capabilities enabled by optical fibre networks, faces both opportunities and challenges within the context of future sensor fusion networks.

Photonic radar's inherent properties offer unique opportunities, including spectrum usage flexibility for dynamic resource allocation, supporting various sensing applications and enabling seamless network integration. Its ability to operate across multiple bands without relying on parallel electronic architectures reduces system complexity and enhances reliability and scalability. Optical fibre networks' distributed sensing capabilities open new paths for advanced, real-time monitoring over large geographical areas, which is crucial for healthcare, aged care and custodial settings. Leveraging photonic radar can thus enhance situational awareness, data-informed decision-making and overall performance in these sectors.

Despite the opportunities mentioned above, photonic radar encounters specific challenges concerning its integration into future sensor fusion networks. One such challenge pertains to cost and power efficiency considerations, which necessitate addressing to promote the widespread adoption of photonic radar systems. This work is contingent upon developing cost-effective basic photonic building blocks, including lasers, electro-optical modulators, and photodetectors. Additionally, constraints on the availability of the RF spectrum may hinder photonic radar from fully realising its potential in terms of wideband, high-resolution, and multi-band operation.

Integrating high-performance photonic radar with infrared and camera technologies can significantly enhance system robustness for diverse

applications. The proposed system, combining vital sign radar with cameras, can be utilised in various contexts via advanced algorithms. It can monitor, predict, and alert to harmful behaviours in custodial settings, facilitating timely intervention. It can also be implemented in aged care facilities to counteract labour shortages (see Appendix C) and for livestock management in agriculture (see Appendix C). Integrating photonic radar with other sensor technologies provides versatile, resilient solutions tailored to various application domains' unique needs and challenges.

### 7.2.5 Photonics for Terahertz Radar Imaging

High-quality terahertz (THz) signals with superior frequency stability and accuracy are needed for many applications. THz sources demonstrating high-precision and low-phase noise are necessary for telecommunications to enable high-throughput and high data-density transmission facilitated by higher-order quadrature amplitude modulation (QAM) [245, 246]. These advancements' significance becomes particularly attractive within the context of the forthcoming next-generation (6G) communications systems. Furthermore, the generation of wide-band THz radar signals, distinguished by high signal quality parameters such as an optimal SNR and time-frequency linearity, presents an opportunity to advance THz radar imaging applications [247, 94, 248]. The scope of these applications is broad such as security inspection, production line quality control measures, and the quantification of material thickness [249, 250]. Therefore, the value of generating robust and stable THz signals underpins applications across various industries.

Photonics-assisted methods have recently gained significant interest in THz radar sensing. Two central factors primarily drive this attention: 1) the extensive optical fractional bandwidth and 2) the advancement of crucial photonic building blocks and components that facilitate THz radar applications. The principle of photonics-based THz wave synthesis is well-established, leveraging the optical spectrum and utilising photonic components and techniques, for instance, sweeping lasers. Simultaneously, the direct optical heterodyning technique for generating THz waves is feasible through photomixers, such as uni-travelling-carrier photodiodes (UTC-PDs) [251] and ultra-high-speed p-i-n photodiodes [252].

Further enhancing the field is the implementation of THz detectors, such as the Fermi-level managed barrier diode (FMBD) [253]. These detectors

can directly mix a proportion of the transmitted and received radar signal within the THz domain, generating a low-frequency beat RF signal that can be processed using low-speed analogue-to-digital converters. This method replaces the conventional RF down-conversion-based radar coherent detection scheme, which typically employs RF mixers and a THz oscillator to down-convert the THz wave, followed by sampling through an ultra-high-speed real-time oscilloscope [121]. Adopting direct mixing in the THz domain not only simplifies the architecture of the radar receiver but also notably enhances the receiver's SNR and overall radar performance. This improvement avoids the need for multi-stage RF mixings, offering a more streamlined and efficient system.

A viable approach for generating high-quality, wideband THz radar signals involves using an optical frequency comb source [90, 91, 92] combined with the proposed frequency-shifting loop. Two comb teeth can be selected via an optical bandpass filter and directed into the frequency-shifting loop to generate two broadband SF signals simultaneously. Another comb tooth can be selected, mixed with the dual-band SF signals, and subsequently beaten in a photodiode, such as a UTC-PD. The radar signal is transmitted by an antenna, typically a high-gain, directional horn antenna. The free-space THz system encompasses two paths [254]: the reference and detection paths. The signals reflected from both these paths are combined and forwarded to a THz receiver, for instance, an FMDB, for analysis.

Adopting an optical frequency comb in generating THz radar signals offers several benefits. First, the high coherence linked with the comb teeth significantly mitigates phase noise within the radar signal, resulting in enhanced sensing performance when up-converting the dual-band (or multi-band) SF signal to the THz domain. Second, this approach facilitates fully exploiting the unlicensed THz spectrum, thus ensuring superior radar resolution and accuracy. Moreover, the multi-band THz radar signal avoids absorption peaks, such as the atmospheric absorption around 550 GHz [248]. In pair with other advanced techniques, such as an electro-optic phase-lock loop [255], it becomes possible to synthesise ultra-stable THz signals. Collectively, these advantages contribute to elevating the performance of the photonic THz radar system, driving it towards achieving superior operational efficiency and expanded capabilities for radar applications.

# Bibliography


[1] Z. Zhang, Y. Liu, M. Burla, and B. J. Eggleton, "5.6-GHz-Bandwidth Photonic Stepped-Frequency Radar using MHz-level Frequency-Shifting Modulation", in *Conference on Lasers and Electro-Optics*, Optica Publishing Group, 2020, AF3M.5.

[2] ——, "Centimetre-Spatial-Resolution Photonics-Based Stepped-Frequency Radar: Implementation and Comparison", in *14th Pacific Rim Conference on Lasers and Electro-Optics (CLEO PR 2020)*, .: Optica Publishing Group, 2020, C6C_2.

[3] Y. Liu, Z. Zhang, M. Burla, and B. J. Eggleton, "11-GHz-Bandwidth Photonic Radar using MHz Electronics", *Laser & Photonics Reviews*, vol. 16, no. 4, p. 2 100 549, Apr. 2022.

[4] Z. Zhang, Y. Liu, and B. J. Eggleton, "Photonic Generation of 30 GHz Bandwidth Stepped-Frequency Signals for Radar Applications", *Journal of Lightwave Technology*, vol. 40, no. 14, pp. 4521–4527, Jul. 2022.

[5] Z. Zhang, Y. Liu, T. Stephens, and B. J. Eggleton, "Photonic Radar for Contactless Vital Sign Detection", 2022. DOI: 10.1038/s41566-023-01245-6100.

[6] ——, "Broadband Photonic Radar Enabling Millimeter Resolution for Vital Sign Detection", in *2023 Conference on Lasers and Electro-Optics (CLEO)*, Optical Society of America., 2023, pp. 1–2.

[7] IEEE, "Standard Radar Definitions", *Ieee Std 686-2008*, vol. 1997, p. 38, 2008.

[8] T. S. Wolters and L. Brown, "A Radar History of World War II: Technical and Military Imperatives", *The Journal of Military History*, vol. 66, no. 1, p. 235, Jan. 2002.

[9] H. Griffiths, P. Knott, and W. Koch, "Christian Hülsmeyer: Invention and Demonstration of Radar, 1904", *IEEE Aerospace and Electronic Systems Magazine*, vol. 34, no. 9, pp. 56–60, Sep. 2019, ISSN: 0885-8985. DOI: 10.1109/MAES.2019.2934814. [Online]. Available: https://ieeexplore.ieee.org/document/8826668/.

[10] R. A. Watson-Watt, *The Pulse of Radar: The Autobiography of Sir Robert Watson-Watt*. Dial Press, 1959.

[11] J. R. Klauder, A. C. Price, S. Darlington, and W. J. Albersheim, "The Theory and Design of Chirp Radars", *Bell System Technical Journal*, vol. 39, no. 4, pp. 745–808, Jul. 1960, ISSN: 00058580.

[12] J. Otto, "Radar applications in level measurement, distance measurement and nondestructive material testing", in *1997 27th European Microwave Conference*, vol. 2, IEEE, 1997, pp. 1113–1121.

[13] C. Wiley, "Synthetic Aperture Radars", *IEEE Transactions on Aerospace and Electronic Systems*, vol. AES-21, no. 3, pp. 440–443, May 1985, ISSN: 0018-9251.

[14] A. Moreira, P. Prats-Iraola, M. Younis, G. Krieger, I. Hajnsek, and K. P. Papathanassiou, "A tutorial on synthetic aperture radar", *IEEE Geoscience and Remote Sensing Magazine*, vol. 1, no. 1, pp. 6–43, Mar. 2013.

[15] R. F. Rincon, M. A. Vega, M. Buenfil, A. Geist, L. Hilliard, and P. Racette, "NASA's L-Band Digital Beamforming Synthetic Aperture Radar", *IEEE Transactions on Geoscience and Remote Sensing*, vol. 49, no. 10, pp. 3622–3628, Oct. 2011, ISSN: 0196-2892.

[16] C. Ozdemir, *Inverse Synthetic Aperture Radar Imaging with MATLAB Algorithms*. Hoboken, UNITED STATES: John Wiley & Sons, Incorporated, 2012, pp. 121–125.

[17] R. J. Mailloux, *Phased array antenna handbook*. Artech house, 2017, ISBN: 163081508X.

[18] T. B. Laboratories, "Integrated 6-bit photonic true-time-delay unit for lightweight 3-6 GHz radar beamformer", pp. 4–7, 1992.

[19] G. L. Tangonan, W. Ng, W. Walston, and J. J. Lee, "Optoelectronic Switching for Radar Steering", in, 1990, pp. 391–394.

[20] C. Lim, A. Nirmalathas, M. Bakaul, P. Gamage, Ka-Lun Lee, Yizhuo Yang, D. Novak, and R. Waterhouse, "Fiber-Wireless Networks and Subsystem Technologies", *Journal of Lightwave Technology*, vol. 28, no. 4, pp. 390–405, Feb. 2010, ISSN: 0733-8724. DOI: 10.1109/JLT.2009.2031423. [Online]. Available: http://ieeexplore.ieee.org/document/5229310/.

[21] D. Novak, R. B. Waterhouse, A. Nirmalathas, C. Lim, P. A. Gamage, T. R. Clark, M. L. Dennis, and J. A. Nanzer, "Radio-Over-Fiber Technologies for Emerging Wireless Systems", *IEEE Journal of Quantum Electronics*, vol. 52, no. 1, pp. 1–11, Jan. 2016, ISSN: 0018-9197. DOI: 10.1109/JQE.2015.2504107. [Online]. Available: http://ieeexplore.ieee.org/document/7339428/.

[22] A. J. Seeds and K. J. Williams, "Microwave Photonics", *Journal of Lightwave Technology*, vol. 24, no. 12, pp. 4628–4641, Dec. 2006, ISSN: 0733-8724. DOI: 10.1109/JLT.2006.885787. [Online]. Available: http://ieeexplore.ieee.org/document/4063431/.

[23] J. Capmany and D. Novak, "Microwave photonics combines two worlds", *Nature Photonics*, vol. 1, no. 6, pp. 319–330, Jun. 2007, ISSN: 1749-4885. DOI: 10.1038/nphoton.2007.89. [Online]. Available: http://www.nature.com/articles/nphoton.2007.89.

[24] J. Yao, "Microwave Photonics", *Journal of Lightwave Technology*, vol. 27, no. 3, pp. 314–335, Feb. 2009, ISSN: 0733-8724. DOI: 10.1109/JLT.2008.2009551. [Online]. Available: http://ieeexplore.ieee.org/document/4785283/.

[25] T. Berceli and P. R. Herczfeld, "Microwave Photonics—A Historical Perspective", *IEEE Transactions on Microwave Theory and Techniques*, vol. 58, no. 11, pp. 2992–3000, Nov. 2010, ISSN: 0018-9480. DOI: 10.1109/TMTT.2010.2076932. [Online]. Available: http://ieeexplore.ieee.org/document/5606211/.

[26] D. Marpaung, M. Pagani, B. Morrison, and B. J. Eggleton, "Nonlinear Integrated Microwave Photonics", *Journal of Lightwave Technology*, vol. 32, no. 20, pp. 3421–3427, Oct. 2014, ISSN: 0733-8724. DOI: 10.1109/JLT.2014.2306676. [Online]. Available: http://ieeexplore.ieee.org/document/6744594/.

[27] J. E. Bowers, "Integrated microwave photonics", in *2015 International Topical Meeting on Microwave Photonics (MWP)*, IEEE, Oct. 2015, pp. 1–4, ISBN: 978-1-4673-9368-3. DOI: 10.1109/MWP.2015.7356697. [Online]. Available: http://ieeexplore.ieee.org/document/7356697/.

[28] P. Ghelfi, F. Laghezza, F. Scotti, G. Serafino, A. Capria, S. Pinna, D. Onori, C. Porzi, M. Scaffardi, A. Malacarne, V. Vercesi, E. Lazzeri, F. Berizzi, and A. Bogoni, "A fully photonics-based coherent radar system", *Nature*, vol. 507, no. 7492, pp. 341–345, 2014.

[29] P. Ghelfi, F. Laghezza, F. Scotti, G. Serafino, S. Pinna, D. Onori, E. Lazzeri, and A. Bogoni, "Photonics in radar systems: RF integration for state-of-the-art functionality", *IEEE Microwave Magazine*, vol. 16, no. 8, pp. 74–83, 2015.

[30] S. Pan and Y. Zhang, "Microwave Photonic Radars", *Journal of Lightwave Technology*, vol. 38, no. 19, pp. 5450–5484, Oct. 2020.

[31] J. C. Stover, "Optical scattering. Measurement and analysis", *SPIE Press Volume*, 1995.

[32] C. F. Bohren and D. R. Huffman, *Absorption and scattering of light by small particles*. John Wiley & Sons, 2008, ISBN: 3527618163.

[33] A. T. Young, "Rayleigh scattering", *Applied Optics*, vol. 20, no. 4, p. 533, Feb. 1981.

[34] E. F. Knott, J. F. Shaeffer, and M. T. Tuley, *Radar Cross Section, 2nd ed*, 1993.

[35] E. F. Knott, *Radar cross section measurements*. Springer Science & Business Media, 2012, ISBN: 1468499041.

[36] H.-J. Li and Y.-W. Kiang, "Radar and Inverse Scattering", in *The Electrical Engineering Handbook*, Elsevier, 2005, pp. 671–690.

[37] M. I. Skolnik, *Radar handbook*. McGraw-Hill Education, 2008, ISBN: 0071485473.

[38] M. I. Skolnik, "Introduction to radar systems", *New York*, 1980.

[39] N. Levanon, "Radar principles", *New York*, 1988.

[40] S. Watts, "Radar detection prediction in K-distributed sea clutter and thermal noise", *IEEE Transactions on Aerospace and Electronic Systems*, no. 1, pp. 40–45, 1987, ISSN: 0018-9251.

[41] B. Edde, "Radar- Principles, technology, applications((Book))", *Englewood Cliffs, NJ, Prentice Hall, 1993, 729*, 1993.

[42] K. Kikuchi, "Fundamentals of coherent optical fiber communications", *Journal of Lightwave Technology*, vol. 34, no. 1, pp. 157–179, 2016, ISSN: 07338724. DOI: 10.1109/JLT.2015.2463719.

[43] M. Carrick, N. Grumman, D. Jaeger, N. Grumman, S. Diego, and S. Diego, "Design and Application of a Hilbert Transformer in a Digital Receiver", *Proceedings of the SDR 11 Technical Conference and Product Exposition*, pp. 1–7, 2011.

[44] C. Nguyen and J. Park, *Stepped-frequency radar sensors: Theory, analysis and design*. Springer, 2016, pp. 52–53, ISBN: 3319122711.

[45] D. A. Noon, "Stepped-frequency radar design and signal processing enhances ground penetrating radar performance", 1996.

[46] S. Pinna, S. Melo, F. Laghezza, F. Scotti, E. Lazzeri, M. Scaffardi, P. Ghelfi, and A. Bogoni, "Photonics-Based Radar for Sub-mm Displacement Sensing", *IEEE Journal of Selected Topics in Quantum Electronics*, vol. 23, no. 2, pp. 168–175, 2017.

[47] A. Freedman, R. Bose, and B. Steinberg, "Thinned stepped frequency waveforms to furnish existing radars with imaging capability", *IEEE Aerospace and Electronic Systems Magazine*, vol. 11, no. 11, pp. 39–43, 1996.

[48] Q. Zhang and Y.-Q. Jin, "Aspects of Radar Imaging Using Frequency-Stepped Chirp Signals", *EURASIP Journal on Advances in Signal Processing*, vol. 2006, no. 1, p. 085 823, Dec. 2006.

[49] Ying Luo, Qun Zhang, Cheng-wei Qiu, Xian-jiao Liang, and Kai-ming Li, "Micro-Doppler Effect Analysis and Feature Extraction in ISAR Imaging With Stepped-Frequency Chirp Signals", *IEEE Transactions on Geoscience and Remote Sensing*, vol. 48, no. 4, pp. 2087–2098, Apr. 2010.

[50] G. Liu, H. Sun, H. Gu, and W. Su, "Development of random signal radars", *Shu Ju Cai Ji Yu Chu Li/Journal of Data Acquisition and Processing*, vol. 16, no. 1, pp. 5–9, 2001, ISSN: 10049037.

[51] Z. LIU, X. ZHU, W. HU, and F. JIANG, "PRINCIPLES OF CHAOTIC SIGNAL RADAR", *International Journal of Bifurcation and Chaos*, vol. 17, no. 05, pp. 1735–1739, May 2007.

[52] H. Leung, "Applying chaos to radar detection in an ocean environment: an experimental study", *IEEE Journal of Oceanic Engineering*, vol. 20, no. 1, pp. 56–64, 1995.

[53] S. Haykin and Xiao Bo Li, "Detection of signals in chaos", *Proceedings of the IEEE*, vol. 83, no. 1, pp. 95–122, 1995.

[54] A. Bauer, T. Kilias, and W. Schwarz, "Chaotic bit stream generators for pulsstream radar application", in *Proc. 5th Int. Workshop Nonlinear Dynamics of Electronic Systems (NDES-1997)*, 1997, p. 410.

[55] V. Venkatasubramanian and H. Leung, "A novel chaos-based high-resolution imaging technique and its application to through-the-wall imaging", *IEEE Signal Processing Letters*, vol. 12, no. 7, pp. 528–531, 2005, ISSN: 10709908. DOI: 10.1109/LSP.2005.849497.

[56] R. W. Yeung, *A first course in information theory*. Springer Science & Business Media, 2002, ISBN: 0306467917.

[57] S. Axelsson, "Noise radar for range/doppler processing and digital beamforming using low-bit adc", *IEEE Transactions on Geoscience and Remote Sensing*, vol. 41, no. 12, pp. 2703–2720, Dec. 2003.

[58] K. Cuomo, A. Oppenheim, and S. Strogatz, "Synchronization of Lorenz-based chaotic circuits with applications to communications", *IEEE Transactions on Circuits and Systems II: Analog and Digital Signal Processing*, vol. 40, no. 10, pp. 626–633, 1993.

[59] A. Lukashchuk, J. Riemensberger, A. Tusnin, J. Liu, and T. Kippenberg, "Chaotic micro-comb based parallel ranging", Dec. 2021. DOI: https://doi.org/10.48550/arXiv.2112.1024. [Online]. Available: http://arxiv.org/abs/2112.10241.

[60] A. Lukashchuk, J. Riemensberger, A. Stroganov, G. Navickaite, and T. J. Kippenberg, "Chaotic microcomb inertia-free parallel ranging", *APL Photonics*, vol. 8, no. 5, May 2023, ISSN: 2378-0967. DOI: 10.1063/5.0141384. [Online]. Available: https://pubs.aip.org/app/article/8/5/056102/2887792/Chaotic-microcomb-inertia-free-parallel-ranging.

[61] R. Chen, H. Shu, B. Shen, L. Chang, W. Xie, W. Liao, Z. Tao, J. E. Bowers, and X. Wang, "Breaking the temporal and frequency congestion of LiDAR by parallel chaos", *Nature Photonics*, vol. 17, no. 4, pp. 306–314, Apr. 2023, ISSN: 1749-4885. DOI: 10.1038/s41566-023-01158-4. [Online]. Available: https://www.nature.com/articles/s41566-023-01158-4.

[62] P. Kylemark, M. Karlsson, T. Torounidis, and P. A. Andrekson, "Noise statistics of fiber optical parametric amplifiers", *2006 Optical Fiber Communication Conference, and the 2006 National Fiber Optic Engineers Conference*, vol. 2006, no. 2, pp. 409–416, 2006. DOI: 10.1109/ofc.2006.215650.

[63] T. Yao, D. Zhu, D. Ben, and S. Pan, "Distributed MIMO chaotic radar based on wavelength-division multiplexing technology", *Optics Letters*, vol. 40, no. 8, p. 1631, Apr. 2015, ISSN: 0146-9592. DOI: 10.1364/ol.40.001631.

[64] V. C. Chen and M. Martorella, "Inverse synthetic aperture radar", *SciTech Publishing*, vol. 55, p. 56, 2014.

[65] Genyuan Wang, X.-g. Xia, and V. Chen, "Three-dimensional ISAR imaging of maneuvering targets using three receivers", *IEEE Transactions on Image Processing*, vol. 10, no. 3, pp. 436–447, Mar. 2001.

[66] M. Martorella, "Novel approach for ISAR image cross-range scaling", *IEEE Transactions on Aerospace and Electronic Systems*, vol. 44, no. 1, pp. 281–294, Jan. 2008.

[67] J. Zheng, T. Su, W. Zhu, L. Zhang, Z. Liu, and Q. H. Liu, "ISAR Imaging of Nonuniformly Rotating Target Based on a Fast Parameter Estimation Algorithm of Cubic Phase Signal", *IEEE Transactions on Geoscience and Remote Sensing*, vol. 53, no. 9, pp. 4727–4740, Sep. 2015.

[68] T. H. Lee, *The design of CMOS radio-frequency integrated circuits*. Cambridge university press, 2003, ISBN: 1139643770.

[69] S. Voinigescu, *High-frequency integrated circuits*. Cambridge University Press, 2013, ISBN: 110731061X.

[70] G. D. Vendelin, A. M. Pavio, U. L. Rohde, and M. Rudolph, *Microwave circuit design using linear and nonlinear techniques*. John Wiley & Sons, 2021, ISBN: 1118449754.

[71] M. Vasconcelos, P. Nallabolu, and C. Li, "Range Resolution Improvement in FMCW Radar Through VCO's Nonlinearity Compensation", in *2023 IEEE Topical Conference on Wireless Sensors and Sensor Networks*, IEEE, 2023, pp. 53–56.

[72] X. Zhang, J. Pouls, and M. C. Wu, "Laser frequency sweep linearization by iterative learning pre-distortion for FMCW LiDAR", *Optics Express*, vol. 27, no. 7, p. 9965, Apr. 2019.

[73] H. Lotsch, "Theory of nonlinear distortion produced in a semiconductor diode", *IEEE Transactions on Electron Devices*, vol. 15, no. 5, pp. 294–307, May 1968.

[74] Z. Tang, Y. Li, J. Yao, and S. Pan, "Photonics-Based Microwave Frequency Mixing: Methodology and Applications", *Laser and Photonics Reviews*, vol. 14, no. 1, pp. 1–25, 2020.

[75] V. J. Urick, J. D. McKinney, and K. J. Williams, *Fundamentals of Microwave Photonics*. 2015, ISBN: 9780470575406.

[76] J. Yao, "Microwave Photonics", *Journal of Lightwave Technology*, vol. 27, no. 3, pp. 314–335, Feb. 2009, ISSN: 0733-8724. DOI: 10.1109/JLT.2008.2009551.

[77] D. Marpaung, J. Yao, and J. Capmany, "Integrated microwave photonics", *Nature Photonics*, vol. 13, no. 2, pp. 80–90, Feb. 2019, ISSN: 1749-4885. DOI: 10.1038/s41566-018-0310-5. [Online]. Available: http://www.nature.com/articles/s41566-018-0310-5.

[78] I. Hayashi, M. B. Panish, P. W. Foy, and S. Sumski, "JUNCTION LASERS WHICH OPERATE CONTINUOUSLY AT ROOM TEMPERATURE", *Applied Physics Letters*, vol. 17, no. 3, pp. 109–111, Aug. 1970.

[79] J. Faist, F. Capasso, D. L. Sivco, C. Sirtori, A. L. Hutchinson, and A. Y. Cho, "Quantum Cascade Laser", *Science*, vol. 264, no. 5158, pp. 553–556, Apr. 1994, ISSN: 0036-8075. DOI: 10.1126/science.264.5158.553. [Online]. Available: https://www.science.org/doi/10.1126/science.264.5158.553.

[80] H. Melchior, "Detectors for lightwave communication", *Physics Today*, vol. 30, no. 11, pp. 32–39, Nov. 1977.

[81] M. Long, P. Wang, H. Fang, and W. Hu, "Progress, Challenges, and Opportunities for 2D Material Based Photodetectors", *Advanced Functional Materials*, vol. 29, no. 19, p. 1 803 807, May 2019, ISSN: 1616-301X. DOI: 10.1002/adfm.201803807. [Online]. Available: https://onlinelibrary.wiley.com/doi/10.1002/adfm.201803807.

[82] A. Seeds, "Microwave photonics", *IEEE Transactions on Microwave Theory and Techniques*, vol. 50, no. 3, pp. 877–887, Mar. 2002, ISSN: 00189480. DOI: 10.1109/22.989971. [Online]. Available: http://ieeexplore.ieee.org/document/989971/.

[83] J. MacChesney, P. O'Connor, and H. Presby, "A new technique for the preparation of low-loss and graded-index optical fibers", *Proceedings of the IEEE*, vol. 62, no. 9, pp. 1280–1281, 1974, ISSN: 0018-9219.

[84] W. E. Martin, "A new waveguide switch/modulator for integrated optics", *Applied Physics Letters*, vol. 26, no. 10, pp. 562–564, May 1975, ISSN: 0003-6951.

[85] P. Ghelfi, F. Laghezza, F. Scotti, D. Onori, and A. Bogoni, "Photonics for Radars Operating on Multiple Coherent Bands", *Journal of Lightwave Technology*, vol. 34, no. 2, pp. 500–507, 2016.

[86] S. Pan and J. Yao, "Photonics-Based Broadband Microwave Measurement", *Journal of Lightwave Technology*, vol. 35, no. 16, pp. 3498–3513, Aug. 2017.

[87] G. Serafino, F. Scotti, L. Lembo, B. Hussain, C. Porzi, A. Malacarne, S. Maresca, D. Onori, P. Ghelfi, and A. Bogoni, "Toward a new generation of radar systems based on microwave photonic technologies", *Journal of Lightwave Technology*, vol. 37, no. 2, pp. 643–650, 2019.

[88] J. Capmany, B. Ortega, and D. Pastor, "A tutorial on microwave photonic filters", *Journal of Lightwave Technology*, vol. 24, no. 1, pp. 201–229, Jan. 2006.

[89] Y. Liu, A. Choudhary, D. Marpaung, and B. J. Eggleton, "Integrated microwave photonic filters", *Advances in Optics and Photonics*, vol. 12, no. 2, p. 485, Jun. 2020, ISSN: 1943-8206. DOI: 10.1364/AOP.378686.

[90] N. Picqué and T. W. Hänsch, "Frequency comb spectroscopy", *Nature Photonics*, vol. 13, no. 3, pp. 146–157, Mar. 2019.

[91] A. Parriaux, K. Hammani, and G. Millot, "Electro-optic frequency combs", *Advances in Optics and Photonics*, vol. 12, no. 1, p. 223, Mar. 2020.

[92] L. Chang, S. Liu, and J. E. Bowers, "Integrated optical frequency comb technologies", *Nature Photonics*, vol. 16, no. 2, pp. 95–108, Feb. 2022.

[93] K. Ho, J. Walker, and J. Kahn, "External optical feedback effects on intensity noise of vertical-cavity surface-emitting lasers", *IEEE Photonics Technology Letters*, vol. 5, no. 8, pp. 892–895, Aug. 1993, ISSN: 1041-1135. DOI: 10.1109/68.238245. [Online]. Available: http://ieeexplore.ieee.org/document/238245/.

[94] E. A. Kittlaus, D. Eliyahu, S. Ganji, S. Williams, A. B. Matsko, K. B. Cooper, and S. Forouhar, "A low-noise photonic heterodyne synthesizer and its application to millimeter-wave radar", *Nature Communications*, vol. 12, no. 1, p. 4397, Jul. 2021, ISSN: 2041-1723. DOI: 10.1038/s41467-021-24637-0. [Online]. Available: https://www.nature.com/articles/s41467-021-24637-0.

[95] S. Jia, M.-C. Lo, L. Zhang, O. Ozolins, A. Udalcovs, D. Kong, X. Pang, R. Guzman, X. Yu, S. Xiao, S. Popov, J. Chen, G. Carpintero, T. Morioka, H. Hu, and L. K. Oxenløwe, "Integrated dual-laser photonic chip for high-purity carrier generation enabling ultrafast terahertz wireless communications", *Nature Communications*, vol. 13, no. 1, p. 1388, Mar. 2022, ISSN: 2041-1723. DOI: 10.1038/s41467-022-29049-2. [Online]. Available: https://www.nature.com/articles/s41467-022-29049-2.

[96] T. Legero, D. G. Matei, S. Häfner, C. Grebing, R. Weyrich, F. Riehle, U. Sterr, W. Zhang, J. Robinson, L. Sonderhouse, E. Oelker, and J. Ye, "1.5 $\mu$m Lasers with sub 10 mHz Linewidth", in *Conference on Lasers and Electro-Optics*, Washington, D.C.: OSA, 2017, SW1J.1, ISBN: 978-1-943580-27-9. DOI: 10.1364/CLEO{_}SI.2017.SW1J.1. [Online]. Available: https://opg.optica.org/abstract.cfm?URI=CLEO_SI-2017-SW1J.1.

[97] D. Hall, A. Yariv, and E. Garmire, "Optical Guiding and electro-optic modulation in GaAs epitaxial layers", *Optics Communications*, vol. 1, no. 9, pp. 403–405, Apr. 1970, ISSN: 00304018. DOI: 10.1016/0030-4018(70)90163-X. [Online]. Available: https://linkinghub.elsevier.com/retrieve/pii/003040187090163X.

[98] Y. Shi, C. Zhang, H. Zhang, J. H. Bechtel, L. R. Dalton, B. H. Robinson, and W. H. Steier, "Low (Sub-1-Volt) Halfwave Voltage Polymeric Electro-optic Modulators Achieved by Controlling Chromophore Shape", *Science*, vol. 288, no. 5463, pp. 119–122, Apr. 2000, ISSN: 0036-8075. DOI: 10.1126/science.288.5463.119. [Online]. Available: https://www.science.org/doi/10.1126/science.288.5463.119.

[99] Fang-Shang Chen, "Modulators for optical communications", *Proceedings of the IEEE*, vol. 58, no. 10, pp. 1440–1457, 1970, ISSN: 0018-9219. DOI: 10.1109/PROC.1970.7970. [Online]. Available: http://ieeexplore.ieee.org/document/1449900/.

[100] A. J. Mercante, S. Shi, P. Yao, L. Xie, R. M. Weikle, and D. W. Prather, "Thin film lithium niobate electro-optic modulator with terahertz operating bandwidth", *Optics Express*, vol. 26, no. 11, p. 14 810, May 2018, ISSN: 1094-4087. DOI: 10.1364/OE.26.014810. [Online]. Available: https://opg.optica.org/abstract.cfm?URI=oe-26-11-14810.

[101] H. Ito, T. Furuta, Y. Muramoto, T. Ito, and T. Ishibashi, "Photonic millimetre- and sub-millimetre-wave generation using J-band rectangular-waveguide-output uni-travelling-carrier photodiode module", *Electronics Letters*, vol. 42, no. 24, p. 1424, 2006, ISSN: 00135194. DOI: 10.1049/el:20063033. [Online]. Available: https://digital-library.theiet.org/content/journals/10.1049/el_20063033.

[102] J.-W. Shi, Y.-S. Wu, C.-Y. Wu, P.-H. Chiu, and C.-C. Hong, "High-speed, high-responsivity, and high-power performance of near-ballistic uni-traveling-carrier photodiode at 1.55-/spl mu/m wavelength", *IEEE Photonics Technology Letters*, vol. 17, no. 9, pp. 1929–1931, Sep. 2005, ISSN: 1041-1135. DOI: 10.1109/LPT.2005.853296. [Online]. Available: http://ieeexplore.ieee.org/document/1498906/.

[103] J. Klamkin, A. Ramaswamy, L. A. Johansson, H.-F. Chou, M. N. Sysak, J. W. Raring, N. Parthasarathy, S. P. DenBaars, J. E. Bowers, and L. A. Coldren, "High Output Saturation and High-Linearity Uni-Traveling-Carrier Waveguide Photodiodes", *IEEE Photonics Technology Letters*, vol. 19, no. 3, pp. 149–151, Feb. 2007, ISSN: 1041-1135. DOI: 10.1109/LPT.2006.890101. [Online]. Available: http://ieeexplore.ieee.org/document/4060967/.

[104] D. Zhu, L. Shao, M. Yu, R. Cheng, B. Desiatov, C. J. Xin, Y. Hu, J. Holzgrafe, S. Ghosh, A. Shams-Ansari, E. Puma, N. Sinclair, C. Reimer, M. Zhang, and M. Lončar, "Integrated photonics on thin-film lithium niobate", *Advances in Optics and Photonics*, vol. 13, no. 2, p. 242, Jun. 2021, ISSN: 1943-8206. DOI: 10.1364/AOP.411024. [Online]. Available: https://opg.optica.org/abstract.cfm?URI=aop-13-2-242.

[105] P. Kaur, A. Boes, G. Ren, T. G. Nguyen, G. Roelkens, and A. Mitchell, "Hybrid and heterogeneous photonic integration", *APL Photonics*, vol. 6, no. 6, p. 061 102, Jun. 2021, ISSN: 2378-0967. DOI: 10.1063/5.0052700.

[106] Y. Li, A. Rashidinejad, J.-M. Wun, D. E. Leaird, J.-W. Shi, and A. M. Weiner, "Photonic generation of W-band arbitrary waveforms with high time-bandwidth products enabling 39 mm range resolution", *Optica*, vol. 1, no. 6, p. 446, Dec. 2014, ISSN: 2334-2536.

[107] M. Burla, C. Hoessbacher, W. Heni, C. Haffner, Y. Fedoryshyn, D. Werner, T. Watanabe, H. Massler, D. L. Elder, L. R. Dalton, and J. Leuthold, "500 GHz plasmonic Mach-Zehnder modulator

enabling sub-THz microwave photonics", *APL Photonics*, vol. 4, no. 5, p. 056 106, May 2019, ISSN: 2378-0967. DOI: 10.1063/1.5086868. [Online]. Available: http://aip.scitation.org/doi/10.1063/1.5086868.

[108] M. Burla, C. Hoessbacher, W. Heni, C. Haffner, Y. Fedoryshyn, D. Werner, T. Watanabe, H. Massler, D. Elder, L. Dalton, and J. Leuthold, "500 GHz Plasmonic Mach-Zehnder Modulator", in *Conference on Lasers and Electro-Optics*, Washington, D.C.: OSA, 2019, SW3F.7, ISBN: 978-1-943580-57-6. DOI: 10.1364/CLEO{_}SI.2019.SW3F.7.

[109] T. Nagatsuma, H. Nishii, and T. Ikeo, "Terahertz imaging based on optical coherence tomography [Invited]", *Photonics Research*, vol. 2, no. 4, B64, Aug. 2014, ISSN: 2327-9125. DOI: 10.1364/PRJ.2.000B64. [Online]. Available: https://opg.optica.org/prj/abstract.cfm?uri=prj-2-4-B64.

[110] A. Keil, S. Mohammadzadeh, L. Liebermeister, L. M. Schwenson, B. Globisch, and F. Friederich, "Synthetic Aperture Terahertz Imaging with an Optoelectronic FMCW Radar", in *2022 19th European Radar Conference (EuRAD)*, IEEE, Sep. 2022, pp. 1–4, ISBN: 978-2-8748-7071-2. DOI: 10.23919/EuRAD54643.2022.9924725. [Online]. Available: https://ieeexplore.ieee.org/document/9924725/.

[111] C. Wang and J. Yao, "Photonic Generation of Chirped Microwave Pulses Using Superimposed Chirped Fiber Bragg Gratings", *IEEE Photonics Technology Letters*, vol. 20, no. 11, pp. 882–884, Jun. 2008, ISSN: 1041-1135. DOI: 10.1109/LPT.2008.922333. [Online]. Available: http://ieeexplore.ieee.org/document/4509499/.

[112] Chao Wang and Jianping Yao, "Chirped Microwave Pulse Generation Based on Optical Spectral Shaping and Wavelength-to-Time Mapping Using a Sagnac Loop Mirror Incorporating a Chirped Fiber Bragg Grating", *Journal of Lightwave Technology*, vol. 27, no. 16, pp. 3336–3341, Aug. 2009, ISSN: 0733-8724. DOI: 10.1109/JLT.2008.2010561. [Online]. Available: http://ieeexplore.ieee.org/document/4815451/.

[113] M. Li, L.-Y. Shao, J. Albert, and J. Yao, "Tilted Fiber Bragg Grating for Chirped Microwave Waveform Generation", *IEEE Photonics Technology Letters*, vol. 23, no. 5, pp. 314–316, Mar. 2011, ISSN: 1041-1135. DOI: 10.1109/LPT.2010.2102013. [Online]. Available: http://ieeexplore.ieee.org/document/5674068/.

[114] F. Zhang, X. Ge, and S. Pan, "Background-free pulsed microwave signal generation based on spectral shaping and frequency-to-time mapping", *Photonics Research*, vol. 2, no. 4, B5, Aug. 2014, ISSN: 2327-9125. DOI: 10.1364/PRJ.2.0000B5. [Online]. Available: https://opg.optica.org/prj/abstract.cfm?uri=prj-2-4-B5.

[115] A. Rashidinejad and A. M. Weiner, "Photonic Radio-Frequency Arbitrary Waveform Generation With Maximal Time-Bandwidth Product Capability", *Journal of Lightwave Technology*, vol. 32, no. 20, pp. 3383–3393, Oct. 2014.

[116] P. Zhou, F. Zhang, Q. Guo, and S. Pan, "Linearly chirped microwave waveform generation with large time-bandwidth product by optically injected semiconductor laser", *Optics Express*, vol. 24, no. 16, p. 18 460, 2016, ISSN: 1094-4087. DOI: 10.1364/oe.24.018460.

[117] P. Zhou, F. Zhang, Q. Guo, S. Li, and S. Pan, "Reconfigurable Radar Waveform Generation Based on an Optically Injected Semiconductor Laser", *IEEE Journal of Selected Topics in Quantum Electronics*, vol. 23, no. 6, pp. 1–9, Nov. 2017.

[118] X. Zhang, H. Zeng, J. Yang, Z. Yin, Q. Sun, and W. Li, "Novel RF-source-free reconfigurable microwave photonic radar", *Optics Express*, vol. 28, no. 9, p. 13 650, Apr. 2020.

[119] T. Hao, Q. Cen, Y. Dai, J. Tang, W. Li, J. Yao, N. Zhu, and M. Li, "Breaking the limitation of mode building time in an optoelectronic oscillator", *Nature Communications*, vol. 9, no. 1, p. 1839, May 2018.

[120] P. Zhou, F. Zhang, X. Ye, Q. Guo, and S. Pan, "Flexible Frequency-Hopping Microwave Generation by Dynamic Control of Optically Injected Semiconductor Laser", *IEEE Photonics Journal*, vol. 8, no. 6, pp. 1–9, Dec. 2016, ISSN: 1943-0655. DOI: 10.1109/JPHOT.2016.2629082. [Online]. Available: http://ieeexplore.ieee.org/document/7745901/.

[121] W. Li and J. Yao, "Generation of Linearly Chirped Microwave Waveform With an Increased Time-Bandwidth Product Based on a Tunable Optoelectronic Oscillator and a Recirculating Phase Modulation Loop", *Journal of Lightwave Technology*, vol. 32, no. 20, pp. 3573–3579, Oct. 2014, ISSN: 0733-8724. DOI: 10.1109/JLT.2014.2309392. [Online]. Available: http://ieeexplore.ieee.org/document/6754143/.

[122] Q. Guo, F. Zhang, P. Zhou, and S. Pan, "Dual-Band LFM Signal Generation by Optical Frequency Quadrupling and Polarization Multiplexing", *IEEE Photonics Technology Letters*, vol. 29, no. 16, pp. 1320–1323, Aug. 2017.

[123] F. Zhang, Q. Guo, Z. Wang, P. Zhou, G. Zhang, J. Sun, and S. Pan, "Photonics-based broadband radar for high-resolution and real-time inverse synthetic aperture imaging", *Optics Express*, vol. 25, no. 14, p. 16 274, Jul. 2017.

[124] Y. Yao, F. Zhang, Y. Zhang, X. Ye, D. Zhu, and S. Pan, "Demonstration of ultra-high-resolution photonics-based Ka-band inverse synthetic aperture radar imaging", in *Optical Fiber Communication Conference*, vol. Part F84-O, Washington, D.C.: OSA, 2018, Th3G.5, ISBN: 978-1-943580-38-5. DOI: 10.1364/OFC.2018.Th3G.5. [Online]. Available: https://opg.optica.org/abstract.cfm?URI=OFC-2018-Th3G.5.

[125] J. Meng, M. Miscuglio, J. K. George, A. Babakhani, and V. J. Sorger, "Electronic Bottleneck Suppression in Next-Generation Networks with Integrated Photonic Digital-to-Analog Converters", *Advanced Photonics Research*, vol. 2, no. 2, p. 2 000 033, Feb. 2021, ISSN: 2699-9293. DOI: 10.1002/adpr.202000033. [Online]. Available: https://onlinelibrary.wiley.com/doi/10.1002/adpr.202000033.

[126] B. Gao, F. Zhang, and S. Pan, "Experimental demonstration of arbitrary waveform generation by a 4-bit photonic digital-to-analog converter", *Optics Communications*, vol. 383, pp. 191–196, Jan. 2017, ISSN: 00304018. DOI: 10.1016/j.optcom.2016.08.083. [Online]. Available: https://linkinghub.elsevier.com/retrieve/pii/S0030401816307696.

[127] S. Peng, S. Li, X. Xue, X. Xiao, D. Wu, X. Zheng, and B. Zhou, "High-resolution W-band ISAR imaging system utilizing a logic-operation-based photonic digital-to-analog converter", *Optics Express*, vol. 26, no. 2, p. 1978, Jan. 2018.

[128] X. Li, J. Yu, Z. Dong, J. Zhang, Y. Shao, and N. Chi, "Multi-channel multi-carrier generation using multi-wavelength frequency shifting recirculating loop", *Optics Express*, vol. 20, no. 20, p. 21 833, Sep. 2012, ISSN: 1094-4087. DOI: 10.1364/OE.20.021833. [Online]. Available: https://opg.optica.org/oe/abstract.cfm?uri=oe-20-20-21833.

[129] J. Clement, C. Schnébelin, H. G. de Chatellus, and C. R. Fernández-Pousa, "Laser ranging using coherent pulse compression with frequency shifting loops", *Optics Express*, vol. 27, no. 9, p. 12 000, Apr. 2019.

[130] Y. Zhang, C. Liu, Y. Zhang, K. Shao, C. Ma, L. Li, L. Sun, S. Li, and S. Pan, "Multi-Functional Radar Waveform Generation Based on Optical Frequency-Time Stitching Method", *Journal of Lightwave Technology*, vol. 39, no. 2, pp. 458–464, Jan. 2021.

[131] Y. Lyu, Y. Li, C. Yu, L. Yi, T. Nagatsuma, and Z. Zheng, "Photonic Generation of Highly-Linear Ultra-Wideband Stepped-Frequency Microwave Signals With Up to 6·10 6 Time-Bandwidth Product", *Journal of Lightwave Technology*, vol. 40, no. 4, pp. 1036–1042, Feb. 2022.

[132] Y. Zhang, C. Liu, K. Shao, Z. Li, and S. Pan, "Multioctave and reconfigurable frequency-stepped radar waveform generation based on an optical frequency shifting loop", *Optics Letters*, vol. 45, no. 7, p. 2038, Apr. 2020.

[133] O. Svelto and D. C. Hanna, *Principles of lasers*. Springer, 2010, vol. 1.

[134] J. Li, T. Pu, J. Zheng, Y. Zhang, Y. Shi, H. Zhu, Y. Li, X. Zhang, G. Zhao, Y. Zhou, and X. Chen, "Photonic generation of linearly chirped microwave waveforms using a monolithic integrated three-section laser", *Optics Express*, vol. 26, no. 8, p. 9676, Apr. 2018, ISSN: 1094-4087. DOI: 10.1364/OE.26.009676. [Online]. Available: https://opg.optica.org/abstract.cfm?URI=oe-26-8-9676.

[135] E. Baumann, F. R. Giorgetta, J.-D. Deschênes, W. C. Swann, I. Coddington, and N. R. Newbury, "Comb-calibrated laser ranging for three-dimensional surface profiling with micrometer-level precision at a distance", *Optics Express*, vol. 22, no. 21, p. 24 914, Oct. 2014, ISSN: 1094-4087. DOI: 10.1364/OE.22.024914. [Online]. Available: https://opg.optica.org/abstract.cfm?URI=oe-22-21-24914.

[136] Guohua Qi, Jianping Yao, J. Seregelyi, S. Paquet, and C. Belisle, "Generation and distribution of a wide-band continuously tunable millimeter-wave signal with an optical external modulation technique", *IEEE Transactions on Microwave Theory and Techniques*, vol. 53, no. 10, pp. 3090–3097, Oct. 2005, ISSN: 0018-9480. DOI: 10.1109/TMTT.2005.855123. [Online]. Available: http://ieeexplore.ieee.org/document/1516310/.

[137] S. Li, Z. Cui, X. Ye, J. Feng, Y. Yang, Z. He, R. Cong, D. Zhu, F. Zhang, and S. Pan, "Chip-Based Microwave-Photonic Radar for High-Resolution Imaging", *Laser & Photonics Reviews*, vol. 14, no. 10, p. 1 900 239, Oct. 2020.

[138] Y. Fu, X. Zhang, B. Hraimel, T. Liu, and D. Shen, "Mach-Zehnder: A Review of Bias Control Techniques for Mach-Zehnder Modulators in Photonic Analog Links", *IEEE Microwave Magazine*, vol. 14, no. 7, pp. 102–107, Nov. 2013, ISSN: 1527-3342. DOI: 10.1109/MMM.2013.2280332. [Online]. Available: http://ieeexplore.ieee.org/document/6668957/.

[139] H. Guillet de Chatellus, L. Romero Cortés, C. Schnébelin, M. Burla, and J. Azaña, "Reconfigurable photonic generation of broadband chirped waveforms using a single CW laser and low-frequency electronics", *Nature Communications*, vol. 9, no. 1, p. 2438, Jun. 2018.

[140] C. Ma, Y. Yang, F. Cao, X. Wang, X. Liu, C. Meng, J. Zhang, and S. Pan, "High-Resolution Microwave Photonic Radar With Sparse Stepped Frequency Chirp Signals", *IEEE Transactions on Geoscience and Remote Sensing*, vol. 60, pp. 1–10, 2022, ISSN: 0196-2892.

[141] P. Zhou, R. R. Zhang, N. Li, Z. Jiang, and S. Pan, "An RF-Source-Free Reconfigurable Microwave Photonic Radar With High-Resolution and Fast Detection Capability", *Journal of Lightwave Technology*, vol. 40, no. 9, pp. 2862–2869, May 2022.

[142] G. Sun, F. Zhang, and S. Pan, "Millimeter-level resolution through-the-wall radar imaging enabled by an optically injected semiconductor laser", *Optics Letters*, vol. 46, no. 22, p. 5659, Nov. 2021.

[143] M. A. Richards, J. Scheer, W. A. Holm, and W. L. Melvin, *Principles of modern radar*. Citeseer, 2010.

[144] R. Klemm, U. Nickel, C. Gierull, P. Lombardo, H. Griffiths, and W. Koch, "Novel radar techniques and applications volume 1: real aperture array radar, imaging radar, and passive and multistatic radar", Tech. Rep., 2017.

[145] W. C. Su, M. C. Tang, R. E. Arif, T. S. Horng, and F. K. Wang, "Stepped-Frequency Continuous-Wave Radar with Self-Injection-Locking Technology for Monitoring Multiple Human Vital Signs", *IEEE Transactions on Microwave Theory and Techniques*, vol. 67, no. 12, pp. 5396–5405, 2019.

[146] G. Serafino, F. Amato, S. Maresca, L. Lembo, P. Ghelfi, and A. Bogoni, "Photonic approach for on-board and ground radars in automotive applications", *IET Radar, Sonar and Navigation*, vol. 12, no. 10, pp. 1179–1186, 2018.

[147] H. Matsumoto, I. Watanabe, A. Kasamatsu, and Y. Monnai, "Integrated terahertz radar based on leaky-wave coherence tomography", *Nature Electronics*, vol. 3, no. 2, pp. 122–129, Jan. 2020, ISSN: 2520-1131.

[148] B. W. Wah, *Wiley encyclopedia of computer science and engineering*. Wiley Online Library, 2009, ISBN: 0471383937.

[149] X. Xiao, S. Li, S. Peng, D. Wu, X. Xue, X. Zheng, and B. Zhou, "Photonics-based wideband distributed coherent aperture radar system", *Optics Express*, vol. 26, no. 26, p. 33 783, Dec. 2018.

[150] F. Scotti, S. Maresca, L. Lembo, G. Serafino, A. Bogoni, and P. Ghelfi, "Widely distributed photonics-based dual-band MIMO radar for harbour surveillance", *IEEE Photonics Technology Letters*, vol. 32, no. 17, pp. 1081–1084, 2020.

[151] A. Malacarne, S. Maresca, F. Scotti, P. Ghelfi, G. Serafino, and A. Bogoni, "Coherent Dual-Band Radar-Over-Fiber Network With VCSEL-Based Signal Distribution", *Journal of Lightwave Technology*, vol. 38, no. 22, pp. 6257–6264, Nov. 2020.

[152] X. Ye, F. Zhang, Y. Yang, and S. Pan, "Photonics-based radar with balanced I/Q de-chirping for interference-suppressed high-resolution detection and imaging", *Photonics Research*, vol. 7, no. 3, p. 265, Mar. 2019.

[153] F. Scotti, F. Laghezza, P. Ghelfi, and A. Bogoni, "Multi-band software-defined coherent radar based on a single photonic transceiver", *IEEE Transactions on Microwave Theory and Techniques*, vol. 63, no. 2, pp. 546–552, 2015.

[154] X. Ma, Y. Wang, L. Lu, X. Zhang, Q. Chen, X. You, J. Lin, and L. Li, "Design of a 100-GHz Double-Sideband Low-IF CW Doppler Radar Transceiver for Micrometer Mechanical Vibration and Vital Sign Detection", *IEEE Transactions on Microwave Theory and Techniques*, vol. 68, no. 7, pp. 2876–2890, Jul. 2020.

[155] J. Tang, B. Zhu, W. Zhang, M. Li, S. Pan, and J. Yao, "Hybrid Fourier-domain mode-locked laser for ultra-wideband linearly chirped microwave waveform generation", *Nature Communications*, vol. 11, no. 1, p. 3814, Jul. 2020.

[156] J. Zhang and J. Yao, "Time-stretched sampling of a fast microwave waveform based on the repetitive use of a linearly chirped fiber Bragg grating in a dispersive loop", *Optica*, vol. 1, no. 2, p. 64, Aug. 2014.

[157] V. C. Chen, *Inverse Synthetic Aperture Radar Imaging; Principles*. Institution of Engineering and Technology, 2014.

[158] L. Yatsenko, B. Shore, and K. Bergmann, "Theory of a frequency-shifted feedback laser", *Optics Communications*, vol. 236, no. 1-3, pp. 183–202, Jun. 2004, ISSN: 00304018. DOI: 10.1016/j.optcom.2004.03.049. [Online]. Available: https://linkinghub.elsevier.com/retrieve/pii/S0030401804003141.

[159] C. Schnébelin, J. Azaña, and H. Guillet de Chatellus, "Programmable broadband optical field spectral shaping with megahertz resolution using a simple frequency shifting loop", *Nature Communications*, vol. 10, no. 1, p. 4654, Oct. 2019, ISSN: 2041-1723. DOI: 10.1038/s41467-019-12688-3. [Online]. Available: https://www.nature.com/articles/s41467-019-12688-3.

[160] H. Guillet de Chatellus, E. Lacot, W. Glastre, O. Jacquin, and O. Hugon, "Theory of Talbot lasers", *Physical Review A*, vol. 88, no. 3, p. 033 828, Sep. 2013, ISSN: 1050-2947. DOI: 10.1103/PhysRevA.88.033828. [Online]. Available: https://link.aps.org/doi/10.1103/PhysRevA.88.033828.

[161] V. Billault, V. Crozatier, G. Baili, L. Morvan, D. Dolfi, and H. Guillet de Chatellus, "Dynamic behavior of frequency combs in frequency-shifting loops", *Journal of the Optical Society of America B*, vol. 37, no. 6, p. 1812, Jun. 2020, ISSN: 0740-3224. DOI: 10.1364/josab.391074. [Online]. Available: https://opg.optica.org/abstract.cfm?URI=josab-37-6-1812.

[162] X. Chen, W. Zhang, W. Rhee, and Z. Wang, "A ¡inline-formula¿ ¡tex-math notation="TeX"¿$\Delta \Sigma$¡/tex-math¿¡/inline-formula¿ -TDC-Based Beamforming Method for Vital Sign Detection Radar Systems", *IEEE Transactions on Circuits and Systems II: Express Briefs*, vol. 61, no. 12, pp. 932–936, Dec. 2014.

[163] A. Gustavsson, P. Frolind, H. Hellsten, T. Jonsson, B. Larsson, and G. Stenstrom, "The airborne VHF SAR system CARABAS", in *Proceedings of IGARSS '93 - IEEE International Geoscience and Remote Sensing Symposium*, IEEE, pp. 558–562, ISBN: 0-7803-1240-6. DOI: 10.1109/IGARSS.1993.322271. [Online]. Available: http://ieeexplore.ieee.org/document/322271/.

[164] Z. Yu and X. Sun, "Gigahertz Acousto-Optic Modulation and Frequency Shifting on Etchless Lithium Niobate Integrated Platform", *ACS Photonics*, vol. 8, no. 3, pp. 798–803, Mar. 2021.

[165] K. Wang, Y. Wang, X. Guo, Y. Zhang, A. He, and Y. Su, "Ultracompact bandwidth-tunable filter based on subwavelength grating-assisted contra-directional couplers", *Frontiers of Optoelectronics*, vol. 14, no. 3, pp. 374–380, Sep. 2021.

[166] Y. Liu, Z. Qiu, X. Ji, A. Lukashchuk, J. He, J. Riemensberger, M. Hafermann, R. N. Wang, J. Liu, C. Ronning, and T. J. Kippenberg, "A photonic integrated circuit–based erbium-doped amplifier", *Science*, vol. 376, no. 6599, pp. 1309–1313, Jun. 2022, ISSN: 0036-8075. DOI: 10.1126/science.abo2631. [Online]. Available: https://www.science.org/doi/10.1126/science.abo2631.

[167] I. Duling and D. Zimdars, "Revealing hidden defects", *Nature Photonics*, vol. 3, no. 11, pp. 630–632, Nov. 2009, ISSN: 1749-4885. DOI: 10.1038/nphoton.2009.206. [Online]. Available: http://www.nature.com/articles/nphoton.2009.206.

[168] H.-W. Hübers, "Towards THz integrated photonics", *Nature Photonics*, vol. 4, no. 8, pp. 503–504, Aug. 2010, ISSN: 1749-4885. DOI: 10.1038/nphoton.2010.169. [Online]. Available: http://www.nature.com/articles/nphoton.2010.169.

[169] A. Gowen, C. O'Sullivan, and C. O'Donnell, "Terahertz time domain spectroscopy and imaging: Emerging techniques for food process monitoring and quality control", *Trends in Food Science & Technology*, vol. 25, no. 1, pp. 40–46, May 2012, ISSN: 09242244. DOI: 10.1016/j.tifs.2011.12.006. [Online]. Available: https://linkinghub.elsevier.com/retrieve/pii/S0924224411002937.

[170] M. Caruso, M. Bassi, A. Bevilacqua, and A. Neviani, "A 2–16 GHz 65 nm CMOS Stepped-Frequency Radar Transmitter With Harmonic Rejection for High-Resolution Medical Imaging Applications", *IEEE Transactions on Circuits and Systems I: Regular Papers*, vol. 62, no. 2, pp. 413–422, Feb. 2015, ISSN: 1549-8328. DOI: 10.1109/TCSI.2014.2362332. [Online]. Available: http://ieeexplore.ieee.org/document/6939739/.

[171] K. Sengupta, T. Nagatsuma, and D. M. Mittleman, "Terahertz integrated electronic and hybrid electronic–photonic systems", *Nature Electronics*, vol. 1, no. 12, pp. 622–635, Dec. 2018, ISSN: 2520-1131. DOI: 10.1038/s41928-018-0173-2. [Online]. Available: https://www.nature.com/articles/s41928-018-0173-2.

[172] S. Tonda-Goldstein, D. Dolfi, A. Monsterleet, S. Formont, J. Chazelas, and Jean-Pierre Huignard, "Optical signal processing in Radar systems", *IEEE Transactions on Microwave Theory and Techniques*, vol. 54, no. 2, pp. 847–853, Feb. 2006, ISSN: 0018-9480. DOI: 10.1109/TMTT.2005.863059. [Online]. Available: http://ieeexplore.ieee.org/document/1589517/.

[173] G. Serafino, S. Maresca, C. Porzi, F. Scotti, P. Ghelfi, and A. Bogoni, "Microwave Photonics for Remote Sensing: From Basic Concepts to High-Level Functionalities", *Journal of Lightwave Technology*, vol. 38, no. 19, pp. 5339–5355, 2020.

[174] B. Li, W. Wei, D. Han, W. Xie, and Y. Dong, "Remote broadband RF signal down-conversion with stable phase and high efficiency using a sideband optical phase-locked loop", *Optics Express*, vol. 28, no. 9, p. 12 588, Apr. 2020.

[175] F. Falconi, C. Porzi, A. Malacarne, F. Scotti, P. Ghelfi, and A. Bogoni, "UWB Fastly–Tunable 0.5–50 GHz RF Transmitter Based on Integrated Photonics", *Journal of Lightwave Technology*, vol. 40, no. 6, pp. 1726–1734, Mar. 2022.

[176] C. Porzi, F. Falconi, M. Sorel, P. Ghelfi, and A. Bogoni, "Flexible Millimeter-Wave Carrier Generation up to the Sub-THz with Silicon Photonics Filters", *Journal of Lightwave Technology*, vol. 39, no. 24, pp. 7689–7697, 2021.

[177] G. Han, S. Li, X. Xue, and X. Zheng, "Photonic fractional Fourier transformer for chirp radar with ghost target elimination", *Optics Letters*, vol. 45, no. 15, p. 4228, Aug. 2020.

[178] J. Tang, T. Hao, W. Li, D. Domenech, R. Baños, P. Muñoz, N. Zhu, J. Capmany, and M. Li, "Integrated optoelectronic oscillator", *Optics Express*, vol. 26, no. 9, p. 12 257, Apr. 2018, ISSN: 1094-4087. DOI: 10.1364/OE.26.012257. [Online]. Available: https://opg.optica.org/abstract.cfm?URI=oe-26-9-12257.

[179] T. Hao, Y. Liu, J. Tang, Q. Cen, W. Li, N. Zhu, Y. Dai, J. Capmany, J. Yao, and M. Li, "Recent advances in optoelectronic oscillators", *Advanced Photonics*, vol. 2, no. 04, p. 1, Jul. 2020, ISSN: 2577-5421. DOI: 10.1117/1.AP.2.4.044001. [Online]. Available: https://www.spiedigitallibrary.org/journals/advanced-photonics/volume-2/issue-04/044001/Recent-advances-in-optoelectronic-oscillators/10.1117/1.AP.2.4.044001.full.

[180] Z. Ge, T. Hao, J. Capmany, W. Li, N. Zhu, and M. Li, "Broadband random optoelectronic oscillator", *Nature Communications*, vol. 11, no. 1, p. 5724, Nov. 2020.

[181] T. Tetsumoto, T. Nagatsuma, M. E. Fermann, G. Navickaite, M. Geiselmann, and A. Rolland, "Optically referenced 300 GHz millimetre-wave oscillator", *Nature Photonics*, vol. 15, no. 7, pp. 516–522, Jul. 2021, ISSN: 1749-4885. DOI: 10.1038/s41566-021-00790-2. [Online]. Available: http://www.nature.com/articles/s41566-021-00790-2.

[182] H. Chi, C. Wang, and J. Yao, "Photonic Generation of Wideband Chirped Microwave Waveforms", *IEEE Journal of Microwaves*, vol. 1, no. 3, pp. 787–803, Jul. 2021, ISSN: 2692-8388. DOI: 10.1109/JMW.2021.3085868. [Online]. Available: https://ieeexplore.ieee.org/document/9464904/.

[183] A. Rashidinejad, Y. Li, J.-M. Wun, D. E. Leaird, J.-W. Shi, and A. M. Weiner, "Photonic Generation and Wireless Transmission of W-band Arbitrary Waveforms with High Time-Bandwidth Products", in *CLEO: 2014*, vol. 1, Washington, D.C.: OSA, 2014, SM1G.1.

[184] W. Liu, M. Li, R. S. Guzzon, E. J. Norberg, J. S. Parker, M. Lu, L. A. Coldren, and J. Yao, "A fully reconfigurable photonic integrated signal processor", *Nature Photonics*, vol. 10, no. 3, pp. 190–195, Mar. 2016.

[185] R. Cheng, W. Wei, W. Xie, and Y. Dong, "Photonic generation of programmable coherent linear frequency modulated signal and its application in X-band radar system", *Optics Express*, vol. 27, no. 26, p. 37 469, Dec. 2019.

[186] W. Xie, Y. Meng, Y. Feng, H. Zhou, L. Zhang, W. Wei, and Y. Dong, "Optical linear frequency sweep based on a mode-spacing swept comb and multi-loop phase-locking for FMCW interferometry", *Optics Express*, vol. 29, no. 2, p. 604, Jan. 2021.

[187] L. Zhang, M. Xing, C.-W. Qiu, J. Li, J. Sheng, Y. Li, and Z. Bao, "Resolution Enhancement for Inversed Synthetic Aperture Radar Imaging Under Low SNR via Improved Compressive Sensing", *IEEE Transactions on Geoscience and Remote Sensing*, vol. 48, no. 10, pp. 3824–3838, Oct. 2010, ISSN: 0196-2892. DOI: 10.1109/TGRS.2010.2048575. [Online]. Available: http://ieeexplore.ieee.org/document/5482210/.

[188] V. Billault, G. Arpison, V. Crozatier, V. Kemlin, L. Morvan, D. Dolfi, and H. G. de Chatellus, "Coherent Optical Fiber Sensing Based on a Frequency Shifting Loop", *Journal of Lightwave Technology*, vol. 39, no. 12, pp. 4118–4123, Jun. 2021, ISSN: 0733-8724. DOI: 10.1109/JLT.2021.3060105. [Online]. Available: https://ieeexplore.ieee.org/document/9369248/.

[189] L. Shao, N. Sinclair, J. Leatham, Y. Hu, M. Yu, T. Turpin, D. Crowe, and M. Loncar, "Integrated Lithium Niobate Acousto-optic Frequency Shifter", in *Conference on Lasers and Electro-Optics*, vol. Part F183-, Washington, D.C.: Optica Publishing Group, 2020, STh1F.5.

[190] Z. Zhang, Z. Tian, and M. Zhou, "Latern: Dynamic Continuous Hand Gesture Recognition Using FMCW Radar Sensor", *IEEE Sensors Journal*, vol. 18, no. 8, pp. 3278–3289, Apr. 2018, ISSN: 1530-437X. DOI: 10.1109/JSEN.2018.2808688. [Online]. Available: http://ieeexplore.ieee.org/document/8300506/.

[191] J. Park, J. Jang, G. Lee, H. Koh, C. Kim, and T. W. Kim, "A Time Domain Artificial Intelligence Radar System Using 33-GHz Direct Sampling for Hand Gesture Recognition", *IEEE Journal of Solid-State Circuits*, vol. 55, no. 4, pp. 879–888, Apr. 2020, ISSN: 0018-9200. DOI: 10.1109/JSSC.2020.2967547. [Online]. Available: https://ieeexplore.ieee.org/document/8976307/.

[192] M. G. Amin, Y. D. Zhang, F. Ahmad, and K. D. Ho, "Radar Signal Processing for Elderly Fall Detection: The future for in-home monitoring", *IEEE Signal Processing Magazine*, vol. 33, no. 2, pp. 71–80, Mar. 2016, ISSN: 1053-5888. DOI: 10.1109/MSP.2015.2502784. [Online]. Available: http://ieeexplore.ieee.org/document/7426551/.

[193] E. Cardillo and A. Caddemi, "A Review on Biomedical MIMO Radars for Vital Sign Detection and Human Localization", *Electronics*, vol. 9, no. 9, p. 1497, Sep. 2020.

[194] J. Dunn, L. Kidzinski, R. Runge, D. Witt, J. L. Hicks, S. M. Schüssler-Fiorenza Rose, X. Li, A. Bahmani, S. L. Delp, T. Hastie, and M. P. Snyder, "Wearable sensors enable personalized predictions of clinical laboratory measurements", *Nature Medicine*, vol. 27, no. 6, pp. 1105–1112, Jun. 2021.

[195] L. Ren, L. Kong, F. Foroughian, H. Wang, P. Theilmann, and A. E. Fathy, "Comparison Study of Noncontact Vital Signs Detection Using a Doppler Stepped-Frequency Continuous-Wave Radar and

Camera-Based Imaging Photoplethysmography", *IEEE Transactions on Microwave Theory and Techniques*, vol. 65, no. 9, pp. 3519–3529, Sep. 2017.

[196] M. Mercuri, Y.-H. Liu, I. Lorato, T. Torfs, A. Bourdoux, and C. Van Hoof, "Frequency-Tracking CW Doppler Radar Solving Small-Angle Approximation and Null Point Issues in Non-Contact Vital Signs Monitoring", *IEEE Transactions on Biomedical Circuits and Systems*, vol. 11, no. 3, pp. 671–680, Jun. 2017.

[197] C. Massaroni, J. Di Tocco, M. Bravi, A. Carnevale, D. Lo Presti, R. Sabbadini, S. Miccinilli, S. Sterzi, D. Formica, and E. Schena, "Respiratory Monitoring During Physical Activities With a Multi-Sensor Smart Garment and Related Algorithms", *IEEE Sensors Journal*, vol. 20, no. 4, pp. 2173–2180, Feb. 2020.

[198] D. Lo Presti, A. Carnevale, J. D'Abbraccio, L. Massari, C. Massaroni, R. Sabbadini, M. Zaltieri, J. Di Tocco, M. Bravi, S. Miccinilli, S. Sterzi, U. G. Longo, V. Denaro, M. A. Caponero, D. Formica, C. M. Oddo, and E. Schena, "A Multi-Parametric Wearable System to Monitor Neck Movements and Respiratory Frequency of Computer Workers", *Sensors*, vol. 20, no. 2, p. 536, Jan. 2020.

[199] H. Liu, J. Allen, D. Zheng, and F. Chen, "Recent development of respiratory rate measurement technologies", *Physiological Measurement*, vol. 40, no. 7, 07TR01, Jul. 2019.

[200] S. Bennett, T. N. El Harake, R. Goubran, and F. Knoefel, "Adaptive Eulerian Video Processing of Thermal Video: An Experimental Analysis", *IEEE Transactions on Instrumentation and Measurement*, vol. 66, no. 10, pp. 2516–2524, Oct. 2017.

[201] S. Chaichulee, M. Villarroel, J. Jorge, C. Arteta, G. Green, K. McCormick, A. Zisserman, and L. Tarassenko, "Multi-Task Convolutional Neural Network for Patient Detection and Skin Segmentation in Continuous Non-Contact Vital Sign Monitoring", in *2017 12th IEEE International Conference on Automatic Face & Gesture Recognition (FG 2017)*, IEEE, May 2017, pp. 266–272.

[202] T. Negishi, S. Abe, T. Matsui, H. Liu, M. Kurosawa, T. Kirimoto, and G. Sun, "Contactless Vital Signs Measurement System Using RGB-Thermal Image Sensors and Its Clinical Screening Test on Patients with Seasonal Influenza", *Sensors*, vol. 20, no. 8, p. 2171, Apr. 2020.

[203] S. Lyra, L. Mayer, L. Ou, D. Chen, P. Timms, A. Tay, P. Y. Chan, B. Ganse, S. Leonhardt, and C. Hoog Antink, "A Deep Learning-Based Camera Approach for Vital Sign Monitoring Using Thermography Images for ICU Patients", *Sensors*, vol. 21, no. 4, p. 1495, Feb. 2021.

[204] Y. Rong, R. Gutierrez, K. V. Mishra, and D. W. Bliss, "Noncontact Vital Sign Detection With UAV-Borne Radars: An Overview of Recent Advances", *IEEE Vehicular Technology Magazine*, vol. 16, no. 3, pp. 118–128, Sep. 2021.

[205] C. Li, V. M. Lubecke, O. Boric-Lubecke, and J. Lin, "A review on recent advances in doppler radar sensors for noncontact healthcare monitoring", *IEEE Transactions on Microwave Theory and Techniques*, vol. 61, no. 5, pp. 2046–2060, 2013.

[206] J. Tu, T. Hwang, and J. Lin, "Respiration Rate Measurement under 1-D Body Motion Using Single Continuous-Wave Doppler Radar Vital Sign Detection System", *IEEE Transactions on Microwave Theory and Techniques*, vol. 64, no. 6, pp. 1937–1946, 2016.

[207] G. Wang, J. M. Munoz-Ferreras, C. Gu, C. Li, and R. Gomez-Garcia, "Application of linear-frequency-modulated continuous-wave (LFMCW) radars for tracking of vital signs", *IEEE Transactions on Microwave Theory and Techniques*, vol. 62, no. 6, pp. 1387–1399, 2014.

[208] F. Quaiyum, L. Ren, S. Nahar, F. Foroughian, and A. E. Fathy, "Development of a reconfigurable low cost multi-mode radar system for contactless vital signs detection", *IEEE MTT-S International Microwave Symposium Digest*, no. 1, pp. 1245–1247, 2017.

[209] A. Ahmad, J. C. Roh, D. Wang, and A. Dubey, "Vital signs monitoring of multiple people using a FMCW millimeter-wave sensor", in *2018 IEEE Radar Conference (RadarConf18)*, IEEE, Apr. 2018, pp. 1450–1455.

[210] M. Mercuri, I. R. Lorato, Y.-H. Liu, F. Wieringa, C. V. Hoof, and T. Torfs, "Vital-sign monitoring and spatial tracking of multiple people using a contactless radar-based sensor", *Nature Electronics*, vol. 2, no. 6, pp. 252–262, Jun. 2019.

[211] Y. Wang, Q. Liu, and A. E. Fathy, "CW and pulse-Doppler radar processing based on FPGA for human sensing applications", *IEEE Transactions on Geoscience and Remote Sensing*, vol. 51, no. 5, pp. 3097–3107, 2013.

[212] G.-W. W. Fang, C.-Y. Y. Huang, and C.-L. L. Yang, "Switch-Based Low Intermediate Frequency System of a Vital Sign Radar for Simultaneous Multitarget and Multidirectional Detection", *IEEE Journal of Electromagnetics, RF and Microwaves in Medicine and Biology*, vol. 4, no. 4, pp. 265–272, Dec. 2020.

[213] G. Serafino, S. Maresca, L. Di Mauro, A. Tardo, A. Cuillo, F. Scotti, P. Ghelfi, P. Pagano, and A. Bogoni, "A Photonics-Assisted Multi-Band MIMO Radar Network for the Port of the Future", *IEEE Journal of Selected Topics in Quantum Electronics*, vol. 27, no. 6, 2021.

[214] F. Falconi, S. Melo, F. Scotti, M. N. Malik, M. Scaffardi, C. Porzi, L. Ansalone, P. Ghelfi, and A. Bogoni, "A Combined Radar & Lidar System Based on Integrated Photonics in Silicon-on-Insulator", *Journal of Lightwave Technology*, vol. 39, no. 1, pp. 17–23, 2021.

[215] F. Zhang, B. Gao, and S. Pan, "Photonics-based MIMO radar with high-resolution and fast detection capability", *Optics Express*, vol. 26, no. 13, p. 17 529, Jun. 2018.

[216] X. Xiao, S. Li, S. Peng, X. Xue, X. Zheng, and B. Zhou, "Microwave Photonic Wideband Distributed Coherent Aperture Radar With High Robustness to Time Synchronization Error", *Journal of Lightwave Technology*, vol. 39, no. 2, pp. 347–356, Jan. 2021.

[217] B. Liu, S. Seshadri, J.-M. Wun, N. P. O'Malley, D. E. Leaird, N.-W. Chen, J.-W. Shi, and A. M. Weiner, "W-Band Photonic Pulse Compression Radar With Dual Transmission Mode Beamforming", *Journal of Lightwave Technology*, vol. 39, no. 6, pp. 1619–1628, Mar. 2021.

[218] S. Ayhan, S. Scherr, A. Bhutani, B. Fischbach, M. Pauli, and T. Zwick, "Impact of Frequency Ramp Nonlinearity, Phase Noise, and SNR on FMCW Radar Accuracy", *IEEE Transactions on Microwave Theory and Techniques*, vol. 64, no. 10, pp. 3290–3301, Oct. 2016.

[219] S. A. Fulop and K. Fitz, "Algorithms for computing the time-corrected instantaneous frequency (reassigned) spectrogram, with applications", *The Journal of the Acoustical Society of America*, vol. 119, no. 1, pp. 360–371, Jan. 2006.

[220] A. V. Oppenheim, *Discrete-time signal processing*. Pearson Education India, 1999, ISBN: 8131704920.

[221] S. S. K. Ho and C. E. Saavedra, "A CMOS Broadband Low-Noise Mixer With Noise Cancellation", *IEEE Transactions on Microwave Theory and Techniques*, vol. 58, no. 5, pp. 1126–1132, May 2010.

[222] M. Jankiraman, *FMCW Radar Design*. Artech House, 2018, pp. 164–179.

[223] L. Chioukh, H. Boutayeb, K. Wu, and D. Deslandes, "Monitoring vital signs using remote harmonic radar concept", *European Microwave Week 2011: "Wave to the Future", EuMW 2011, Conference Proceedings - 41st European Microwave Conference, EuMC 2011*, no. October, pp. 1269–1272, 2011.

[224] S. Nahar, T. Phan, F. Quaiyum, L. Ren, A. E. Fathy, and O. Kilic, "An Electromagnetic Model of Human Vital Signs Detection and Its Experimental Validation", *IEEE Journal on Emerging and Selected Topics in Circuits and Systems*, vol. 8, no. 2, pp. 338–349, Jun. 2018.

[225] S. Jenkin, "The Effect of Temperature on the Chronic Hypoxia-induced Changes to pH/CO2-sensitive Fictive Breathing in the Cane Toad (Bufo marinus)", *Systems Biology*, 2011.

[226] J. Stinner and L. Hartzler, "Effect of temperature on pH and electrolyte concentration in air-breathing ectotherms", *Journal of Experimental Biology*, vol. 203, no. 13, pp. 2065–2074, Jul. 2000.

[227] S. G. Reid, W. K. Milsom, J. T. Meier, S. Munns, and N. H. West, "Pulmonary vagal modulation of ventilation in toads (Bufo marinus)", *Respiration Physiology*, vol. 120, no. 3, pp. 213–230, May 2000.

[228] T. Nagatsuma, H. Ito, and T. Ishibashi, "High-power RF photodiodes and their applications", *Laser & Photonics Review*, vol. 3, no. 1-2, pp. 123–137, Feb. 2009.

[229] V. Camarchia, R. Quaglia, A. Piacibello, D. P. Nguyen, H. Wang, and A.-V. Pham, "A Review of Technologies and Design Techniques of Millimeter-Wave Power Amplifiers", *IEEE Transactions on Microwave Theory and Techniques*, vol. 68, no. 7, pp. 2957–2983, Jul. 2020.

[230] C. Vagionas, A. Tsakyridis, T. Chrysostomidis, I. Roumpos, K. Fotiadis, A. Manolis, J. Mu, M. Dijkstra, S. Garcia Blanco, R. M. Oldenbeuving, P. W. L. van Dijk, C. G. H. Roeloffzen, K. Vyrsokinos, N. Pleros, and T. Alexoudi, "Lossless 1 by 4 Silicon Photonic ROADM Based on a Monolithic Integrated Erbium Doped

Waveguide Amplifier on a Si3N4 Platform", *Journal of Lightwave Technology*, vol. 40, no. 6, pp. 1718–1725, Mar. 2022.

[231] S. Wang, A. Pohl, T. Jaeschke, M. Czaplik, M. Kony, S. Leonhardt, and N. Pohl, "A novel ultra-wideband 80 GHz FMCW radar system for contactless monitoring of vital signs", in *2015 37th Annual International Conference of the IEEE Engineering in Medicine and Biology Society (EMBC)*, vol. 2015-Novem, IEEE, Aug. 2015, pp. 4978–4981.

[232] Z. Peng, J. M. Munoz-Ferreras, Y. Tang, C. Liu, R. Gomez-Garcia, L. Ran, and C. Li, "A Portable FMCW Interferometry Radar With Programmable Low-IF Architecture for Localization, ISAR Imaging, and Vital Sign Tracking", *IEEE Transactions on Microwave Theory and Techniques*, vol. 65, no. 4, pp. 1334–1344, Apr. 2017.

[233] F.-K. Wang, T.-S. Horng, K.-C. Peng, J.-K. Jau, J.-Y. Li, and C.-C. Chen, "Single-Antenna Doppler Radars Using Self and Mutual Injection Locking for Vital Sign Detection With Random Body Movement Cancellation", *IEEE Transactions on Microwave Theory and Techniques*, vol. 59, no. 12, pp. 3577–3587, Dec. 2011.

[234] T.-Y. J. Kao, A. Y.-K. Chen, Y. Yan, T.-M. Shen, and J. Lin, "A flip-chip-packaged and fully integrated 60 GHz CMOS micro-radar sensor for heartbeat and mechanical vibration detections", in *2012 IEEE Radio Frequency Integrated Circuits Symposium*, IEEE, Jun. 2012, pp. 443–446.

[235] N. Kuse and M. E. Fermann, "Frequency-modulated comb LIDAR", *APL Photonics*, vol. 4, no. 10, p. 106 105, Oct. 2019, ISSN: 2378-0967. DOI: 10.1063/1.5120321. [Online]. Available: http://aip.scitation.org/doi/10.1063/1.5120321.

[236] J. Li, X. Xue, B. Yang, M. Wang, S. Li, and X. Zheng, "Broadband linear frequency-modulated waveform generation based on optical frequency comb assisted spectrum stitching", *Optics Express*, vol. 30, no. 13, p. 24 145, Jun. 2022, ISSN: 1094-4087.

[237] C. Wang, M. Zhang, X. Chen, M. Bertrand, A. Shams-Ansari, S. Chandrasekhar, P. Winzer, and M. Lončar, "Integrated lithium niobate electro-optic modulators operating at CMOS-compatible voltages", *Nature*, vol. 562, no. 7725, pp. 101–104, Oct. 2018, ISSN: 0028-0836. DOI: 10.1038/s41586-018-0551-y. [Online]. Available: http://www.nature.com/articles/s41586-018-0551-y.

[238] A. E. Hassanien, E. Chow, S. Link, Y. Yang, L. Goddard, and S. Gong, "Wideband Acousto-Optical Modulation on Suspended Thin-Film Lithium Niobate", in *Conference on Lasers and Electro-Optics*, Washington, D.C.: Optica Publishing Group, 2021, SW3H.7, ISBN: 978-1-943580-91-0. DOI: 10.1364/CLEO{_}SI.2021.SW3H.7. [Online]. Available: https://opg.optica.org/abstract.cfm?URI=CLEO_SI-2021-SW3H.7.

[239] L. Shao, S. W. Ding, Y. Ma, Y. Zhang, N. Sinclair, and M. Lončar, "Thermal Modulation of Gigahertz Surface Acoustic Waves on Lithium Niobate", *Physical Review Applied*, vol. 18, no. 5, p. 054 078, Nov. 2022, ISSN: 2331-7019. DOI: 10.1103/PhysRevApplied.18.054078. [Online]. Available: https://link.aps.org/doi/10.1103/PhysRevApplied.18.054078.

[240] G. Bashan, H. H. Diamandi, Y. London, K. Sharma, K. Shemer, E. Zehavi, and A. Zadok, "Forward stimulated Brillouin scattering and opto-mechanical non-reciprocity in standard polarization maintaining fibres", *Light: Science & Applications*, vol. 10, no. 1, p. 119, Jun. 2021, ISSN: 2047-7538. DOI: 10.1038/s41377-021-00557-y. [Online]. Available: https://www.nature.com/articles/s41377-021-00557-y.

[241] L. A. Sánchez, A. Díez, J. L. Cruz, and M. V. Andrés, "High accuracy measurement of Poisson's ratio of optical fibers and its temperature dependence using forward-stimulated Brillouin scattering", *Optics Express*, vol. 30, no. 1, p. 42, Jan. 2022, ISSN: 1094-4087. DOI: 10.1364/OE.442295. [Online]. Available: https://opg.optica.org/abstract.cfm?URI=oe-30-1-42.

[242] C. K. Lai, M. Merklein, A. Casas-Bedoya, Y. Liu, S. J. Madden, C. G. Poulton, M. J. Steel, and B. J. Eggleton, "Optimizing performance for an on-chip stimulated Brillouin scattering-based isolator", *Journal of the Optical Society of America B*, vol. 40, no. 3, p. 523, Mar. 2023, ISSN: 0740-3224. DOI: 10.1364/JOSAB.479629. [Online]. Available: https://opg.optica.org/abstract.cfm?URI=josab-40-3-523.

[243] H. Cho, Y.-W. Seo, B. V. Kumar, and R. R. Rajkumar, "A multi-sensor fusion system for moving object detection and tracking in urban driving environments", in *2014 IEEE International Conference on Robotics and Automation (ICRA)*, IEEE, May 2014, pp. 1836–1843, ISBN: 978-1-4799-3685-4. DOI: 10.1109/ICRA.2014.6907100.

[Online]. Available: http://ieeexplore.ieee.org/document/6907100/.

[244] J. Kocic, N. Jovicic, and V. Drndarevic, "Sensors and Sensor Fusion in Autonomous Vehicles", in *2018 26th Telecommunications Forum (TELFOR)*, IEEE, Nov. 2018, pp. 420–425, ISBN: 978-1-5386-7171-9. DOI: 10.1109/TELFOR.2018.8612054. [Online]. Available: https://ieeexplore.ieee.org/document/8612054/.

[245] T. Nagatsuma, G. Ducournau, and C. C. Renaud, "Advances in terahertz communications accelerated by photonics", *Nature Photonics*, vol. 10, no. 6, pp. 371–379, Jun. 2016, ISSN: 1749-4885. DOI: 10.1038/nphoton.2016.65. [Online]. Available: https://www.nature.com/articles/nphoton.2016.65.

[246] S. Lee, S. Hara, T. Yoshida, S. Amakawa, R. Dong, A. Kasamatsu, J. Sato, and M. Fujishima, "An 80-Gb/s 300-GHz-Band Single-Chip CMOS Transceiver", *IEEE Journal of Solid-State Circuits*, vol. 54, no. 12, pp. 3577–3588, Dec. 2019, ISSN: 0018-9200. DOI: 10.1109/JSSC.2019.2944855. [Online]. Available: https://ieeexplore.ieee.org/document/8869897/.

[247] K. B. Cooper, R. J. Dengler, N. Llombart, A. Talukder, A. V. Panangadan, C. S. Peay, I. Mehdi, and P. H. Siegel, "Fast high-resolution terahertz radar imaging at 25 meters", M. Anwar, N. K. Dhar, and T. W. Crowe, Eds., Apr. 2010, 76710Y. DOI: 10.1117/12.850395. [Online]. Available: http://proceedings.spiedigitallibrary.org/proceeding.aspx?doi=10.1117/12.850395.

[248] R. Kaname, L. Yi, and T. Nagatsuma, "Investigation on 600-GHz-Band FMCW Photonic Radar System for a Flexible Inspection Distance", in *2021 IEEE Asia-Pacific Microwave Conference (APMC)*, IEEE, Nov. 2021, pp. 437–439, ISBN: 978-1-6654-3782-0. DOI: 10.1109/APMC52720.2021.9661657. [Online]. Available: https://ieeexplore.ieee.org/document/9661657/.

[249] F. Ellrich, M. Bauer, N. Schreiner, A. Keil, T. Pfeiffer, J. Klier, S. Weber, J. Jonuscheit, F. Friederich, and D. Molter, "Terahertz Quality Inspection for Automotive and Aviation Industries", *Journal of Infrared, Millimeter, and Terahertz Waves*, vol. 41, no. 4, pp. 470–489, Apr. 2020, ISSN: 1866-6892. DOI: 10.1007/s10762-019-00639-4. [Online]. Available: http://link.springer.com/10.1007/s10762-019-00639-4.

[250] D. Nüßler and J. Jonuscheit, "Terahertz based non-destructive testing (NDT)", *tm - Technisches Messen*, vol. 88, no. 4, pp. 199–210, Apr. 2021, ISSN: 2196-7113. DOI: 10.1515/teme-2019-0100. [Online]. Available: https://www.degruyter.com/document/doi/10.1515/teme-2019-0100/html.

[251] H. Ito, T. Furuta, F. Nakajima, K. Yoshino, and T. Ishibashi, "Photonic generation of continuous THz wave using uni-traveling-carrier photodiode", *Journal of Lightwave Technology*, vol. 23, no. 12, pp. 4016–4021, Dec. 2005, ISSN: 0733-8724. DOI: 10.1109/JLT.2005.858221. [Online]. Available: http://ieeexplore.ieee.org/document/1566728/.

[252] A. J. Deninger, A. Roggenbuck, S. Schindler, and S. Preu, "2.75 THz tuning with a triple-DFB laser system at 1550 nm and InGaAs photomixers", *Journal of Infrared, Millimeter, and Terahertz Waves*, vol. 36, no. 3, pp. 269–277, Mar. 2015, ISSN: 1866-6892. DOI: 10.1007/s10762-014-0125-5. [Online]. Available: http://link.springer.com/10.1007/s10762-014-0125-5.

[253] H. Ito and T. Ishibashi, "InP/InGaAs Fermi-level managed barrier diode for broadband and low-noise terahertz-wave detection", *Japanese Journal of Applied Physics*, vol. 56, no. 1, p. 014101, Jan. 2017, ISSN: 0021-4922. DOI: 10.7567/JJAP.56.014101. [Online]. Available: https://iopscience.iop.org/article/10.7567/JJAP.56.014101.

[254] L. Yi, R. Kaname, R. Mizuno, Y. Li, M. Fujita, H. Ito, and T. Nagatsuma, "Ultra-Wideband Frequency Modulated Continuous Wave Photonic Radar System for Three-Dimensional Terahertz Synthetic Aperture Radar Imaging", *Journal of Lightwave Technology*, vol. 40, no. 20, pp. 6719–6728, Oct. 2022, ISSN: 0733-8724. DOI: 10.1109/JLT.2022.3193397. [Online]. Available: https://ieeexplore.ieee.org/document/9839440/.

[255] D.-C. Shin, B. S. Kim, H. Jang, Y.-J. Kim, and S.-W. Kim, "Photonic comb-rooted synthesis of ultra-stable terahertz frequencies", *Nature Communications*, vol. 14, no. 1, p. 790, Feb. 2023, ISSN: 2041-1723. DOI: 10.1038/s41467-023-36507-y. [Online]. Available: https://www.nature.com/articles/s41467-023-36507-y.

Appendix A

# Appendix - Animal Ethics Approval

THE UNIVERSITY OF SYDNEY

RESEARCH INTEGRITY &
ETHICS ADMINISTRATION

Animal Research Authority (ARA)

This ARA must be kept in the facility/farm where animals are housed or carried with you during field work

# Animal Research Authority

| | |
|---|---|
| **Project title:** | Contact-less Vital Sign Detection using Photonic Radar and LiDAR |
| **Project number:** | 2022/2090 |
| **Chief investigator:** | Benjamin Eggleton |
| **ARA approval period:** | 27 April 2022 – 27 April 2023<br>An annual report must be submitted and approved prior to the ARA expiration date above. |
| **Project type:** | Experimental (non-wildlife) |

In compliance with Section 27 of the NSW *Animal Research Act 1985*, this Animal Research Authority (ARA) remains in force for a period of 12 months, unless cancelled sooner.

Renewal of the ARA is conditional upon submission of a satisfactory annual report to the AEC in accordance with the *Australian code for the care and use of animals for scientific purposes 8th Edition 2013*.

Research Integrity & Ethics Administration
Research Portfolio
Level 3, Michael Spence Building (F23)
The University of Sydney
NSW 2006 Australia

**T** +61 2 8627 8174
**F** +61 2 8627 8177
**E** animal.ethics@sydney.edu.au
intranet.sydney.edu.au/ethics

ABN 15 211 513 464
CRICOS 00026A

Appendix B

# Appendix - Electric Field of the Demodulated Signal based on Stitched Chirp

$$E_{\text{tx}}(t) = \alpha \sum_{n=0}^{N-1} \text{rect}\left(\frac{t - n\tau_{\text{loop}}}{\tau_{\text{pulse}}}\right) \cdot \exp\left[i2\pi f_{\text{tx}}(t) \cdot (t - n\tau_{\text{loop}})\right] \quad \text{(B.1)}$$

and

$$f_{\text{tx}}(t) = f_{\text{c}} + n \cdot \Delta f + k \cdot (t - n\tau_{\text{loop}}) \quad \text{(B.2)}$$

where $f_{\text{c}}$ is the laser carrier frequency, $n$ is the round-trip number, $\Delta f$ is the frequency shift per round-trip time, $k = bw/\tau_{\text{pulse}}$ is the chirp rate, and $\tau_{\text{loop}}$ is the fibre cavity round-trip time.

Assume a stationary target is located at a distance $d$ and the speed of light propagation in free space is $c$, so a time delay $\tau$, where

$$\tau = \frac{2 \cdot d}{c} \quad \text{(B.3)}$$

Then, the received signal can be written as

$$\begin{aligned} E_{\text{rx}}(t) = \beta \sum_{n=0}^{N-1} \text{rect}\left(\frac{t - n\tau_{\text{loop}} - \tau}{\tau_{\text{pulse}}}\right) \\ \times \exp\left[i2\pi f_{\text{tx}}(t - \tau) \cdot (t - n\tau_{\text{loop}} - \tau)\right] \end{aligned} \quad \text{(B.4)}$$

Assume the delayed chirp signal in each sub-pulse has not reached the beginning of the following adjacent sub-pulse, which means $\tau_{\text{pulse}} + \tau \leq$

$\tau_{\text{loop}}$. Therefore, the following changes apply in the photodetection.

$$\sum_{n=0}^{N-1} \text{rect}\left(\frac{t - n\tau_{\text{loop}} - \tau}{\tau_{\text{pulse}}}\right) \Rightarrow \sum_{n=0}^{N-1} \text{rect}\left(\frac{t - n\tau_{\text{loop}} - \tau}{\tau_{\text{pulse}} - \tau}\right) \tag{B.5}$$

The coherent detection is a process that mixes the transmitted and received signals through an optical coupler and sends them into a photodetector. Thus the demodulated signal can be expressed as

$$E_{\text{pd}}(t) \propto \text{Re}\left\{[E_{\text{tx}}(t) + E_{\text{rx}}(t)] \cdot \text{conj}\left[(E_{\text{tx}}(t) + E_{\text{rx}}(t)\right]\right\} \tag{B.6}$$

However, the transmitted signal also mixes with the leakage from the cross-talk. Therefore, the equation can be rewritten as follows

$$E_{\text{pd}}(t) \propto \text{Re}\left\{[E_{\text{tx}}(t) + E_{\text{rx}}(t) + E_{\text{leak}}(t)] \cdot \text{conj}\left[(E_{\text{tx}}(t) + E_{\text{rx}}(t) + E_{\text{leak}}(t)\right]\right\} \tag{B.7}$$

where

$$\begin{aligned} E_{\text{leak}}(t) = \gamma \sum_{n=0}^{N-1} \text{rect}\left(\frac{t - n\tau_{\text{loop}} - \tau_{\text{leak}}}{\tau_{\text{pulse}}}\right) \\ \times \exp\left[i2\pi f_{\text{tx}}(t - \tau_{\text{leak}}) \cdot (t - n\tau_{\text{loop}} - \tau_{\text{leak}})\right] \end{aligned} \tag{B.8}$$

Now, we expand Eq. (B.7)

$$\begin{aligned} E_{\text{pd}}(t) \propto 2\alpha\beta \sum_{n=0}^{N-1} \text{rect}\left(\frac{t - n\tau_{\text{loop}} - \tau}{\tau_{\text{pulse}} - \tau}\right) \\ \times \left[\cos(\omega_{\text{tx}})\cos(\omega_{\text{rx}}) + sin(\omega_{\text{tx}})\sin(\omega_{\text{rx}})\right] \\ +2\alpha\gamma \sum_{n=0}^{N-1} \text{rect}\left(\frac{t - n\tau_{\text{loop}} - \tau_{\text{leak}}}{\tau_{\text{pulse}} - \tau_{\text{leak}}}\right) \\ \times \left[\cos(\omega_{\text{tx}})\cos(\omega_{\text{leak}}) + sin(\omega_{\text{tx}})sin(\omega_{\text{leak}})\right] \\ +2\beta\gamma \sum_{n=0}^{N-1} \text{rect}\left(\frac{t - n\tau_{\text{loop}} - \max(\tau_{\text{leak}}, \tau)}{\tau_{\text{pulse}} - |\tau_{\text{leak}} - \tau|}\right) \\ \times \left[\cos(\omega_{\text{rx}})\cos(\omega_{\text{leak}}) + \cos(\omega_{\text{rx}})\cos(\omega_{\text{leak}})\right] \end{aligned} \tag{B.9}$$

Then,

$$
\begin{aligned}
E_{\mathrm{pd}}(t) \propto\ & 2\alpha\beta \sum_{n=0}^{N-1} \mathrm{rect}\left(\frac{t-n\tau_{\mathrm{loop}}-\tau}{\tau_{\mathrm{pulse}}-\tau}\right)\left[\cos(\omega_{\mathrm{tx}}-\omega_{\mathrm{rx}})\right] \\
& +2\alpha\gamma \sum_{n=0}^{N-1} \mathrm{rect}\left(\frac{t-n\tau_{\mathrm{loop}}-\tau_{\mathrm{leak}}}{\tau_{\mathrm{pulse}}-\tau_{\mathrm{leak}}}\right)\left[\cos(\omega_{\mathrm{tx}}-\omega_{\mathrm{leak}})\right] \\
& +2\beta\gamma \sum_{n=0}^{N-1} \mathrm{rect}\left(\frac{t-n\tau_{\mathrm{loop}}-\max(\tau_{\mathrm{leak}},\tau)}{\tau_{\mathrm{pulse}}-|\tau_{\mathrm{leak}}-\tau|}\right)\left[\cos(\omega_{\mathrm{rx}}-\omega_{\mathrm{leak}})\right]
\end{aligned}
\tag{B.10}
$$

Then,

$$
\begin{aligned}
E_{\mathrm{pd}}(t) \propto\ & 2\alpha\beta \sum_{n=0}^{N-1} \mathrm{rect}\left(\frac{t-n\tau_{\mathrm{loop}}-\tau}{\tau_{\mathrm{pulse}}-\tau}\right) \\
& \cdot\cos\left[2\pi\cdot 2k\tau\cdot t+2\pi(f_{\mathrm{c}}-k\tau)\tau+2\pi n(\Delta f\tau-2k\tau_{\mathrm{loop}})\right] \\
& +2\alpha\gamma \sum_{n=0}^{N-1} \mathrm{rect}\left(\frac{t-n\tau_{\mathrm{loop}}-\tau_{\mathrm{leak}}}{\tau_{\mathrm{pulse}}-\tau_{\mathrm{leak}}}\right) \\
& \cdot\cos\left[2\pi\cdot 2k\tau_{\mathrm{leak}}\cdot t+2\pi(f_{\mathrm{c}}-k\tau_{\mathrm{leak}})\tau_{\mathrm{leak}}+2\pi n(\Delta f\tau_{\mathrm{leak}}-2k\tau_{\mathrm{loop}})\right] \\
& +2\beta\gamma \sum_{n=0}^{N-1} \mathrm{rect}\left(\frac{t-n\tau_{\mathrm{loop}}-\max(\tau_{\mathrm{leak}},\tau)}{\tau_{\mathrm{pulse}}-|\tau_{\mathrm{leak}}-\tau|}\right) \\
& \cdot\cos\left\{2\pi\cdot\Delta\tau\cdot t+2\pi\left[f_{\mathrm{c}}-k(\tau+\tau_{\mathrm{leak}})\right]\Delta\tau+2\pi n\left[(\Delta f-2k\tau_{\mathrm{loop}})\right]\Delta\tau\right\}
\end{aligned}
\tag{B.11}
$$

where $\Delta\tau = \tau_{\mathrm{leak}} - \tau$. We simplify the expression by removing the constant phase term and the terms approaching zero. $\tau_{\mathrm{leak}}$ and $\tau_{\mathrm{loop}}$ are constant terms but can be tuned by altering the experimental setup. In the experiment, $f_{\mathrm{c}}$ is the laser carrier frequency around 193 THz. In reality, $f_{\mathrm{c}}$ is a time-dependent variable due to the laser's linewidth, which could translate into the demodulated signal's phase noise. Here, we assume the variation period of $f_{\mathrm{c}}$ is much longer than the whole N-pulse duration, $N\cdot\tau_{\mathrm{pulse}}$. Thus we could simplify them into constant phase terms, i.e., $\theta_1 \triangleq 2\pi(f_{\mathrm{c}}-k\tau)\tau$, $\theta_2 \triangleq 2\pi(f_{\mathrm{c}}-k\tau_{\mathrm{leak}})\tau_{\mathrm{leak}}$, and $\theta_3 \triangleq 2\pi\left[f_{\mathrm{c}}-k(\tau+\tau_{\mathrm{leak}})\right]\Delta\tau$. Because the cross-talk from the circulator is around $-50$ dB, which means $\gamma < \alpha/10^5$. Therefore, the last terms could

be omitted. Thus, Eq. (B.11) can be rewritten as

$$\begin{aligned} E_{\mathrm{pd}}(t) \propto 2\alpha\beta \sum_{n=0}^{N-1} \mathrm{rect}\left(\frac{t - n\tau_{\mathrm{loop}} - \tau}{\tau_{\mathrm{pulse}} - \tau}\right) \\ \times \cos\Big[2\pi \cdot 2k\tau \cdot t + \theta_1 + 2\pi n(\Delta f \tau - 2k\tau_{\mathrm{loop}})\Big] \\ + 2\alpha\gamma \sum_{n=0}^{N-1} \mathrm{rect}\left(\frac{t - n\tau_{\mathrm{loop}} - \tau_{\mathrm{leak}}}{\tau_{\mathrm{pulse}} - \tau_{\mathrm{leak}}}\right) \\ \times \cos\Big[2\pi \cdot 2k\tau_{\mathrm{leak}} \cdot t + \theta_2 + 2\pi n(\Delta f \tau_{\mathrm{leak}} - 2k\tau_{\mathrm{loop}})\Big] \end{aligned} \tag{B.12}$$

Since, $\mathcal{F}(af + bg) = a\mathcal{F}f + b\mathcal{F}g$, where $\mathcal{F}$ is the Fourier transform operator. We will deduce the first term here, given the terms are similar.

$$\begin{aligned} \mathcal{F}\Big[f_1(t)\Big] = 2\alpha\beta\mathcal{F}\Bigg\{ \sum_{n=0}^{N-1} \mathrm{rect}\left(\frac{t - n\tau_{\mathrm{loop}} - \tau}{\tau_{\mathrm{pulse}} - \tau}\right) \\ \times \cos\Big[2\pi \cdot 2k\tau \cdot t + \theta_1 + 2\pi n(\Delta f \tau - 2k\tau_{\mathrm{loop}})\Big]\Bigg\} \end{aligned} \tag{B.13}$$

Appendix C

# Appendix - Commercial Prospects and Market Analysis for Sensor Fusion Systems Employing Photonic Radar and Cameras in Vital Sign Detection and Situational Awareness

**Age care facility -** In Australia, over 1.3 million individuals utilised aged care services during the period of 2019-2020, as reported by the Australian Institute of Health and Welfare (AIHW). This figure continues to grow, with the population of Australians over the age of 65 projected to reach approximately 16 million by 2025 and 18 million by 2040 (AIHW, IBIS World). A parallel report by KPMG revealed that the aged care market expanded substantially from 487 providers in 2016 to 906 as of June 2021. However, in the 2021 financial year (FY21), more than 58 per cent of aged care providers reported operating losses due to high demand and workforce shortages. Consequently, our robust vital sign alerting system holds the potential to significantly reduce the number of required carers, particularly during night-time hours.

**Livestock -** Rearing livestock is a high-risk and resource-intensive endeavour. According to an estimation by Meat & Livestock Australia (MLA) in the 2021 financial year (FY21), up to 15 per cent of livestock succumbed to premature death, resulting in an approximate annual loss of AUD

4 billion for farmers and abattoirs. This figure represents 5.5 per cent of the total agricultural industry revenue (AUD 73 billion) generated in 2021. Studies have indicated that nearly 5 per cent of these fatalities (approximately AUD 250 million per year) were attributable to preventable causes, such as illness, injury, birth complications, and attacks by wild animals. However, existing technologies related to livestock management are expensive and ineffective in actively monitoring the vital signs of livestock to avert death and losses. In conjunction with computer vision, our photonic radar approach is ideal for monitoring livestock vital signs throughout the breeding, raising, and transportation cycle. This system operates under virtually all weather conditions (although radar is less effective during extreme weather than cameras and infrared), offering enhanced accuracy and multi-target detection capabilities to provide early warning to end-users regarding signs of disease and wild animal attacks.

**Sleep apnoea diagnostics and monitoring -** Sleep apnoea is a potentially severe sleep disorder characterised by recurrent cessation and resumption of breathing. Research (https://www.healthdirect.gov.au/obstructive-sleep-apnoea) indicates that individuals with untreated obstructive sleep apnoea (OSA) face an elevated risk of additional medical complications, including diabetes, stroke, poor memory, reduced concentration, headaches, depression, and even personality alterations. In Australia, 1 in 4 people experience apnoea issues, resulting in an estimated AUD 541 million in burdens on the Australian Medicare system (accounting for 57 per cent of the cost of treating sleep disorders).

However, existing apnoea diagnostic methods are exceedingly uncomfortable and heavily dependent on contact sensors. Consequently, our non-contact sensor fusion-based vital sign system could substantially reduce the number of contact sensors required (retaining only EEG for brain activity monitoring), offering enhanced comfort and promising accuracy. More importantly, such a device can also be employed beyond medical diagnostic settings within private homes for early detection and monitoring during rehabilitation and treatment.

# Responses to Referee Report

PhD Thesis Title: Millimetre-Resolution Photonics-Assisted Radar

First and foremost, I would like to express my deepest appreciation for both reviewers' thorough review of my thesis. I am thrilled to receive such positive feedback from all two reviewers. Here, I present detailed point-to-point responses to the comments raised by Reviewer #2. My responses are highlighted in blue, and any changes made to the manuscript are also highlighted for easy identification.

**Responses to Reviewer #2**

General Comment R1.1: There are 7 chapters in the thesis with the first 3 chapters providing the background and theoretical study of various topics within the field that form the foundation for the last 4 chapters. The last 4 chapters formed the basis of the proposed techniques and the corresponding experimental results. Based on this configuration, I find that the readability is not as smooth as the background information/theory of the related schemes in the later chapters has to be constantly referred to the earlier chapters.

**Response**: I greatly appreciate the reviewer's suggestion. I have made necessary changes to the last 4 chapters.

Changes to the manuscript:

In Chapter 4, page 80: This chapter delves into a photonic stepped-frequency radar system based on a frequency-shifting loop. We start from its conceptual implementation to experimental radar ranging and 2D imaging demonstrations, highlighting the potential of an approach that offers a broad bandwidth using a relatively low-complexity system setup, ideal for high refresh rate 2D radar imaging applications. Notably, the system explored in this chapter was developed using single-mode fibre without using polarisation-maintaining components, thus highlighting the effects of polarisation scrambling and polarisation-dependent noise originating from such a non-polarisation-maintaining system, setting the stage for substantial performance enhancements discussed in Chapter 5.

General Comment R1.2: The experiments carried out in the thesis were impressive with very convincing results. Although the final results were outstanding, I find that there were gaps from the description of the proposed schemes to the actual experimental demonstration for all the technical chapters (chapter 4-6) presented. For instance, in chapter 5, there is lack of characterisation of the polarisation maintaining fibre-based loop – i.e. improvement in the stability compared to without PM fibre.

**Response**: I appreciate these insightful comments and have edited description of the system throughout the technical chapters.

Chapter 5 compares the stability and attributes of systems utilising PM components with those not using them. This comparison is based on the achievable number of recirculations and the enhanced SNR of the generated signal to understand the influence of polarisation scrambling and the polarisation-dependent amplified spontaneous emission noise, as presented in Figure 5.2 and Figure 5.3. It should be

noted in the manuscript that both Figure 5.2 and Figure 5.3 depict experimental results, showcasing the differences in stability and characteristics between PM and non-PM systems, which have been clarified in the manuscript.

Changes to the manuscript:

In Chapter 5, page 102: In the subsequent discussion, we construct two photonic stepped-frequency signal generators based on the schematic depicted in Figure 5.1a, both with and without polarisation-maintaining components. We evaluate system stability improvements by examining the achievable number of recirculations (the bandwidth) and the improved SNR of the generated signal, aiming to understand the impact of polarisation scrambling and the polarisation-dependent amplified spontaneous emission noise.

General Comment R1.3: For Chapter 6, with the incorporation of LIDAR as a comparison, there was very limited discussion and minimal information on the LIDAR system that was used. How about the ambiguity range with this combined system? Is it better than before? How about the power sensitivity?

**Response**: I have added the following discussion to address this concern.

Changes to the manuscript:

In Chapter 6, page 123: The proposed radar system can also be employed for LiDAR sensing, as shown in Figure 6.8. In this context, RF components like the RF amplifier and antennas no longer dictate the system's bandwidth. Both the radar and LiDAR systems utilise the same optical source. The optically generated SF signal, boasting a bandwidth of 25 GHz, is directed to an optical circulator, which is then guided by a 2D scanning mirror (Galvo scanner) to focus the beam on the buccal area of the cane toad, thereby detecting its movements. Scattered light returns to the circulator and mixes with a tap of the transmitted optical signal for coherent LiDAR demodulation. The ambiguity range of the LiDAR is consistent with that of the radar, as they share the same frequency shift (100 MHz) that ultimately determines the ambiguity range. As a result, the integrated sensor system retains this ambiguity range.

Notably, the energy of the received LiDAR signal is influenced by several factors related to the objects, including surface roughness, reflectivity, and the aperture of the fibre collimator, all of which play pivotal roles. In our experiment, we employ an optical amplifier to elevate the energy level to approximately 20 mW, well below the safety threshold for this wavelength, even though the peak power can surge to kilowatt levels. Consequently, the ambiguity range can be expanded by minimising the step size, for instance, by using AOMs with opposing frequency shifts. Simultaneously, by augmenting the optical power on the transmitter end, we can increase both the received signal's energy level and the detection range.

General Comment R1.4: More minor chapter-by-chapter comments are given below and hopefully these are useful to further improve the quality of the thesis.

Non-typo comment: A table that summarises the current achievements of MWP radar would be a good considering you are benchmarking your work against other MWP radars. This would be nice way to start of Chapter 4.

**Response**:

- All the typos throughout the thesis mentioned by the reviewer have been addressed.
- As recommended by the reviewer, a comparative table (Table 3.1), accompanied by illustrative figures depicted in Figure 3.7, has been incorporated into Chapter 3.

Changes to the manuscript:

In Chapter 3, page 75 – 77:

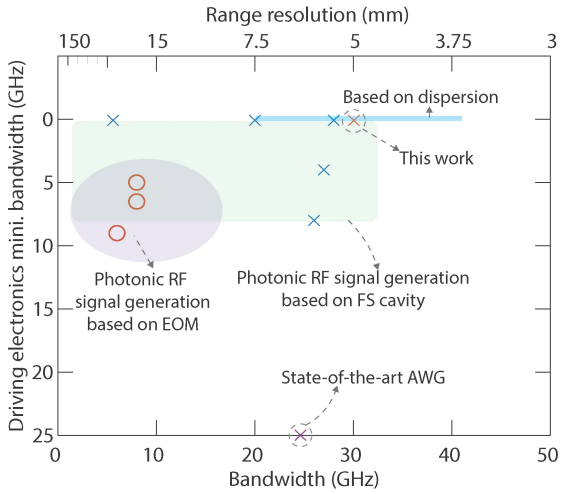


*Figure 3.7 Comparison of the photonics-based wideband RF signal generation in terms of the speed of the system's driving electronics and the radar signal bandwidth across various photonic approaches.*

We provide a table that compares the system used in this thesis with several other photonic approaches previously mentioned for generating radar signals (Table 3.1). Figure 3.7 illustrates a figure of merit based on Table 3.1. This figure contrasts the photonics-based wideband RF signal generation by evaluating the speed of the system's driving electronics and the showcased radar signal bandwidth across various photonic strategies. These include using frequency-shifting cavities, laser sweeping, EOMs, and engineered fibre dispersion.

| Demonstrated bandwidth (GHz) | Formality | linearity (%) | Mini. RF bandwidth (GHz) | Reference |
|---|---|---|---|---|
| **30** | **SF** | **0.0036** | **0.1** | **This Work** |
| Photonic RF signal generation based on FS cavity | | | | |
| 5.6 | SF | NA | 0.08 | [2] |
| 26 | LFM,SFCS | NA | 8 | [130] |
| 20 | SF | NA | 0.08 | [131] |
| 27 | SF | NA | 4 | [132] |
| ¿28 | LFM | NA | 0.08 | [139] |
| Photonic RF signal generation based on laser sweeping | | | | |
| 4 | LFM | NA | NA | [141] |
| 2 | LFM | 7.8** | NA | [1] |
| 7.5 | LFM | NA | NA | [119] |
| 18.5 | LFM | NA | 0.12 | [142] |
| Photonic RF signal generation based on dispersion | | | | |
| ¿30 | LFM | NA | NA | [106] |
| Photonic RF signal generation-based EOM | | | | |
| 8 | LFM | NA | 12 Gbit/s | [127] |
| 6 | LFM | NA | 9 | [137] |
| 8 | LFM | NA | 6.5 | [123] |
| State-of-the-art AWG | | | | |
| 25 | SF | 0.0013 | 25 | Keysight |

*Table 3.1 Comparison with reported photonic approaches. SF, stepped-frequency; LFM, linear-frequency modulated waveform; CW, continuous wave; NA, data not available or not mentioned in the literature; **, the linearity in the reference is the ratio between the maximum frequency deviation to the total bandwidth; -, not applicable.*

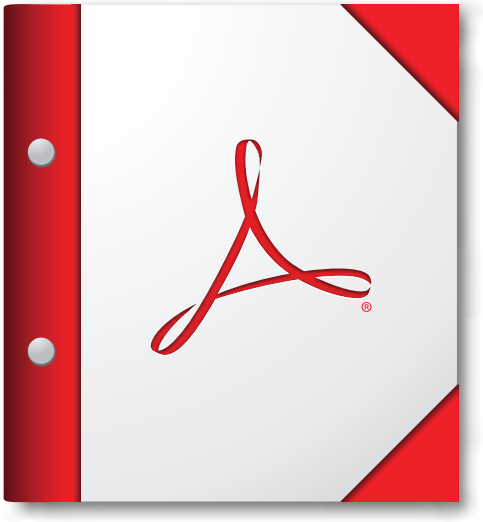

**For the best experience, open this PDF portfolio in Acrobat X or Adobe Reader X, or later.**

Get Adobe Reader Now!